Magnetism in Quantum Materials Probed by X-ray and Neutron Scattering

Marein C. Rahn

A thesis submitted for the degree of
Doctor of Philosophy

Department of Physics
University of Oxford
Trinity Term 2017

Magnetism in Quantum Materials Probed by X-ray and Neutron Scattering

MAREIN C. RAHN
Jesus College, University of Oxford
DPhil Thesis, Trinity Term 2017

Abstract

In his programmatic article *More Is Different* (1972), Nobel laureate P. W. Anderson captured the fundamental interest in quantum matter in a nutshell [1, 2]. The central motive in this field is *emergence*. In the inaugural volume of the homonymous journal, J. Goldstein defined this as "the arising of novel and coherent structures, patterns and properties during the process of self-organization in complex systems" [3, 4]. Famously, the idea that the "the whole is greater than the sum of its parts" goes back to Aristotle's *metaphysics*, and it has served as a stimulating concept in 19th century biology [5], economics [6] and philosophy [7].

The study of emergence in condensed matter physics is unique in that the underlying *complex systems* are sufficiently "simple" to be modelled from first principles [2, 8]. Notably, the emergent phenomena discovered in this field, such as high-temperature superconductivity [9], giant magnetoresistance [10], and strong permanent magnetism [11] have had an enormous impact on technology, and thus, society. Historically, there has been a distinction between materials with localized, strongly interacting (or *correlated*) electrons — and non-interacting, itinerant electronic states. In the last decade, several new states of matter have been discovered, which emerge not from correlations, but from peculiar symmetries (or *topology*) of itinerant electronic states [12]. The term *quantum materials* has therefore become popular to subsume these two strands of condensed matter physics [13]: Electronic correlations and topology.

In this thesis, I report investigations of four quantum materials which each illustrate present key interests in the field: The mechanism of high temperature superconductivity (1.1), the search for materials that combine both electronic correlations and non-trivial topology (1.2) and novel emergent phenomena that arise from the synergy of electronic correlations and a strong coupling of spin- and orbital degrees of freedom (1.3). The common factor and potential key to understanding these materials is *magnetism*. My experimental work is focused on neutron and x-ray scattering techniques, which are able to determine both *order* and *dynamics* of magnetic states at the atomic scale.

I illustrate the full scope of these methods with experimental studies at neutron and synchrotron radiation facilities. This includes both diffraction and spectroscopy, of either single- or polycrystalline samples. My in-depth analysis of each dataset is aided by structural, magnetic and charge transport experiments. Thus, I provide a quantitative characterization of magnetic fluctuations in an iron-based superconductor (3) and in two Dirac materials (4), and determine the magnetic order in a Dirac semimetal candidate (5) and a complex oxide (6). As a whole, these results demonstrate the elegant complementarity of modern scattering techniques. Although such methods have a venerable history, they are presently developing at a rapid pace. Several results of this thesis have only been enabled by very recent instrumental advances.

Magnetes Geheimnis, erkläre mir das!

Johann Wolfgang v. Goethe

Hanabusa Itchō (1652–1724), *Blind monks examining an elephant*

Acknowledgements

It has been a privilege to do my doctoral research at the University of Oxford and to work with the people of the Clarendon Laboratory. This would not have been possible without the financial support of the Clarendon Fund and the John Houghton award of Jesus College. For this I am very grateful.

I want to thank my supervisor Andrew Boothroyd for his guidance and patience. There have been very few days when he was not immediately available to give me useful feedback and encouraging advice. It will be tough not to be able to fall back on his intuition and profound experimental experience. For me, Andrew's diligence, rigour, integrity and approach to management have set a standard of scientific work to aspire to. I have also gained a lot of experience from the collaboration with Des McMorrow, and his students Christian Donnerer, James Vale and Davide Pincini. The ups and downs of weeks without sleep, spent together in narrow experimental cabins throughout Europe necessarily forge special friendships. I hope we will stay in contact for a long time.

Physics departments have to strike a balance between professionalism and casualness to enable good science. But this is less a choice of management, than an emergent phenomenon from interactions between the people sharing this workplace. The Clarendon Laboratory has been an extremely friendly and open environment. I have always felt encouraged to ask questions and to seek advice from colleagues of all Quantum Materials groups. Many, if not most of the breakthroughs in data interpretation, and ideas for new experiments in the last years have had their origin in such conversations. I hope that the staff and students in the Clarendon will uphold this style of interaction for many years. Some of the most useful tips and advice came from Roger Johnson, Steve Blundell and Radu and Amalia Coldea. Yulin Chen and Thorsten Hesjedal also gave me invaluable career advice. The common room would have been a less interesting place without Mike Glazer, Bill Hayes, Val Crowder and Sonia Trigueros. It would have been less silly without Thorsten Hesjedal and Amir Haghighirad.

I have been impressed and surprised by the dedication and enthusiasm of the scientific and technical staff at neutron and synchrotron radiation facilities. They have never been reluctant to work long hours and sacrifice weekends to ensure the best instrumental performance — even when the experimental plans were clearly too ambitious. My special thanks go to Sonia Francoual, Larissa Veiga, Jose Mardegan, David Reuther and Jörg Strempfer (formerly) in Hamburg, Jiri Kulda, Andrea Piovano, Emmanuelle Suard, Thomas Hansen, Kurt Kummer and Marco Moretti Sala in Grenoble, Pascal Manuel, Dmitry Khalyavin, Helen Walker, Devashibhai Adroja, Russell Ewings, Dave Keen, Matthias Gutmann, Steve Collins, Federica Fabrizi and Gareth Nisbet at Harwell and Enrico Schierle in Berlin. Notably, quantum materials are not discovered at beamlines, but in chemistry labs. Mine were provided by the expert crystal growers Dharmalingam Prabhakaran, Simon Clarke, Yanfeng Guo, Youguo Shi, Kazunari Yamaura and Amir Haghighirad.

I shall also take this opportunity to express my gratitude to the mentors who inspired the necessary enthusiasm to come thus far. This includes Claus Deser, Peter Böni, Taku J. Sato, Teruo Yamazaki and Christian Pfleiderer. Finally, I want to thank my family for their love and support. Memories of Saturdays spent in Blackwell's, walks to The Perch and our spontaneous wedding will always make Oxford a special place for Adriana and me.

Contents

1 Scientific context **1**
- 1.1 Iron-based high temperature superconductivity . . . 3
- 1.2 Dirac materials . . . 11
- 1.3 Heavy transition metal oxides . . . 22

2 Experimental methods **31**
- 2.1 Sample characterization . . . 33
- 2.2 Scattering from condensed matter . . . 37
- 2.3 Neutron scattering . . . 42
- 2.4 X-ray scattering . . . 51
- 2.5 Muon spin rotation and relaxation . . . 61

3 Strong $(\pi, 0)$ spin fluctuations in β-FeSe **65**
- 3.1 Introduction . . . 67
- 3.2 Inelastic neutron scattering on MERLIN, ISIS . . . 69
- 3.3 Resonant inelastic x-ray scattering at ID32, ESRF . . . 80
- 3.4 Conclusion . . . 91

4 Spin dispersion in the anisotropic Dirac semimetals AMnBi$_2$ (A=Ca,Sr) **95**
- 4.1 Introduction . . . 97
- 4.2 Characterization . . . 101
- 4.3 Inelastic neutron scattering at IN8 (ILL) . . . 102
- 4.4 Results and analysis . . . 104
- 4.5 Discussion . . . 109
- 4.6 Conclusion . . . 112

5 Magnetic ground state of Dirac semimetal candidate EuCd$_2$As$_2$ **115**
- 5.1 Introduction . . . 117
- 5.2 Structural, transport and magnetic measurements . . . 118
- 5.3 Resonant x-ray scattering at P09 (PETRA-III) . . . 124
- 5.4 Results . . . 129

5.5 Discussion . . . 132
5.6 Conclusion . . . 139

6 Varying degrees of magnetic frustration in two polymorphs of $Ca_2Os_2O_7$ 141
6.1 Introduction . . . 143
6.2 Structural, transport and magnetic measurements . . . 146
6.3 Neutron diffraction and MuSR experiments . . . 153
6.4 Results and analysis . . . 154
6.5 Discussion . . . 163
6.6 Conclusion . . . 166

7 Summary and conclusion 169

A XRES multipolar coefficients 217

B Linear spin-wave theory 221

C REXS polarization analysis 227

Publications

- Spin dynamics in the antiferromagnetic phases of Dirac metals AMnBi$_2$ (A = Sr, Ca)
  Physical Review B 95, 134405 (2017)
  M. C. Rahn, A. J. Princep, A. Piovano, J. Kulda, Y. F. Guo, Y. G. Shi, and A. T. Boothroyd
- Spin resonance in the superconducting state of $Li_{1-x}Fe_xODFeSe_{1-y}$
  observed by neutron spectroscopy
  Physical Review B 94, 144503 (2016)
  N. R. Davies, **M. C. Rahn**, H. C. Walker, R. A. Ewings, D. N. Woodruff, S. J. Clarke, and A. T. Boothroyd,
- All-in–all-out magnetic structure and dispersing spin waves in $Sm_2Ir_2O_7$
  Physical Review Letters 117, 037201 (2016)
  C. Donnerer, **M. C. Rahn**, M. Moretti Sala, J. G. Vale, D. Pincini, J. Strempfer, M. Krisch, D. Prabhakaran, A. T. Boothroyd, and D. F. McMorrow
- Weyl-semimetal phase in the non-centrosymmetric compound TaAs
  Nature Physics 11, 728 (2015)
  L. X. Yang, Z. K. Liu, Y. Sun, H. Peng, H. F. Yang, T. Zhang, B. Zhou, Y. Zhang, Y. F. Guo, **M. C. Rahn**, D. Prabhakaran, Z. Hussain, S.-K. Mo, C. Felser, B. Yan, and Y. L. Chen
- Strong spin-fluctuations in β-FeSe observed by neutron spectroscopy
  Physical Review B 91, 180501(R) (2015)
  M. C. Rahn, R. A. Ewings, S. J. Sedlmaier, S. J. Clarke, and A. T. Boothroyd

Unpublished work not reported in this thesis

- Magnetically driven loss of inversion symmetry in metallic Pb_2CoOsO_6,
  A. J. Princep, **M. C. Rahn**, H. L. Feng, Y. F. Guo, H. M. Weng, P. Manuel,D. Khalyavin, A. Senyshin, Y. H. Yuan, M. Nagao, Y. Matsushita, K. Yamaura, and A. T. Boothroyd (*in preparation*)
- Unconventional magnetic state and spin glass behaviour in the frustrated pyrochlore $Y_2Os_2O_7$
- Magnetic structures of Ca_4IrO_6 and Sr_4RhO_6 determined by neutron powder diffraction
- All-in–all-out magnetic order on both pyrochlore sublattices in $Tb_2Ir_2O_7$ determined by Ir L_3 and Tb M_4 REXS

Abbreviations and acronyms

1/2/3D	one-/two-/three-dimensional
ACT	alternating current transport
AFM	antiferromagnetic
AHE	anomalous Hall effect
BCS	Bardeen-Cooper-Schrieffer theory
CCD	charge coupled device
CEF	crystal electric field
CW	constant wavelength
DC	direct current
DESY	Deutsches Elektronen Synchrotron (Hamburg, Germany)
DHO	damped harmonic ocillator
DIAMOND	Diamod Light Source (Didcot, UK)
EC	electronic correlations
ESRF	European Synchrotron Radiation Facility (Grenoble, France)
FC	field cooled
FM	ferromagnetic
FiM	ferrimagnetic
FWHM	full-width at half-maximum
IBSC	iron-based superconductor
ILL	Institut Laue Langevin (Grenoble, France)
INS	inelastic neutron scattering
ISIS	ISIS facility (Didcot, UK)
MIT	metal–insulator transition
MPMS	magnetic property measurement system
MuSR	muon spin rotation and relaxation
NMR	nuclear magnetic resonance
NPD	neutron powder diffraction
PPMS	physical property measurement system
QCP	quantum critical point
QHE	quantum Hall effect
QSHE	quantum spin Hall effect
REXS	resonant elastic x-ray scattering
RIXS	resonant inelastic x-ray scattering
SDW	spin-density wave
SOC	spin-orbit–coupling
SQUID	superconductiong quantum interference device
TAS	triple axis (neutron) spectrometer/spectroscopy
TEY	total electron yield
TI	topological insulator
TOF	time-of-flight
UB	Busing-Levy orientation matrix
UHV	ultra high vacuum
WSM	Weyl semimetal
ZFC	zero-field cooled

Instruments

D2B	high resolution two-axis neutron powder diffractometer (ILL)
HRPD	high resolution time-of-flight neutron powder diffractometer (ISIS)
I11	high resolution x-ray powder diffractometer (DIAMOND)
ID32	soft x-ray spectrometer (ESRF)
IN8	thermal neutron three-axis spectrometer (ILL)
MERLIN	direct geometry chopper neutron spectrometer (ISIS)
MuSR	muon spectrometer, European Muon Source (ISIS)
P09	x-ray resonant scattering diffractometer (PETRA-III, DESY)
WISH	long-wavelength neutron time-of-flight diffractometer (ISIS)

Constants

c	speed of light	$2.998 \times 10^8\,\mathrm{m/s}$
e	electron charge	$1.602 \times 10^{-19}\,\mathrm{C}$
m_e	electron rest mass	$510.999\,\mathrm{keV}/c^2$
m_n	neutron rest mass	$939.565\,\mathrm{MeV}/c^2$
m_p	proton rest mass	$938.272\,\mathrm{MeV}/c^2$
μ_0	vacuum permeability	$4\pi \times 10^{-7}\,\mathrm{V\,s/(A\,m)}$
$\varepsilon_0 = \frac{1}{\mu_0 c^2}$	vacuum permittivity	$8.854 \times 10^{-12}\,\mathrm{F/m}$
$r_0 = \frac{\mu_0}{4\pi}\frac{e^2}{m_e}$	classical electron radius or *Thomson scattering length*	$2.818 \times 10^{-15}\,\mathrm{m}$
$\hbar$	reduced Planck constant	$6.582 \times 10^{-16}\mathrm{eV\,s}$
$\mu_\mathrm{B} = \frac{e\hbar}{2m_e}$	Bohr magneton	$5.788 \times 10^{-5}\,\mathrm{eV/T}$
$\mu_\mathrm{N} = \frac{e\hbar}{2m_p}$	nuclear magneton	$3.152 \times 10^{-8}\,\mathrm{eV/T}$
γ	neutron magnetic constant	1.913

Chapter 1

Scientific context

The materials investigated in this thesis represent three key topics of condensed matter physics: (1) high temperature superconductivity, (2) unusual topology of electronic bands and (3) effects of strong spin-orbit coupling in complex oxides. To provide the necessary context for the more in-depth discussions in Chapters 3–6, I point out the historical development of each field and give an overview of the existing literature and current state of research.

Even though the compounds discussed in the subsequent chapters are chemically unrelated, the underlying emergent phenomena discussed in this section feature a number of recurrent themes. I hope to convey these common threads of interest, such as the consequences of a coupling of spin and orbital degrees of freedom of electronic states and the dichotomy between local and itinerant electronic behaviour.

Contents

1.1 Iron-based high temperature superconductivity 3

1.1.1 Overview 3

1.1.2 Electronic structure 5

1.1.3 Pairing mechanism and symmetry 7

1.1.4 Magnetism 8

1.2 Dirac materials 11

1.2.1 Overview 11

1.2.2 Graphene 12

1.2.3 Nodal superconductors 14

1.2.4 Topological insulators 14

1.2.5 Weyl semimetals 16

1.2.6 3D Dirac semimetals 19

1.3 Heavy transition metal oxides 22

1.3.1 Strong correlations and spin-orbit coupling 22

1.3.2 The d^5, $J_{\text{eff}} = 1/2$ state 24

1.3.3 Perovskite iridates 25

1.3.4 Honeycomb iridates 25

1.3.5 Pyrochlore iridates 26

1.3.6 Hexagonal iridates 28

1.3.7 Osmates: d^1, d^2 and d^3 states 28

1.3.8 Experiment: Limitations and opportunities 29

1.1 Iron-based high temperature superconductivity

1.1.1 Overview

A consistent understanding of the mechanisms underlying unconventional (i.e. not phonon-mediated) superconductivity is arguably the most sought-after advance in modern condensed matter physics. In spite of three decades of intense research on heavy fermion [16] and cuprate [17] superconductors, as well over 15000 publications [18] on iron-based superconducting phases alone, the complexity of the issue appears to be still increasing. In this section, I attempt to provide a broad overview of the most important issues in this field. I draw from a large number of review articles [18, 19, 20, 21, 22, 23, 24, 25, 26, 27, 28, 29, 30] and the references cited therein.

The systematic survey of transition metal pnictides by the group of Hideo Hosono [18] was awarded with the discovery of superconductivity at $T_c \approx 4\,\mathrm{K}$ in LaFePO (2006) [31], followed in 2008 by the discovery of a new form of high-temperature superconductivity in $LaFeAsO_{1-x}F_x$ ($T_c = 26\,\mathrm{K}$) [32]. Within the same year, the superconducting transition temperature of this compound was raised to 43 K by application of pressure [33] and to the present record of 55–56 K by ionic substitution [34, 35]. Roughly one decade later, several dozen of related iron-based superconductors (IBSCs) are known [18], which fall into ten structural families. Apart from "1111" materials such as LaFeAsO (using the common stoichiometry shorthand), the best-known structural families are of 122 ($BaFe_2As_2$ [36]), 111 (NaFeAs [37]) and 11 (FeSe [38]) composition. Figure 1.1(a) illustrates the tetragonal structures of these materials. The common structural motif is the square FeX *antifluorite* layers, where X is a pnictogen (group 15) or chalcogen (group 16) cation, as highlighted in Fig. 1.1. In all these materials, iron is divalent and in a tetrahedral coordination, and the adjacent cations form an alternating ("staggered") arrangement above and below the Fe layer. The various structural classes differ by the intercalation of additional cations in *blocking layers*, which act as insulating charge reservoirs and add to the two-dimensionality of the electronic state.

For the two decades preceding the discovery of these iron-based materials, high-temperature superconductivity appeared to be a peculiar phenomenon exclusive to cuprates. The discovery of IBSCs has had an enormous impact, because it contradicts this long-standing paradigm and points to the fact that the underlying physics may be more generic than previously appreciated [15]. In some respects, cuprates and IBSCs show some striking similarities: In both families, the Cooper pairs carrying the superconducting current form a spin singlet ($|\uparrow\downarrow\rangle$) and originate from square layers of $3d$ transition metal ions. Besides, both copper- and iron-based superconducting states occur in the vicinity of magnetically ordered phases. This had indicated early on that the associated high-energy antiferro-

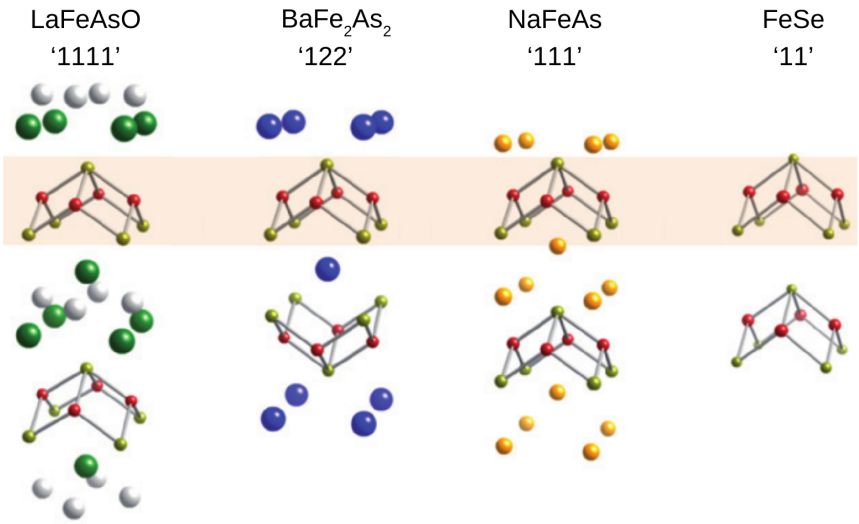

Figure 1.1: (adapted from [14]). The best known structural classes of iron-based superconductors. The superconducting state arises in the common *antifluorite* layers, which consist of distorted edge-sharing $FeAs_4$ ($FeSe_4$) tetrahedra.

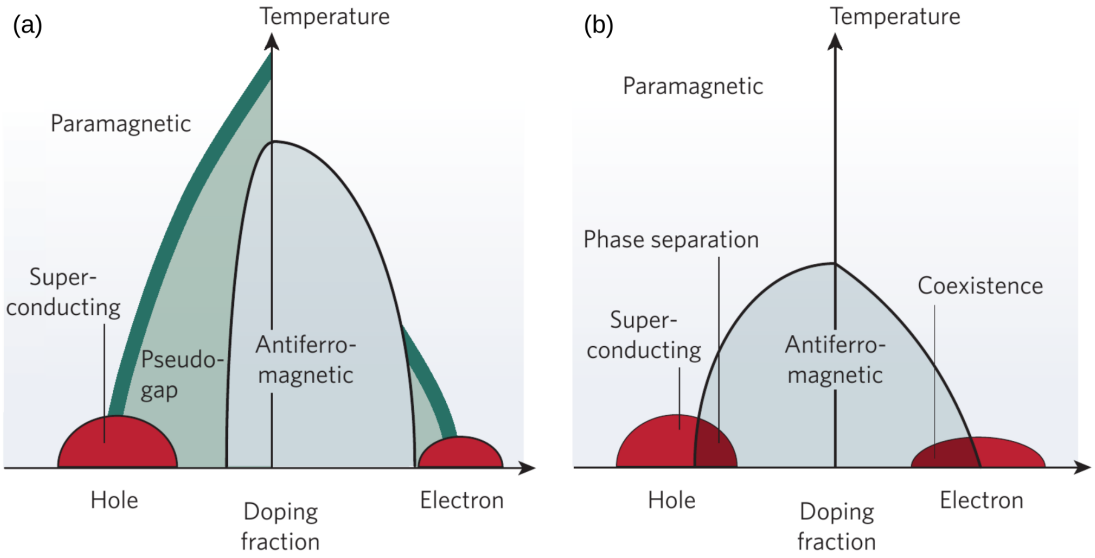

Figure 1.2: (adapted from [15]). Schematic simplified phase diagrams of (a) cuprate and (b) iron-based superconductors. In both cases, the superconducting state forms a *dome* around the quantum critical points where the magnetic order is fully suppressed (in this case by electron- or hole doping).

magnetic spin fluctuations could be the common fundamental ingredient of high temperature superconductivity. Indeed, a comparison of the low temperature phase diagrams of cuprates and IBSCs (see Fig. 1.2), as well as heavy fermion and organic superconductors suggests that, in essence, unconventional superconductivity is a generic quantum critical phenomenon which arises when a magnetically ordered parent phase is suppressed [39].

1.1.2 Electronic structure

A closer look at materials properties reveals that the electronic ground states in cuprates and IBSCs are far from identical, and even appear antithetic in important aspects.

The parent compounds of cuprate superconductors are archetypal Mott-Hubbard insulators [40]. This implies that the underlying electronic states lie in the localized limit. For instance, the magnetism of cuprates is very well described in the local Heisenberg exchange picture. Copper is divalent (Cu^{2+}) in these materials, and the resulting $3d^9$ state can be treated as a single spin-$\frac{1}{2}$ hole in the $3d$-manifold [41]. The strong Coulomb interaction of electrons sharing this single ($d_{x^2-y^2}$) orbital lies at the heart of the complexity that can give rise to superconductivity. However, in the case of cuprates, these correlations can be reduced to a single parameter — the Hubbard repulsion U. Phase-sensitive corner-junction tunnelling and scanning SQUID microscopy experiments [42] have established that the pairing symmetry in these materials is of $S = 0$, $L = 2$, i.e. d-wave character [40].

The Fe^{2+} ($3d^6$) states of iron pnictides and chalcogenides contrast strongly with the cuprate scenario described above. The most obvious difference is that IBSCs are considerably metallic. The local environment of Fe^{2+} ions in the antifluorite layers combines both tetragonal and tetrahedral symmetries. Consequently, the sense of the crystal electric field (CEF) splitting of e_g and t_{2g} manifolds is not clear. In general, all five d orbitals (d_{yz}, d_{xz}, d_{xy}, $d_{x^2-y^2}$ and $d_{3z^2-r^2}$) have to be taken into account [44, 41]. Furthermore, the "staggering" of cation position mentioned above effectively doubles the one-Fe unit cell in two directions, so that *two* distinct iron sites have to be considered.

From this local (orbital-based) point of view, a description of IBSCs must therefore include not one, but ten orbitals [45, 46, 47]. Moreover, even though electronic correlations are considerably screened, first principles calculations suggest that their role is potentially as important as in the cuprates [48, 49, 50, 51, 52]. But instead of a single Hubbard U, it becomes necessary to include *four* terms, to model both intra- and inter-, Hund- and Hubbard interactions [41, 53, 54, 55].

Angle-resolved photoemission spectroscopy (ARPES) [56, 57] and quantum oscillation [58, 59] measurements of the Fermi surfaces in IBSCs reveal a folded Brillouin zone with two

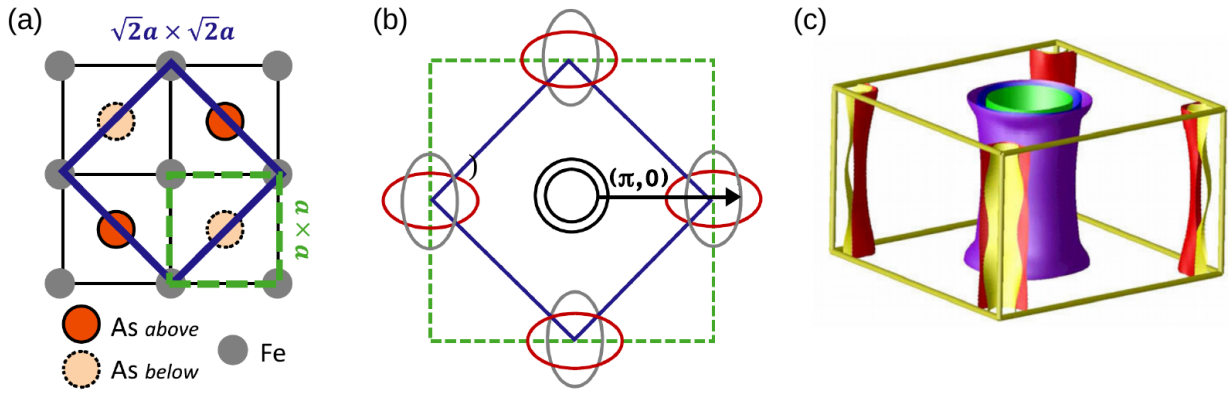

Figure 1.3: (adapted from [20, 43]). (a) Definitions of the tetragonal (blue solid line) and *one-Fe* (green dashed line) unit cell in the FeAs antifluorite layer. (b) Schematic (unfolded) view of Fermi surface pockets, with Brillouin zones indicated in correspondence to panel (a). The black arrow indicates the common nesting vector between the cylindrical hole pockets at the zone centre and electron pockets at $(\pi,0)$ (in reference to the *one-Fe* Brillouin zone). (c) Computational Fermi-surface of hole-doped $Ba_{1.6}K_{0.4}Fe_2As_2$.

near-cylindrical Fermi surface hole pockets at $(0,0)$[1], another hole pocket at (π,π)[2] and two electron-pockets at the $(\pi,0)$ position. In many compounds, there is evidence for a significant out-of-plane dispersion or "warping" of the electronic states along the c axis, which indicates that these systems are more three-dimensional than cuprates. In a Fermi surface nesting picture of magnetism (see below), this has the potential of modifying the spin fluctuations and thus it may be decisive for the stability of the superconducting state. Several theoretical studies confirm that the adjacent higher-energy cation (As/Se) states cannot be neglected in a realistic model of the band structure and electronic interactions [41].

Contrary to the orbital-based view of the electronic states in IBSCs, the application of ARPES and quantum oscillation techniques in itself implies that itinerant electrons are being probed. This metallic picture was also corroborated by x-ray absorption spectroscopy (XAS) and resonant inelastic x-ray scattering (RIXS), which has revealed characteristics that are largely reminiscent of elemental (metallic) iron [50, 60].

The local-itinerant ambiguity is also observed in inelastic neutron scattering (INS): The momentum dependence of the dynamic magnetic susceptibility measured in these experiments is generally interpreted in terms of the nesting phenomenon (see below, and Chapter 3). Indeed, the magnetic propagation vectors are mostly consistent with the

[1] There are several conventions for labelling the reciprocal space of IBSCs, depending on the referenced unit cell (which may be tetragonal, orthorhombic or monoclinic in some cases). Throughout this thesis, I refer to the simple "one-iron" unit cell of the two-dimensional square iron layer and state propagation- and nesting vectors by two in-plane indices (H,K). In this way, the notation is consistent across all IBSCs — at the cost of omitting information about the stacking of magnetic moments along the c axis.

[2] In the context of iron-based superconductors, propagation- and nesting-vectors are commonly denoted in units of the inverse lattice constant $(1/a)$, i.e. $\pi \equiv 0.5$ r.l.u. (reciprocal lattice units).

separation of Fermi surface pockets observed in ARPES [61, 62, 63, 64, 65, 66, 67]. In principle, this view would point to itinerant *Stoner* magnetism, which implies the decay of magnons into a broad continuum of itinerant spin excitations above a characteristic energy [68]. However, in order to model INS data and extract information about exchange parameters, local-moment Heisenberg spin-exchange models have been applied with success in many cases [69]. A complete description of iron-based superconductors must therefore capture both itinerant electron (band structure) and localized electron (electronic correlation) aspects, which continues to be a formidable challenge [41].

In the parent compounds of cuprate superconductors, the magnetic ordering transitions are associated with a structural distortion (from tetragonal to orthorhombic or monoclinic symmetry). For the parent compounds of 1111 IBSCs, an analogous structural transition has been evidenced $\approx 10\,\mathrm{K}$ *above* the magnetic ordering [70, 71]. On the other hand, in the 122 family, structural and magnetic transitions only become separated by doping. The width of the intermediate phase appears to be sensitive to disorder in the system [72], and its relevance to the mechanism of superconductivity is debated.

More recently, it has been discovered that in certain compounds, such as the isovalently doped $BaFe_2(As_{1-x}P_x)_2$ [73] and FeSe [74], the fourfold symmetry of the electronic state may already break (from point group C_4 to C_2) before the structural distortion sets in. The intermediate, *electronic nematic* phase manifests as a distortion of the Fermi surface pockets [57], and is expected to be associated with strong orbital fluctuations. This has raised the question whether the nematic instability is unrelated, a consequence, or even directly or indirectly involved in the superconducting pairing mechanism.

1.1.3 Pairing mechanism and symmetry

In all known superconductors, the flux-quantization measurements imply charge transport in multiples of two electron charges. It is therefore widely accepted that unconventional superconductivity can also be described in a BCS-like picture of Cooper pairs, which form due to a minimal interaction of fermionic quasiparticles. The two key questions in the characterization of an unconventional superconductor concern the pairing mechanism (or nature of the exchange-boson) and the resulting pairing symmetry (i.e. the symmetry of the superconducting gap function).

NMR experiments have evidenced a spin-singlet ($S = 0$) state of Cooper pairs in all IBSC structural families [75, 76, 77, 78]. The commutation of the Cooper pair wave function therefore requires that the orbital part of the wave function must carry an *even* angular momentum quantum number, i.e. $L = 0$ (s-wave) or $L = 2$ (d-wave). Unfortunately, Josephson corner-junction tunnelling experiments in IBSCs have proven to be

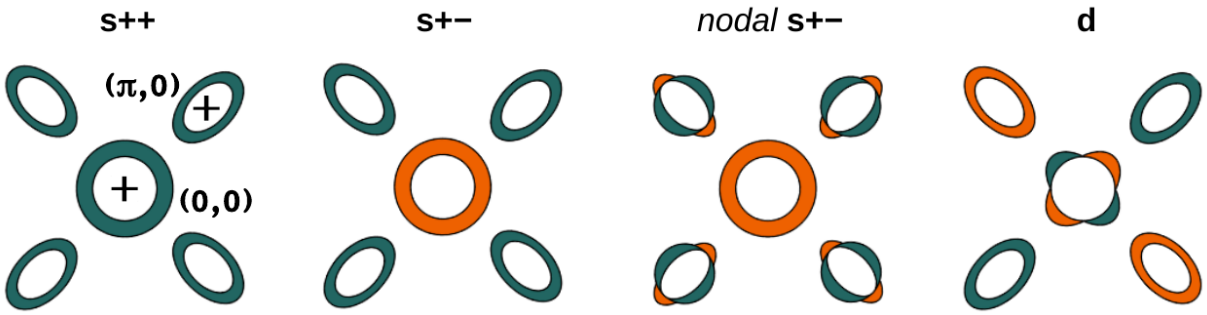

Figure 1.4: (adapted from [20]). Schematics of proposed gap symmetries at the $(0,0)$ and $(\pi,0)$ Fermi surface pockets in high-temperature superconductors. For cuprates, d wave ($L=2$) symmetry has been evidenced by tunnelling experiments. In iron-based superconductors, the order parameter likely has s wave ($L=0$) symmetry, but there exists no consensus as to whether this also involves a sign change (here indicated by colours) or nodes.

much more difficult [79, 80, 81, 82] than in cuprates [42]. Even though the available evidence is only circumstantial and certain ambiguities remain, most results point towards a sign-changing s-wave ($s_{\pm}$) pairing symmetry (see Fig. 1.4).

The question of pairing symmetry is intimately related to the nature of the Cooper-pairing mechanism. Isotope-effect experiments confirmed early on that high-temperature superconductivity of iron-based materials cannot be mediated by lattice vibrations (as expected when the transition temperatures are much larger than characteristic phonon energies). On the other hand, some studies have implied at least a weak isotope-effect. In the face of the structural transitions noted above, it cannot be excluded that a magneto-elastic coupling could play an indirect role in the pairing mechanism.

Due to the proximity to magnetically ordered phases of all high-temperature superconducting phases, magnetic fluctuations had been a candidate pairing interaction from the beginning of the field [83, 43]. Indeed, the possibility of a magnetic pairing mechanism had already been postulated in the context of heavy fermion superconductors — long before the discovery of IBSCs [84, 43, 85, 86]. Notably, Scalapino [87] had pointed out that magnetic fluctuations could only mediate the pairing interaction if they would span parts of the Fermi surface with gap functions of opposite sign. This condition is satisfied in cuprates, where d-wave pairing is widely accepted.

1.1.4 Magnetism

In all IBSC parent compounds, the presence of strong magnetic fluctuations can be recognized by the reduction of the ordered magnetic moment from $3.32\,\mu_B$ in FeO ($2.2\,\mu_B$ in Fe metal) to $\approx 2\,\mu_B$, $\approx 1\,\mu_B$ and $\approx 0.4\,\mu_B$ in the 11, 112 and 1111 families, respec-

tively [88, 89, 90, 91, 92, 70]. Inelastic neutron studies of the spin-wave dispersion have been reported for all these materials (1111 [93], 11 [94] and 122 [95, 96, 97, 98, 99, 100, 101, 102]). The spectra obtained by INS generally show a steep magnon dispersion, up to energies of $\approx$ 200–300 meV. The in-plane spin waves are strongly anisotropic (e.g. with a ratio of spin-wave velocities parallel and perpendicular to the propagation vector of $v_{\parallel}/v_{\perp} \approx 4$ in $BaFe_2As_2$ [95, 96]). The magnetic spectra also differ from the quasi-2D situation in cuprates [103] in that there is a sizeable out-of-plane dispersion. Several studies of strongly over-doped compounds have found that the spin waves are completely suppressed as the superconducting state disappears [104]. This lends further support to the view that magnetic fluctuations mediate the superconducting pairing.

For most IBSCs, the magnetic instability occurs at the propagation vector $\boldsymbol{q}_{\mathrm{m}} = (\pi, 0)$. Even though the out-of-plane stacking or propagation of the magnetic order or fluctuations c axis may vary, first principles electronic structure calculations had generally predicted this "stripe-like" magnetism within the iron layers [43], before first experimental evidence was reported [83, 105]. As in these early predictions, the $(\pi, 0)$ magnetic instability is commonly attributed to nesting between parallel Fermi surface pockets at the $(0,0)$ and $(\pi, 0)$ positions in the Brillouin zone [106] (see Fig. 1.3(b)). However, there is still an ongoing debate whether the magnetic ground state of IBSCs should not rather be interpreted as a result of frustrated superexchange interactions [69, 107, 108], long-range itinerant interactions between local moments [109], or even as a consequence of orbital order and nematicity of the electronic state.

Notably, $(\pi, 0)$-type magnetic fluctuations are not universal for all IBSCs. For example, in iron-deficient $A_xF_{2-y}Se_2$, superconductivity coexists with a *block-antiferromagnetic* state [110]. The itinerant magnetism (nesting) argument seems to be particularly contradicted in FeTe, which shows yet another propagation vector, $\boldsymbol{q}_{\mathrm{m}} = (\pi/2, \pi/2)$ [89]. Upon isovalent doping [111, 112], the magnetic correlations in Fe(Te,Se) become incommensurate, moving from $(\pi/2, \pi/2)$ towards $(\pi, 0)$ [113, 94, 114, 71]. Such incommensurate distortions are reminiscent of the situation in $(La,Sr)_2CuO_4$ cuprate superconductors [115] (in this case, the fluctuations are close to Néel-type, $\boldsymbol{q}_{\mathrm{m}} = (\pi, \pi)$). This behaviour of the Fe(Se,Te) system is at odds with band structure calculations [116] and ARPES data [117] which indicate a particularly good nesting condition. In Chapter 3 of this thesis, I show that the compound FeSe shows strong $(\pi, 0)$ fluctuations, and therefore resembles the 111, 1111 and 112 families, rather than the strongly Te-doped 11 chalcogenide.

Within the superconducting phase, the INS spectra of many IBSCs develop a neutron magnetic resonant feature at a characteristic energy E_{R} at the magnetic propagation vector [120]. This effect had been previously observed in cuprates [121, 122, 123, 124], as well as in heavy-fermion superconductors [125, 126]. In IBSCs, it was first observed in

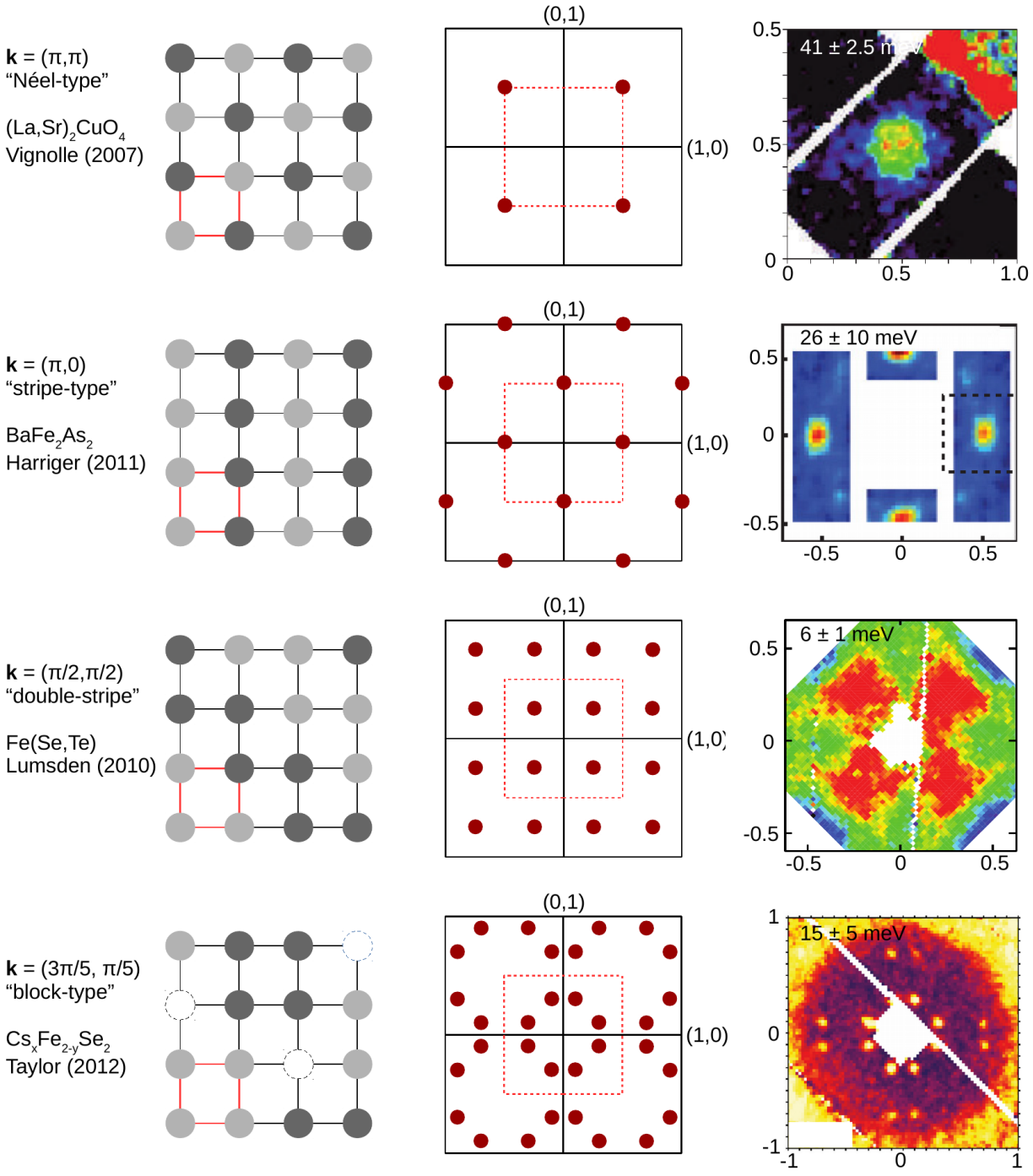

Figure 1.5: (adapted from [118, 115, 119, 71, 110]). Magnetic propagation vectors in high-temperature superconductors. Illustrations of the periodicity of the magnetic order or fluctuations in real space (left-hand panels), loci of magnetic Bragg scattering in reciprocal space (centre panels) and corresponding time-of-flight constant-energy neutron data (right-hand panels). The one-Fe unit cell and Brillouin zones (indicated by red squares) are used throughout.

(Ba,K)Fe_2As_2 [127], but has since also been found in the other 122 [128, 129, 130] and 11 [113, 131, 132, 133, 114, 134] materials. Given this universality, the neutron magnetic resonance is presently one of the strongest leads to a unified understanding of non-phonon-mediated superconducting pairing. However, its actual origin is still strongly debated [135, 136, 137, 40, 138, 139, 140]. For example, it can be interpreted as a redistribution of magnetic spectral weight, in the regime where the opening of a superconducting gap prevents the magnon-decay into a continuum of itinerant particle-hole pairs. On the other hand, alternative interpretations, for example as singlet-triplet excitation of the Cooper-pairs, have also been proposed [141, 142].

One widely accepted view is that the neutron magnetic resonance is an amplified nesting effect between parts of the Fermi surface with opposite sign of the superconducting gap function. The observation of this characteristic peak at E_R in the neutron data is therefore often accepted as circumstantial evidence for unconventional d-wave or $s\pm$-wave pairing symmetries. However, such reasoning has also been called into question [143]. A conclusive explanation of the effect is therefore still absent. At present, the magnetic neutron resonance phenomenon is mostly interpreted phenomenologically, e.g. by scaling laws which relate the resonance energy to the critical temperature $E_\mathrm{R} \approx 5 k_\mathrm{B} T_c$ (this appears to hold for both IBSCs and cuprates [144]), or the superconducting gap $E_\mathrm{R} \approx 0.64 \times 2\Delta$ (which also holds for heavy fermion compounds [126, 145]).

1.2 Dirac materials

1.2.1 Overview

Arguably the most fruitful concept in 21st century condensed matter physics has been the topological classification of electronic states [12]. Sparked by the discovery of graphene in 2004 [146, 147], various novel electronic phases have been discovered in which the dispersion of low-energy charge carriers is mathematically distinct from that common (Schrödinger) electrons. All such "topologically non-trivial" systems have a constellation of symmetries (crystalline or magnetic) that protects a subspace of states at the Fermi surface from opening a gap. No perturbation can then continuously distort these band-crossings into a *topologically trivial* band metal or insulator.

The hallmark of such states is the reduction in dimensionality, e.g. the reduction of a two- or three-dimensional Fermi surface to arcs or point nodes. Many physical (transport, thermal and optical) properties implied by this reduced dimensionality do not depend on specific material properties, but only on the topological classification. This *universality* has proven a powerful tool, as it allows the prediction of diverse unusual phases, purely

by symmetry arguments.

The key characteristic of topologically non-trivial states in condensed matter is that their low-energy dynamics resemble those of freely propagating high-energy fermions. They are therefore governed by variations of P. A. M. Dirac's 1928 relativistic quantum theory of the electron [148]. The electronic dispersion in two-dimensional *Dirac* materials such as graphene is described by the Hamiltonian operator

$$\mathcal{H}_{\mathrm{D}} = v_{\mathrm{F}}\,\boldsymbol{\sigma}\cdot\boldsymbol{p} + m v_{\mathrm{F}}^2\,\sigma_z \quad , \tag{1.1}$$

where v_{F} is the Fermi velocity, and $\boldsymbol{\sigma} = (\sigma_x, \sigma_y)$ and σ_z are the Pauli spin matrices. $\boldsymbol{p} = (\hat{p}_x, \hat{p}_y)$ is the 2D-momentum operator and m is the mass of the Dirac fermions. The eigenstates of this term are 2-spinor wave functions that correspond to particle-hole pairs. They disperse linearly in reciprocal space, with a gap of $\Delta = 2m v_{\mathrm{F}}^2$ at the Fermi surface. In the limit of a vanishing σ_z term, this leads to a continuous *Dirac cone*, and the Fermi surface is reduced to a point node. Notably, the *charge-conjugation* symmetry inherited from quantum electrodynamics [149] implies that the quasiparticle-hole–pairs are entangled. Consequently, all transport-related properties will be heavily renormalized, regardless whether the system is massless or massive (gapped).

In the present section I discuss the origin of such phenomena in a diverse range of Dirac materials, as recently reviewed by Wehling [12]. The motif of topologically non-trivial phases is present across most classes of materials that I have investigated in the context of this dissertation: This includes two-dimensional Dirac systems (AMnBi$_2$, Chapter 4), the derivative of a recently discovered bulk Dirac semimetal (EuCd$_2$As$_2$, Chapter 5), as well as Weyl-semimetal candidates (R$_2$Ir$_2$O$_7$ [150], experiments not described in this thesis). Lastly, also the quasiparticle excitations in nodal superconductors share Dirac characteristics, which relates back to the issue of Cooper pairing symmetry discussed in the preceding section.

1.2.2 Graphene

The unusual properties of carbon honeycomb layers and the potential relevance of topology in graphite had been recognized early on and there had been several efforts to model its electronic structure by simplified tight-binding models [154, 155, 156, 157]. However, the experimental verification of the associated quantum phenomena was not achieved until 2004, when Novoselov and Geim realized that graphene can be prepared by a simple exfoliation technique [146, 147]. This discovery has been seminal to an intense search for experimental realizations of Dirac physics. Throughout the last decade, this has been rewarded with the discovery of several unprecedented states of matter.

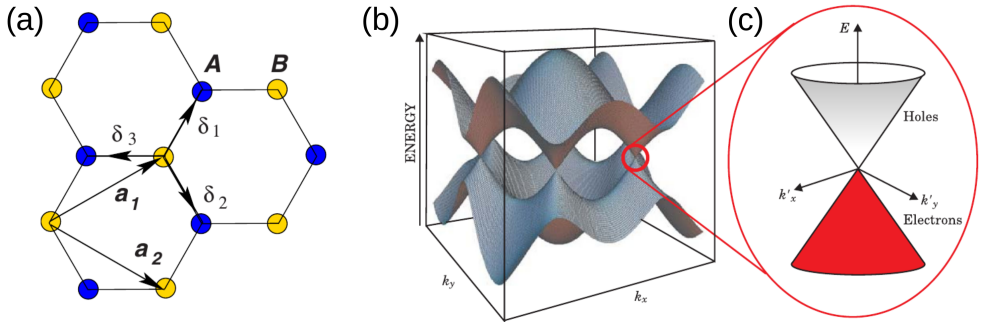

Figure 1.6: (adapted from [151, 152]). (a) Atomic structure of graphene, with the two sublattices drawn in distinct colours. (b) Corresponding view of reciprocal space with one Dirac cone at every corner (K point) of the Brillouin zone. (c) In graphene, the Dirac fermions are almost massless [153]. The Fermi surface lies exactly at this node, which separates the electron (positive chirality) and hole (negative chirality) bands.

As indicated by Eq. 1.1, Dirac physics implies a coupling of momentum to Pauli spin matrices. In condensed matter systems, such 2-spinor "pseudo-spin-$^1/_2$" degrees of freedom can be of varied origin. In graphene, they arise from peculiar structural properties (the actual electron spin is largely neglected in this material). Graphene consists of a simple carbon honeycomb monolayer. The honeycomb structure is itself not a Bravais lattice, but corresponds to a hexagonal lattice with a basis of two atoms (i.e. two atoms per unit cell) [151, 158]. Since there is only one active (p_z) orbital per carbon atom, simple nearest-neighbour tight-binding models [154] are a good approximation of this system.

The bipartite (two-sublattice) character of the structure results in two distinct bands, separated by the Fermi surface (see Fig. 1.6). However, at each corner of the hexagonal Brillouin zone, the hopping amplitudes (of three adjoining 120° bonds) interfere destructively [159]. In effect, this exactly cancels the σ_z term of Eq. 1.1 and produces an almost massless Dirac node (or *cone*) at each Brillouin zone corner (corrections due to weak spin-orbit interactions open a gap on the order of $\approx 1\,\mu$eV [153]). The existence of these Dirac cones, with a Fermi-velocity of $\hbar v_\mathrm{F} \simeq 5.8\,$eVÅ, is evident in low-temperature transport experiments (e.g. the observation of a quantized Hall effect [160, 149]) and has also been directly observed by angle-resolved photoemission spectroscopy [161].

Notably, the term $\boldsymbol{\sigma} \cdot \boldsymbol{p}$ in Eq. 1.1 implies that Dirac fermions can be assigned a *chirality*. In the case of graphene, the sublattice degree of freedom ($\boldsymbol{\sigma}$) corresponds to the splitting into electron- and hole bands. The chirality quantum number of Dirac fermions in graphene is therefore fixed at $(+1)$ for electrons and (-1) for holes, which can be exploited in tunnelling phenomena [162].

Recently, the interest in graphene research has largely shifted towards technological application (e.g. engineering modifications of the Dirac cone [163]) and attempts of industrial-scale preparation [164]. *Carbon copies* of graphene have been experimen-

tally realized in the form of silicene [165] and germanene [166, 167]. A number of artificial honeycomb structures with Dirac properties has also been realized at the nanoscale [168, 169] and in optical lattices [170].

1.2.3 Nodal superconductors

The ubiquity of Dirac physics across unrelated condensed matter systems illustrates the universality of this concept. As discussed in Section 1.1, there exists convincing evidence that the gap function in high-T_c cuprates [17, 42, 171] as well as heavy fermion [16, 172] and organic superconductors [173, 174] is of $L = 2$, d-wave symmetry (see Fig. 1.4). This implies that the low-temperature transport in these systems is dominated by the Bogoliubov excitons that can occur at vanishing cost at the nodes along the $(\pm\pi, \pm\pi)$ directions on the Fermi surface [175, 12]. It has been demonstrated that the unusual low-temperature magnetothermal response of these systems can be explained by a model of these excitations as linearly dispersing Dirac fermions at the four d-nodes [176, 177]. Notably, such *Bogoliubons* originate from symmetries of the superconducting state, carry no charge and do not interact — both origin and appearance of this Dirac phenomenon is fundamentally distinct from the situation in graphene.

Recently, Ran *et al.* have pointed out that Dirac dispersions may also be relevant in iron-based superconductors [178, 179]. In this case, it is the hybridization of iron $3d$ orbitals with $4p$ states on the adjacent pnictogens which leads to Dirac points at the Fermi surface pockets. It has been proposed that the nesting between these nodes may lead to an unusual magnetic spin density wave instability, which would be of relevance to the pairing mechanism [180]. Indeed, ARPES [181] and quantum oscillation [182] measurements have evidenced such Dirac cones in parent compounds of the 122 family. Nevertheless, a potential relevance of Dirac physics to the pairing mechanism and symmetry of the superconducting state in these materials is still unclear.

1.2.4 Topological insulators

1980s condensed matter physics had seen the first application of topology to electronic states, in the form of the integer quantum Hall effect (QHE) [187, 157]. The discovery of graphene moved this body of work back into the focus of scientific attention. This also inspired the work by Kane and Melé, who predicted new electronic states, which would feature protected surface currents reminiscent of the QHE, but without the need to apply a magnetic field [188, 189]. Instead, the breaking of time-reversal symmetry would be provided by a strong coupling of the spin and orbital degrees of freedom [190]. Consequently, such a *quantum spin Hall effect* (QSHE) would feature protected edge states in

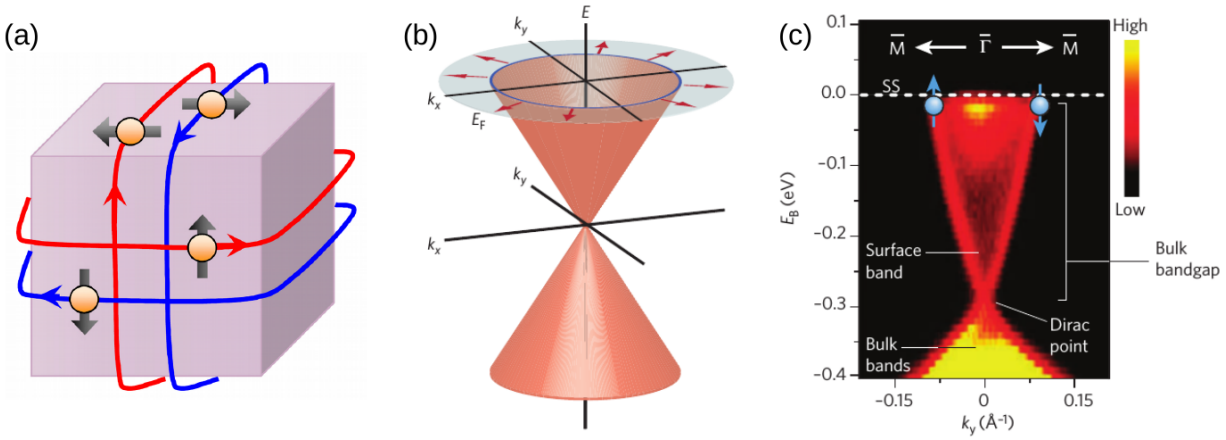

Figure 1.7: (adapted from [183, 184, 185, 186]). Illustrations of charge- and spin transport in the surface states of topological insulators, (a) in real space and (b) in momentum space. Spin-polarized ARPES studies confirm that the relative direction of spin and momentum is fixed. (c) ARPES spectrum of the topological insulator Bi_2Se_3 observed by Xia *et al.* [185]. The $\approx 0.3\,$eV gap between bulk states is superposed by a Dirac cone surface contribution.

zero field. In the model of Kane and Melé, this distinction from a trivial band material is expressed by a $\mathbb{Z}_2$ *topological invariant* (an integer that is non-zero if topologically protected states exist in the material) [191, 192, 193].

Due to the weakness of spin-orbit coupling in carbon ($\approx 4\,$meV [153]), the proposed QSHE effect was never observed in graphene. Instead, its bulk analogy, the topological insulator (TI) was proposed [194] and then realized [195] in a heterostructure (*quantum well*) of HgTe and (Hg,Cd)Te in 2007. As in the QSHE, this state is insulating in the bulk, but characterized by a non-zero $\mathbb{Z}_2$ number (see [196, 197, 198, 183] for reviews and [184, 199, 200] for viewpoints). This integer classification implies that there can be no continuous transition from a TI to a trivial insulator, such as the vacuum. Instead, the electronic bands are forced to unravel via a protected metallic state on any surface.

In effect, the charge carriers in this surface state behave just as the Dirac fermions in graphene, except that there is only one node per Brillouin zone (not two) and due to strong spin-orbit interaction, the orientations of spin and momentum are strictly coupled. This results in a separation of opposite surface spin currents, as they are locked to the forward/backward direction of charge transport. Notably, this complete lifting of node- and spin-degeneracy provides full topological protection, i.e. massless Dirac transport in these surface spin channels [184] (distinct from graphene, which is slightly gapped by spin-orbit coupling). One experimental complication is that the chemical potential in TIs does not necessarily coincide with the Dirac node (as in graphene), but has to be fine-tuned by chemical doping [201].

A three-dimensional TI [192] was reported a little later in doped bismuth [202, 201, 200] and finally in "second generation" TI materials such as Bi_2Se_3 and Bi_2Te_3 [203, 185, 204]. The significance of this second generation lies in their relatively large bulk gap of $\approx 0.3\,\mathrm{eV}$ ($\hat{=}\,3600\,\mathrm{K}$), which promises the application of Dirac transport phenomena in room-temperature spintronics devices [184, 205]. Beyond spintronics, a quantized electromagnetic effect ("axion electrodynamics") [206] adds to the technological potential of TIs. Furthermore, large efforts are presently being made in pursuit of Majorana fermions at TI–superconductor interfaces [207, 208]. The potential room temperature quantum coherence of such Majorana qubits could enable a new generation of quantum computing devices [209].

1.2.5 Weyl semimetals

The discovery of topological insulators stimulated an extensive search for new phases with topologically protected conduction states. Notably, the Dirac fermions in all systems described above (in graphene, d-wave superconductors and and the surfaces of topological insulators) are purely two-dimensional [12]. The idea that quantum spin Hall states could be stabilized in the bulk of a 3D insulator had already been present in an early proposal by Murakami [210] and was fist postulated for a real system by Wan *et al.* in 2011 [211] (in the context of rare earth iridates $R_2Ir_2O_7$, see Section 1.3).

Behind this stands the basic idea that a crossing of two bands in the bulk of a material can be protected from gapping if both are non-degenerate. Curiously, this scenario had been considered as early as 1937 [212]. The new realization was that, since the dispersion at such a node would be to first order linear, and by definition continuous, it is described by a Dirac equation in three dimensions, but necessarily without a mass term ($m\sigma_z$):

$$\mathcal{H}_\mathrm{W} = \hbar v_\mathrm{F} \left(q_x\sigma_x + q_y\sigma_y + q_z\sigma_z\right) \quad , \quad \boldsymbol{q} = \boldsymbol{k} \pm \boldsymbol{k}_0 \quad , \tag{1.2}$$

where the low-energy excitations in the vicinity of two nodes at $\boldsymbol{k} = \pm\boldsymbol{k}_0$ are being considered. This massless limit of Dirac's theory [148] had been discussed by Hermann Weyl in 1929 [213]. Consequently, this new bulk topological state was christened *Weyl semimetal* (WSM).

The equal use of all three Pauli matrices has two important consequences: (1) it cannot be gapped by perturbations and (2) eigenfunctions of this equation are two-spinors. Furthermore, according to the *Fermion doubling* or "no-go" theorem [214, 215], solutions to the Weyl equations exits in pairs of opposite chirality — corresponding to two nodes at opposite momenta $\pm\boldsymbol{k}_0$.

Notably, the coupling of momentum and pseudospin can be rewritten in the form of a vector potential [12]:

$$\boldsymbol{A}(\boldsymbol{k}) = -i \sum_n \langle u_n | \boldsymbol{\nabla}_{\boldsymbol{k}} | u_n \rangle \quad , \tag{1.3}$$

where the sum runs over all occupied Bloch states $|u\rangle$. This implies an emergent topological field or *Berry curvature* in momentum space:

$$\boldsymbol{B}(\boldsymbol{k}) = \boldsymbol{\nabla}_{\boldsymbol{k}} \times \boldsymbol{A}(\boldsymbol{k}) \tag{1.4}$$

In this picture, Weyl nodes are monopoles of opposite topological charge, or, equivalently, point-sources and -drains of *Berry flux* (or *curvature*) [216]. As for electric charges, the Gaussian theorem applies, and so the conservation of Berry flux corresponds directly to the Fermion doubling theorem mentioned above. The topological stability of this state is equivalent the conservation of topological charge. The only means to destroy Weyl nodes, i.e. the only means of a topological phase transition, is the annihilation of two nodes of opposite chirality.

A striking consequence of such topological phase transitions is observed at the interface between a Weyl semimetal and the vacuum. This is best understood by considering the winding number (a line integral of Berry flux, corresponding to the $\mathbb{Z}_2$ number of TIs) of closed trajectories in momentum space [217]. Closed trajectories that include (in projection along the surface-normal) no Weyl nodes, or Weyl nodes of cancelling charge, are topologically trivial. Consequently, such states are equivalent to the vacuum and there will be no topological phase transition at the surface. The inverse applies for trajectories with a finite winding number. In analogy to topological insulators (as discussed above), such states have to *unwind* via a metallic surface state. Taken together, this argument implies that Weyl semimetals have metallic surface states that form open lines in momentum space, connecting the projections of Weyl-node–pairs. By virtue of recent advances in angular resolved photoemission spectroscopy (ARPES), these *Fermi arcs* are the most accessible experimental evidence of Weyl physics.

The key condition to safeguard the stability of Weyl nodes in condensed matter is the non-degeneracy of the crossing bands [212]. This last splitting of Kramers bands can be achieved by breaking *either* inversion symmetry (IS) *or* time-reversal symmetry (TRS) [3]. Both of these possibilities have been pursued in experiment.

Following the originial proposal by Wan [211], the search for an experimental realization was initially focused on pyrochlore iridates, i.e. inversion-symmetric phases with broken

[3] The case that *both* inversion- and time-reversal–symmetry are broken or conserved, would imply the coincidence of several Weyl nodes (see Fig. 1.9). An appropriate model would then require 4-spinors. The Weyl nodes would therefore merge into (generally massive) Dirac nodes, i.e. perturbations would be expected to open a gap.

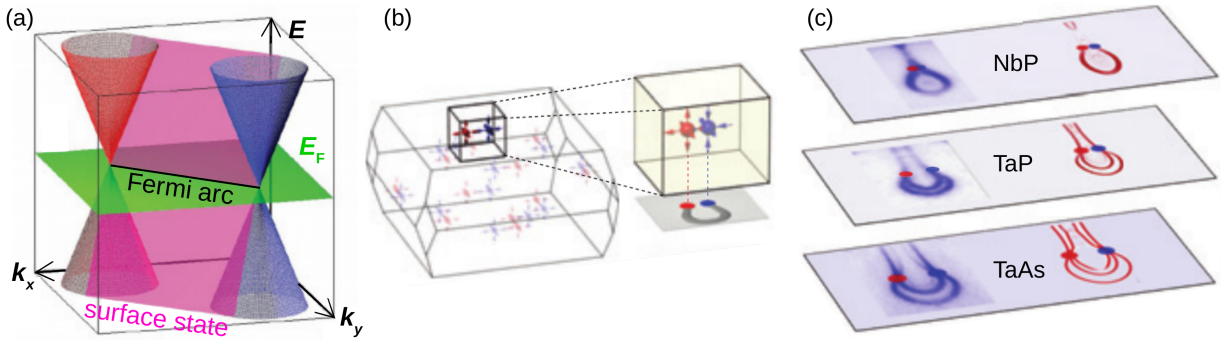

Figure 1.8: (adapted from [221]). (a) Brillouin zone of monopnictide Weyl semimetals, including 12 pairs of Weyl nodes with opposite topological charge (blue/red). In projection onto the surface plane, these Weyl points form the ends of open *Fermi arc* surface states. (b) ARPES spectra of Fermi arcs evidenced in various compounds of this family. Due to the multitude of Weyl nodes in the Brillouin zone, the ends of several Fermi arcs coincide and form a crescent-shaped surface state.

time-reversal symmetry [218]. This case would be of special interest as it would mean a first interplay between Dirac bands and electronic correlations[4]. I have contributed to this search with the determination of magnetic order and dynamics in the candidate material $Sm_2Ir_2O_7$ [150]. I also discuss these materials in the context of 5*d* transition metal oxides in Section 1.3 (the results of [150] are not reported in this thesis). There have also been other proposals to engineer TRS-breaking Weyl phases in layered heterostructures [219, 220], or by doping Dirac semimetals [217]. So far, these efforts have have been thwarted by problems with sample preparation, disorder and domain formation [217].

By contrast, the search for non-centrosymmetric, non-magnetic WSMs is more straightforward, both experimentally and computationally [217]: Lists of non-centrosymmetric semimetals featuring heavy, (i.e. strongly spin-orbit coupled) elements are available from crystallographic databases and density-functional calculations of their electronic structure are much simplified in the absence of electronic interactions. Earlier proposals of structurally more complex candidate materials (hetero-structures [222, 223] or doped compounds [224]) were followed in 2015 by the identification of a much simpler class of binary transition metal monophosphides [225, 226].

The recent advances of the ARPES technique (driven by the discovery of topological insulators [227], see above), allowed a rapid discovery of Fermi arc surface states. The effect was first identified in TaAs [228, 229] and then in NbAs [230], TaP [231] and

[4]Apart from the more exotic from of Dirac excitations in *d*-wave superconductors, electronic correlations are not relevant in any of the known Dirac materials (graphene, topological insulators, bulk Dirac semimetals and non-inversionsymmetric Weyl semimetals). The class of ternary bismuthides that I present in Chapter 4, and possibly also the compound $EuCd_2As_2$ presented in Chapter 5, are an interesting exception as they feature Dirac physics and electronic correlations in separate layers of the same material.

NbP [221]. I contributed to these discoveries by characterizing TaAs single crystals that were used in the study by Yang *et al.* [232].

The experimental verification of a Weyl semimetal in TaAs is illustrated in Fig. 1.8. In agreement with computational predictions [225, 226], two non-degenerate bands cross at 24 points in the Brillouin zone, corresponding to 12 Weyl node pairs of opposite chirality. In these tetragonal compounds, ARPES experiments are generally restricted to probe the (001) cleavage plane. Consequently, the 24 Weyl nodes appear projected onto 16 points, half of which correspond to a topological charge of ± 1 and the other half to ± 2. Due to this multiplicity, *two* Fermi arcs appear, which form a characteristic crescent shape (see Fig. 1.8(c)) [233].

Following the observation of Fermi arcs in TaAs, there has been a rapid sequence of new proposals [234, 235, 236, 237, 238, 239] for non-centrosymmetric WSM candidates. One interesting development has been the discovery of "type-2" Weyl states in $MoTe_2$ and $TaIrTe_4$ [240, 241, 242]. In these materials, an additional *kinetic* term in the Dirac dispersion tilts the Weyl cone, so that the chemical potential is cutting a section of the Weyl cone. This involves a violation of Lorentz-invariance and thus goes beyond what would be possible within the standard model of particle physics.

Apart from the ongoing search for time-reversal symmetry breaking ("interacting") WSMs, the key experimental challenge at present is an unequivocal confirmation of Weyl physics in transport measurements. The low-energy excitations in WSMs are expected to inherit the *chiral anomaly* [240] or Adler-Bell-Jackiw anomaly from particle physics [243, 244, 245, 243]. In the context of condensed matter, this can give rise to a negative magnetoresistance, semi-quantized anomalous Hall effect and a chiral charge pumping effect [246, 247]. The latter corresponds to an offset in quasiparticle population at opposite Weyl nodes, which may occur when parallel magnetic and electric fields are applied ($\boldsymbol{E} \cdot \boldsymbol{B} \neq 0$). However, the interpretation of such data is not straightforward if many pairs of Weyl nodes contribute to to the transport. The necessary fine-tuning of the chemical potential, contributions from charge carriers from secondary, topologically trivial bands and various scattering processes are adding to the experimental challenge [245, 217].

1.2.6 3D Dirac semimetals

The stability of the Weyl phases described in the previous section is only "accidental", i.e. there is no symmetry condition that prevents the Weyl nodes from coinciding and thus annihilating. As illustrated in Fig. 1.9, this *coincidence* occurs necessarily if *both* time-reversal and inversion symmetry are conserved or broken. Fu *et al.* suggested early on that such a multiple bulk band crossing could be stable in condensed matter if each

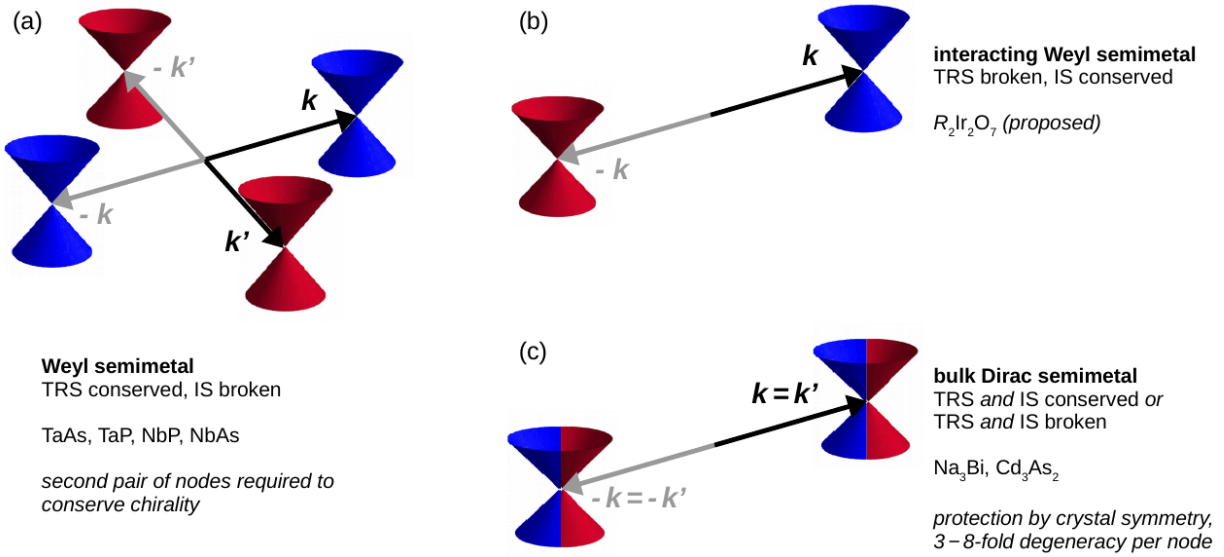

Figure 1.9: Dirac Fermions in three-dimensional materials. The colour of the cones indicates Dirac/Weyl nodes of opposite chirality (note that these cones are actually 4D-surfaces). Time-reversal symmetry implies nodes of the *same* chirality at the momenta $\pm\boldsymbol{k}$, whereas inversion symmetry implies nodes of *opposite* chirality at $\pm\boldsymbol{k}$. (a) In non-magnetic Weyl semimetals, these conditions demand a multiple of four nodes. (b) In centrosymmetric Weyl semimetals with electronic correlations (magnetic order), a single pair of opposite nodes satisfies these requirements. (c) If time-reversal and inversion symmetry are *both violated* or *both conserved*, opposite topological charges would in general coincide and annihilate. However, special non-symmorphic crystal symmetries can protect such double (or multiple) Dirac nodes.

involved band would transform according to distinct crystal symmetries [203]. The strategy to identify materials which host bulk Dirac fermions is to decompose the crystal's space group into the *little group* of high-symmetry points (or lines) in the Brillouin zone and search for irreducible representations (IRs) whose degeneracy corresponds to the number of bands that meet at this point [248]. As such "double Dirac" crossings of multiple bands are only protected by crystal symmetry (in particular, by non-symmorphic symmetry elements), they break the Lorentz symmetry required of free particles. Hence, the low-energy quasiparticle excitations in these 3D Dirac materials have no equivalent in the standard model of particle physics.

In 2012, Mañes reported a complete survey of the 230 (non-magnetic) space groups with regards to single-valued IRs, listing 19 space groups that may host bulk Dirac nodes [248]. A search for *single-valued* IRs implies that only the orbital (not spin) degree of freedom is considered, and thus, this result applies to non-magnetic, weakly spin orbit coupled materials. Young *et al.* suggested that this search could be extended to double-valued IRs (i.e. for non-magnetic strongly spin-orbit coupled materials) [249]. Indeed, a very recent exhaustive search identified 16 space groups which either *may* or *must* host protected (3-, 4-, 6- or 8-fold) linear band crossings in the bulk [250, 251].

A 3D Dirac semimetallic state had also been observed in transport measurements of elemental Bi, where it is however masked by additional topologically trivial bands at the Fermi level [252]. "Pure" bulk Dirac systems were verified by ARPES as well as transport signatures in Na_3Bi [253, 254, 255] and Cd_3As_2 [256, 257, 258, 259, 260]. For the first time, these systems show a true 3D-dispersion, i.e. the surface of such Dirac "metacones" are actually four-dimensional objects. Transport experiments on micro-machined samples indeed confirm the expected consequences of Fermi arc transport [260], and first technological applications are now being engineered [261].

Notably, a 3D "double Dirac" node could potentially also be protected in TRS-broken phases. This case would promise added tunability by external fields and the possibility to switch between Dirac- and Weyl- or Schrödinger-transport at a magnetic phase transition. A guided search for such materials would require a full survey of the 1651 magnetic space groups [248, 251], which has not been reported at present. In Chapter 5 of this thesis I report my investigation of $EuCd_2As_2$, which is a magnetic derivative of Cd_3As_2 with an unusual negative magnetoresistance in the ordered phase.

1.3 Heavy transition metal oxides

1.3.1 Strong correlations and spin-orbit coupling

Magnetic oxides of $3d$ transition metal ions feature strongly correlated electronic states that have led to the most important (and technologically relevant) insights of 20th century condensed matter physics. This includes metal–insulator transitions in vanadates, spin-ice and related effects of magnetic frustration in titanates, multiferroic properties of manganates, and high-temperature superconductivity in cuprates. A common feature of these electronic states is that, even though the $3d$ states are well-localized, the extent of the d wave allows a sizeable orbital overlap of valence states with the ligands. This leads to strong exchange interaction via networks of transition-metal–oxygen bonds. Such strong electronic correlations provide the complexity that lies at the heart of these emergent phenomena.

Starting with theoretical predictions at the beginning of this decade [262], recently there has been an intense interest in oxides of heavy transition metals. Primarily, this concerns compounds with $4d$ and $5d$ electron valence states such as rhodates, osmates and iridates. Due to the larger spatial extent of $5d$ orbitals, the valence states in these materials are considerably more itinerant than in $3d$ transition metal oxides (TMOs). Consequently, the importance of electronic correlations in these materials is reduced. On the other hand, the coupling of spin and orbital degree of freedom, which is negligible for $3d$ oxides, is strongly enhanced in their heavy counterparts. The relevant electronic interactions in these materials can be summarized by the following Hamiltonian:

$$\mathcal{H} = \sum_{i,j;\,\alpha,\beta} t_{ij,\alpha\beta}\, c^{\dagger}_{i\alpha} c_{j\beta} + \text{h.c.} + \lambda \sum_{i} \mathbf{L}_i \cdot \mathbf{S}_i + U \sum_{i,\alpha} n_{i\alpha}(n_{i\alpha} - 1) \tag{1.5}$$

The first term and its hermite conjugate (h.c.) represents the itinerancy of electronic states, with the transfer integrals t as a scale of the probability for an electron to be annihilated (c) in an orbital β at site j and created ($c^{\dagger}$) in an orbital α at site i. In the second term, a constant λ is used to measure the strength of the coupling of spin ($\mathbf{S}$) and orbital ($\mathbf{L}$) angular momentum at a site i. Finally, the third term assigns a cost in Mott-Hubbard repulsion U to two electrons occupying the same orbital at the same site ($n_{i\alpha} = c^{\dagger}_{i\alpha} c_{i\alpha}$).

Electronic correlations, which may be as strong as $U \approx 10\,\text{eV}$ in $3d$ compounds, are typically limited to 0.5–1 in $5d$ TMOs. On the other hand, spin-orbit-coupling increases with the fourth power of the atomic number, and so from 0.5 meV ($3d$) to 0.5 eV ($5d$) [218]. Consequently, electronic correlations and spin-orbit coupling lie on the same energy scale in $5d$ TMOs. Due to the competition of these strong effects, small variations in the local

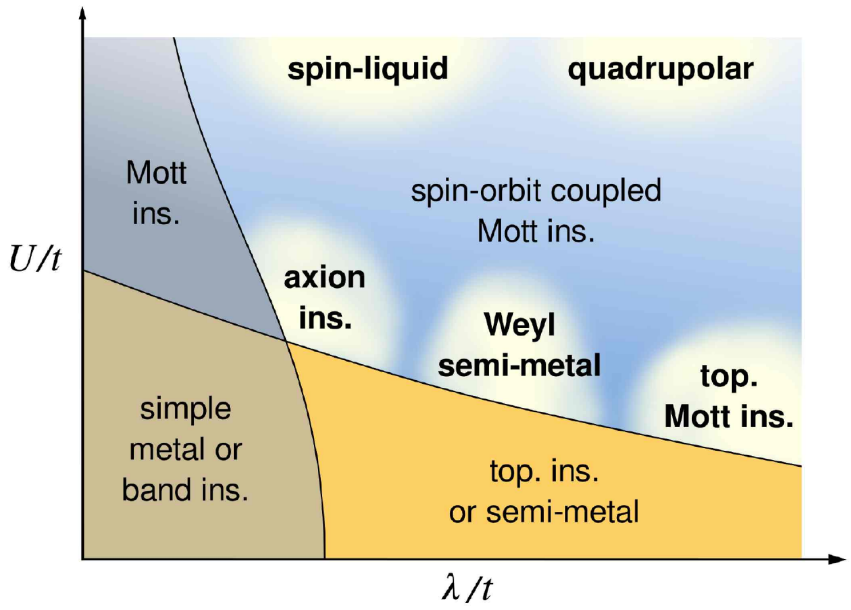

Figure 1.10: (adapted from [218]). Conceptual phase diagram of electronic states, as a function of correlations U and spin-orbit-coupling λ (on the scale of electronic itinerancy t). Until recently, most of quantum materials research has been focused on materials that represent one of the limiting cases: Strong correlation or strong spin-orbit coupling. The study of heavy transition metal oxides opens up a new regime, in which *both* interactions are relevant. The figure also indicates some of the predicted emergent phases, such as the correlated Weyl semi-metal, which may be realized in pyrochlore iridates.

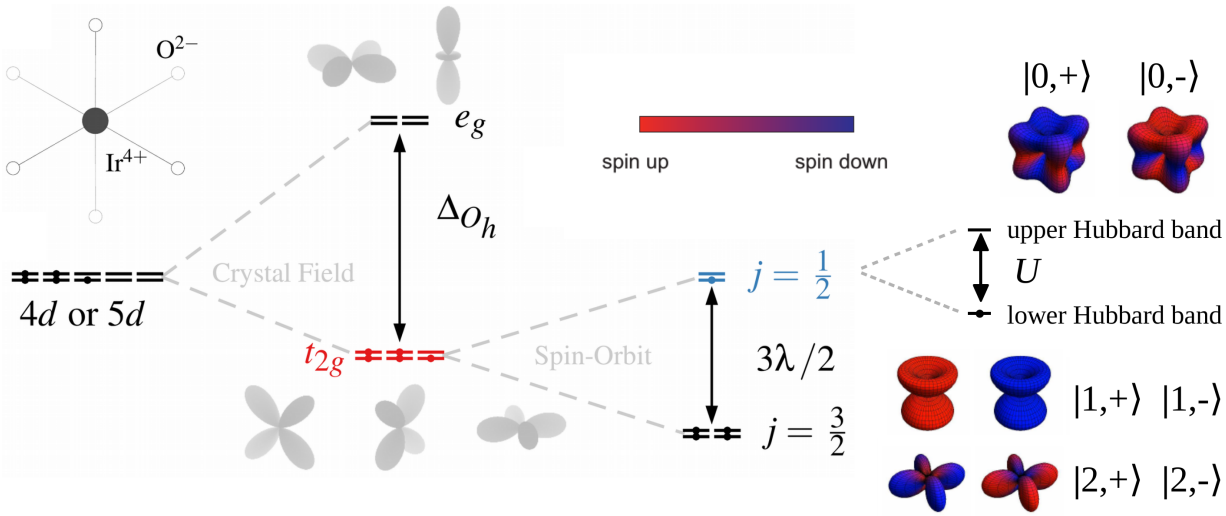

Figure 1.11: (adapted from [263, 264]). Origin of the "$J_{\text{eff}} = \frac{1}{2}$" state of Ir^{4+} ($5d^5$) iridates. The cubic crystal electric field Δ_{O_h} of a IrO_6 octahedron (inset) splits the $5d$ manifold into a t_{2g} triplet and a e_g doublet. The strong spin-orbit coupling λ further splits the t_{2g} state into a completely filled quadruplet and a half-filled $J_{\text{eff}} = \frac{1}{2}$ doublet. Since correlations are also strong, this remaining Kramers doublet acts as an effective Hubbard band. This scenario leads to a spin-orbit assisted Mott-Hubbard insulator, in which the electron spin is replaced by a composite $J_{\text{eff}} = \frac{1}{2}$ pseudospin with entangled spin- and orbital degrees of freedom.

environment or magnetic interactions and frustration may have an unexpected impact on macroscopic properties.

The current state of this young field of research has been summarized in a recent review by Witczak-Krempa *et al.* [218]. Figure 1.10 shows a conceptual phase diagram of the relative strengths of electronic correlations U/t vs. spin-orbit coupling λ/t. In the current regime of interest, where both interactions are relevant, theoretical studies have predicted a great potential for unusual emergent phenomena, such as metal–insulator transitions or topologically non-trivial electronic states. Conceptually, this situation is particularly interesting because it promises links between the previous work on strongly correlated materials and the more recent interest in electronic topology. In view of technological applications, electronic correlations are promising a handle to tune the charge transport in topologically non-trivial bands (e.g., via coupling to magnetic order). It has been envisioned such effects may be exploited in future *Dirac*-electronic devices.

1.3.2 The d^5, $J_{\text{eff}} = 1/2$ state

The materials that have received the most attention in this recent line of research are iridates with the valence state Ir^{4+}, i.e. a state with five electrons occupying the $5d$ shell. This interest had been sparked in 2009 by the seminal proposal by Jackeli and Khaliullin of the $J_{\text{eff}} = \frac{1}{2}$ spin-orbit assisted Mott insulator [262]. When located in the cubic environment of an octahedral cage of anions, the strong ($\approx 2\,\text{eV}$) crystal electric field (CEF) will split off the higher-energy e_g doublet. This effectively reduces the system to a single hole in the lower t_{2g} triplet. In the case of strong spin-orbit coupling, the t_{2g} level further splits, which leaves a fully occupied quadruplet with an effective total angular momentum $J_{\text{eff}} = \frac{3}{2}$ well separated from a $J_{\text{eff}} = \frac{1}{2}$ Kramers doublet. In this effective "pseudospin $\frac{1}{2}$" state, the spin and orbital degrees of freedom are fully entangled, with contributions from d_{yz}, d_{xz} and d_{xy} orbitals:

$$\left|\frac{1}{2}, \pm\frac{1}{2}\right\rangle = \sqrt{\frac{1}{3}}\left(|yz, \mp\rangle \pm i\,|xz, \mp\rangle \pm |xy, \pm\rangle\right) \tag{1.6}$$

Notably, this remaining $J_{\text{eff}} = \frac{1}{2}$ band is narrow enough so it can be split by even moderate electronic correlations U, in full analogy to the one band Hubbard model. By projecting the relevant superexchange interactions onto this effective Kramers doublet, Jackeli and Khaliullin realized that the unusual coupling between $J_{\text{eff}} = \frac{1}{2}$ pseudospins can produce varied novel phenomena, depending on the connectivity of IrO_6 octahedra [262]. Fortuitously, three different scenarios are realized in three iridate structural families, and each has led to intense experimental and theoretical efforts since 2009. In particular, this concerns (1) the Ruddlesden-Popper series of $Sr_{n+1}Ir_nO_{3n+1}$ perovskite-related structures,

(2) structural variations of honeycomb layers, as found in Li_2IrO_3 and Na_2IrO_3 and (3) the rare earth pyrochlore iridates $R_2Ir_2O_7$ (R: rare earth).

1.3.3 Perovskite iridates

The layered iridates Sr_2IrO_4 and $Sr_3Ir_2O_7$ share the structural symmetries of the cuprate superconductors (as e.g. La_2CuO_4). The fundamental motif are *corner*-sharing IrO_6 octahedra that form square planes, in this case carrying $J_{\text{eff}} = \frac{1}{2}$ pseudospins. There has been a long-standing interest in realizing superconductivity in other (non-cuprate) perovskites, but so far only one instance, Sr_2RuO_4, has been found [265], albeit with a different superconducting pairing mechanism and with a relatively low $T_c < 1$ K. Around the same time, investigations of Sr_2IrO_4 had revealed an insulating, weakly ferromagnetic state, which seemed to contradict the odd number of valence electrons [266].

The present interest in these materials is due to the photoemission, optical spectroscopy and resonant x-ray scattering experiments by Kim *et al.*, which demonstrated that these materials can be considered spin-orbit assisted Mott insulators [267, 268]. Many efforts have been made in pursuit of the tempting idea of stabilizing a heavily spin-orbit coupled analogue of cuprate high-temperature superconductivity by hole or electron-doping these compounds [269]. While similar characteristics as in the cuprates have been found in some cases [270, 264], no superconducting state has been achieved to date.

1.3.4 Honeycomb iridates

The interaction of $J_{\text{eff}} = \frac{1}{2}$ pseudospins is radically different in systems with *edge*-sharing IrO_6 octahedra. This had been also been realized by Jackeli and Khaliullin, who found that in this case isotropic Heisenberg correlations cancel and the interactions are dominated by a second-order exchange paths involving the lower-lying $J_{\text{eff}} = \frac{1}{2}$ manifold [262]. Unexpectedly, the ground state of this system corresponds to a "compass model" [271] which had been applied to a magnetic honeycomb layer and explored in great depth by Kitaev only a few years earlier [272].

In this scenario, the three pseudospin components couple to each other separately, each along one of the three bonds that are separated by 120° in the honeycomb structure (see Fig. 1.12(c)). Theoretical studies had been indicated that the elusive *quantum spin liquid* would be the natural ground state of such systems [272]. However, this state would not be protected by symmetry and therefore unstable to higher order interactions, which could for example be induced by weak structural distortions [264].

The relevant honeycomb-iridates Na_2IrO_3 and $\alpha-Li_2IrO_3$ (as well as its β- and γ- hyper-honeycomb and *stripy* honeycomb phases) have all been found to exhibit magnetic order at low temperatures [273, 274, 275]. Converging experimental evidence shows that the $J_{\text{eff}} = \frac{1}{2}$ state in these materials is indeed well within the spin-orbit assisted Mott regime and structural distortions are comparatively small [275, 276]. Consequently, there is at the moment a great interest in understanding how these systems can be tuned towards pure Kitaev physics, e.g. by ionic substitution or external tuning parameters.

1.3.5 Pyrochlore iridates

In the rare earth iridates $R_2Ir_2O_7$ (R: rare earth) iridates, each Ir^{4+} site is fully connected to six neighbouring IrO_6 octahedra. The resulting three-dimensional *pyrochlore* network of corner-sharing transition metal tetrahedra had already been investigated in great depth, mainly due to the inherent effects of magnetic frustration [277, 278]. Compared to the compounds discussed above, the electronic states in this family of iridates are more itinerant. They represent the *weakly correlated* limit of the $J_{\text{eff}} = \frac{1}{2}$ scenario, where electronic states are further extended, and the effects of strong spin orbit coupling are best analysed in terms of band topology.

The interest in the $R_2Ir_2O_7$ series was sparked by early findings of a continuous metal–insulator transition that can be continuously suppressed by ionic substitution [279, 280, 281]. Placement of a larger rare earth R^{3+} ion relieves trigonal distortions of the structure, which in turn increases the overlap between the $5d$ states and their ligands and thus facilitates electron hopping [282]. Trigonal distortions of the local environment play another important role in pyrochlore iridates by tuning the electronic state away from the $J_{\text{eff}} = \frac{1}{2}$ scenario towards a simple $S = \frac{1}{2}$ state. Such factors may have a decisive impact on the mechanism of the charge gap opening, but a consistent understanding of this phase transition has not been achieved.

A number of theoretical studies have suggested that the $R_2Ir_2O_7$ ground state may be in the vicinity of unprecedented topological electronic phases such as the Axion insulator or a Weyl-semimetallic phase with broken time-reversal-symmetry [211, 283, 284]. At present, this scenario has not been conclusively confirmed, and overall only few in-depth experimental studies of these materials are available. I have contributed to this search with several resonant x-ray studies of the magnetic order in these systems (not reported in this thesis). Together with my collaborators, I was able to demonstrate that $Sm_2Ir_2O_7$ is indeed host to the elusive all-in–all-out order, which had been predicted by theory and represents a prerequisite for the stabilization of the correlated WSM phase in these systems [150].

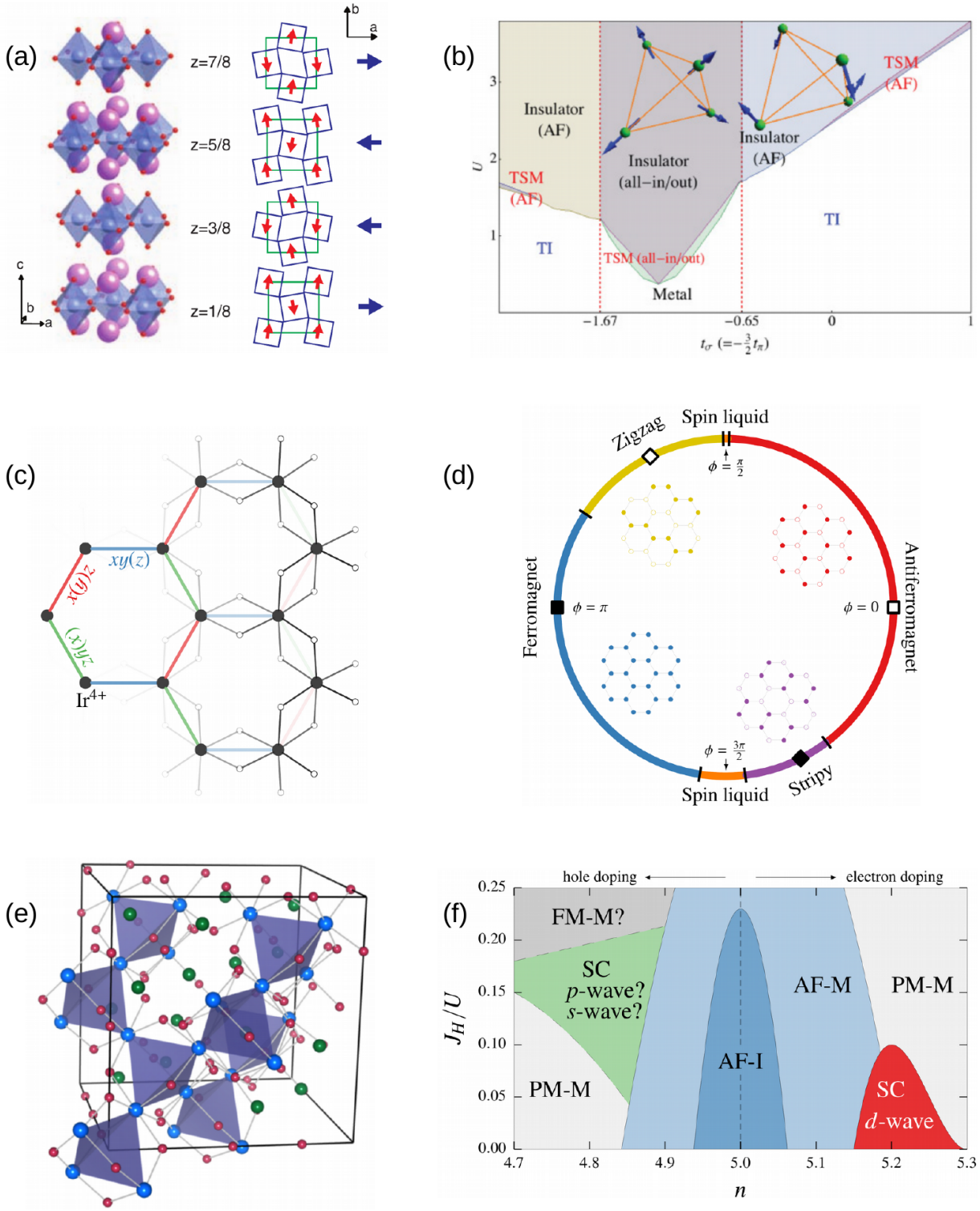

Figure 1.12: (adapted from [283, 218, 264]). Three structural classes of Ir^{4+} ($5d^5$) iridates, with corresponding theoretical phase diagrams, as discussed in the main text. (a,b) Perovskite iridates, e.g. Sr_2IrO_4, (c,d) honeycomb iridate, e.g. Na_2IrO_3, (e,f) pyrochlore iridates, e.g. $Nd_2Ir_2O_7$

1.3.6 Hexagonal iridates

Another realization of the $4d^5/5d^5$ valence state is found in the hexagonal family of A_4BO_6 iridates [285]. In this case, the BO_6 octahedra form face-sharing chains along the c axis. In the iridate families noted above, octahedral environment is to some extent distorted. The extend to which the $J_{\text{eff}} = \frac{1}{2}$ picture actually applies, has therefore been debated. By contrast, the A_4BO_6 structure provides an almost ideal BO_6 octahedron [286]. Consequently, the effects of spin–orbit coupling are enhanced and the spin–orbit assisted Mott state can be observed also in the $4d$ (Rh, Z=45) compound. Using the neutron powder diffractometers D2B and D20 (ILL), I have determined the magnetic order in two of these materials, Sr_4IrO_6 and Ca_4RhO_6 (results not reported in this dissertation).

1.3.7 Osmates: d^1, d^2 and d^3 states

The interest in 5d TMOs is not restricted to the Ir^{4+} $5d^5$ valence state. Unusual effects of strong spin orbit coupling are also observed in several *osmates*. For example, there is a large family of double perovskite osmates A_2BOsO_6 with the oxidation states Os^{6+} or Os^{7+}, corresponding to $5d^1$, $J_{\text{eff}} = \frac{3}{2}$ and $5d^2$, $J_{\text{eff}} = 2$ states [218, 287]. Consequently, the orbital degeneracy is not only partially lifted, and spin- and orbital degrees of freedom are entangled. This manifests in an anomalous reduction of magnetic moments [288], unusual charge gaps [289], orbital ordering phenomena [290] and multipolar exchange interactions [291, 287, 218].

I have investigated unusual structural and magnetic phenomena in two such double-perovskite osmates, Pb_2CoOsO_6 and Pb_2CoOsO_6 using resonant and non-resonant x-ray diffraction techniques (not reported in this dissertation). Furthermore, I also used neutron diffraction and muon spin-rotation to investigate the case of a $5d^4$ magnetic ground state in a new pyrochlore osmate $Y_2Os_2O_7$. As the t_{2g} manifold is fully occupied, such compounds should be nominally non-magnetic, but may host an unusual condensation of $J_{\text{eff}} = 1$ triplon excitations [292] (not reported in this dissertation).

Unusual insulating phases reminiscent of the Ir^{4+} compounds have also been reported in several Os^{5+} ($5d^3$, nominally $S = 1$, $L = 0$) compounds. This includes the post perovskite $NaOsO_3$ [293, 294], as well as the pyrochlore $Cd_2Os_2O_7$ [295, 296]. In Chapter 6 of this thesis, I present my investigation of two polymorphs of the related $Ca_2Os_2O_7$ $5d^3$ system. The character of the metal-insulator transitions observed in these materials is not well understood: Several limiting scenarios (the Lifshitz [297], Slater [298] and spin-orbit-assisted Mott [267] mechanisms) have been proposed, but in most cases the available experimental data does not allow a clear distinction. One important motivation in the field of heavy TMOs is to establish a unified explanation of these phenomena.

1.3.8 Experiment: Limitations and opportunities

Even though the scientific interest in heavy transition metal oxides has been growing at a fast pace since the beginning of the decade, experimental progress has been slow. This can be attributed to several reasons. Firstly, the sample preparation for many of the above materials is not well established; samples may commonly suffer from off-stoichiometry ($R_2Ir_2O_7$), require specialized high-pressure techniques (e.g. Pb_2CoOsO_6, Ca_2OsO_7) or are chemically unstable in ambient conditions (Na_2IrO_3, Li_2IrO_3). The extreme toxicity of Os byproducts is an additional impediment to systematic crystal growth studies. As a consequence, there are few cases in which single crystals with dimensions sufficient for neutron inelastic studies can be grown. Even if this was possible, the strong neutron-absorption cross section of Ir would be another limiting factor. The situation is also made more difficult by the fact that the modulus of the ordered magnetic moment of many of these heavily spin-orbit coupled compounds is reduced to $< 1\,\mu_B$. Due to such limitations, neutron studies of the magnetic ground states of iridates have so far been limited to powder diffraction [299, 300].

This situation has accelerated the development of complementary scattering techniques. Fortuitously, the rise of interest in $5d$ TMOs coincided with significant instrumental advances at 3rd generation synchrotron radiation sources [301]. The brilliance of photon beams produced by undulator devices, together with the strong enhancement of magnetic scattering at the $5d$ $L_{2,3}$ edges have made resonant elastic and inelastic x-ray scattering (REXS/RIXS) powerful experimental alternatives (see Section 2.4). In this way, the requirements of $5d$ TMOs have inspired the first bulk-sensitive determinations of magnetic order and dynamics in single crystals with dimensions on the order of tenths of micrometers [273, 276, 275]. However, rather than being just a substitute for the case of small samples, the complexity of the resonant–x-ray scattering cross section offers new experimental possibilities that have yet to be fully exploited [302, 303].

Chapter 2

Experimental methods

In this chapter I present the methods that I used in my research and summarize the basic formalism needed to describe the experimental results. This is intended as a background for the more detailed discussion of specific experiments and data analysis in Sections 3–6.

First, I describe the sample alignment and characterization techniques that I performed with standard laboratory equipment. The main focus of my work lies on the use of state-of-the-art scattering experiments that are performed at synchrotron and neutron radiation facilities. The common goal of these experiments is either (1) to determine the magnetic order of novel quantum materials, or (2) to characterize the corresponding magnetic dynamics. This is achieved by diffraction and spectroscopy, respectively. In each project, a number of factors determines whether it is most favourable to use neutron or synchrotron radiation, and whether to investigate polycrystalline or single crystal samples.

The theory of coherent scattering from condensed matter is independent of the type of radiation. Therefore, I present the most fundamental relations in parallel for both types of radiation, before relating the specific properties of either in detail. The complementarity of the nuclear and electromagnetic interactions adds to a versatile toolbox for the investigation of condensed matter. Radiation sources and instrumentation are presently improving at a rapid pace and the scientific possibilities of scattering techniques appear far from exploited.

Finally, I outline basic aspects of the muon spin rotation and relaxation. This technique proved a useful tool in resolving ambiguities in the neutron powder diffraction data presented in Chapter 6.

Contents

2.1 Sample characterization 33

2.1.1 Magnetic properties 33

2.1.2 Resistivity and Hall effect 33

2.1.3 Laboratory x-ray diffraction 35

2.2 Scattering from condensed matter 37

2.3 Neutron scattering 42

2.3.1 Nuclear neutron scattering 42

2.3.2 Magnetic neutron scattering 46

2.3.3 Neutron sources and instruments 49

2.4 X-ray scattering 51

2.4.1 Thomson scattering 51

2.4.2 Full x-ray scattering cross section 52

2.4.3 Nonresonant magnetic x-ray scattering 54

2.4.4 Resonant exchange x-ray scattering 55

2.4.5 Resonant inelastic x-ray scattering 59

2.5 Muon spin rotation and relaxation 61

2.1 Sample characterization

2.1.1 Magnetic properties

The first, straightforward approach to probe the magnetic response of a material is to measure its magnetization as a function of temperature and applied magnetic field. For all samples that I investigated, both poly- and single-crystalline, I performed such measurements using a commercial superconducting quantum interference device (SQUID) magnetometer (MPMS, Quantum Design [304]). This instrument features a cylindrical sample space surrounded by liquid helium and liquid nitrogen jackets. This allows a continuous variation of the temperature in the range of 2–350 K. A pair of superconducting Helmholtz coils provides a magnetic field up to 7 T. The sample is mounted in a plastic straw, attached to a sample rod, and lowered into the dewar .

The measurement (*direct current mode*) is then performed by translating the straw through a set of pick-up coils at the sample position. By Faraday's law, a magnetic moment of the sample induces a current in the pick up coils, which in turn are coupled to the SQUID. The system achieves a resolution on the order of 10^{-8} emu. When operating in the DC-mode, a finite excitation field must be applied to observe a response from a sample in its paramagnetic state. In order to minimise the effect of the field on the ground state properties, I generally chose this extrinsic field as low as possible (ca. 50–1000 Oe), depending on sample mass and magnitude of magnetic moment.

I used this setup to characterize single crystals as well as polycrystalline samples (packed into a plastic capsule). For a direction-dependent measurement of the anisotropic properties of single crystals, I first mounted the samples on a quartz capillary and aligned it on a four-cycle x-ray diffractometer (see below). Once oriented in the desired direction, I transferred the capillary carrying the sample into to the SQUID straw and fixed it using cryogenic varnish.

2.1.2 Resistivity and Hall effect

To characterize the transport of charge as a function of temperature and field, I performed alternating current resistivity and Hall effect measurements using a commercial Physical Properties Measurement System (ACT option, PPMS, Quantum Design [304]). In analogy to the MPMS system, this instrument features a dewar with concentric liquid helium and liquid nitrogen vessels and a superconducting 14 T cryomagnet surrounding the sample position. I mounted the samples (either in single- or polycrystalline/pellet form) on a standard ACT sample holder (see Fig. 2.1(c)). This *puck* features two sets of

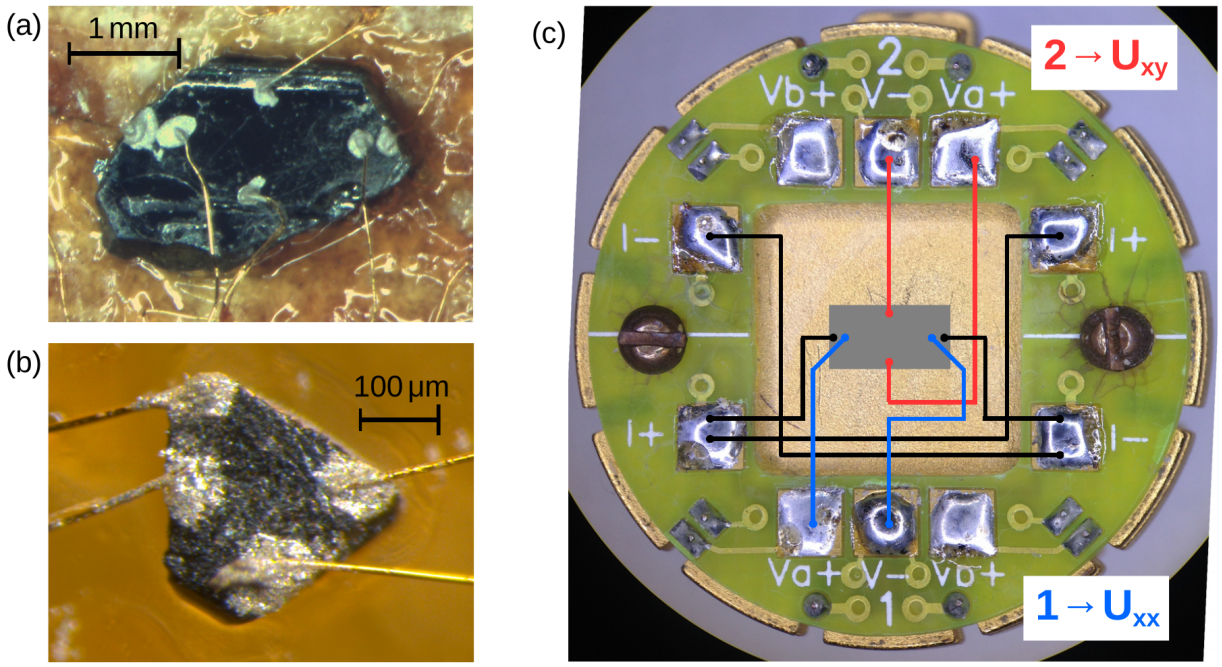

Figure 2.1: AC transport using the Quantum Design PPMS system [304]. (a) Single crystal contacted for a six-point measurement ($EuCd_2As_2$), and (b) for a four-point measurement ($Nd_2Ir_2O_7$). (c) Wiring scheme of the PPMS *puck* for six-point measurements using both lock-in amplifiers of the system to measure both longitudinal and transversal voltages.

voltage and current terminals, intended for the simultaneous measurement of two samples. When inserted in the dewar, these terminals connect to two lock-in amplifiers and a high precision current source.

I performed transport measurements using either a four-point contacting (resistivity) or a six-point contacting pattern to measure resistivity and Hall effect simultaneously (see Fig. 2.1(a,b)). Contacts to the sample surfaces were made using 10–25 μm gold wire and *Epotek* silver epoxy [305].

The six-point wiring scheme used to simultaneously measure resistivity and Hall effect on the same sample is drawn in Fig. 2.1(c). The current leads of the two terminal sets are shorted and the voltage terminals of set (1) and (2) are contacted to the sample in a longitudinal (voltage U_{xx}) and transversal geometry (voltage U_{xy}), respectively. Due to the imperfect contact positions in any real measurement, the U_{xy} signal will necessarily be contaminated (and generally dominated) by a U_{xx} component. In order to correct for this, for each field (H) sweep at constant temperature (T), I therefore measured *up* and *down* H-ramps. For each T-sweep (at constant H), I repeated the measurement at with positive and negative applied field (w.r.t. the magnet axis).

The *true* transversal and longitudinal voltages are then obtained by (anti-)symmetrization of the signal, according to

$$U_{xx}(H) = \frac{1}{2}\left(U_{xx}^{\mathrm{up}} + U_{xx}^{\mathrm{down}}\right) \qquad U_{xy}(H) = \frac{1}{2}\left(U_{xy}^{\mathrm{up}} - U_{xy}^{\mathrm{down}}\right)$$
$$U_{xx}(T) = \frac{1}{2}\left(U_{xx}^{(+H)} + U_{xx}^{(-H)}\right) \qquad U_{xy}(T) = \frac{1}{2}\left(U_{xy}^{(+H)} - U_{xy}^{(-H)}\right)$$

The measured voltages can be converted to resistivity ρ_{xx} and Hall resistivity ρ_{xy} by application of the appropriate sample *geometry factors*:

$$\rho_{xx} = F_{xx} \cdot U_{xx} \quad \left(F_{xx} = \frac{A_{xx}}{l_{xx} I}\right) \qquad \rho_{xy} = F_{xy} \cdot U_{xy} \quad \left(F_{xy} = \frac{A_{xy}}{l_{xy} I}\right)$$

Here, I is the applied current and A_{xx} (A_{xy}) and l_{xx} (l_{xy}) are the cross sections and lengths of the longitudinal (transversal) current path.

2.1.3 Laboratory x-ray diffraction

As noted above, knowledge of the orientation of the crystallographic axes with respect to the faces of a single crystal is necessary in order to be able quantify the anisotropy of a magnetic state in direction-dependent magnetization measurements. Laboratory x-ray diffraction is also an indispensable tool to prepare single crystals for scattering experiments at neutron and synchrotron radiation facilities. The incident flux is generally a limiting factor in such experiments, and much information (or counting statistics / experimental time) can be lost from samples with poor mosaicity. Moreover, twinned crystals or samples containing multiple grains will complicate an experiment and waste valuable measurement time. Given a batch of crystallites grown by the flux or vapour deposition method, I therefore dedicated some effort to select highest quality specimen.

Constraints of the scattering geometry at synchrotron and neutron beamlines also call for a precise in-house sample alignment. The sample environment (cryostats, magnets and pressure cells) at these instruments often limits the accessible range of scattering angles. Therefore, a strategic orientation and mounting of single crystals becomes an important part of such experiments. This applies particularly for large high-resolution diffractometers at synchrotron sources, as illustrated in Section 5.3. At such beamlines, the in-situ alignment of an unknown or poor quality crystal can be time-consuming or not feasible. Most single crystal samples that I studied had dimensions on the order of 50 μm–1 mm. I generally prepared such samples in three steps:

First, I screened several samples for crystal quality using the four-cycle x-ray diffractometer shown in Fig. 2.2(a) (Agilent Technologies [306]). This instrument features a

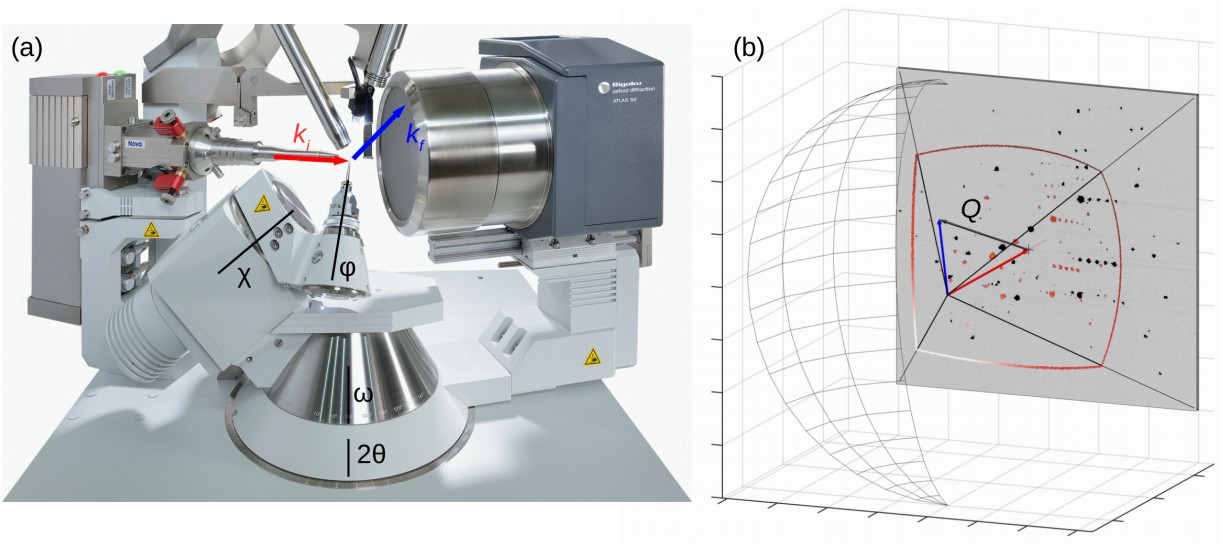

Figure 2.2: Laboratory Mo K_α x-ray diffraction. (a) Commercial x-ray diffractometer used for single crystal alignment and structure determination [306]. The axes of the miniature four-circle kappa diffractometer are labelled and the directions of incident and scattered wave vectors are indicated. (b) Corresponding view of reciprocal space, which illustrates the projection of a CCD detector image (grayscale) onto the Ewald sphere.

focusing Mo K-α x-ray tube with a beam diameter of 200 μm, a kappa-diffractometer and an CCD area detector (Agilent Technologies Atlas 135 mm). In Figure 2.2, this scattering geometry is illustrated in real and reciprocal space (see Section 2.2). In momentum space, the rectangular detector chip is mapped onto a section of the Ewald sphere (the diameter of the sphere is fixed by the Mo K_α incident energy). By performing a series of ω-scans at various ϕ orientations, the spherical section is rotated in reciprocal space. Thus, scattered intensity can be collected for a large continuous volume of reciprocal space. A unit cell can then be assigned and Bragg peaks indexed for a crystal that was initially mounted in an arbitrary orientation (commercial algorithm, [306]). Having assigned a unit cell and orientation (UB) matrix to a given dataset, the system also allows to visually display the orientation of the assigned cell with respect to the mounted crystal (see Fig. 2.3(b)). Thus, the desired crystallographic plane, which may correspond to a facet of the crystal, can be identified.

In x-ray scattering experiments it is often advantageous to use a plate-like sample with the relevant reflection specular. Such sample can easily be mounted flat on a standard sample holder (typically a threaded copper or brass cylinder). Once the orientation of a crystal is known, it can be shaped by grinding or polishing. To this end, I mounted the crystallites in clear hard wax on top of a heated steel die, shown in Fig. 2.3(a). Generally, I first shaped the samples by grinding with 2400 grit abrasive paper and, if required, polished the resulting facet down to 0.5 μm using diamond paste on a planar polishing machine.

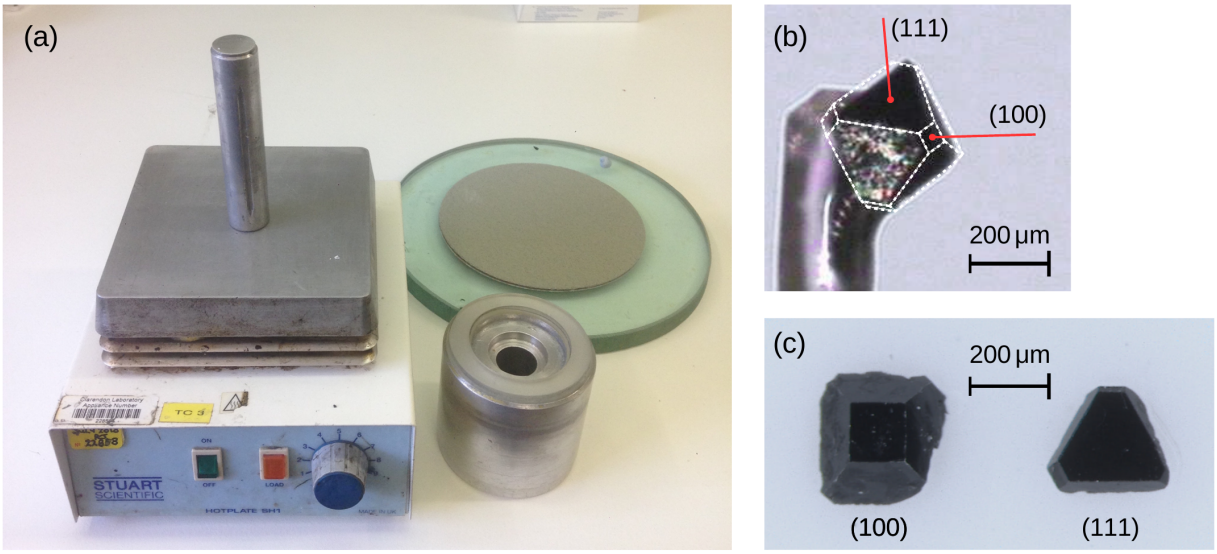

Figure 2.3: (a) Setup for grinding sample surfaces parallel to desired crystallographic planes. (b) Octahedral crystallite mounted (on a quartz capillary) on the four circle Mo K_α diffractometer of Fig. 2.2(a). A UB matrix has been assigned to the crystal and corresponding orientations of high symmetry directions are indicated by white dashed lines. (c) Similar crystallites shaped into flat platelets intended for REXS studies of $(H00)$ and (HHH)-type Bragg reflections in a specular geometry.

When mounted in clear wax on the polishing die, samples that do not already have a parallel facet are easily offset from the desired orientation by several degrees. I used a Cu K_α high-resolution diffractometer (Rigaku Smartlab [307], not shown) to determine the azimuthal direction and extent of this tilt to within 0.01°. I mounted the polished plate-like sample flat, in Bragg-Brentano geometry. Then I recorded the *experimental* θ angle of a specular reflection for a series of azimuthal angles. This produces a sinusoidal curve around the baseline of the *true* scattering angle $(2\theta)/2$. The extrema of this curve indicate the azimuthal angle of the tilt direction. At the synchrotron beamline, the sample can then be mounted with this tilt direction in the scattering plane, which reduces a lengthy alignment procedure to a scan of one axis.

2.2 Scattering from condensed matter

Bulk probes measure *macroscopic* properties of materials, such as magnetic, electric, thermal and elastic constants. This provides basic information about the magnetic and electronic state of a material. When measured as a function of external parameters, it may also indicate the presence and character of symmetry-breaking phase transitions. However, information about microscopic order and dynamics can at most be be inferred with ambiguity from such data.

By contrast, x-ray and neutron radiation penetrate into and probe materials with wavelengths and energies on the atomic scale. Through positive interference of *scattered* neutron and x-ray waves, this *microscopic* information becomes accessible on the macroscopic scale. The century following the 1912 observation of "secondary rays" from $CuSO_4.(H_2O)_5$ by Laue [308] and the correct interpretation by Bragg and Bragg [309] has seen an impressive evolution of experimental capabilities [310, 311]. These developments have enabled fundamental discoveries ranging from magnetic order [312, 313] to the structure of DNA [314]. The scientific merit and technological impact of these techniques cannot be overstated.

All scattering techniques probe the response of a sample (poly- or single-crystalline), referred to as *scattering system* below, at a certain momentum-transfer $\boldsymbol{Q}$ and energy-transfer $\hbar\omega$. The measured quantity is the differential scattering cross section,

$$\frac{\mathrm{d}^2\sigma}{\mathrm{d}\Omega\mathrm{d}\omega} = \frac{I_{\mathrm{SC}}}{\Phi_0\,\Delta\Omega\,\Delta\omega} = \frac{\rho(E_f)}{\Phi_0\,\Delta\Omega}\,\mathcal{W} \quad . \tag{2.1}$$

For an incoming flux of Φ_0 (photons or neutrons per area per second), this describes the number of particles I_{SC} (in an energy-transfer range $\Delta\omega$) that is scattered each second into a detector area subtending the solid angle $\Delta\Omega$ with respect to the sample position. By *Fermi's golden rule*, the scattering cross section is proportional to the product of the transition probability $\mathcal{W}$ from the initial state $|i\rangle$ to the final state $|f\rangle$ of the scattering system (including the scattered particle) and the probability of the final state $\rho(E_f)$. Depending on the context, the scattering cross section may be expressed with or without explicit reference to an energy transfer $\mathrm{d}\omega$ of the scattered particles. Accordingly, it is referred to as the elastic (single-differential) or inelastic (double-differential) scattering cross section.

The key difference between neutron- and x-ray scattering is the dispersion of *massive*, as opposed to *massless* particles:

$$\omega = \frac{\hbar k^2}{2m} \quad \text{(neutron)} \qquad\qquad \omega = c\,k \quad \text{(photon)} \quad , \tag{2.2}$$

where ω is the angular frequency of the radiation and $k = 2\pi/\lambda$ is the modulus of the wavevector for radiation of a wavelength λ. $\hbar = h/(2\pi)$ is the Planck constant, m is the neutron mass and c is the speed of light. This corresponds to a picture of particles of energy $E = \hbar\omega$ moving with a velocity $v = \frac{\mathrm{d}\omega}{\mathrm{d}k}$:

$$v = \frac{\hbar k}{m} \quad \text{(neutron)} \qquad\qquad v = c \quad \text{(photon)} \tag{2.3}$$

In order to find expressions for the incoming flux Φ_0 and the (energy-) density of scattering states $\rho(E_f)$ in Eq. 2.1, one considers a beam of particles with a density of $1/\mathcal{V}$ in real space, thus occupying a *quantization volume* of $\mathcal{V}^* = (2\pi)^3/\mathcal{V}$ in momentum space. The incoming flux is then given by the product of real space density and velocity, $\Phi_0 = v/\mathcal{V}$:

$$\Phi_0 = \frac{1}{\mathcal{V}}\frac{\hbar k_i}{m} \quad \text{(neutron)} \qquad\qquad \Phi_0 = \frac{c}{\mathcal{V}} \quad \text{(photon)} \tag{2.4}$$

Furthermore, the number of particles scattered into an energy range $\mathrm{d}E_f$ must be identical to the number of particles in the corresponding volume $k_f^2\,\mathrm{d}k_f\,\mathrm{d}\Omega$ of reciprocal space:

$$\begin{aligned} \rho(E_f)\cdot \mathrm{d}E_f &= \frac{1}{\mathcal{V}^*}\cdot k_f^2\,\mathrm{d}k_f\,\Delta\Omega \\ \rho(E_f) = \frac{\mathcal{V}}{(2\pi)^3}k_f^2\frac{\mathrm{d}k_f}{\mathrm{d}E_f}\Delta\Omega &= \begin{cases} \frac{\mathcal{V}}{(2\pi)^3}\,k_f\,\frac{m}{\hbar^2}\,\Delta\Omega & \text{(neutron)} \\ \frac{\mathcal{V}}{(2\pi)^3}\,\frac{k_f^2}{\hbar c}\,\Delta\Omega & \text{(photon)} \end{cases} \end{aligned} \tag{2.5}$$

so that

$$\frac{\mathrm{d}^2\sigma}{\mathrm{d}\Omega\mathrm{d}\omega} = \frac{\mathcal{V}^2}{(2\pi)^3}\frac{m^2}{\hbar^3}\frac{k_f}{k_i}\mathcal{W} \quad \text{(neutron)} \qquad \frac{\mathrm{d}^2\sigma}{\mathrm{d}\Omega\mathrm{d}\omega} = \frac{\mathcal{V}^2}{(2\pi)^3}\frac{k_f^2}{\hbar c^2}\mathcal{W} \quad \text{(photon)} \tag{2.6}$$

In the following sections, I will show how equation 2.6 can be evaluated to describe various scattering phenomena. The microscropic character of the scattering process demands a quantum mechanical evaluation of $\mathcal{W}$. Regardless of the type of radiation or subject of study (electrons or nuclei) the interaction with the incident beam can be treated as a weak perturbation of a quantum mechanical system. The transition probability thus corresponds to the squares of the matrix elements of the appropriate perturbation Hamiltonian *or interaction operator* $\mathcal{H}_{\mathrm{int}}$. To include resonant processes, $\mathcal{W}$ can be considered up to second order. This adds a sum over intermediate states $|n\rangle$:

$$\mathcal{W} = \frac{2\pi}{\hbar}\left|\langle f|\mathcal{H}_{\mathrm{int}}|i\rangle + \sum_n \frac{\langle f|\mathcal{H}_{\mathrm{int}}|n\rangle\langle n|\mathcal{H}_{\mathrm{int}}|i\rangle}{\hbar\omega - (E_i - E_n)}\right|^2 \delta(\hbar\omega - (E_i - E_f)) \tag{2.7}$$

Here, $|i/n/f\rangle = |\psi_{i/n/f}, \zeta_{i/n/f}\rangle$ represent compound wave functions that contain both the state $|\zeta\rangle$ of the sample and the state $|\psi\rangle$ of the scattering particle (which, in turn, may be separated into spatial and spin degree of freedoms).

The availability of neutron and x-ray radiation gives access to *three interactions* that can be substituted for $\mathcal{H}_{\mathrm{int}}$: (1) The nuclear interaction of the neutron with the nucleus, (2) the dipolar interaction of the magnetic moment of the neutron with the magnetic moment of an ion and (3) the multipolar interaction of electromagnetic radiation with a

distribution of electric and magnetic fields at an atom. This versatility explains the great number of applications of scattering techniques in condensed matter physics.

Both neutrons and x-rays have three physical properties that can be controlled and measured before and after the scattering event: Energy, momentum and polarization. The different cases for which I evalute $\mathcal{W}$ below demonstrate how these quantities link to physical properties of the scattering system. Each result for $\mathcal{W}$ naturally implies a particular scattering geometry and an experimental setup which is optimized for control and measurement of the relevant neutron and x-ray properties. The expressions derived in this section have fuelled the development of a large family of specialized instruments or *beamlines* which is now available at user facilites. None of these applications are redundant, and this thesis illustrates how this "toolbox" of scattering techniques inherits a (somewhat coincidental) elegance from the complementary properties of the x-ray and the neutron.

Irrespectively of the scattering potential and resulting form of $\mathcal{W}$, the intensities measured in experiment are due to the coherent interference of radiation that is scattered from a periodic arrangement of atoms (i.e. a crystal). Although valuable information may also be gleaned from incoherent (diffuse) scattering, such effects lie beyond the scope of this dissertation. The correct interpretation of coherent x-ray scattering was first provided by William Henry and William Lawrence Bragg in 1913 [309]. Since this *kinematic theory* applies for any form of radiation, I first summarize these concepts, before evaluating the scattering cross sections for neutrons and x-rays.

Crystalline structure is defined in terms of a lattice $\boldsymbol{R}$, spanned by primitive lattice vectors $\boldsymbol{a}_i$:

$$\boldsymbol{R} = u\,\boldsymbol{a}_1 + v\,\boldsymbol{a}_2 + w\,\boldsymbol{a}_3, \quad u,v,w \in \mathbb{Z} \tag{2.8}$$

Notably, the concept of a *lattice* is purely mathematical, as it is defined by the symmetries of a crystal. The full description of a *crystal structure* further requires the definition of a *basis* of atoms, which is repeated in space with the periodicity of the lattice. The Fourier transform of $\boldsymbol{R}$ yields a corresponding lattice $\boldsymbol{G}$ in momentum or *reciprocal* space:

$$\begin{aligned} \boldsymbol{G}_{HKL} &= H\,\boldsymbol{b}_1 + K\,\boldsymbol{b}_2 + L\,\boldsymbol{b}_3 \quad , \quad H,K,L \in \mathbb{Z} \\ \boldsymbol{b}_1 &= 2\pi \frac{\boldsymbol{a}_2 \times \boldsymbol{a}_3}{\boldsymbol{a}_1 \cdot (\boldsymbol{a}_2 \times \boldsymbol{a}_3)} \qquad \text{(and permutations)} \end{aligned} \tag{2.9}$$

In real space, the vector $\boldsymbol{G}_{HKL}$ is normal to a set of crystal planes, which is then referred to by the indices $[H,K,L]$. Furthermore, from eqs. 2.8/2.9 it follows that its modulus is inversely proportional to the spacing d of these planes: $|\boldsymbol{G}_{HKL}| = 2\pi/d_{HKL}$.

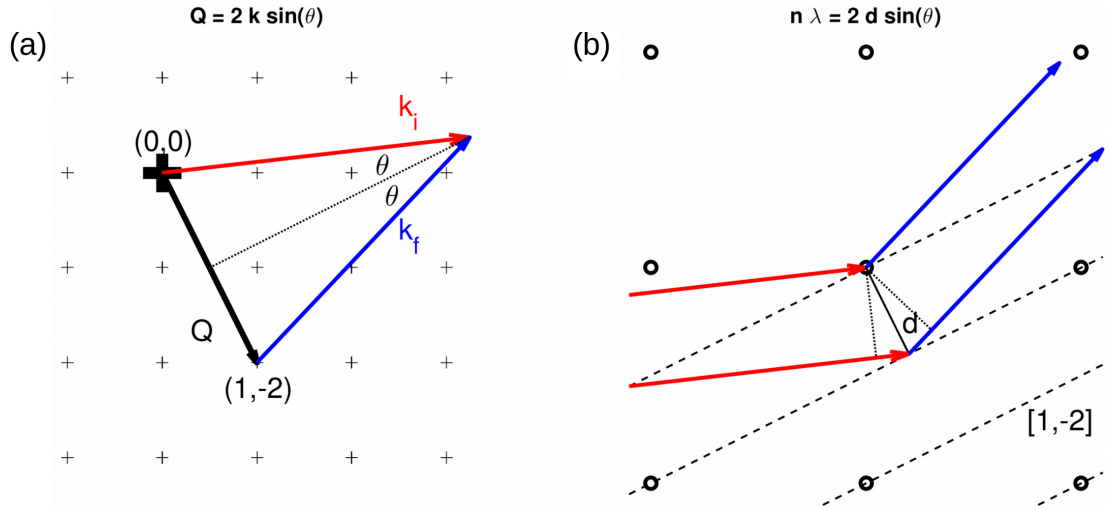

Figure 2.4: An elastic scattering (diffraction) event, illustrated on a square lattice in reciprocal space (a) and real space (b). The direction and momentum of the incoming ($\mathbf{k}_i$) and outgoing ($\mathbf{k}_f$) beam define the momentum transfer $\mathbf{Q}$. If $\mathbf{Q} = \mathbf{G}_{HKL}$, the radiation scattered from the $[HKL]$ set of planes interferes positively. This *Laue condition* indicated in panel (a) is equivalent to the construction of *Bragg's law* shown in panel (b).

In a scattering experiment, the four-dimensional space spanned by vectors $\boldsymbol{b}_i$ and the energy $E = \hbar\omega$ is mapped by varying the direction and magnitudes of the wavevectors $\boldsymbol{k}_i$ and $\boldsymbol{k}_f$ of the incoming and scattered radiation. As indicated in Fig. 2.4(a), the wavevectors $\boldsymbol{k}_i$ and $\boldsymbol{k}_f$ of the incoming and scattered beam define a *scattering triangle* in reciprocal space, which subtends the momentum transfer vector $\boldsymbol{Q} = \boldsymbol{k}_i - \boldsymbol{k}_f$. Waves scattered from the crystal will interfere positively if the *Laue condition* $\boldsymbol{Q} = \boldsymbol{G}_{HKL}$ is satisfied, i.e. if the momentum transfer corresponds to a reciprocal lattice vector. The construction in Fig. 2.4(a) shows that this implies $|\boldsymbol{Q}| = 2k\sin(\theta)$. The corresponding real space picture, Fig. 2.4(b), illustrates that the Laue condition is equivalent to Bragg's law,

$$n\lambda = 2d\sin(\theta) \quad , \quad n \in \mathbb{N}, \tag{2.10}$$

since $k = 2\pi/\lambda$ and, here, $Q = |\boldsymbol{G}_{HKL}| = 2\pi/d$. Scattered radiation detected under this condition is referred to as a *Bragg reflection* or *peak* and is indexed by the integer triple (H,K,L).

Magnetic structures inherit the translation symmetry of the crystal structure and are therefore also best described by a Fourier series. The coordinates $\boldsymbol{R}_{l\alpha}$ of magnetic ions in a crystal can be separated, $\boldsymbol{R}_{l\alpha} = \boldsymbol{R}_l + \boldsymbol{d}_\alpha$ into the *lattice* coordinate $\boldsymbol{R}_l$ of a primitive unit cell and the relative positions $\boldsymbol{d}_\alpha$ of magnetic scattering sites therein. The arrangement

of magnetic moments $\boldsymbol{m}_{l\alpha}$ in any magnetic structure can then be defined as [315]

$$\boldsymbol{m}_{l\alpha} = \sum_{\mathbf{q}_\mathrm{m}} \mathbf{m}^*_{\mathbf{q}_\mathrm{m}\alpha}\, e^{-2\pi i\, \boldsymbol{q}_\mathrm{m}\cdot\boldsymbol{R}_l} \quad . \tag{2.11}$$

This sum includes $\pm\boldsymbol{q}_\mathrm{m}$ for each *magnetic propagation vector* $\boldsymbol{q}_\mathrm{m}$ of the Fourier components $\mathbf{m}^*_{\mathbf{q}_\mathrm{m}\alpha}$. Notably, Eq. 2.11 may describe a ferromagnet ($\boldsymbol{q}_\mathrm{m} = 0$), simple commensurate antiferromagnetic order, multiaxial and "multi-$\boldsymbol{q}_\mathrm{m}$" antiferromagnetic order, as well as long-range modulated magnetic structures (in the case of complex Fourier components).

2.3 Neutron scattering

In neutron scattering, it is generally sufficient to evaluate Eq. 2.7 to within first order. Under the assumption that the neutron radiation at a point $\boldsymbol{r}$ is described, both before and after the scattering, by a plane wave (the Born approximation), the states of the scattering system (including the scattering particle) can be written as

$$|i\rangle \equiv |\psi_i\zeta_i\rangle = \frac{1}{\sqrt{\mathcal{V}}}\, e^{i\boldsymbol{k}_i\cdot\boldsymbol{r}}\, |\zeta_i\rangle \equiv \frac{1}{\sqrt{\mathcal{V}}}\, |\boldsymbol{k}_i\zeta_i\rangle \quad , \tag{2.12}$$

where $1/\sqrt{\mathcal{V}}$ is a normalization factor. Equation 2.7 thus reduces to

$$\mathcal{W} = \frac{2\pi}{\hbar}\frac{1}{\mathcal{V}^2}\, |\langle \boldsymbol{k}_f\zeta_f|\mathcal{H}_\mathrm{int}|\boldsymbol{k}_i\zeta_i\rangle|^2\, \delta(\hbar\omega - (E_i - E_f)) \quad . \tag{2.13}$$

Substituting this into Eq. 2.6 yields the double differential scattering cross section for neutron scattering [316, 317]:

$$\boxed{\left(\frac{\mathrm{d}^2\sigma}{\mathrm{d}\Omega\mathrm{d}\hbar\omega}\right)_{\zeta_i\to\zeta_f} = \frac{k_f}{k_i}\left(\frac{m}{2\pi\hbar^2}\right)^2 \left|\left\langle \boldsymbol{k}_f\,\zeta_f\right|\mathcal{H}_\mathrm{int}\left|\boldsymbol{k}_i\,\zeta_i\right\rangle\right|^2 \delta(\hbar\omega - (E_i - E_f))} \tag{2.14}$$

2.3.1 Nuclear neutron scattering

Equation 2.14 is best evaluated in Fourier ($\boldsymbol{Q}$) space. Assuming an array of nuclear potentials $U(\boldsymbol{x}_j)$ at the relative coordinates $\boldsymbol{x}_j = \boldsymbol{r} - \boldsymbol{R}_j$ of the jth nuclei (at $\boldsymbol{R}_j$, with respect to the scattering neutron at $\boldsymbol{r}$), the nuclear interaction can be stated as a Fourier

sum:

$$\mathcal{H}_{\text{nuc}} = \sum_j U_j(\boldsymbol{Q}) = \sum_j \int U_j(\boldsymbol{x}_j)\, e^{i\,\boldsymbol{Q}\cdot\boldsymbol{x}_j} \mathrm{d}\boldsymbol{x}_j \tag{2.15}$$

so that the matrix element becomes

$$\langle \boldsymbol{k}_f\, \zeta_f | \mathcal{H}_{\text{nuc}} | \boldsymbol{k}_i\, \zeta_i \rangle = \sum_j U_j(\boldsymbol{Q}) \int \zeta_f^*\, e^{i\,\boldsymbol{Q}\cdot\boldsymbol{R}_j}\, \zeta_i \, \mathrm{d}\boldsymbol{R}_j = \sum_j U_j(\boldsymbol{Q})\, \langle \zeta_f | e^{i\,\boldsymbol{Q}\cdot\boldsymbol{R}_j} | \zeta_i \rangle \quad , \tag{2.16}$$

where $\mathrm{d}\boldsymbol{R}_j$ actually represents many integrals over all nuclear sites. Due to the negligible spatial extent of the atomic core, the interaction of the neutron with the jth nucleus in the sample is well approximated by the point-like *Fermi pseudopotential* (or its corresponding Fourier transform):

$$U_j(\boldsymbol{x}_j) = \frac{2\pi\hbar^2}{m}\, b_j\, \delta(\boldsymbol{x}_j) \quad , \quad U_j(\boldsymbol{Q}) = \frac{2\pi\hbar^2}{m}\, b_j \tag{2.17}$$

The weak nuclear interaction is thus independent of momentum transfer and parametrized by a single parameter b, the neutron bound scattering length. b may be both positive (repulsive) or negative (attractive) and may vary, both between different isotopes of the same element and between different nuclear spin states of the same isotope.

In analogy to the transformation of the scattering potential, the energy delta function in Eq. 2.14 can be transformed to its conjugate variable, time t:

$$\delta(\hbar\omega - (E_i - E_f)) = \frac{1}{2\pi\hbar} \int_{-\infty}^{\infty} e^{i\,\frac{E_i - E_f}{\hbar}\,t}\, e^{-i\omega t}\, \mathrm{d}t \tag{2.18}$$

For a full evaluation of the scattering cross section, the square of the matrix element (Eq. 2.16) must then be summed over final states $|\zeta_f\rangle$ of the scattering system and averaged over initial states $|\zeta_i\rangle$. The final result can be separated into a coherent and an incoherent scattering contribution [316]:

$$\begin{aligned} \left(\frac{\mathrm{d}^2\sigma}{\mathrm{d}\Omega \mathrm{d}\omega}\right)_{\text{coh.}} &= \frac{\sigma_{\text{coh.}}}{4\pi}\, \frac{k_f}{k_i}\, \frac{1}{2\pi\hbar} \sum_{j,j'} \int_{-\infty}^{\infty} \langle j', j \rangle\, e^{-i\omega t} \mathrm{d}t \\ \left(\frac{\mathrm{d}^2\sigma}{\mathrm{d}\Omega \mathrm{d}\omega}\right)_{\text{inc.}} &= \frac{\sigma_{\text{inc.}}}{4\pi}\, \frac{k_f}{k_i}\, \frac{1}{2\pi\hbar} \sum_{j} \int_{-\infty}^{\infty} \langle j, j \rangle\, e^{-i\omega t} \mathrm{d}t \quad , \end{aligned} \tag{2.19}$$

where

$$\langle j', j \rangle = \sum_\zeta \left(\frac{e^{-E_\zeta/(k_\mathrm{B}T)}}{\sum_\zeta e^{-E_\zeta/(k_\mathrm{B}T)}} \right) \left\langle \zeta \left| e^{-i\boldsymbol{Q}\cdot\boldsymbol{R}_{j'}(0)}\, e^{i\boldsymbol{Q}\cdot\boldsymbol{R}_j(t)} \right| \zeta \right\rangle \tag{2.20}$$

is the thermal average of the correlation function of the time-dependent (*Heisenberg*)

operators $\boldsymbol{R}_j(t)$ (for a thorough derivation, see [316, 317]):

$$\boldsymbol{R}_j(t) = e^{i\mathcal{H}t/\hbar}\boldsymbol{R}_j e^{-i\mathcal{H}t/\hbar} \quad , \tag{2.21}$$

where $\mathcal{H}$ is the Hamiltonian describing the scattering system. The total coherent and incoherent neutron scattering cross sections $\sigma_{\text{coh.}}$ and $\sigma_{\text{inc.}}$ in Eq. 2.19 are given by the squared *average* and *variance* of bound scattering lengths b, respectively:

$$\sigma_{\text{coh.}} = 4\pi(\bar{b})^2 \quad , \quad \sigma_{\text{inc.}} = 4\pi[\bar{b^2} - (\bar{b})^2] \tag{2.22}$$

Empirical values of b, $\sigma_{\text{coh.}}$ and $\sigma_{\text{inc.}}$ for each element (and isotope) have been tabulated by Sears [318]. Equations 2.19 describe the full nuclear neutron response of a sample, including both elastic and inelastic neutron scattering.

In this thesis, the excitation of lattice vibrations (*phonons*) only plays a peripheral role. For example, I observed phonon scattering in FeSe (see Chapter 3), where it obscures the weaker low-energy intensity contributions from magnetic excitations (*magnons*). As there is no interest in the structural dynamics in this context, I focus on the nuclear *elastic* response. This implies $k_i = k_f$ and the time dependence of the Heisenberg operators $\boldsymbol{R}_j$ in Eq. 2.20 can be neglected (they are then simple space coordinates). The time integral in 2.19 thus simplifies to [317]:

$$\frac{1}{2\pi\hbar}\int_{-\infty}^{\infty} e^{-i\omega t}\,\mathrm{d}t = \delta(\hbar\omega) \tag{2.23}$$

By integrating Eq. 2.19 over the energy transfer $\hbar\omega$, the *single*-differential neutron cross sections can then be obtained:

$$\left(\frac{\mathrm{d}\sigma}{\mathrm{d}\omega}\right)_{\text{coh.}} = \frac{\sigma_{\text{coh.}}}{4\pi}\sum_{j,j'} e^{-i\boldsymbol{Q}\cdot(\boldsymbol{R}_{j'}-\boldsymbol{R}_j)} \tag{2.24}$$

$$\left(\frac{\mathrm{d}\sigma}{\mathrm{d}\omega}\right)_{\text{inc.}} = \frac{\sigma_{\text{inc.}}}{4\pi} \tag{2.25}$$

This shows that the nuclear *incoherent* elastic part of the neutron response contributes an isotropic background signal, proportional to the variance of scattering lengths in the sample. The *coherent* term (Eq. 2.24) is further simplified by the translational symmetry of the crystal. In particular, the sum over phase factors relative to $\boldsymbol{r} := \boldsymbol{R}_{j'} - \boldsymbol{R}_j$ can be substituted by a sum over reciprocal lattice sites $\boldsymbol{G}$ (equivalent to the definition of reciprocal space in Section 2.2, but omitting the subscript (HKL) for brevity),

$$\sum_{\mathbf{r}} e^{i\boldsymbol{Q}\cdot\boldsymbol{r}} = \frac{(2\pi)^3}{v_0} N \sum_{\mathbf{G}} \delta(\boldsymbol{Q}-\boldsymbol{G}) \quad (v_0\text{: unit cell volume}). \tag{2.26}$$

Where N is the number of lattice sites in real space. The nuclear coherent elastic single-differential neutron scattering cross section becomes

$$\frac{\mathrm{d}\sigma}{\mathrm{d}\omega} = \frac{(2\pi)^3}{v_0}\frac{\sigma_{\mathrm{coh.}}}{4\pi} N \sum_{\mathbf{G}} \delta(\boldsymbol{Q}-\boldsymbol{G}) \tag{2.27}$$

Below, the subscript *coh.* is omitted for brevity. Since the materials discussed in this thesis contain more than one atom per unit cell, an additional summation over the atomic *basis* has to be introduced. The lattice sum in Eq. 2.24 is thus partitioned, $\boldsymbol{R}_j := \boldsymbol{R}_{l\alpha} = \boldsymbol{R}_l + \boldsymbol{d}_\alpha$, into two sums, over the positions of unit cells and the nuclei (of scattering length b_α) therein, respectively:

$$\frac{\mathrm{d}\sigma}{\mathrm{d}\Omega} = \sum_{l,l'} e^{i\boldsymbol{Q}\cdot(\boldsymbol{R}_l-\boldsymbol{R}_{l'})} \sum_{\alpha,\alpha'} b_\alpha b_{\alpha'} e^{i\boldsymbol{Q}\cdot(\boldsymbol{d}_\alpha-\boldsymbol{d}_{\alpha'})} \tag{2.28}$$

$$= \sum_{l,l'} e^{i\boldsymbol{Q}\cdot(\boldsymbol{R}_l-\boldsymbol{R}_{l'})} \left|\sum_{\boldsymbol{d}} b_{\boldsymbol{d}}\, e^{i\boldsymbol{Q}\cdot\boldsymbol{d}}\right|^2 \tag{2.29}$$

$$= \frac{(2\pi)^3}{v_0} N \sum_{\boldsymbol{G}} |S_{\boldsymbol{G}}|^2\, \delta(\boldsymbol{Q}-\boldsymbol{G}) \tag{2.30}$$

Here, a *basis* relative nuclear coordinate $\boldsymbol{d} = \boldsymbol{d}_\alpha - \boldsymbol{d}_{\alpha'}$ was introduced and the expression was simplified in analogy to Eq. 2.24. Depending on their relative phases, the waves scattered from nuclei with scattering lengths $b_{\boldsymbol{d}}$ (at positions $\boldsymbol{d}$ in the unit cell) interfere positively or negatively. The observed intensity of a Bragg reflection at $\boldsymbol{G}$ is therefore governed by the *neutron nuclear structure factor*,

$$S_{\boldsymbol{G}} = \sum_{\boldsymbol{d}} b_{\boldsymbol{d}}\, e^{i\boldsymbol{G}\cdot\boldsymbol{d}} \quad . \tag{2.31}$$

An additional coefficient e^{-2W} (the *Debye-Waller factor*) arises if a finite thermal displacement of the nuclei is taken into account. The thermal variable W grows quadratically with momentum transfer and is proportional to the mean-squared displacements $\langle u^2 \rangle$ ($W = Q^2\langle u^2\rangle/3$, for an explicit derivation see [316]). This leads to the final result for the elastic nuclear neutron scattering cross section [316, 317]:

$$\boxed{\frac{\mathrm{d}\sigma}{\mathrm{d}\Omega} = \frac{(2\pi)^3}{v_0} e^{-2W} N \sum_{\boldsymbol{G}} |S_{\boldsymbol{G}}|^2\, \delta(\boldsymbol{Q}-\boldsymbol{G})} \tag{2.32}$$

2.3.2 Magnetic neutron scattering

Independently of the nuclear interaction discussed above, there exists another scattering channel for the neutron due to its magnetic moment [313],

$$\boldsymbol{\mu}_n = -\gamma \mu_N \boldsymbol{\sigma} \quad , \quad \mu_\mathrm{N} = \frac{e\hbar}{2m_p} \quad . \tag{2.33}$$

Here, $\gamma = 1.913$ is a constant, $\boldsymbol{\sigma}$ are the Pauli spin matrices and μ_N is the nuclear magneton, which is inversely proportional to the proton mass m_p. Although the interaction of this magnetic moment with nuclei is negligible, its potential in the magnetic field $\boldsymbol{B}$ of an unpaired electron is of similar strength as the nuclear interaction:

$$\mathcal{H}_\mathrm{mag} = -\boldsymbol{\mu}_n \cdot \boldsymbol{B} = -\frac{\mu_0}{4\pi} \gamma \mu_\mathrm{N} 2\mu_\mathrm{B} \boldsymbol{\sigma} \cdot (\mathcal{V}_\mathrm{S} + \mathcal{V}_\mathrm{L}) \tag{2.34}$$

The magnetic field at an ionic site has separate contributions from spin and orbital angular momenta of unbound electrons:

$$\mathcal{V}_\mathrm{S} = \nabla \times \left(\frac{\boldsymbol{s} \times \hat{\boldsymbol{R}}}{R^2}\right) \quad \text{and} \quad \mathcal{V}_\mathrm{L} = \frac{1}{\hbar} \frac{\mathbf{p} \times \hat{\mathbf{R}}}{R^2} \tag{2.35}$$

As derived in [316], the evaluation of the momentum eigenstates of this potential in Eq. 2.14 leads to

$$\left(\frac{\mathrm{d}^2\sigma}{\mathrm{d}\Omega \mathrm{d}\omega}\right)_{\sigma_i\zeta_i \to \sigma_f\zeta_f} = \left(\frac{\gamma r_0}{2\mu_\mathrm{B}}\right)^2 \frac{k_f}{k_i} \left| \left\langle \sigma_f \zeta_f \left| \boldsymbol{\sigma} \cdot \mathcal{M}_\perp \right| \sigma_i \zeta_i \right\rangle \right|^2 \delta(\hbar\omega - (E_f - E_i)) \quad , \tag{2.36}$$

where $r_0 = \frac{\mu_0}{4\pi} \frac{e^2}{m_e}$ is the classical electron radius. The *total magnetization (vector) operator* $\mathcal{M}(\boldsymbol{Q}) = \mathcal{M}_\mathrm{S}(\boldsymbol{Q}) + \mathcal{M}_\mathrm{L}(\boldsymbol{Q})$ derives from $\mathcal{V}_\mathrm{S}$ and $\mathcal{V}_\mathrm{L}$ and corresponds to the Fourier transform of magnetization density due to the free spin and orbital angular momenta at an ion. The subscript $\perp$ indicates that only the components of this magnetization vector that are perpendicular to the momentum transfer $\boldsymbol{Q}$ contribute to the scattering. By use of the Kronecker delta function, this orthogonality condition can also be expressed as a sum $\sum_{\alpha,\beta}[\delta_{\alpha\beta} - (Q_\alpha Q_\beta)/Q^2]$ over the cartesian components $\alpha, \beta = x, y, z$.

In analogy to the matrix elements of the nuclear interactions (Eq. 2.16), equation 2.36 must be summed over final states $(\sigma_f \zeta_f)$ and averaged over initial states $(\sigma_i \zeta_i)$ of the neutron. The evaluation of this transition probablility finally leads to the *master formula* for magnetic neutron scattering [316, 317]:

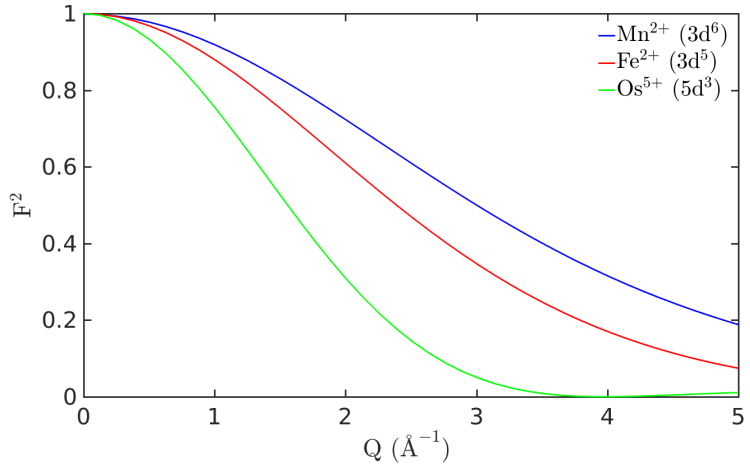

Figure 2.5: Magnetic form factors $F^2(Q)$ for magnetic ions that I probed by neutron techniques (see chapters 3, 4 and 6). These approximate expansions in spherical Bessel functions are obtained from the empirical coefficients tabulated in [320, 321], assuming *LS* coupling.

$$\frac{\mathrm{d}\sigma}{\mathrm{d}\Omega\mathrm{d}\omega} = \left(\frac{\gamma r_0 g}{2}\right)^2 \frac{k_f}{k_i} F^2(\boldsymbol{Q})\, e^{-2W(\boldsymbol{Q})} \sum_{\alpha,\beta} \left(\delta_{\alpha,\beta} - \frac{Q_\alpha Q_\beta}{Q^2}\right) S_{\alpha,\beta}(\boldsymbol{Q},\omega)\ , \tag{2.37}$$

Here, it has been assumed that the spin directions of the incoming neutrons are random (*unpolarized*), that all magnetic scattering centres are identical and that the magnetism is well described in a local-ion (non-itinerant) picture. g is the Landè splitting factor ($g = 2$ for vanishing orbital angular momenta) and $F(\boldsymbol{Q})$ is the *magnetic form factor*, which is given by the normalized Fourier transform of the density of unpaired electrons in real space. An analytical evaluation of this function is cumbersome [319]. Expansion of $F(\boldsymbol{Q})$ in terms of spherical Bessel functions have therefore been tabulated for most magnetic ions [320, 321].

As illustrated in Fig. 2.5 for the magnetic ions that I investigated by neutron techniques, the key characteristic of the magnetic form factor is the fast decrease of magnetic neutron scattering intensity with increasing momentum transfer. By contrast, the Fermi pseudopotential of the core is point-shaped and therefore nuclear scattering is not affected by this kind of suppression. The shape of $F(\boldsymbol{Q})$ also provides a weak ion-specificity to the technique.

The *magnetic scattering function* ($S_{\alpha,\beta}$ in Eq. 2.37) contains the phase differences between the scattering sites j, j' and correlates the total angular momentum operators $\hat{\boldsymbol{S}}$ between the initial and final neutron states ζ_i, ζ_f. In the case of localized moments, in

which a spin can be assigned to each site, it can be stated as

$$S_{\alpha,\beta}(\boldsymbol{Q},\omega) = \sum_{j,j'} e^{i\boldsymbol{Q}\cdot(\boldsymbol{R}_j-\boldsymbol{R}_{j'})} \sum_{\zeta_i,\zeta_f} p_\zeta \left\langle \zeta_i \left| \hat{\boldsymbol{S}}^\alpha_{j'} \right| \zeta_f \right\rangle \left\langle \zeta_f \left| \hat{\boldsymbol{S}}^\beta_{j} \right| \zeta_i \right\rangle \delta(\hbar\omega - (E_f - E_i)) \quad . \tag{2.38}$$

In analogy to the discussion of the nuclear scattering cross section in the preceding section, the energy transfer condition can be stated in Fourier (time-integral) form (Eq. 2.18), and thus the magnetic scattering function can be expressed in terms of a thermal average (Eq. 2.20):

$$\boxed{S_{\alpha,\beta}(\boldsymbol{Q},\omega) = \frac{1}{2\pi\hbar} \sum_{j,j'} \int_{-\infty}^{\infty} e^{i\boldsymbol{Q}\cdot(\boldsymbol{R}_j-\boldsymbol{R}_{j'})} \left\langle \hat{\boldsymbol{S}}^\alpha_j(0)\, \hat{\boldsymbol{S}}^\beta_{j'}(t) \right\rangle e^{-i\omega t}\, \mathrm{d}t} \tag{2.39}$$

Put into words, the magnetic response measured in neutron scattering is the Fourier transform in space and time of the pair correlation function between any two magnetic moments in the system [317]. According to the *fluctuation-dissipation theorem*, this quantity can also be expressed as

$$\boxed{S_{\alpha,\beta}(\boldsymbol{Q},\omega) = \frac{1}{\pi} \frac{1}{1-\exp(-\beta E)} \chi''_{\alpha\beta}(\boldsymbol{Q},\omega) \qquad (\beta = 1/(k_\mathrm{B}T))} \tag{2.40}$$

i.e. it measures the imaginary (dissipative) part of the dynamical magnetic susceptibility tensor $\chi_{\alpha,\beta}(\boldsymbol{Q},\omega)$, which descibes the magnetization ($\boldsymbol{M}$) response of the sample to an applied field ($\boldsymbol{H}$), as a function of both momentum and frequency:

$$M_\alpha(\boldsymbol{Q},\omega) = \chi_{\alpha\beta}(\boldsymbol{Q},\omega) H_\beta(\boldsymbol{Q},\omega) \quad (\alpha,\beta:\ x,y,z) \tag{2.41}$$

For the case of *elastic* magnetic neutron scattering, the matrix elements in Eq. 2.37 are evaluated in the time limit $t \to \infty$ and integrated with respect to E_f. This leads to the single-differential magnetic cross section [322, 323, 316, 317]

$$\boxed{\frac{\mathrm{d}\sigma}{\mathrm{d}\Omega} = N \left(\frac{\gamma r_0}{2\,\mu_\mathrm{B}}\right)^2 \frac{(2\pi)^3}{v_0} e^{-2W(\boldsymbol{Q})} \left|\boldsymbol{M}_\perp(\boldsymbol{Q})\right|^2} \tag{2.42}$$

$\mathbf{M}(\boldsymbol{Q})$ is the Fourier transform of the magnetization operator and may be considered a *magnetic structure factor* vector. Using the convention of describing magnetic structures defined in Eq. 2.11,

$$\boldsymbol{M}(\boldsymbol{Q}) = \sum_{\boldsymbol{q}_\mathrm{m}} \sum_{\alpha} \frac{g}{2} F_\alpha(\boldsymbol{Q})\, \boldsymbol{m}^*_{\boldsymbol{q}_\mathrm{m}\alpha}\, e^{2\pi i\, \boldsymbol{Q}\cdot\boldsymbol{d}_\alpha}\, \delta(\boldsymbol{Q} - (\boldsymbol{G} + \boldsymbol{q}_\mathrm{m})) \tag{2.43}$$

Where the sums run over the magnetic propagation vectors $\pm\boldsymbol{q}_\mathrm{m}$ and the sites $\boldsymbol{d}_\alpha$ of magnetic ions in the unit cell (with magnetic form factors $\frac{g}{2}F_\alpha$). As in Eq. 2.36, the subscript $\perp$ in Eq. 2.42 denotes the component which is perpendicular to the momentum transfer. This condition can also be expressed in form of vector products:

$$\boldsymbol{M}_\perp = \hat{\boldsymbol{Q}} \times \boldsymbol{M} \times \hat{\boldsymbol{Q}} \equiv \boldsymbol{M} - \hat{\boldsymbol{Q}}(\hat{\boldsymbol{Q}} \cdot \boldsymbol{M}) \quad \text{, with } \hat{\boldsymbol{Q}} = \boldsymbol{Q}/Q \ . \tag{2.44}$$

2.3.3 Neutron sources and instruments

Neutron beams are obtained from nuclear decay processes, either by controlled fission of enriched uranium (in a nuclear reactor), or by bombardment of heavy metals with high energy protons — a process known as *spallation*. Today, high flux neutron reactor- and spallation sources are available for user experiments at several international facilities. The two methods of neutron creation imply distinct beam properties, which in turn determine the design of experimental setups and modes of data collection.

Reactor sources such as at the Institut Laue-Langevin (ILL) supply a *constant* flux of high energy neutrons. By contrast, at a spallation source such as the ISIS facility, neutrons are created in intense bursts, at the frequency of the proton pulse onto the heavy metal target (50 and 10 Hz at the two *target stations* of ISIS). In either case, high energy neutrons are obtained which must be thermalised in appropriate moderating media. For applications in condensed matter, a cold (0.5–5 meV) or thermal (5–100 meV) neutron beam may be desirable, depending on the range of energy- and momentum transfer of interest. This is be achieved by room temperature (liquid D_2O) or cold (e.g., solid methane, CH_4, at 40 K) moderators.

At a neutron scattering beamline, a specific neutron wavelength (or a band of wavelengths) is selected from the moderator spectrum, either by diffraction from a monochromator crystal, or by rotating chopper devices (see Fig. 2.6). Similarly, the energy of the scattered beam is determined either by diffraction from an analyzer crystal (triple axis method) or by relating the time stamps of chopper and detector events to the length of the beam path. (time-of-flight method). For best efficiency, the former method is usually employed in reactor sources and the latter at spallation sources.

The purpose of any such experiment is to probe the scattering cross sections derived in the preceding section (Eqs. 2.32 and 2.42). In effect, this can be seen as a survey of a four-dimensional momentum- and energy transfer $(\boldsymbol{Q}, \hbar\omega)$ space. In real space, this 4-space is navigated by varying the scattering angles, the orientation of the sample, and the incident and detected neutron energies.

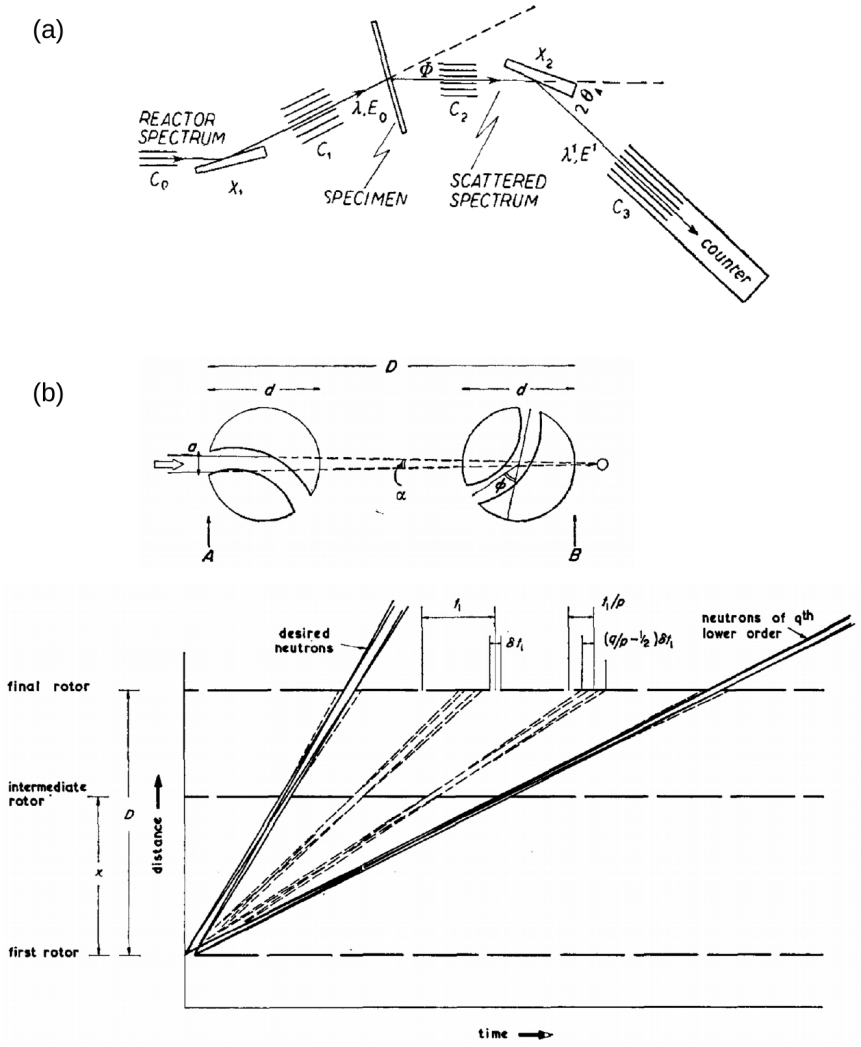

Figure 2.6: Selection of neutron energies from continuous and pulsed beams. (a) Schematic of a triple axis spectrometer at a reactor neutron source. By diffraction from appropriate *monochromator* and *analyzer* crystals, the desired neutron energies can be selected from the incoming and scattered beams (from Brockhouse, 1958 [324]). (b) Plane view of a simple rotating chopper device (top). The energy (velocity) of neutrons that pass the curved path without being absorbed is determined by the chopper angular frequency. In general, a sequence of choppers is needed to select the desired *world-line* of neutron pulses (bottom). This method of monochromation is commonly employed at spallation neutron sources (from Lowde, 1960 [325]).

The key distinction between different neutron scattering setups is whether they discriminate between zero and finite energy transfer. As elastic Bragg intensities generally eclipse phonon and magnon scattering by several orders of magnitude, this corresponds to the distinction between diffraction and spectroscopy. Depending on the application, the beam may be monochromated (analyzed) before or after, or both before and after scattering from the sample.

In this thesis, I report use of the following neutron scattering techniques:

- **Time-of-flight powder inelastic neutron scattering**
  in Chapter 3 to probe magnetic excitations in FeSe
- **Time-of-flight neutron powder diffraction**
  in Chapter 3, for a high-resolution structural study of FeSe and
  in Chapter 6, to probe for magnetic order in $Ca_2Os_2O_7$
- **Triple axis inelastic neutron scattering**
  in Chapter 4, to probe magnetic excitations in single crystals of AMnBi$_2$
- **Constant wavelength neutron powder diffraction**
  in Chapter 6, to probe the magnetic order in $Ca_2Os_2O_7$

2.4 X-ray scattering

2.4.1 Thomson scattering

The electric field $\boldsymbol{\mathcal{E}}$ of an electromagnetic wave is characterized by a polarization unit vector $\hat{\boldsymbol{\varepsilon}}$ and an amplitude $\mathcal{E}$:

$$\boldsymbol{\mathcal{E}}(\boldsymbol{r},t) = \hat{\boldsymbol{\varepsilon}}\,\mathcal{E}\,e^{i(\boldsymbol{k}\cdot\boldsymbol{r}-\omega t)} \tag{2.45}$$

Instead of using Fermi's golden rule, for massless particles, Eq. 2.1 can be simply evaluated by recognizing that the energy density of the beam is proportional to $|\mathcal{E}|^2$. Assuming elastic scattering, the single-differential scattering cross-section can be rewritten in terms of electric fields [311]:

$$\frac{\mathrm{d}\sigma}{\mathrm{d}\Omega} = R^2\,\frac{\mathcal{E}_f^2}{\mathcal{E}_i^2} \quad \text{, since} \quad I_{\mathrm{sc}} \propto \frac{\mathcal{E}_f^2}{\hbar\omega}\,(R^2\Delta\Omega) \quad \text{and} \quad \Phi_0 \propto \frac{\mathcal{E}_i^2}{\hbar\omega}\,c \quad . \tag{2.46}$$

Therefore, in the context of x-ray scattering Eq. 2.1 is generally expressed in terms of the *scattering amplitude* (or *scattering length*) $\mathcal{F}$:

$$\frac{\mathrm{d}\sigma}{\mathrm{d}\Omega} = |\mathcal{F}|^2 \tag{2.47}$$

When scattering from a single unbound electron, the incoming wave will cause a harmonic oscillation along $\hat{\boldsymbol{\varepsilon}}$ (perpendicular to $\boldsymbol{\mathcal{E}}_i$). From dimensional analysis, it can be argued that the resulting response must be proportional to the free electron radius, which is therefore also referred to as the *Thomson scattering length*:

$$\mathcal{F} = r_0 P \quad , \quad P = |\hat{\boldsymbol{\varepsilon}}_f \cdot \hat{\boldsymbol{\varepsilon}}_i| \qquad \left(r_0 = \frac{e^2}{mc^2} \right) \tag{2.48}$$

For *bound* electronic states at an atomic site, details of the charge distibution $\rho(\boldsymbol{r})$ are taken into account as an *electronic form factor*:

$$f(\boldsymbol{Q}, \hbar\omega) = \int \rho(\boldsymbol{r}) e^{i\boldsymbol{Q}\cdot\boldsymbol{r}} \, \mathrm{d}^3\boldsymbol{r} + f'(\hbar\omega) + f''(\hbar\omega) \tag{2.49}$$

Where $f' + i\,f''$ are *dispersion corrections* that become important for x-ray energies in the vicinity of electronic binding energies. To describe the scattering from a *crystal*, amplitude contributions of $(-r_0 P)$ from the electrons at the sites $\boldsymbol{R}_{l\alpha} = \boldsymbol{R}_l + \boldsymbol{d}_\alpha$ are summed with the appropriate phase shifts:

$$\mathcal{F}(\boldsymbol{Q}) = -r_0 P \sum_l e^{i\boldsymbol{Q}\cdot\boldsymbol{R}_l} \sum_\alpha f_\alpha(\boldsymbol{Q}) \, e^{i\boldsymbol{Q}\cdot\boldsymbol{d}_\alpha} \tag{2.50}$$

and thus

$$\boxed{\frac{\mathrm{d}\sigma}{\mathrm{d}\Omega} = r_0^2 P^2 N \frac{(2\pi)^3}{v_0} \sum_{\boldsymbol{G}} \delta(\boldsymbol{Q} - \boldsymbol{G}) \, |F(\boldsymbol{G})|^2} \tag{2.51}$$

Here, the lattice sum has been transformed to the Laue condition (as in the case of neutron scattering) and $F(\boldsymbol{G})$ has been introduced to denote the unit cell structure factor.

2.4.2 Full x-ray scattering cross section

The minimal derivation of Thomson scattering shown above is appropriate for traditional laboratory-based experiments (see 2.1). In this section I show how a rigourous evaluation of $\mathcal{W}$ to second order perturbation theory gives access to a spectrum of subtle scattering phenomena that are sensitive to both magnetic and orbital degrees of freedom. This full derivation was originally put forward by Blume [326] and has been discussed more recently by Altarelli [327].

The electric and magnetic fields $\boldsymbol{\mathcal{E}}(\boldsymbol{r})$ and $\boldsymbol{B}(\boldsymbol{r})$ of the x-ray are described by a vector potential $\boldsymbol{A}(\boldsymbol{r})$ (for clarity, the explicit reference to the space coordinate $\boldsymbol{r}$ is frequently omitted below). Inside a material, charged particles create a Coulomb potential V, which contributes an additional static component to $\boldsymbol{\mathcal{E}}$:

$$\boldsymbol{B} = \nabla \times \boldsymbol{A} \quad , \quad \boldsymbol{\mathcal{E}} = -\nabla V - \frac{1}{c}\frac{\partial}{\partial t}\boldsymbol{A} \quad , \quad \nabla \cdot \boldsymbol{A} \equiv 0 \tag{2.52}$$

In the non-relativistic limit, the (self-consistent) Hamiltonian of a system of N electrons with momenta $\boldsymbol{p}_i$ at positions $\boldsymbol{r}_i$ is given by

$$\mathcal{H}_{\mathrm{el}} = \sum_{i=1}^{N} \underbrace{\frac{\left(\boldsymbol{p}_i - \frac{e}{c}\boldsymbol{A}\right)^2}{2m}}_{\text{kinetic}} + \underbrace{V(\boldsymbol{r}_i)}_{\text{Coulomb}} - \underbrace{\frac{e\hbar}{mc}\boldsymbol{s}_i \cdot \boldsymbol{B}}_{\text{Zeeman}} - \underbrace{\frac{e\hbar}{2m^2c^2}\boldsymbol{s}_i \cdot \left[\boldsymbol{E} \times \left(\boldsymbol{p}_i - \frac{e}{c}\boldsymbol{A}\right)\right]}_{\text{spin-orbit}} \tag{2.53}$$

The *interaction Hamiltonian* of this system with the electromagnetic radiation is obtained by omitting all terms that do not couple to $\boldsymbol{A}$:

$$\mathcal{H}_{\mathrm{int}} = \sum_{i=1}^{N} \underbrace{\frac{e^2}{2mc^2}\boldsymbol{A}^2}_{\mathcal{H}_1} \underbrace{- \frac{e}{mc}\boldsymbol{p}_i \cdot \boldsymbol{A}}_{\mathcal{H}_2} \underbrace{- \frac{e\hbar}{mc}\boldsymbol{s}_i \cdot (\nabla \times \boldsymbol{A})}_{\mathcal{H}_3} \underbrace{+ \frac{e\hbar}{2m^2c^3}\boldsymbol{s}_i \cdot \left[\left(\frac{\partial}{\partial t}\boldsymbol{A}\right) \times \left(\boldsymbol{p}_i - \frac{e}{c}\boldsymbol{A}\right)\right]}_{\mathcal{H}_4} \tag{2.54}$$

Terms that are quadratic in the vector potential ($\mathcal{H}_1$ and $\mathcal{H}_4$) will contribute in first order perturbation theory, while the terms that are linear in $\boldsymbol{A}$ ($\mathcal{H}_2$ and $\mathcal{H}_3$) will contribute only to second order. Thus, the substitution into Eq. 2.7 yields

$$\mathcal{W} = \frac{2\pi}{\hbar}\left|\langle f|\mathcal{H}_1 + \mathcal{H}_4|i\rangle + \sum_n \frac{\langle f|\mathcal{H}_2 + \mathcal{H}_3|n\rangle\langle n|\mathcal{H}_2 + \mathcal{H}_3|i\rangle}{\hbar\omega - (E_i - E_n)}\right|^2 \delta(\hbar\omega - (E_i - E_f)) \tag{2.55}$$

To evaluate these terms, it is most convenient to express the vector potential in *second quantization*, i.e. as an expansion in terms of plane waves, created and annihilated by operators $\hat{a}^\dagger$ and $\hat{a}$, respectively:

$$\boldsymbol{A}(\boldsymbol{r},t) = \sum_{\boldsymbol{k},\eta} \sqrt{\frac{2\pi\hbar c^2}{\mathcal{V}\omega_{\boldsymbol{k}}}}\left[\hat{\boldsymbol{\varepsilon}}^{\eta}(\boldsymbol{k})\, e^{i(\mathbf{k}\cdot\mathbf{r} - \omega_{\mathbf{k}}t)}\, \hat{a}(\mathbf{k},\eta) + \hat{\boldsymbol{\varepsilon}}^{\eta *}(\mathbf{k})\, e^{-i(\mathbf{k}\cdot\mathbf{r} - \omega_{\mathbf{k}}t)}\, \hat{a}^\dagger(\mathbf{k},\eta)\right] \tag{2.56}$$

The index η labels the two possible orthogonal modes of the polarization unit vectors. The evaluation of the square of this operator in $\mathcal{H}_1$ leads to [327]:

$$\langle f|\mathcal{H}_1|i\rangle = \frac{2\pi\hbar e^2}{\mathcal{V}ckm}(\hat{\boldsymbol{\varepsilon}}_f \cdot \hat{\boldsymbol{\varepsilon}}_i)\sum_{i=1}^{N} e^{i\boldsymbol{Q}\cdot r_i} \tag{2.57}$$

Thus (assuming elastic scattering),

$$\mathcal{W}_1 = \frac{(2\pi)^3 \hbar e^4}{(\mathcal{V} ckm)^2} (\hat{\boldsymbol{\varepsilon}}_f \cdot \hat{\boldsymbol{\varepsilon}}_i)^2 \left| \sum_{i=1}^{N} e^{i\boldsymbol{Q}\cdot r_i} \right|^2 \tag{2.58}$$

And therefore, by Eqs. 2.6 and 2.7,

$$\left(\frac{\mathrm{d}\sigma}{\mathrm{d}\Omega}\right)_1 = \left(\frac{e^2}{mc^2}\right)^2 (\hat{\boldsymbol{\varepsilon}}_f \cdot \hat{\boldsymbol{\varepsilon}}_i)^2 \left| \sum_{i=1}^{N} e^{i\boldsymbol{Q}\cdot r_i} \right|^2 \tag{2.59}$$

which corresponds to the Thomson scattering previously derived in Eq. 2.51.

2.4.3 Nonresonant magnetic x-ray scattering

The evaluation of the nonresonant magnetic contributions in Eq. 2.55 is rather involved and has been presented in detail by Altarelli [327]. A key finding is that these terms are reduced by the energy ratio $\mathcal{R} = (\hbar\omega/mc^2)$ compared to Thomson scattering. For the x-ray studies reported in this thesis, this reduction factor varies between $\mathcal{R} \approx 0.001$ (Fe L_3) and $\mathcal{R} \approx 0.01$ (Eu L_3). Although this implies a reduction of the cross section of $\mathcal{R}^2 \propto 10^{-4}$–$10^{-6}$ compared to charge scattering, the observed non-resonant magnetic intensities are even weaker, since only a fraction of the electrons (those in unpaired orbitals) contributes.

As seen in Eq. 2.54, the first order contribution $\langle f|\mathcal{H}_4|i\rangle$ actually contains two terms, $\dot{\boldsymbol{A}} \times \boldsymbol{p}$ and $\dot{\boldsymbol{A}} \times \boldsymbol{A}$. It turns out that the first term is reduced by an *additional* factor $\mathcal{R}$ (i.e., $\mathcal{R}^2$ compared to Thomson scattering) and can therefore be neglected. On the other hand, one finds a residual non-resonant magnetic contribution form the second order ($\propto \langle f|\mathcal{H}_2 + \mathcal{H}_3|n\rangle\langle \mathcal{H}_2 + \mathcal{H}_3|i\rangle$) term (by considering the limit $\hbar\omega \gg (E_n - E_i)$). The final result for the non-resonant x-ray scattering cross section can be stated in terms of the Fourier transforms of the spin and orbital magnetization $\boldsymbol{M}_\mathrm{S}$ and $\boldsymbol{M}_\mathrm{L}$ [326, 327]:

$$\left(\frac{\mathrm{d}\sigma}{\mathrm{d}\Omega}\right)_{\text{non-res.}} = r_0^2 \left| \sum_j e^{i\boldsymbol{Q}\cdot\boldsymbol{r}_j} P - i\frac{mc}{e\hbar} \mathcal{R} \left(\boldsymbol{M}_{\mathrm{L},\perp} \cdot \boldsymbol{P}_\mathrm{L} + \boldsymbol{M}_\mathrm{S} \cdot \boldsymbol{P}_\mathrm{S} \right) \right|^2 \quad ,$$

with the polarization factors

$$\begin{aligned} P &= (\hat{\boldsymbol{\varepsilon}}_f \cdot \hat{\boldsymbol{\varepsilon}}_i) \\ \boldsymbol{P}_\mathrm{L} &= 4\sin(\theta)\,(\hat{\boldsymbol{\varepsilon}}_f \times \hat{\boldsymbol{\varepsilon}}_i) \\ \boldsymbol{P}_\mathrm{S} &= (\boldsymbol{k}_f \times \hat{\boldsymbol{\varepsilon}}_f)(\boldsymbol{k}_f \cdot \hat{\boldsymbol{\varepsilon}}_i) - (\boldsymbol{k}_i \times \hat{\boldsymbol{\varepsilon}}_i)(\boldsymbol{k}_i \cdot \hat{\boldsymbol{\varepsilon}}_f) - (\boldsymbol{k}_f \times \hat{\boldsymbol{\varepsilon}}_f) \times (\boldsymbol{k}_i \times \hat{\boldsymbol{\varepsilon}}_i) \quad , \end{aligned} \tag{2.60}$$

where, reminiscent of neutron scattering, $\mathbf{M}_{\mathrm{L},\perp}(\mathbf{Q})$ is the component of $\boldsymbol{M}_\mathrm{L}$ that is perpendicular to the momentum transfer $\boldsymbol{Q}$. In this form it is also evident that, apart from

pure charge and pure magnetic scattering, interference terms may also arise.

The possibility of observing magnetic x-ray diffraction intensities was originally suggested by Platzman and Tsoar in 1970 [328]. It was experimentally realized in 1972 by Bergevin and Brunel [329]. Using a background-optimized laboratory Cu K_α source and counting 25 minutes per point (3 days per θ–2θ scan), the authors were able to distinguish magnetic superstructure peaks in in NiO (a room temperature antiferromagnet). The $(\frac{1}{2}\frac{1}{2}\frac{1}{2})$ and $(\frac{3}{2}\frac{3}{2}\frac{3}{2})$ peaks that were observed were $\approx 4\times10^{-8}$ times weaker than the adjacent (111) charge peak.

2.4.4 Resonant exchange x-ray scattering

It remains to consider the resonant ($\hbar\omega \approx (E_n - E_i)$) second order contribution of the $\mathcal{H}_2 + \mathcal{H}_3$ term in Eq. 2.55. This interaction gives rise to the resonant inelastic and elastic x-ray scattering (RIXS/REXS) effects that I observed in the context of chapters 3 and 5. Notably, these effects are distinct from the "genuinely magnetic" nonresonant effects outlined in the preceding section in that they do *not* couple directly to spin or orbital magnetic moments in the sample. Instead, the sensitivity to magnetism has its subtle origin in the Pauli exclusion principle (selecting which intermediate state can be excited) and the spin-orbit interaction with unfilled d- and f-shell states. To emphasize this, RIXS and REXS phenomena are also referred to as x-ray resonant *exchange* scattering (XRES).

Due to the requirement of tunable x-ray energies, the exploitation of the strong resonant enhancement had to await the advent of modern synchrotron radiation sources in the 1980s. The fact that the resulting resonant magnetic Bragg intensities may be comparable to those observed in neutron scattering was first emphasized by Blume [326]. Initial experiments were performed by switching the magnetization direction in (ferromagnetic) nickel [330], before Gibbs (1988) reported his seminal REXS study of the L_3 edge in elemental holmium [331]. This data revealed a 50-fold enhancement of the scattering from the incommensurate (helical) magnetic structure. Both resonance energy and magnetic intensity showed an intricate polarization dependence, and were observed not only at the magnetic propagation vector, but also at scattering vectors corresponding second, third and fourth harmonics of the magnetic helix.

A first explanation of the XRES process was provided by Hannon [332] and its polarization dependence was then explicitly formulated by Blume [333]. By expanding the wave functions $e^{i\boldsymbol{k}\cdot\boldsymbol{r}}$ (since $\boldsymbol{k}\cdot\boldsymbol{r} \ll 1$), it can be shown that the contribution due to $\mathcal{H}_3$ is negligible in the vicinity of the resonances ($\hbar\omega \approx (E_n - E_i)$) [327]. The remaining resonant contribution is thus due entirely to $\mathcal{H}_2 \propto \boldsymbol{p}\cdot\boldsymbol{A}$. For vanishing energy transfer, i.e. resonant

elastic x-ray scattering (REXS),

$$\mathcal{W}_{\text{res}} = \frac{2\pi}{\hbar} \left| \sum_n \frac{\langle f|\mathcal{H}_2|n\rangle\langle n|\mathcal{H}_2|i\rangle}{E_i - E_n + \hbar\omega_{k_i} + i\Gamma_n/2} \right|^2 \delta(\hbar\omega) \tag{2.61}$$

Where $\hbar\omega_{\boldsymbol{k}_i}$ is the incident photon energy, not to be confused with the vanishing energy transfer $\hbar\omega \equiv \hbar\omega_{\boldsymbol{Q}}$. A finite lifetime / width Γ_n of the intermediate state $|n\rangle$ has been introduced to limit the divergence of this term.

In order to address the coupling to the virtual intermediate states, this term is treated in *multipole expansion*, a formalism inherited from γ-ray scattering [334, 335]. As the coupling via *magnetic* multipoles is reduced by factors $\mathcal{R}$, these considerations are usually restricted to electric multipole transitions on the order of L, commonly labelled "EL" [332]. In particular, it is generally sufficient to consider electric dipole (E1) and electric quadrupole (E2) processes.

The coupling terms are thus expanded into a sum of *vector spherical harmonics* $\boldsymbol{Y}_{LM}$ ($M = -L...L$) [332, 336]:

$$\begin{aligned} \hat{\boldsymbol{\varepsilon}} \cdot \boldsymbol{Y}_{LM}(\hat{\boldsymbol{k}}) &= \sqrt{\frac{4\pi(2L+1)}{3(L+1)}} \sum_{\mu=-1}^{1} C(1, L-1, L; \mu, M-\mu, M)\, Y_{L-1,M-\mu}(\hat{\boldsymbol{k}})\, Y_{1,\mu}(\hat{\boldsymbol{\varepsilon}}), \\ Y_{LM}(\theta,\phi) &= (-1)^M \sqrt{\frac{(2L+1)}{4\pi}\frac{(L-M)!}{(L+M)!}}\, P_{LM}(\cos(\theta))\, e^{iM\phi} \end{aligned} \tag{2.62}$$

Where P_{LM} are the *Legendre polynomials* and $C(l, s, j; m_l, m_s, m)$ are the *Clebsch-Gordan coefficients* that describe the coupling of an orbital angular momentum with quantum numbers (l, m_l) and a spin angular momentum with quantum numbers (s, m_s) to a total angular momentum with quantum numbers (j, m). Assuming that excitation and relaxation occur via the same multipolar transition ($L \equiv L'$, $M \equiv M'$), the *resonant scattering amplitude* becomes

$$\mathcal{F}_{LM}^{\text{res}} = \sqrt{\frac{(\mathcal{V} k_f)^2}{(2\pi)^3 \hbar c^2} \mathcal{W}_{\text{res}}} \to \frac{4\pi}{k_i} \sum_{M=-L}^{L} P_{LM}^* F_{LM}(\omega) \tag{2.63}$$

with the vector spherical harmonics polarization factor

$$P_{LM}^* = \hat{\boldsymbol{\varepsilon}}_f \cdot \boldsymbol{Y}_{LM}(\boldsymbol{k}_f) \boldsymbol{Y}_{LM}^*(\boldsymbol{k}_i) \cdot \hat{\boldsymbol{\varepsilon}}_i \tag{2.64}$$

The details of the resonant process is here encoded in the multipolar coefficients F_{LM}. This includes a sum of Fourier components of the multipolar transition operator and their appropriate weighting by Clebsch-Gordan coefficients.

x-ray edge	$\|i\rangle \equiv \|f\rangle$	ion	$\|n\rangle$	$\hbar\omega$ (keV)	type	amplitude
L_2 $(j=\frac{1}{2})$, L_3 $(j=\frac{3}{2})$	$2p_j$	$3d$ TM	$3d$	0.5–0.9	E1	$\approx 0.1\,r_0$
		$4d$ TM	$4d$	2.2–3.8	E1	$\approx 0.1\,r_0$
		$5d$ TM	$5d$	10–13	E1	$\approx 0.1\,r_0$
		Ltn.	$4f$	5.7–10	E2	$\approx 0.1\,r_0$
			$5d$	5.7–10	E1	$\approx 0.1\,r_0$
M_2 $(j=\frac{1}{2})$, M_3 $(j=\frac{3}{2})$	$3p_j$	Ltn.	$4f$	1.2–2.2	E2	$\approx 0.1\,r_0$
			$5d$	1.2–2.2	E1	$\approx 0.1\,r_0$
M_4 $(j=\frac{3}{2})$, M_5 $(j=\frac{5}{2})$	$3d_j$	Ltn.	$4f$	0.9–1.6	E1	$\approx 100\,r_0$
		Act.	$5f$	3.3–3.7	E1	$\approx 100\,r_0$

Table 2.1: Overview of the energies and resonant x-ray scattering amplitudes of the most commonly investigated electric dipole (E1) and quadrupole (E2) resonances (TM: transition metals, Ltn.: Lanthanides, Act.: Actinides).

I attempt so summarize the derivation of F_{LM} in an accessible way in Appendix A, in which I follow the work of Hamrick [336]. Even though an evaluation of *absolute intensities* is normally not feasible (or necessary) in x-ray scattering, an evaluation of these terms can yield useful information on the relative strengths of the different multipolar processes that are expected for the ion that is being investigated.

Which transitions are allowed depends on the resonant x-ray edge that is being investigated. The most common cases are summarized in Table 2.1.

In this thesis I report resonant x-ray studies at the Fe L_3 edge (a dipole excitation, in Chapter 3) and at the Eu L_3 edge (Chapter 5). As evident from Table 2.1, the latter is a special case, since the valence states not only include the rare earth $4f$ shell (accessible via quadrupole coupling), but also the lower-energy $5d$ shell (accessible via dipole coupling). Indeed I found that it was not necessary to take into account E2 contributions in order to model my data.

In the course of my dissertation work, I have also performed several resonant x-ray studies of $5d$ transition metal (Os and Ir) L_2/L_3 edges (see [150]) and also soft x-ray studies of rare earth (Tb and Sm) M_4 and M_5 edges (not reported in this thesis).

Due to the complex polarization dependence of Eqs. 2.63 and 2.64, it is convenient to express the REXS scattering amplitude in a basis of polarization vectors perpendicular ($\boldsymbol{\sigma}$) and parallel ($\hat{\boldsymbol{\varepsilon}}_{\|}$) to the scattering plane. The orientation of these vectors is illustrated in Fig. 2.7. Thus, the polarization factor takes on a matrix form, e.g.

$$P = \hat{\boldsymbol{\varepsilon}}_f \cdot \hat{\boldsymbol{\varepsilon}}_i \;\rightarrow\; \begin{pmatrix} 1 & 0 \\ 0 & \cos 2\theta \end{pmatrix} \tag{2.65}$$

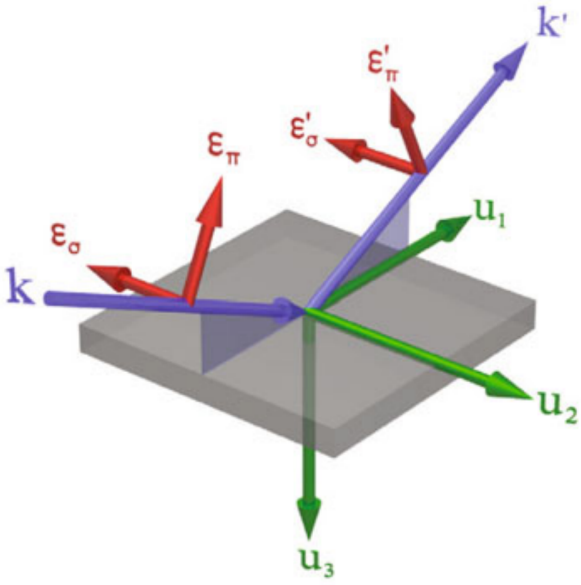

Figure 2.7: (From [337]). The $\hat{\boldsymbol{u}}_i$ reference frame commonly used in x-ray polarization analysis. The orientations of the incoming ($\hat{\boldsymbol{\varepsilon}}$) and scattered ($\hat{\boldsymbol{\varepsilon}}'$) polarization unit vectors parallel (π) and perpendicular (σ) to the scattering plane are also indicated. These conventions are identical to the illustration of the *horizontal* scattering geometry at instrument P09-EH2 in Fig. 5.5 (Chapter 5).

To interpret polarized x-ray scattering experiments it is useful to choose the conventional $\hat{\boldsymbol{u}}_i$ reference frame shown in Fig. 2.7, and defined in Eq. 5.1 (Chapter 5). Hill and McMorrow have provided an expression of Eq. 2.63 in this reference frame. In terms of the components of the magnetic structure factor vector $\boldsymbol{M}^{\hat{\boldsymbol{u}}} = (M_1^{\hat{\boldsymbol{u}}}, M_2^{\hat{\boldsymbol{u}}}, M_3^{\hat{\boldsymbol{u}}})$, the dipolar (E1) part is given by

$$\begin{aligned}\mathcal{F}_{\mathrm{E1}} = F^{(0)} \begin{pmatrix} 1 & 0 \\ 0 & \cos 2\theta \end{pmatrix} - iF^{(1)} \begin{pmatrix} 0 & M_1^{\hat{\boldsymbol{u}}} \cos\theta + M_2^{\hat{\boldsymbol{u}}} \sin\theta \\ M_3^{\hat{\boldsymbol{u}}} \sin\theta - M_1^{\hat{\boldsymbol{u}}} \cos\theta & -M_2^{\hat{\boldsymbol{u}}} \sin 2\theta \end{pmatrix} + \\ + F^{(2)} \begin{pmatrix} (M_2^{\hat{\boldsymbol{u}}})^2 & -M_2^{\hat{\boldsymbol{u}}} \left[M_1^{\hat{\boldsymbol{u}}} \sin\theta - M_3^{\hat{\boldsymbol{u}}} \cos\theta\right] \\ M_2^{\hat{\boldsymbol{u}}} \left[M_1^{\hat{\boldsymbol{u}}} \sin\theta + M_3^{\hat{\boldsymbol{u}}} \cos\theta\right] & -\cos^2\theta \left[(M_1^{\hat{\boldsymbol{u}}})^2 \tan^2\theta + (M_3^{\hat{\boldsymbol{u}}})^2\right] \end{pmatrix}\end{aligned} \tag{2.66}$$

The dipole coefficients $F_{\mathrm{E1}}^{(i)}$ in this equation are given by (see Appendix A for a discussion of the full evaluation of these F_{LM} terms)

$$\begin{aligned} F_{\mathrm{E1}}^{(0)} &= 3/(4k_i)(F_{11} + F_{1-1}) \\ F_{\mathrm{E1}}^{(1)} &= 3/(4k_i)(F_{11} - F_{1-1}) \\ F_{\mathrm{E1}}^{(2)} &= 3/(4k_i)(2F_{10-}F_{11} - F_{1-1}) \end{aligned} \tag{2.67}$$

For quadrupolar transitions, an expression similar to Eq. 2.66, but with *ten* matrix terms and *five* coefficients $F_{\mathrm{E2}}^{(i)}$ is obtained [338]. In my Eu L_3 study of $EuCd_2As_2$ (Chapter 5),

I considered the relevance of such higher order terms but found that the data are dominated by the E1 ($2p_{\frac{3}{2}} \leftrightarrow 5d$) excitation. In most applications, all relevant information can be obtained without evaluating the multipolar amplitude coefficients. They are then treated as arbitrary scale factors.

2.4.5 Resonant inelastic x-ray scattering

Resonant inelastic x-ray scattering is one of the youngest scattering techniques and has seen great instrumental advances in the last ten years [303]. The direct inelastic resonant process is illustrated in Fig. 2.8. As in the elastic case, a core electron is excited to the valence shell. However, the resulting core-hole is filled by another (lower energy) electron of the valence shell, such that the system experiences a net energy transfer. In RIXS, the final state of the scattering site depends on *which atom* is being excited. This is a key difference from REXS process (which does not distinguish between sites). As a consequence, RIXS scattering amplitudes have to be squared before being added [327]. In effect, this means that the scattered intensity will be proportional to the total number N of sites — much weaker than for the elastic situation ($\propto N^2$).

In the last decade or so, it has become possible to offset this disadvantage of weak intensities with the extreme brilliance of modern synchrotron radiation sources [301, 311]. Compared to inelastic neutron scattering, the highly focused undulator radiation (with beam sizes on the order of 10 μm) has the added advantage of being able to investigate very small samples. With penetration depths of 0.1μm (soft x-ray regime) to several μm (hard x-ray regime), RIXS is still a bulk probe [303].

Compared to any *massive* particles, photons have much higher energies in the relevant momentum regime. For RIXS, this implies that the energy range of atomic excitations that can be probed is effectively unlimited. On the downside, energies in the range of 1–10 keV demand an extreme resolution to address the energy range that is most relevant for magnetic fluctuations (< 100 meV). The available photon count rate turns out to be the key limiting factor in RIXS spectrometers. The focus of the technique has therefore shifted commensurately with the improvement in photon brilliance. Until recently, it had been used mostly to probe high energy inter-level or charge transfer electronic excitations ($\approx$eV range). This situation is now changing as a new generation of RIXS beamlines with energy resolution on the order of 25 meV (both in the hard and soft x-ray regimes) is becoming available [339].

Another advantage is afforded by the orbital specificity and intricate polarization dependence of the XRES cross section. In principle, this allows access to momentum-resolved information on the mixing, symmetry and spatial distribution of electronic states. How-

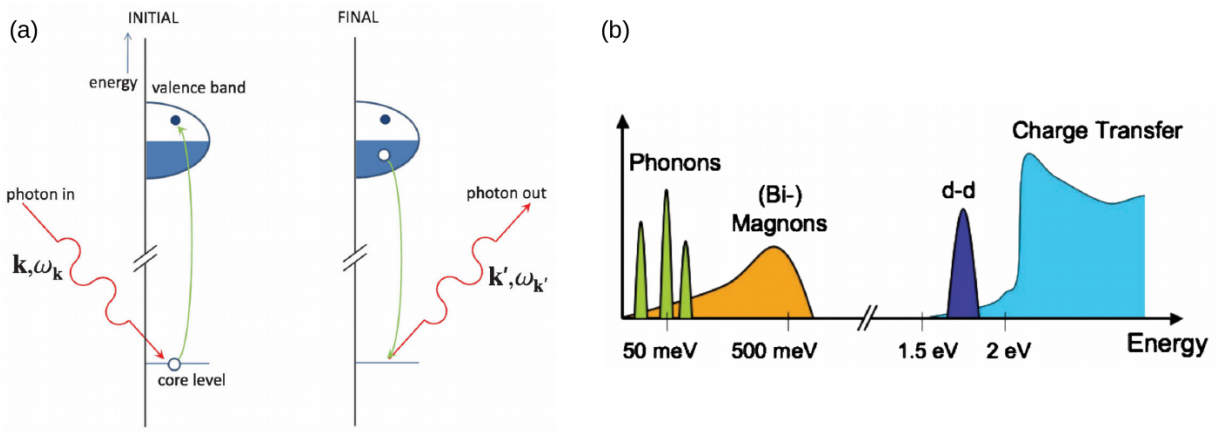

Figure 2.8: (From [303]). (a) The two-step direct RIXS process. First, a core electron is excited to the valence band. For a few femtoseconds, the system is in a complex, highly unstable state, before another valence electron combines with the core-hole. In this process, energy can be dissipated in various electronic, magnetic processes, as well as lattice vibrations. (b) Schematic RIXS spectrum, illustrating the energy ranges of four typical spectral contributions.

ever, Since the insertion of polarization analysers implies additional intensity losses, at present these possibilities have only been partially realized [340].

A RIXS event can be described by the term

$$\mathcal{W}_{\text{res}} = \frac{2\pi}{\hbar} \sum_f \left| \sum_n \frac{\langle f|\mathcal{H}_2|n\rangle\langle n|\mathcal{H}_2|i\rangle}{E_i - E_n + \hbar\omega_{k_i} + i\Gamma_n/2} \right|^2 \delta(\hbar\omega_{\boldsymbol{Q}} - (E_f - E_i)) \quad , \tag{2.68}$$

which corresponds to Eq. 2.61, except that here the energy of the final state $|f\rangle$ is explicitly different from $|i\rangle$ ($E_f - E_i \neq 0$). Instead, a sum over possible final states is introduced. This energy can be transferred to various excitations that may (directly or indirectly) couple to the momentum and polarization of the x-ray photon. This includes not only electron-hole excitons of the states near the Fermi surface, but also lattice vibrations (phonons), transfer of electrons from ligand ions, excitations within crystal-field split valence manifolds and spin-wave excitations (magnons). A schematic RIXS spectrum indicating the relevant energy transfer regimes is shown in Fig. (b) [303].

An analytical modelling of the non-equilibrium intermediate state is not feasible. Instead, various complex numerical approaches have been proposed, which are presently one of the most active parts of scattering theory [303].

2.5 Muon spin rotation and relaxation

In the context of Chapter 6, I have used *muon spin rotation and relaxation* (MuSR) to aid the interpretation of magnetic neutron powder diffraction data. MuSR is an unusual case of a *bulk* microscopic probe, i.e. it does *not* involve a scattering process. Instead of coherent interference of scattered waves, the access to microscopic information is provided by a concatenation of radioactive particle decay phenomena.

The MuSR process entails the implantation of positive muons (μ^+) with a well-defined spin-orientation into the sample. The *parity violation* [341] of the muon's *weak decay* correlates the emission of decay products with the muon- spin–orientation at the time of disintegration. In this way, it is possible to follow the Larmor precession of muon spins in the local magnetic field at the muon stopping site [342].

Like electrons and positrons, muons are *leptons* that carry a positive or negative electron charge ($\pm e$) — however with a rest-mass of $m_\mu = 207\,m_e = 105.66\,\mathrm{MeV}/c^2$ and a limited lifetime of $\tau_\mu = 2.2\,\mu\mathrm{s}$. Muons were originally discovered due to their natural occurrence in the form of *cosmic rays* [343]. Muon beams appropriate for condensed matter research are today obtained as a byproduct at synchrotron- or linear accelerator facilities, e.g. at the ISIS neutron spallation source. Here, the 800 MeV proton pulse intended for neutron creation at Target Station 1 passes through a 10 mm thick graphite target. In this process, 2–3% of the protons (p) collide with protons and neutrons (n) in the carbon nuclei and are lost to pion (π^+/π^-) creation processes [344]:

$$p + p \rightarrow p + n + \pi^+$$
$$p + n \rightarrow p + p + \pi^-$$

After a mean lifetime of 26 ns, these pions decay almost entirely (99.99 %) into muon and muon-neutrino (ν_μ) pairs. For positive muons, $\pi^+ \rightarrow \mu^+ + \nu_\mu$. In this two-particle decay, the conservation of angular momentum guarantees a fully spin-polarized muon beam, i.e. all muons thus obtained carry their spin antiparallel to their momentum. In the absence of electric fields, this left-handedness is conserved, and thus a beam of positive muons can be selected, focused, and directed onto a sample using evacuated beam pipes and multipole magnets.

Most muons arise from the surface of the graphite target and arrive at the sample with a kinetic energy of $\approx 4.1\,\mathrm{MeV}$, as dictated by the pion rest mass. Within the sample, they are slowed down by Coulomb collisions. After about 2 ns, and several mm into the sample, they come to rest and thermalise at interstitial sites of the host structure. Due to the details of this stopping process [345, 342], it can be assumed that the stopping site lies approximately $2\,\mu$m beyond any radiation damage to the sample. To first order, the

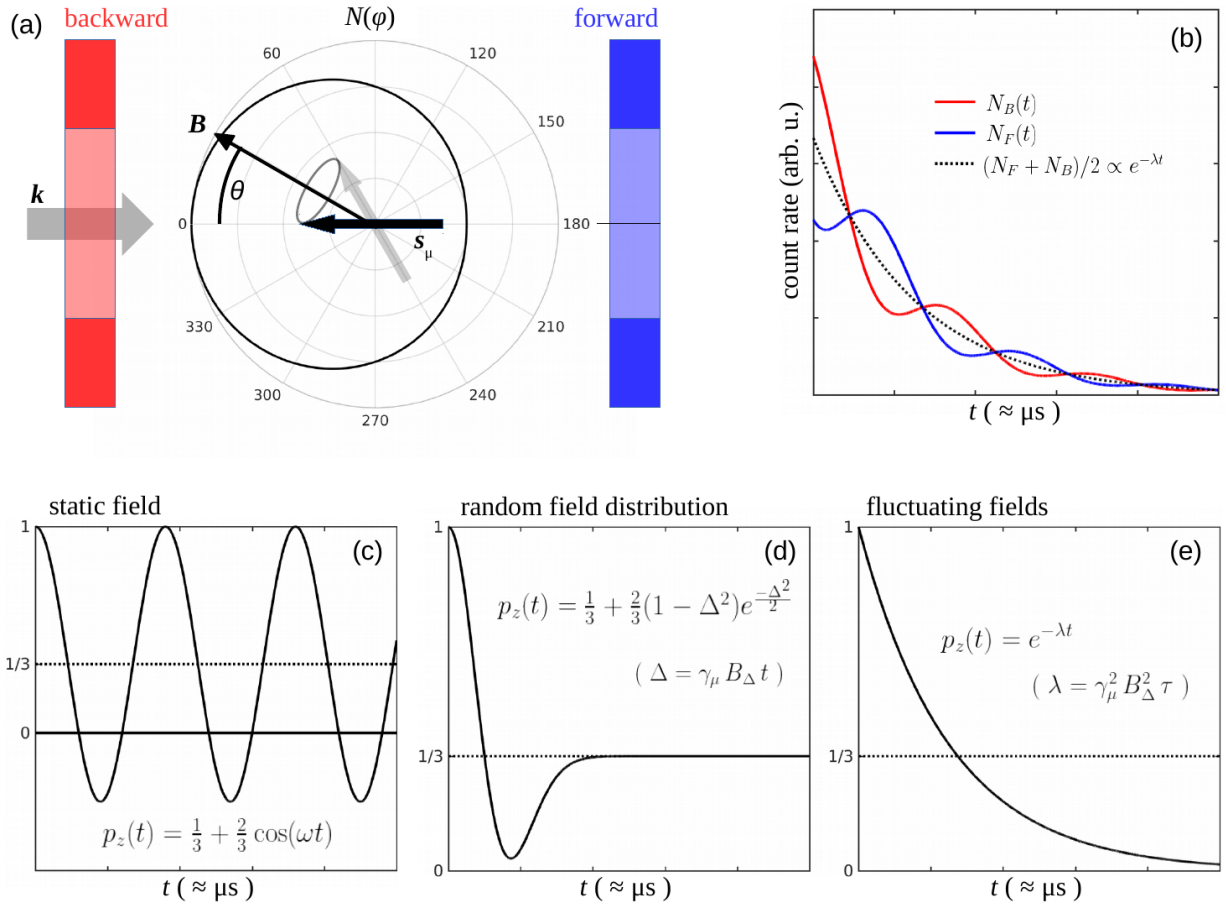

Figure 2.9: (a) Schematic of the MuSR process. Muons enter the instrument (momentum $\boldsymbol{k}$) and penetrate the sample, placed between the forward and backward detectors. Initially, the muons come to rest with their spins $\boldsymbol{s}_\mu$ directed towards the backward detector. The angular dependence of the positron emission $N(\varphi)$ is indicated as a polar plot. (b) Typical evolution of forward (red) and backward (blue) positron counting rates as the muon precesses in a magnetic field $\boldsymbol{B}$. (c-e) Limiting cases of the mean muon spin polarization $p_z(t)$ in a polycrystalline sample: (c) In the case of a fixed static field, (d) for a random distribution of static fields, and (e) for fluctuating fields.

implanted particle can therefore be expected to experience an unaltered host environment. Notably, negative muons would not be favourable for condensed matter studies as they penetrate into atomic shells and form bound states with the nuclei, or are absorbed ($\mu^- + p \rightarrow n + \nu_\mu$).

As spin $s = \frac{1}{2}$ particles, muons carry a magnetic moment ($|\boldsymbol{\mu}| = 1/207\,\mu_\mathrm{B}$) and thus experience a torque $\boldsymbol{\tau} = \boldsymbol{\mu} \times \boldsymbol{B}$ in the magnetic field $\boldsymbol{B}$ inside the sample. This results in a Larmor precession with the frequency $\omega = \gamma_\mu B$ where $\gamma_\mu = \frac{g\,e}{2m_\mu} \approx \frac{e}{m_\mu} = 2\pi \times 135.5\,\mathrm{MHz/T}$ is the gyromagnetic ratio of the muon. The number of the implanted muons decreases as $\exp(-t/\tau_\mu)$ as each disintegrates into a positron, an electron neutrino and a muon antineutrino [346]:

$$\mu^+ \rightarrow e^+ + \nu_e + \bar{\nu}_\mu$$

Due to the third decay product, this process has more degrees of freedom than the pion decay which created the muon. Nevertheless, the *parity violation* of the weak nuclear interaction still implies a bias of positron emission towards the direction of the muon spin. On average, the number of positrons emitted at an angle φ with respect to the muon spin is given by (see Fig. 2.9(a)):

$$N(\theta) = N_0(1+\cos(\varphi)/3) \quad \text{(averaged over } e^+ \text{ energies)} \tag{2.69}$$

In a MuSR experiment, the sample is positioned in between two (*forward* and *backward*) positron detectors. The measured quantity is the *asymmetry ratio* between the forward and backward counting rates N_F and N_B:

$$A(t) = \frac{N_F - \alpha N_B}{N_F + \alpha N_B} = A_0\, p_z(t) \tag{2.70}$$

Here, α is a calibration constant that accounts for relative detector efficiencies. As indicated in Eq. 2.70, the measured asymmetry is proportional to the total muon polarization along the instrument axis, p_z. For the solid angles covered by detector banks of real MuSR instruments, the initial asymmetry ratio is on the order of $A_0 \approx 25\%$ (see Sections 6.4.1 and 6.4.2). For a magnetic field B at an angle θ to the muon spin direction (see Fig. 2.9a), the Larmor precession of p_z is given by

$$\begin{aligned} p_z(t) &= \cos(\theta)^2 + \sin(\theta)^2 \cos\left(\gamma_\mu B t\right) \\ &\rightarrow {}^1\!/_3 + {}^2\!/_3 \cos\left(\gamma_\mu B t\right) \qquad \text{(polycrystal)} \end{aligned} \tag{2.71}$$

In the case of powder samples, as for the experiments discussed in Chapter 6, the internal fields of each crystallite will be randomly oriented with respect to the fixed initial direction of muon spins. Therefore, an average over an isotropic distribution of the field directions has been introduced in the second line of Eq. 2.71. The corresponding oscillation of $A(t)$ and $p_z(t)$ is illustrated in Fig. 2.9(c).

Eq. 2.71 describes the muon response of a magnetically ordered system with a well-defined stopping site, so that a single value of B applies across all sites. This will not be the case in materials with static disorder or random stopping sites, where the magnetic fields at the muon sites vary. In this situation, the fields experienced by the muons are better described by a (static) Gaussian distribution, $\exp\left(-\gamma_\mu^2 \langle B^2 \rangle t^2/2\right)$. This results in a *dephasing* of the harmonic oscillation (Eq. 2.71, Fig. 2.9(c)), which leaves a single minimum in the muon spin polarization relaxation [342]. This is described by the Kubo-Toyabe formula:

$$p_z(t) = {}^1\!/_3 + {}^2\!/_3 \left(1 - (\gamma_\mu B_\Delta t)^2\right) e^{-(\gamma_\mu B_\Delta t)^2/2} \quad \text{, with} \quad B_\Delta = \sqrt{\langle B^2 \rangle}\ . \tag{2.72}$$

A key characteristic of *static* fields, whether ordered (Eq. 2.71) or random (Eq. 2.72) is that the asymmetry ratio decays to a finite constant value of $A_0/3$. This allows a clear distinction from the case of rapidly *fluctuating* magnetic moments. In this case,

$$p_z(t) = e^{-\lambda t} \quad \text{, with the relaxation rate } \lambda = \gamma_\mu^2 B_\Delta^2 \tau \ , \tag{2.73}$$

where τ is a characteristic correlation time. A decay of $A(t)$ towards zero, as illustrated in Fig. 2.9(e) thus indicates the absence of static order (a slower decay of $A(t)$ indicates smaller τ, i.e., faster fluctuations).

Building on the basic relations laid out above, more elaborate situations can be constructed if external fields are applied, or single crystals are probed. Several thorough reviews of the techniques are available [347, 348, 349, 342, 350]. To extract quantitative microscopic information from muon data, it is necessary to determine the crystallographic positions of muon stopping sites, as well as the distribution of magnetic fields. This can be achieved by numerical models of the surrounding Coulomb potentials and dipole fields [344, 351]. Recently, attention has also been devoted to study and account for possible perturbations of the ionic environment introduced by the presence of the muon [352].

Such complications aside, it is a great advantage of the MuSR technique that some information can be gleaned from *qualitative* features of $A(t)$, as for example the presence or absence of oscillations or an "$A_0/3$-tail". For the purpose of the present thesis (Chapter 6), such information proved sufficient to resolve an ambiguity in a magnetic neutron powder diffraction dataset.

Chapter 3

Strong $(\pi, 0)$ spin fluctuations in β-FeSe

In this chapter, I present a powder inelastic neutron scattering (INS) study and a single crystal resonant inelastic x-ray scattering (RIXS) study of paramagnon excitations in the unusual superconductor FeSe. With around 400 publications in 2015–2016[1], FeSe may currently be receiving more scientific attention than any other single material. Knowledge of its magnetic fluctuation spectrum has been sought after as a touchstone for theories trying to model high-T_c superconductors (see 1.1).

Using powder INS, I was able to discern collective paramagnetic spin fluctuations emerging from $\boldsymbol{q}_m = (\pi, 0)$ and equivalent wave vectors, and extending to energies greater than 80 meV. I did not observe any significant change in the low energy (≈10–15 meV) part of the spectrum on crossing the orthorhombic-to-tetragonal transition. The neutron results presented in this chapter appeared in Physical Review B **91**, 180501(R) (2015).

Using Fe L_3 edge RIXS from a single crystal, I observed an anomalous dispersing signal in the range of 100–300 meV. As noted in Section 2.4.5, RIXS is a relatively young technique. The quantitative modeling of my data is not straightforward, because a multitude of complex processes may contribute RIXS spectral weight. Nevertheless, a comparison with the available literature suggests that my observations can indeed be attributed to spin-flip excitations. There exist no previous reports of successful soft RIXS studies of magnetic states that are as itinerant as in FeSe.

[1] Thomson-Reuters *Web of Science*, http://www.webofknowledge.com

Contents

3.1 Introduction 67

3.2 Inelastic neutron scattering on MERLIN, ISIS 69

3.2.1 Characterization of polycrystalline sample 69

3.2.2 Experimental setup 71

3.2.3 Results 72

3.2.4 Analysis and discussion 76

3.3 Resonant inelastic x-ray scattering at ID32, ESRF 80

3.3.1 Characterization of single-crystalline sample 80

3.3.2 Experimental setup 81

3.3.3 Results 83

3.3.4 Discussion 89

3.4 Conclusion 91

3.1 Introduction

Iron selenide (β-$Fe_{1+x}Se$, hereafter denoted "FeSe") is structurally the simplest of the iron-based superconductors, as it consist only of antifluorite layers - without intercalating ions or "blocking layers" (see Fig. 3.1 (a) and Section 1.1). The layers are separated by ≈ 5.5 Å and the interstitial space contains only trace amounts of iron ($x \approx 1$ %).

Contrary to this apparent simplicity, FeSe is one of the most intriguing compounds of its family. The superconducting transition temperature of the pure bulk phase is relatively low, $T_c \approx 8$ K [38], but it increases to 37 K under pressure [353] (see Fig. 3.1 (b)) and rises above 40 K with intercalation of alkali ions A^+ to form $A_xFe_{2-y}Se_2$ [354] or by co-intercalation of ammonia molecules and amide ions or organic molecules along with A^+ [355, 356, 357]. Superconductivity was even reported at temperatures as high as 100 K in monolayers of FeSe grown on $SrTiO_3$ [358, 359] (however, the role of the substrate remains controversial). There is evidence that superconductivity at ambient pressure is favoured by reduction of Fe below the 2+ oxidation state and minimisation of vacancies in the FeSe layers [356, 360]. Nevertheless, there is currently no simple explanation for such an extraordinary variation in T_c among derivatives containing very similar antifluorite layers of FeSe.

The structural and electronic ordering properties of FeSe differ qualitatively from those of the related iron pnictide compounds in two important ways. First, superconductivity appears in FeSe without the need for doping and is very sensitive to composition [361]. Second, FeSe has a tetragonal-to-orthorhombic structural transition ($T_s \simeq 90$ K [38, 362]), as in the parent phases of the iron pnictide superconductors, but this transition is *not* followed by the development of long-range magnetic order [363]. The phase below T_s is considered to be some form of *electronic nematic*, but opinions divide over whether the nematic transition is driven by orbital ordering [74, 364, 365, 366] or by spin degrees of freedom [367, 368, 369, 370].

As laid out in Section 1.1, spin fluctuations are a prominent feature of the iron-based superconductors and are thought to play a significant role in the pairing interaction [20, 27, 371]. In the iron arsenide superconductors, spin fluctuations emerge from the same (or nearly so) characteristic in-plane wave vector $\mathbf{q}_m = (\pi, 0)$[2], as the spin density wave (SDW) order of the parent phases. This magnetic instability is understood to be assisted by nesting of hole and electron Fermi surface pockets centred around the Γ and X points of the square lattice.

[2] As in Section 1.1, I quote in-plane propagation vectors with respect to the *one-Fe* unit cell of the square iron sub-lattice.

Spin fluctuations have also been observed in the superconducting iron selenides, but the characteristic wave vector varies from system to system. For example, it is $(\pi,0)$ in $FeTe_{1-x}Se_x$ ($x \approx 0.5$) [114], $(\pi,\pi/2)$ in $A_xFe_{2-y}Se_2$ (A = K, Rb, Cs) [372, 373, 110], and different again in $Li_x(ND_2)_y(ND_3)_{1-y}Fe_2Se_2$ [374] (see also Fig. 1.5).

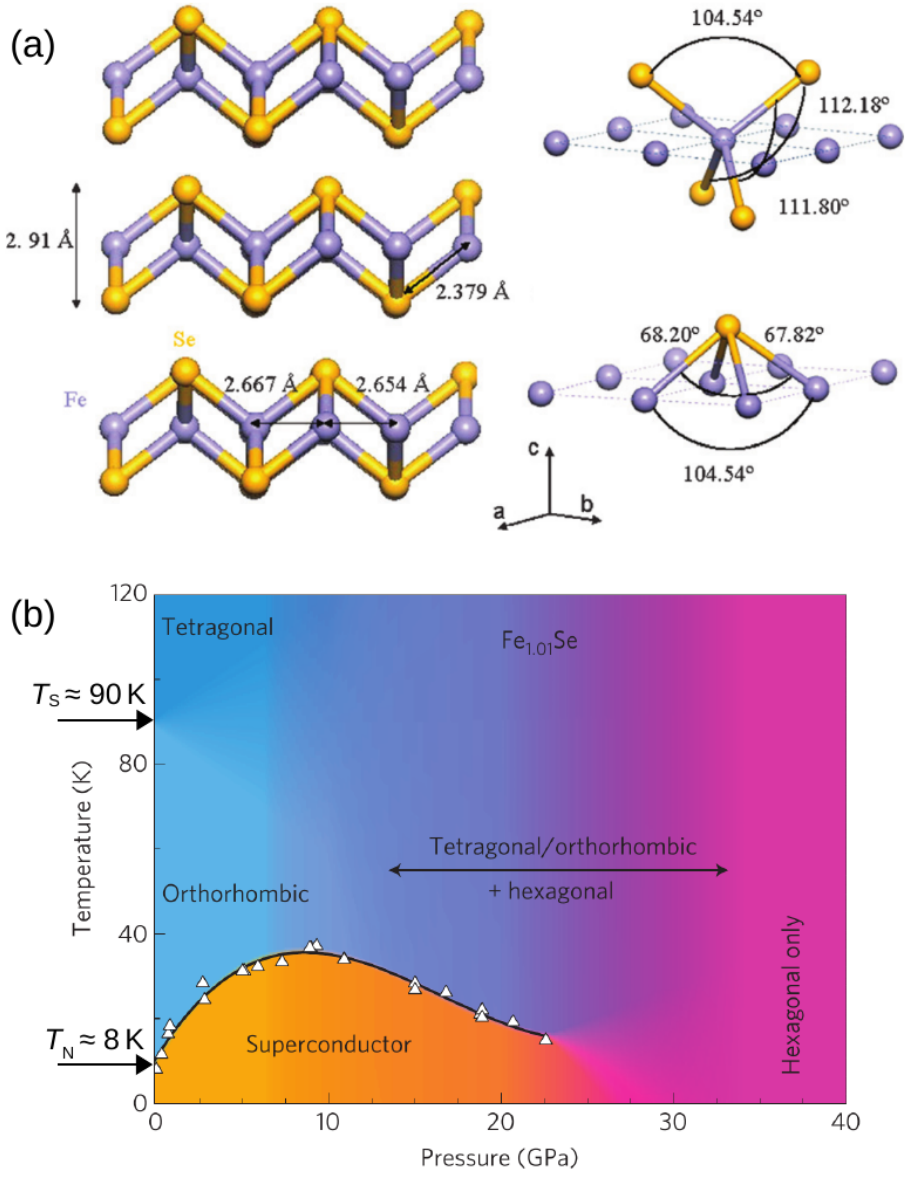

Figure 3.1: (adapted from [375, 353]). (a) Among the different families of iron-based superconducting materials, FeSe is the structurally simplest *prototype* compound, as it consists purely of *antifluorite* layers of edge-sharing $FeSe_4$ tetrahedra. (b) The low temperature electronic and structural phase diagram is atypical for iron-based superconductors as discussed in Section 1.1. In particular, there is no magnetically ordered phase and the temperature scales of the structural and superconducting transitions are separated by one order of magnitude.

Ab initio electronic structure calculations indicate that FeSe is close to a magnetic ordering instability with characteristic wave vector $\boldsymbol{q}_{\rm m} = (\pi, 0)$ [116, 376, 377]. However, angle-resolved photoemission spectroscopy and quantum oscillation studies have revealed that the Fermi surface deviates significantly from the predictions [378, 379, 364, 365, 380, 57], and several models for the nematic phase predict competing magnetic phases with $\mathbf{q}_{\rm m} = (\pi, \xi)$, $0 \leq \xi \leq \pi/2$ [367, 368, 369, 370]. Experimental information on the magnetic ground state of FeSe has been lacking, and is needed to elucidate the nematic phase and to assess the role of spin fluctuations in the superconducting state.

3.2 Inelastic neutron scattering on MERLIN, ISIS

3.2.1 Characterization of polycrystalline sample

A powder sample of FeSe of total mass 13.8 g was prepared by my collaborators Prof. Simon Clarke and Dr. Stefan Sedlmaier[3], as described in Rahn *et al.* [381]. Throughout the synthesis process and during all sample handling, special care was taken to avoid contact with the ambient atmosphere. This was crucial due to the chemical reactivity of FeSe (to avoid oxidation) as well as to avoid absorption of hydrogen-containing molecules. Hydrogen has a large incoherent neutron scattering cross section ($\sigma_{\rm inc} = 80.26\,$barn), which would add to the diffuse background signal. This can be a particular issue if weak or diffuse magnetic scattering contributions are to be discerned, as in the present case. Preliminary laboratory x-ray powder diffraction showed that this powder sample was of very high phase purity, with trace amounts ($< 1\%$) of hexagonal α-FeSe and unreacted Fe as the only detectable impurities.

In order to confirm the onset of superconductivity at $T_{\rm c} \simeq 8\,$K in this sample, I performed magnetization measurements using a SQUID magnetometer (see Section 2.1). An example of field-cooled and zero-field-cooled data is shown in Fig. 3.2(a). Measurements retaken after the neutron scattering experiment confirmed that the sample did not deteriorate. The right-hand panel of Fig. 3.2(a) shows a broad magnetic anomaly at the structural transition $T_{\rm s} \simeq 90\,K$, consistent with previous data on FeSe powders [38].

For a detailed structural analysis, my collaborator Dr. Stefan Sedlmaier[4] probed this sample by high resolution neutron powder diffraction at the HRPD instrument (ISIS). Measurements were made at several temperatures between 10 K and room temperature. Figure 3.2(b) shows data collected at room temperature, together with a Rietveld fit (FullProf algorithm [382]). The temperature dependence of the lattice parameters

[3]Department of Chemistry, University of Oxford, Inorganic Chemistry Laboratory, Oxford OX1 3QR, UK
[4]Department of Chemistry, University of Oxford, Inorganic Chemistry Laboratory, Oxford OX1 3QR, UK

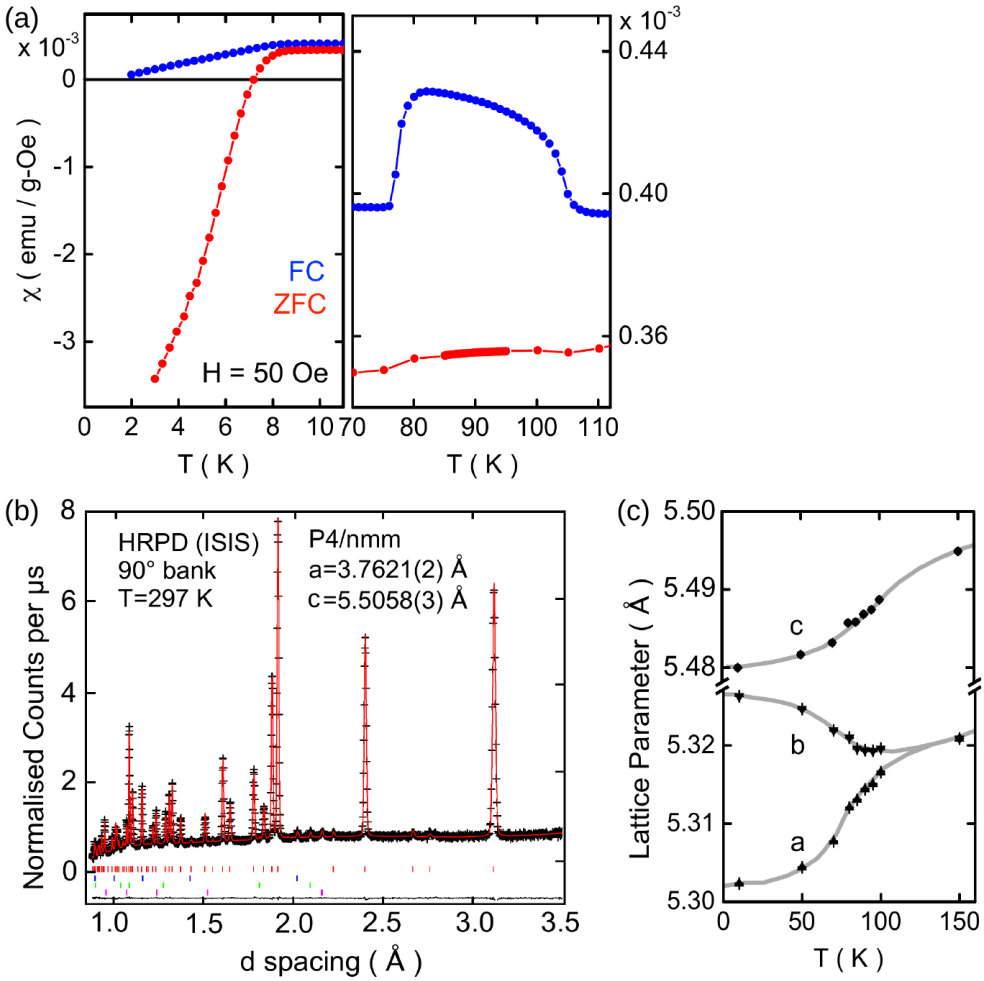

Figure 3.2: (a) Magnetic susceptibility of FeSe powder. The field-cooled (FC) and zero-field cooled (ZFC) curves confirm the onset of superconductivity at $T_c \simeq 8\,\mathrm{K}$ (left). The tetragonal-to-orthorhombic structural transition at $T_s \simeq 90\,\mathrm{K}$ is signalled by a broad magnetic anomaly (right). (b) Rietveld refinement against room temperature neutron powder diffraction data of FeSe. Peak positions for the β-FeSe phase are marked by vertical red ticks beneath the data. The other ticks indicate peak positions for Fe impurities and the vanadium sample can. (c) Temperature dependence of the orthorhombic lattice parameters of FeSe. The points at 150 K are the tetragonal parameters with a multiplied by $\sqrt{2}$. The lines are visual guides.

obtained from these refinements is shown in Fig. 3.2(c). The continuous tetragonal ($P4/nmm$) to orthorhombic ($Cmma$) transition at $T_s \simeq 90\,\mathrm{K}$ is consistent with earlier results [38, 375, 362]. The orthorhombic distortion $(b-a)/a$ approaches $0.5\,\%$ at $10\,\mathrm{K}$. Refinement of the composition $Fe_{1+x}Se$ against data above and below T_s yielded $x = 0.01(1)$, i.e. with interstitial Fe sites between the stoichiometric FeSe layers occupied at the 1% level, a finding consistent with a previous report correlating composition with T_c [361].

3.2.2 Experimental setup

As discussed in Section 2.3, inelastic neutron scattering is usually the method of choice to probe magnetic fluctuations with good energy and momentum resolution. In the case of FeSe, no previous information on the magnetic fluctuations was available at the time these measurements were performed. Since the material does not order magnetically, it was not clear whether a well-defined magnon response could be observed. The high flux direct geometry chopper spectrometer MERLIN (ISIS) is particularly suited for resolving possibly weak magnetic scattering contributions (see Section 2.3).

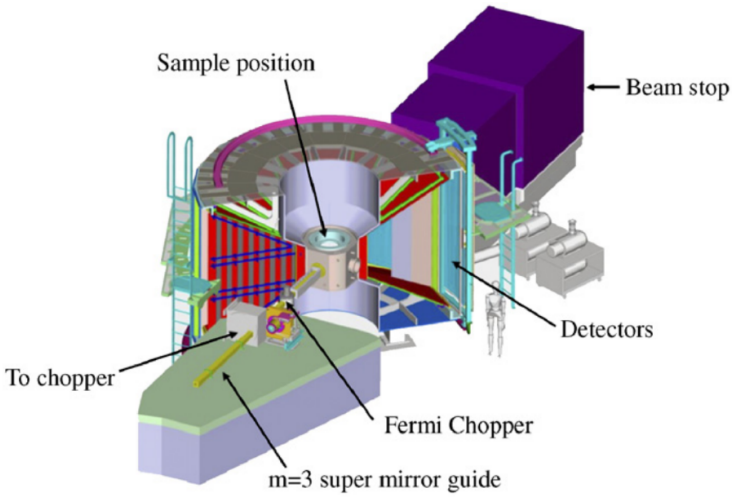

Figure 3.3: (from [383]). Technical drawing of the MERLIN high flux neutron TOF spectrometer at ISIS. An incident neutron energy is selected using a chopper assembly. After scattering from the sample, neutrons are detected on a wide time- and position-resolving detector bank. By relating the scattering angle to the chopper and detector time stamps, an energy- and momentum transfer can be assigned to each neutron event.

Merlin receives neutrons from a 300 K heavy water moderator, and thus reaches its peak flux in the relevant energy range, $E_i \approx 30\,\mathrm{meV}$. The use of supermirror neutron guides, an evacuated detector vessel and a short sample-detector distance (2.5 m) further optimize the neutron flux, at the expense of energy resolution ($\Delta E/E_i \approx 3$–$5\,\%$) [383]. The wide detector array, which covers scattering angles from $2\theta = -45^\circ$ to 135° gives access to

a wide range of momentum transfer without moving any parts of the instrument. The range of possible kinematic conditions is determined by E_i and the extremal scattering angles, $\theta_{\text{min}} \approx 0$ and $\theta_{\text{max}} = 135°$. This constrains the neutron events to a paraboloid $(\hbar\omega, Q)$ map, with a maximum at $(\hbar\omega, Q) = (E_i, k_i)$ and momentum transfer limits at $(0, 2k_i \sin\theta_{\text{min/max}})$.

Because the magnetic response of sample was expected to be weak, I optimized the sample geometry for neutron absorption effects. The powder sample was loaded into aluminium foil packets and placed in an aluminium can in an annular arrangement. The can was then attached to a closed-cycle refrigerator. Neutron spectra were recorded with incident energies of $E_{\text{i}} = 34$, 50 and 100 meV at temperatures from 8 to 104 K. The spectra were normalised to the incoherent scattering from a standard vanadium sample measured with the same incident energies. This enables a presentation of the data in absolute units of $\text{mb}\,\text{sr}^{-1}\,\text{meV}^{-1}\text{f.u.}^{-1}$ (where f.u. refers to one formula unit of FeSe).

3.2.3 Results

Figure 3.5(a) shows an intensity map of part of the $E_{\text{i}} = 100$ meV spectrum measured at 8 K on MERLIN. The spectrum is dominated by scattering from phonons for energies E below the phonon cut-off at 40 meV [384]. Above 40 meV, there is a broad vertical column of scattering centred on the wave vector $Q = 2.6\,\text{Å}^{-1}$, and a weaker column centred on $3.5\,\text{Å}^{-1}$. Figure 3.5(b) is a similar intensity map measured with $E_{\text{i}} = 34$ meV to probe the low (Q, E) part of the spectrum. Phonon scattering dominates in this regime, but there is a window between 10 and 15 meV in which the phonon signal is small, and a vertical column of weak scattering can be seen centred near $Q = 1.2\,\text{Å}^{-1}$. Such scattering columns are observed in neutron powder spectra of other iron-based superconductors and have been confirmed to arise from strongly dispersive spin fluctuations [95, 127, 93, 385].

The magnetic signals identified in the intensity maps can be seen in more detail in the Q cuts made at fixed average energy shown in Fig. 3.6(b). The cuts contain peaks centred on $Q = 1.2$, 2.6 and $3.5\,\text{Å}^{-1}$, and there are additional weak signals near $Q = 4.5\,\text{Å}^{-1}$. The series of magnetic peaks can be indexed as orders of the square lattice wave vector $(\pi, 0)$, illustrated by the red markers in Fig. 3.4. The magnetic signal will also extend in the out-of-plane direction, either as a diffuse rod of scattering if the correlations are quasi-two-dimensional or as a series of peaks if there are strong inter-layer correlations. Simulations of such types of out-of-plane scattering show that, after *powder averaging*, the peaks have a tail on the high Q side but the maxima shift by only a small amount ($< 0.06\,\text{Å}^{-1}$) from the ideal two-dimensional wave vectors.

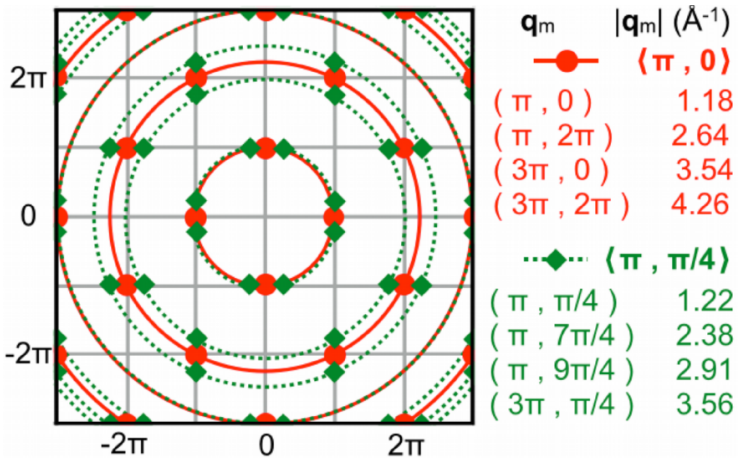

Figure 3.4: Reciprocal lattice of the square iron layer in FeSe. The red and green markers indicate the symmetry-equivalent positions of the $(\pi,0)$-type and $(\pi,\pi/4)$-type propagation vectors, respectively (including the equivalent 90° domains). The circles show the corresponding effect of powder averaging, and the table lists the corresponding values of $Q = |\boldsymbol{q}_\mathrm{m}|$.

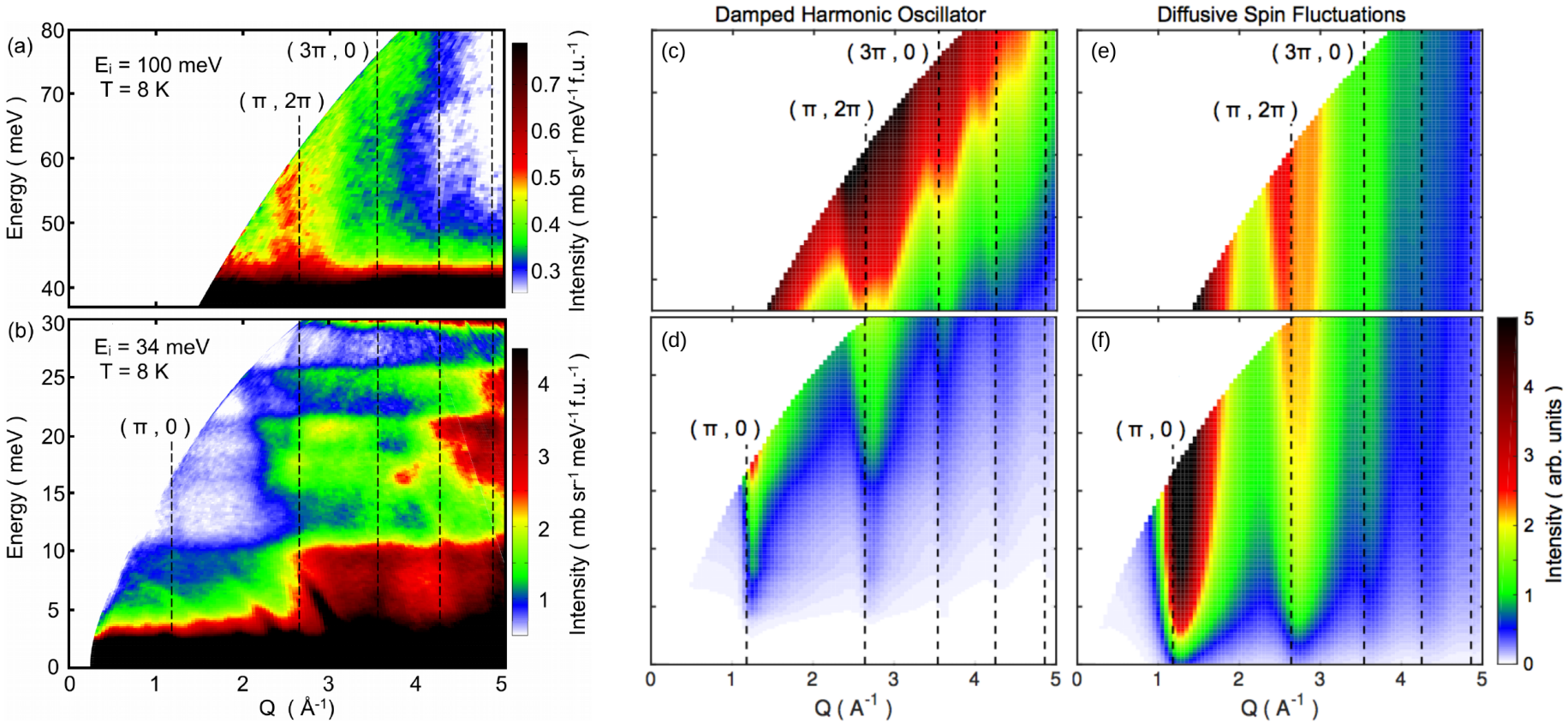

Figure 3.5: (a) Neutron powder spectra of FeSe, obtained on MERLIN at $T = 8\,\mathrm{K} \simeq T_c$. The vertical dashed lines show the 2D wave vector $(\pi,0)$ and equivalent positions. (a) High-energy part of the spectrum, recorded with an incident energy $E_i = 100\,\mathrm{meV}$. The vertical bands of scattering above the phonon cut-off at 40 meV are caused by steeply dispersing cooperative paramagnetic fluctuations. (b) Low energy data measured with $E_i = 34\,\mathrm{meV}$. Magnetic scattering is visible in the energy window 10–15 meV where phonon scattering is weak. (c,d) Simulated intensity maps for the best damped harmonic oscillator (DHO) model and (e,f) for the diffusive model (see text).

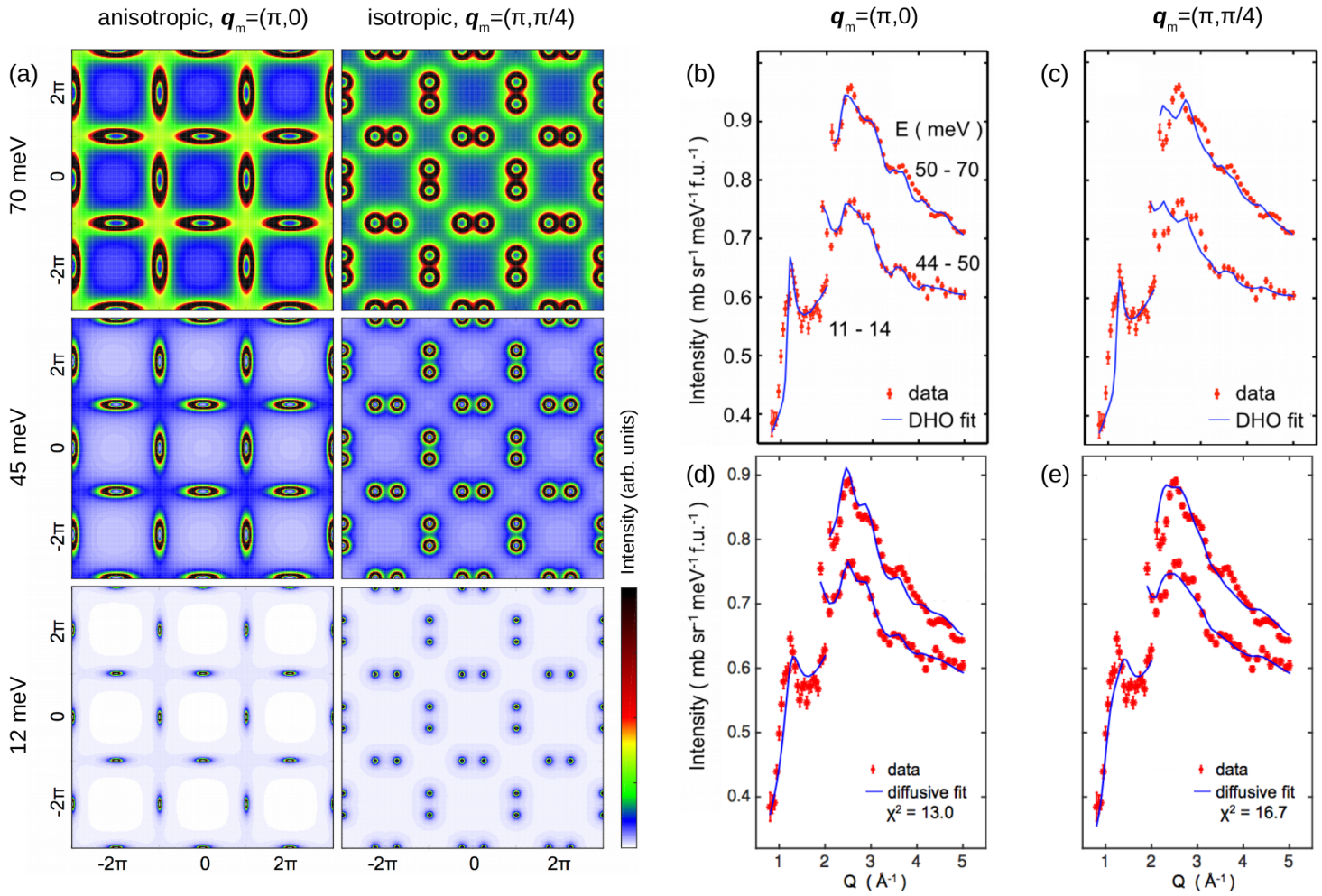

Figure 3.6: (a) Simulated constant-energy intensity maps of the DHO model, at energies corresponding to the line-cuts shown in (b-e). The magnetic wave vector is $\boldsymbol{q}_{\mathrm{m}} = (\pi, 0)$ in the left panels, and $\boldsymbol{q}_{\mathrm{m}} = (\pi, \pm\pi/4)$ in the right panels. (b-e) Constant-energy cuts through the data in Fig. 3.5, integrated over the three energy windows in which magnetic scattering is observed. The upper two cuts are offset vertically. The red symbols are the data and the blue lines are the best fits obtained for a various models: DHO model (top), diffusive model (bottom), $\boldsymbol{q}_{\mathrm{m}} = (\pi, 0)$ (left), and $\boldsymbol{q}_{\mathrm{m}} = (\pi, \pm\pi/4)$ (right). After powder-averaging, the choice of $\boldsymbol{q}_{\mathrm{m}} = (\pi, \pm\pi/4)$ causes an exaggerated splitting around $Q = 2.4\,\text{Å}$ at high energies, which can be understood by reference to panel (a). The diffusive model by Tucker *et al.* [386] contains more free parameters, but does not significantly improve on the DHO model fits.

3.2.4 Analysis and discussion

Although FeSe does not order magnetically, the present inelastic neutron scattering data show that it has a strong magnetic response at $(\pi,0)$ and equivalent positions which characterise the in-plane SDW order found in the parent phases of the iron arsenide superconductors.

To quantify the analysis, I compare the data to a phenomenological model for the low energy response of a two-dimensional (2D) antiferromagnetically-correlated paramagnet. This model has been used previously to describe the low energy part of the spectrum of superconducting $Ba(Fe_{1-x}Co_x)_2As_2$ [387]. The neutron scattering cross section is given by Eqs. 2.37 and 2.40 in Section 2.3.1. For an isotropic paramagnet, the absorptive part of the generalized susceptibility $\chi''(\boldsymbol{q},\omega)$ becomes a scalar quantity and the orientation term in Eq. 2.37 reduces to a factor 2. This leaves

$$\frac{\mathrm{d}^2\sigma}{\mathrm{d}\Omega\mathrm{d}\omega} = \left(\frac{\gamma r_0}{2}\right)^2 \frac{k_\mathrm{f}}{k_\mathrm{i}} \frac{1}{1-\exp(-\beta\hbar\omega)} \frac{2}{\pi} F(\boldsymbol{Q})^2 \chi''(\boldsymbol{q},\omega), \tag{3.1}$$

where $(\gamma r_0/2)^2 = 72.7\,\mathrm{mb}$, $\beta = 1/k_\mathrm{B}T$, and $F(\boldsymbol{Q})$ is the magnetic form factor of Fe^{2+}, as plotted in Fig. 2.5.

The low-energy magnetic excitations are envisaged as damped spin waves with a linear dispersion. To capture this behaviour in simplest terms, I modelled χ'' as a damped harmonic oscillation (DHO):

$$\chi''(\boldsymbol{q},\omega) \propto \frac{E_\mathbf{q}^2\, 2\hbar\omega\Gamma}{[E_\mathbf{q}^2-(\hbar\omega)^2]^2+(2\hbar\omega\Gamma)^2} \quad , \tag{3.2}$$

with the anisotropic linear dispersion

$$E_\mathbf{q} = \hbar\sqrt{(v_\parallel q_\parallel)^2+(v_\perp q_\perp)^2} \tag{3.3}$$

described by the spin velocities $v_\parallel$ and $v_\perp$ in the longitudinal and transverse directions relative to 2D magnetic propagation vector $\boldsymbol{q}_\mathrm{m} = (\pi,0)$. $\Gamma = \Gamma^*\hbar\omega$ is the inverse lifetime, and $\boldsymbol{q}$ is the *spin-wave* wave vector.

Under the assumptions that the magnetic correlations are purely in-plane, $\chi''(\boldsymbol{q},\omega)$ does not vary with q_z, and is repeated in 2D momentum space with the periodicity of $\boldsymbol{q}_\mathrm{m}$. In order to to fit the model to the constant-energy cuts, I first calculated the cross section (Eq. 3.1) in three dimensions. For each iteration of the least square algorithm, a numerical *powder average* was then performed over constant-Q spheres, also taking into account the experimental Q resolution.

The DHO model contains three physical parameters that were allowed to vary (Γ^*, $v_\parallel$, $v_\perp$), along with an intensity scale factor and a linear background. The results determined from the fit are $\Gamma^* = 0.13 \pm 0.06$, $v_\parallel = 460 \pm 120$ meVÅ and $v_\perp = 150 \pm 20$ meVÅ. The anisotropy ratio $v_\parallel / v_\perp \approx 3$ obtained from this analysis is statistically significant. Spectra simulated with the best-fit parameters are shown as blue lines in Fig. 3.6(b) and as a colour map in Figs. 3.5(c,d). The simulations match the peak at $Q = 1.2$ Å^{-1} and closely reproduce the observed dispersion of the signals centred near 2.6, 3.5 and 4.5 Å^{-1}. The model parameters are similar to those found for $Ba(Fe_{1-x}Co_x)_2As_2$: $\Gamma^* = 0.15$, $v_\parallel = 580$ meVÅ, $v_\perp = 230$ meVÅ [387].

Despite the limitations inherent in powder-averaging, the success of the model in accounting for features in the data over several Brillouin zones places a tight constraint on the wave vector $\boldsymbol{q}_\mathrm{m}$ that describes the dominant mode of paramagnon excitations in FeSe. To determine how tightly $\boldsymbol{q}_\mathrm{m}$ is constrained by the data, I carried out fits with the damped spin-wave model modified to have $\mathbf{q}_\mathrm{m} = (\pi, \xi)$, as suggested by some theoretical studies. To perform a simple test, I modified the periodicity in reciprocal space of $\chi''(\boldsymbol{q}, \omega)$ (for the DHO model) accordingly (see Fig. 3.4). I then fitted the model to the data for $0 \leq \xi \leq \pi/2$, while constraining for simplicity the spin-wave velocity to be isotropic.

Figure 3.6(c) shows the best fit that could be achieved with this modified DHO model, which was with $\xi \approx \pi/4$. The fit is not as good as the DHO model with anisotropic velocity and $\boldsymbol{q}_\mathrm{m} = (\pi, 0)$. The discrepancies are most noticeable for the signal near 2.6 Å^{-1} at low energies. The reason for this is illustrated by the schematic of reciprocal space shown in Fig. 3.4. The unmodified DHO model (red markers) converges at low energies to $\boldsymbol{q}_\mathrm{m} = (\pi, 0)$ and equivalent points, whereas the *modified* DHO model dispersion converges to two points at $\boldsymbol{q}_\mathrm{m} = (\pi, \pm\pi/4)$, and equivalent positions (green markers). Therefore, in a powder-averaged spectrum, at low energies the anisotropic model will show a rise in intensity at $Q = 2.64$ Å^{-1} corresponding to $\boldsymbol{q}_\mathrm{m} = (\pi, 2\pi)$, whereas the isotropic model will show a rise in intensity at $Q = 2.38$ Å^{-1}, corresponding to $\boldsymbol{q}_\mathrm{m} = (\pi, 7\pi/4)$. To illustrate this effect more directly, I show in Fig. 3.6(a) the intensity distribution in 2D momentum space for the two choices of $\boldsymbol{q}_\mathrm{m}$, calculated for energy ranges that correspond to the momentum-transfer cuts in 3.6(b).

Strictly speaking, the DHO spin-wave model applies to systems with short-range magnetic order. The justification for applying it to FeSe is that there are strong magnetic correlations, which means that the spins will appear ordered over sufficiently short distances and time scales. Therefore, above some crossover energy scale the spectrum is expected to be very similar to that of a system whose spins are ordered with propagation vector $\boldsymbol{q}_\mathrm{m}$ and whose excitations are propagating damped spin waves.

An alternative approach is to employ a description that does not imply any magnetic order in the ground state. Such a phenomenological model was used by Tucker *et al.* to analyse neutron scattering data on superconducting $Ba(Fe_{1-x}Co_x)_2As_2$ with $x = 0.047$ [386]. This model is designed to capture the diffusive nature of the spin dynamics inherent in a paramagnet while at the same time allowing spatial and temporal magnetic correlations. The corresponding imaginary part of the dynamic magnetic susceptibility is modified to

$$\chi''(\boldsymbol{q},\omega) \propto \frac{\Gamma_{\mathbf{q}}\hbar\omega}{(\hbar\omega)^2 + \Gamma_{\mathbf{q}}(1+\xi_{\mathbf{q}}^2 q^2)^2} \quad , \tag{3.4}$$

with momentum-dependent correlation lengths $\xi_{\mathbf{q}}$ and relaxation rates $1/\Gamma_{\mathbf{q}}$:

$$\begin{aligned} \xi_{\mathbf{q}}^2 q^2 &= \xi_{\parallel}^2 q_{\parallel}^2 + \xi_{\perp}^2 q_{\perp}^2 \\ \Gamma_{\mathbf{q}} &= \Gamma + \frac{\alpha^2}{\Gamma}\left(\Gamma_{\parallel}^2 q_{\parallel}^2 + \Gamma_{\perp}^2 q_{\perp}^2\right) \end{aligned} \tag{3.5}$$

This *diffusive* model thus has *five* physical parameters ($\xi_{\parallel}$, $\xi_{\perp}$, $\Gamma_{\parallel}$, $\Gamma_{\perp}$, α). These are related to the reduced parameters used by Tucker *et al.* [386] by

$$\begin{aligned} \xi_{\parallel}^2 &= \xi^2(1+\eta_{\xi}) \ , & \xi_{\perp}^2 &= \xi^2(1-\eta_{\xi}) \ , \\ \Gamma_{\parallel}^2 &= \Gamma^2(1+\eta_{\Gamma}) \ , & \Gamma_{\perp}^2 &= \Gamma(1-\eta_{\Gamma}) \end{aligned} \tag{3.6}$$

In Eqs. 3.4 and 3.5, $\boldsymbol{q} = (q_{\parallel}, q_{\perp})$ is the reduced wave vector measured relative to a magnetic wave vector, i.e. $\boldsymbol{q} = 0$ is at $\boldsymbol{q}_{\mathrm{m}}$. The components $q_{\parallel}$ and $q_{\perp}$ are parallel and perpendicular to the vector joining $\boldsymbol{q}_{\mathrm{m}}$ to the nearest reciprocal lattice vector, e.g. for $\boldsymbol{q}_{\mathrm{m}} = (\pi, 0)$, $q_{\parallel}$ and $q_{\perp}$ are components parallel and perpendicular to $\boldsymbol{q}_{\mathrm{m}}$. At low energies this model describes an elliptical intensity distribution centred on $\boldsymbol{q} = 0$, with $q_{\parallel}$ and $q_{\perp}$ as the principal axes of the ellipse. $\chi''(\boldsymbol{q},\omega)$ is repeated in 2D momentum space at each of the 2D wave vectors $\boldsymbol{q}_m$.

The best fit of the diffusive model to the data was obtained with parameters $\xi_{\parallel} = 7 \pm 2$ Å, $\xi_{\perp} = 1.5 \pm 0.8$ Å, $\Gamma_{\parallel} = 0$ meV, $\Gamma_{\perp} = 7 \pm 5$ meV and $\alpha = 7 \pm 5$ Å. The parameter $\Gamma_{\parallel}$ was not well controlled and had little effect on the fit. The large difference between $\xi_{\parallel}$ and $\xi_{\perp}$ means that the intensity distribution is highly anisotropic, consistent with what was found with the DHO model. Spectra simulated with the best-fit parameters of the diffusive model are shown in Figs. 3.6(d,e) and 3.5(e,f). As for the DHO model, the simulated Q cuts match the data well when $\boldsymbol{q}_{\mathrm{m}} = (\pi, 0)$ (Fig. 3.6(d)), but less well for $\boldsymbol{q}_{\mathrm{m}} = (\pi, \pm\pi/4)$ (Fig. 3.6(e)). The main conclusions are, firstly, that the phenomenological diffusive model provides a good description of the magnetic dynamics of FeSe, and secondly, that the analysis with the diffusive model reinforces the findings from the DHO spin-wave model analysis that FeSe is close to an instability towards $(\pi, 0)$ antiferromagnetism and has highly anisotropic magnetic correlations.

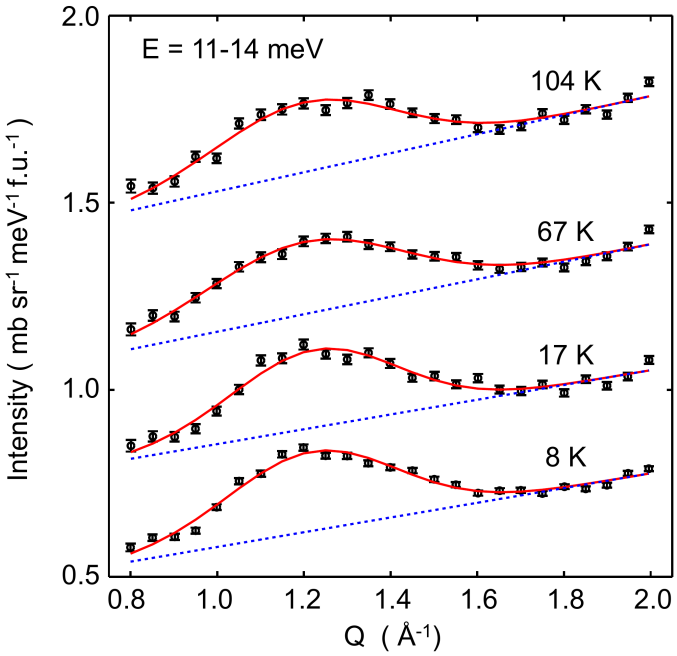

Figure 3.7: Temperature dependence of the magnetic scattering at $(\pi,0) \approx 1.2\,\text{Å}^{-1}$ averaged over the energy range $11-14\,$meV. The solid lines are fits to a Gaussian function on a linear background (dotted). The upper three scans are offset vertically by 0.25, 0.5 and 0.75 units, respectively.

Using the closed-cycle refrigerator at MERLIN, it was not possible to cool the sample below 8 K, and thus I did not study the magnetic signal in the superconducting state ($T_c \approx 8\,K$) at low energies, where a neutron spin resonance could be expected (see Section 1.1.4). Instead, I investigated the influence of the structural transition on the magnetic response by performing runs with an incident energy $E_i = 50\,$meV at temperatures of 8, 17, 67 and 104 K.

Figure 3.7 shows Q cuts through the $(\pi,0)$ position at each temperature. The data are averaged over the energy interval from 11 to 14 meV to stay within the window where phonon scattering is weak. The magnetic peaks show very little variation with temperature. To quantify this, I fitted a Gaussian function on a linear background to each cut. To within the fitting error, the integrated intensity remains constant at $0.10 \pm 0.01\,\text{mb}\,\text{sr}^{-1}\,\text{meV}^{-1}\,\text{Å}^{-1}\,\text{f.u.}^{-1}$, which compares with the value 0.08 ± 0.01 found at the same energy for LiFeAs at $T = 20\,\text{K} > T_c$ [385]. This shows that the spin fluctuations in FeSe have a similar strength to those in other Fe-based superconductors.

3.3 Resonant inelastic x-ray scattering at ID32, ESRF

3.3.1 Characterization of single-crystalline sample

High quality single crystals of tetragonal (space group *P4/nmm*) β-FeSe were synthesized by my colleague Dr. Amir-Abbas Haghighirad[5] using a KCl-$AlCl_3$ vapour deposition technique [388]. The Fe–Se system has a complex metallurgical phase diagram [389]. In particular, the 1:1 tetragonal β-phase does not crystallize from the melt and so its preparation had been a long-standing challenge. The growth from the gas phase avoids this issue and produces small crystallites of very high quality (see Fig. 3.8(a,b)).

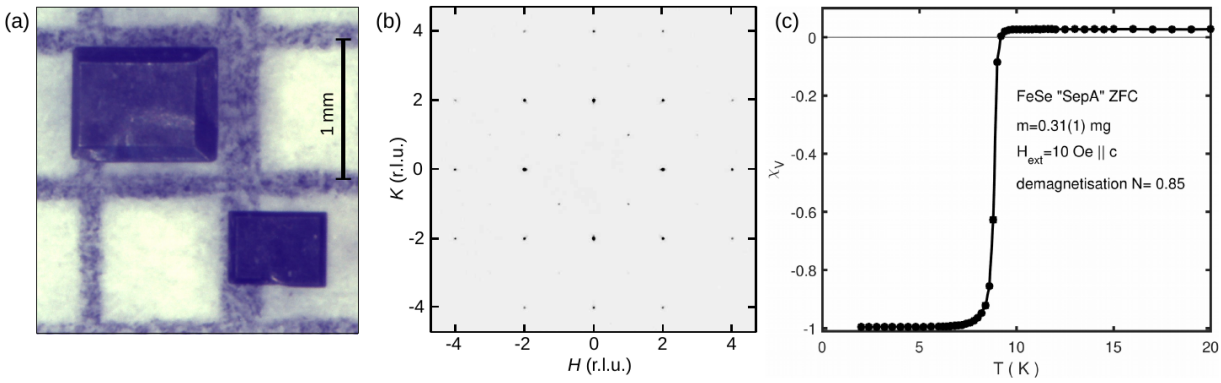

Figure 3.8: (a) β-FeSe single crystals grown by the vapour deposition technique. The crystallites have dimensions on the order of $1\,\mathrm{mm}^2$, $\approx 200\,\mu\mathrm{m}$ thickness, and masses of $< 1\,\mathrm{mg}$. (b) $(HK0)$ reciprocal space intensity map integrated from a Mo-K_α four-circle x-ray diffraction dataset. (c) SQUID magnetometry of the single crystal investigated by inelastic x-ray scattering, with a clean superconducting transition at $T_c \approx 8\,\mathrm{K}$.

I characterized a number of such FeSe single crystals by four-circle Mo K_α single-crystal x-ray diffraction (see Section 2.1.3) to select a specimen of highest crystalline quality. The crystals generally grow as rectangular platelets and x-ray diffraction revealed that their edges are parallel to the tetragonal unit cell. Figure 3.8(c) shows an example of laboratory x-ray data, with intensity integrated over a margin perpendicular to the $(HK0)$ plane of reciprocal space. The negligible spread of the Bragg reflections confirms the high intrinsic crystalline quality. As the material is relatively soft, the platelets easily bend, which causes imperfections in the vertical stacking of the atomic planes. In x-ray diffraction, this can be quantified by the mosaic spread of Bragg reflections along the $(00L)$ direction (not shown).

For selected crystallites, I performed SQUID magnetization measurements (see Section 2.1.1) to confirm the onset of ideal diamagnetism associated with superconductivity (the Meissner-Ochsenfeld effect). The zero-field-cooled temperature sweep in Fig. 3.8(b) shows this

[5] Clarendon Laboratory, Department of Physics, University of Oxford, Oxford OX1 3DW, UK

abrupt expulsion of the magnetic field (10 Oe) at the superconducting critical temperature at $T_c \approx 8\,\mathrm{K}$.

3.3.2 Experimental setup

As described in Section 2.4, the excitation of electric dipole transitions of electrons from $2p$ core levels to the correlated d-orbitals can strongly enhance the resonant part of the x-ray scattering cross section (Eqs. 2.61 and 2.55). Resonant inelastic x-ray scattering (RIXS) at transition metal L edges has proven to be a powerful tool for the study of electronic correlations in cuprate high temperature superconductors [390, 391, 392, 393]. This success has motivated the development of a new generation of spectrometers [394]. Naturally, it is of interest to extend the application of this technique beyond the Cu $3d^9$ states in cuprates. In the present context, one key advantage is that the highly focused beams obtained from undulator devices enable experiments with minute samples ($< 100\,\mu\mathrm{m}$).

I performed a single crystal RIXS study of FeSe at beamline ID32 at the European Synchrotron Radiation Facility (ESRF) [340]. The RIXS endstation of this beamline, which had been commissioned only few months before this experiment, offers an unprecedented energy resolving power of up to $E/\Delta E = 30000$ (a quantity that is generally limited by count rate of the scattered signal). The extreme brilliance of the beam and sensitivity of the detector notwithstanding, the weakness of the inelastic signal is the main limiting factor — especially in the case of partly delocalized valence states, as in FeSe. Here, most of the observed RIXS spectral weight is due to excitations into the continuum of itinerant states. In the present experiment, the intensity which may be due to magnetic excitations contributed less than one photon per minute to the spectra (for an estimated flux of 10^{14} photons per second at the sample position). In a compromise for intensity, the spectrometer had to be used in a "low resolution" configuration of $E/\Delta E \approx 14000$. At the Fe L_3 edge (707 eV), this corresponds to an energy resolution of 50–60 meV (FWHM).

Figure 3.9 illustrates the instrumental setup at ID32. The beam enters the hutch from the right-hand side (not seen) and scatters from the sample, which is mounted on a four-cicle goniometer inside the ultra-high vacuum (UHV) vessel seen on the left hand side. After scattering from the sample, the outgoing beam is collimated by a mirror, dispersed by a spherical grating and then imaged using a CCD detector placed in the focus of the grating. The $\approx 11\,\mathrm{m}$ long detector arm can be rotated over a 100° range of scattering angle. To minimize the attenuation of the soft x-ray beam, the beam pipes form an uninterrupted vacuum which contains both undulator and detector.

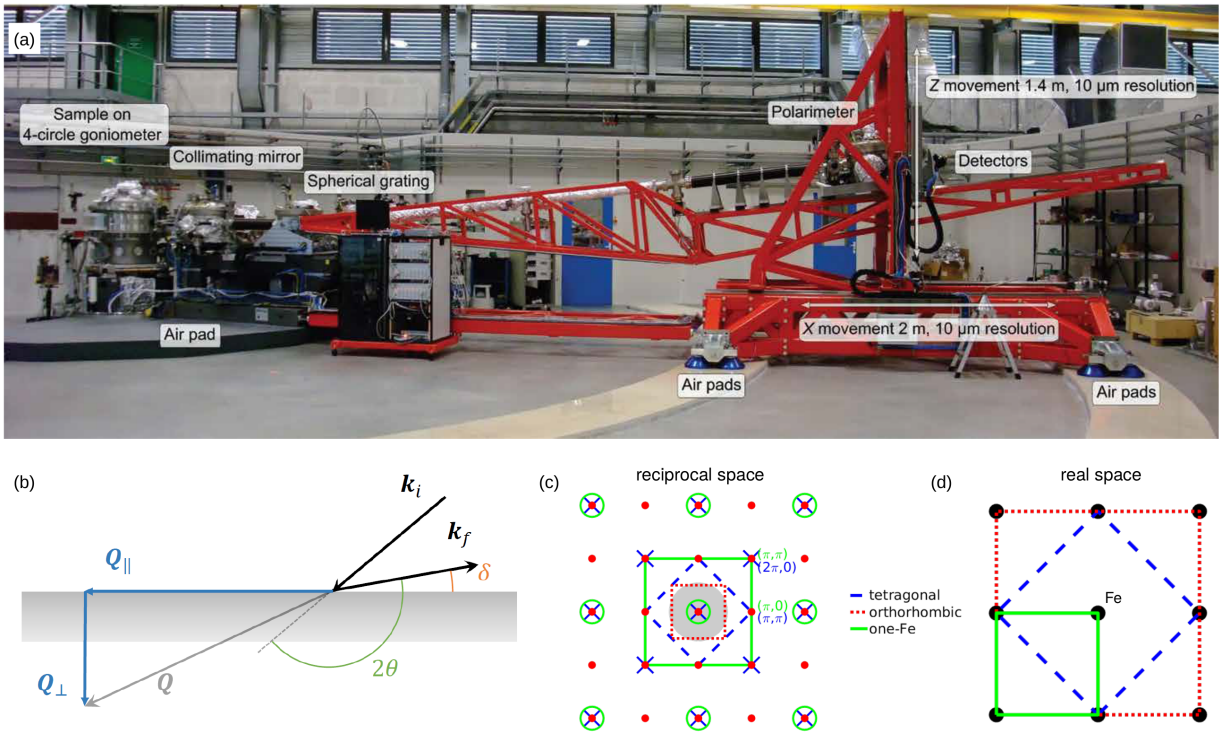

Figure 3.9: (a) The RIXS endstation of beamline ID32, ESRF (from [340]). (b) Schematic of the RIXS scattering geometry commonly used to probe samples with quasi-two-dimensional electronic states. (c) Conventions for labelling the Brillouin zones of iron-based superconductors. The range of in-plane momentum transfer $Q_\parallel$ accessible at the Fe L_3 edge is indicated as a gray circle. (d) The corresponding definition of unit cells in real space square iron lattice.

When exposed to air, FeSe crystals quickly tarnish. Before the RIXS measurement, a surface layer was therefore stripped from the sample using adhesive tape. This revealed a clean, mirror-like surface. The sample was then immediately transferred to the UHV tank. Inside this sample chamber, the copper sample carrier is mounted on a four circle goniometer, which is connected to the cold finger of a helium flow cryostat via copper braids. Throughout the experiment, the temperature of this sample stage was held at the base temperature of 21 K. The sample holder also is also connected to an ampere meter which allows to measure the drain current or *total electron yield* (TEY) during irradiation. This quantity is usually proportional to the x-ray fluorescence (or absorption) of the sample surface. The beam size at the sample position is $4 \times 60\,\mu\mathrm{m}^2$.

Due to the thermal expansion of the liquid-nitrogen-cooled CCD detector, the position of the image on the chip drifted over time. I therefore collected the data in short cycles of 2.5–5 minutes. Tens of such short scans comprising one RIXS spectrum are then calibrated and centred with respect to each other using the quasielastic line as reference. The amount of thermal drift within the minimal exposure time that is required to obtain adequate counting statistics on the quasielastic line is an additional limiting factor to the energy resolution of the experiment.

Soft x-rays are on the border of what can be considered a probe of the bulk of the sample. With the incident x-ray energy tuned to the Fe L_3 edge ($E_i = 706.8\,\mathrm{eV}$, $\lambda = 17.54\,\text{Å}$), the penetration depth into FeSe is on the order of $\approx 200\,\mathrm{nm}$. The scattering triangle of the present experiment is drawn in Figure 3.9 (c), which corresponds to a top-view of the instrument. Since the magnetic fluctuations are assumed to be purely two dimensional, the momentum transfer perpendicular to the sample (parallel to the c axis) is neglected. Instead, only the in-plane momentum transfer $Q_{\parallel}$ is considered. The range of $Q_{\parallel}$ is limited by the fixed incident energy, the maximum scattering angles (here, $2\theta_{\mathrm{max}} = 150^{\mathrm{o}}$), and the minimum grazing angle δ. The accessible regime is marked as a grey circle in Fig. 3.9(c).

I aligned the crystal using the specular (001) reflection, which was only accessible by increasing the incident energy to 1.7 keV. Since no other Bragg reflection is accessible as a second reference, I aligned the azimuth of the sample by half-cutting the beam with one edge of the quadratic platelet (which is parallel to a $\langle 100 \rangle$ direction of the tetragonal cell).

3.3.3 Results

I collected RIXS spectra up to energy-transfers of $\approx 3.5\,\mathrm{eV}$ for a number of momentum transfers $Q_{\parallel}$ along the (100) and (110) crystallographic directions. As an example, the

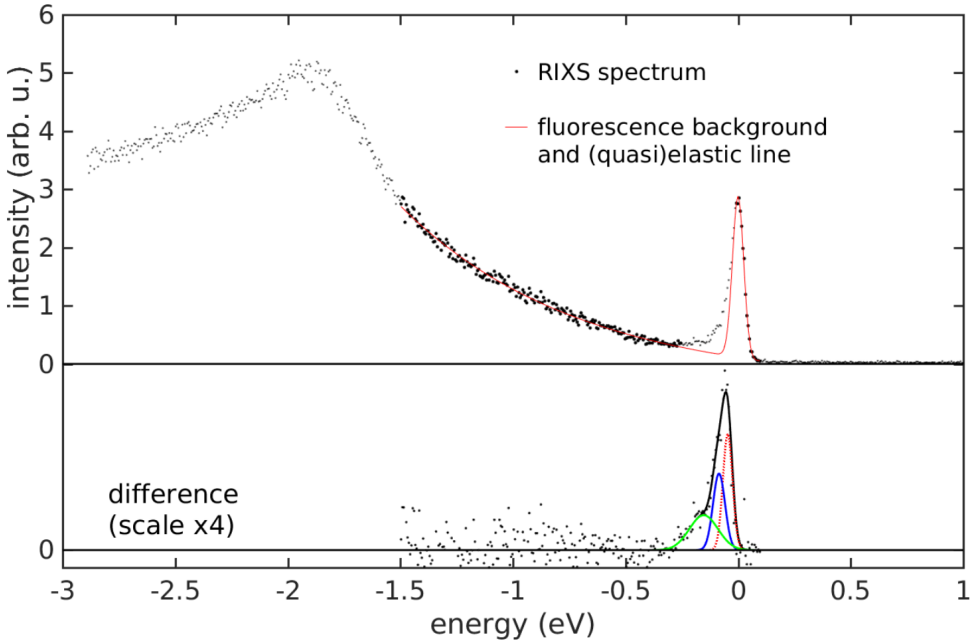

Figure 3.10: Example of a β-FeSe L_3 RIXS spectrum, recorded at $Q_{\parallel} = 0$. The top panel shows the summed and calibrated data measured over a total of eight hours. The fit of the sloping fluorescent background and quasielastic line is drawn as a red line (fitted data indicated by thick black markers). The lower panel shows a magnified view of the difference signal, fitted by several Gaussian contributions as detailed below in Figs. 3.12 and 3.13.

RIXS spectrum at $Q_{\parallel} = 0$, collected over a total of eight hours, is shown in Figure 3.10. Apart from the atomic-like excitations of interest (below $E \leq 400\,\text{meV}$), each spectrum contains a quasielastic peak and is dominated by the *fluorescent background* due to excitations of the continuum of itinerant states.

In experiments with previous generation soft RIXS spectrometers, it had already been observed that the Fe L_3 RIXS spectra of iron based superconductors are generally dominated by this broad feature, peaked at several eV energy transfer [50]. This is due to the tetrahedral environment of the Fe ions, which allows a hybridization of Fe $3d$ states with empty $4p$ bands [395]. By contrast, such excitations are not observed in Cu L_3 RIXS studies of cuprate superconductors, where the $3d$ states are octahedrally coordinated and remain more localized [392]. The detailed shape of this resonant x-ray fluorescence has been studied in the related system $Fe_{1.087}Te$ [396]. Here, it was established that the fluorescent slope at low energy transfers and its decay (up to energy transfers of $\approx 10\,\text{eV}$) may yield characteristic information about the low temperature Fermi liquid state of metallic samples.

In the present context, continuum electronic excitations are not of direct interest, but only add to a background signal which partly obscures the spin-flip excitations. As a minimal phenomenological model for the fluorescent background and quasielastic scat-

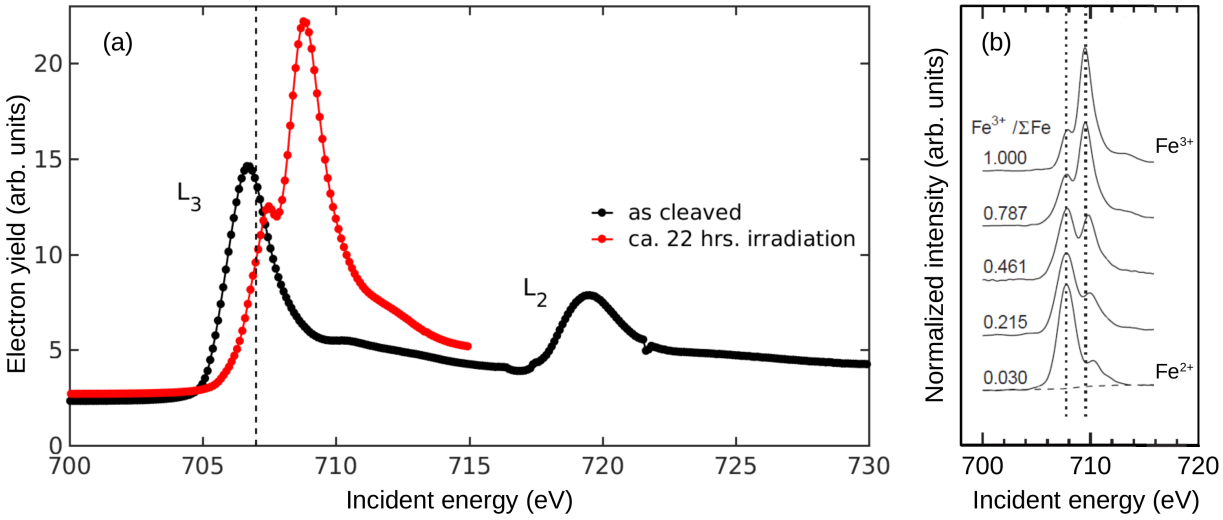

Figure 3.11: Deterioration of the sample surface by x-ray irradiation. (a) TEY spectra at the beginning of the experiment and after several hours of irradiation. (b) (adapted from [397]) *L*-edge electron energy-loss near-edge spectra for various mixed-valent minerals, which illustrate the evolution from the Fe^{2+} to the Fe^{3+} oxidation state.

tering, I fitted and subtracted the following function from the RIXS spectra, as indicated by the red line in Figure 3.10 (upper panel):

$$I(\hbar\omega) = c_1 + c_2 \cdot (1/2)^{(2\hbar\omega/\alpha_1)^2} + \left(c_3 + c_4 \cdot (e^{-\alpha_2 * \hbar\omega} - 1)\right) \cdot \frac{1}{e^{\hbar\omega/\alpha_3} + 1} \tag{3.7}$$

This contains a constant background, a Gaussian peak centred at $\hbar\omega = 0$, a stretched exponential decay function and an intensity cutoff at $\hbar\omega = 0$ (c_i are scale constants and α_i determine the slope of the background and the widths of the Gaussian and cutoff). To ensure a fit to the relevant part of the spectral weight I excluded the regime with relevant atomic-like excitations from the fit (from -300 to -10 meV). The FWHM of the fitted Gaussian peak was *not* constrained to the *intrinsic* width of elastic reference measurements. Therefore, the remaining difference signal does not represent the full excitation spectrum but may be overcompensated for low-energy excitations adding to the quasielastic line. This applies in particular to those data obtained at a scattering angle $2\theta = 90$: Given the polarization factor of Eq. 2.48), Thomson scattering vanishes in this setting — yet the spectra feature a sizeable Gaussian peak at $\hbar\omega = 0$. Moving the detector arm away from the $2\theta = 90$ condition in small steps revealed that this low energy inelastic intensity is indeed centred at the position of the then emerging elastic line.

The difference spectra thus obtained are summarized in Fig. 3.12 for momentum transfers along the (π,π) direction in the one-Fe lattice and in Fig. 3.13 for the $(\pi,0)$ direction. In all cases, residual RIXS intensity is observed up to energies of ≈ 300 meV. Moreover,

the spectra show significant structure and show some weak dispersive trends. To quantify these effects, I fitted the data with three Gaussian peaks, indicated as red, blue and green lines. The dispersion of these features is indicated in panels (f) of Figs. 3.12 and 3.13 in the corresponding colours.

As an important caveat, the details of these difference spectra shown here are correlated to the choice and fit of the background function, Eq. 3.7. The energy-calibration and alignment of individual spectra can act as an additional source of small systematic errors (varying approaches of calibration and alignment however do not shift or broaden the composite spectra by more than a few meV). Overall, this implies some limit on the amount of information that can reasonably be interpreted into the difference spectra. Nevertheless, the presence of additional spectral weight in the energy-range up to 300 meV and a weak dispersive trend of this signal are features that are relatively independent of any assumptions made in the processing of the raw data.

An additional source of uncertainty comes from possible irradiation damage to the sample. Even though the experiment was performed under UHV conditions and at ≈ 20 K, the chemical reactivity of FeSe proved to be an issue in RIXS. All data were obtained at an incident energy of 707 eV, which is slightly above the Fe L_3 edge. Incident-energy scans of the total electron yield (TEY) over this absorption edge changed to over time with beam irradiation. As shown in Fig. 3.11, the spectrum of the pristine sample surface is peaked at a 707 meV. After few minutes of irradiation, a hump at ≈709 meV begins to gain in in spectral weight and the overall electron yield increases. After several hours of irradiation, the feature at ≈709 meV saturates. I confirmed that the same characteristics were also observed in the x-ray absorption spectrum, which suggests that it is not merely a surface effect. Moving the beam to a different position on the sample surface readily restored the original features.

The iron L_3 absorption edge characteristics of fluorides, oxides and covalent compounds have recently been reviewed by Miedema *et al.* [398]. Across various compounds, it is seen that the second peak (2 meV above the first L_3 edge peak) is a general feature of the Fe^{3+} oxidation state. The variation of electron energy loss spectroscopy (EELS) characteristics between minerals of varying Fe^{3+} / Fe^{2+} proportion has been studied by van Aken *et al.* [397] (reproduced in Figure 3.12(b)). This implies that some of the sample volume probed in this experiment may have been altered by the beam, possibly locally forming an Fe^{3+} compound such as Fe_2O_3 or Fe_2Se_3.

These observations call into question the validity of the present results, as some of the extracted signal presented in Figs. 3.12 and 3.13 could arise from near-surface electronic states which are altered during the measurement. Additional test measurements were

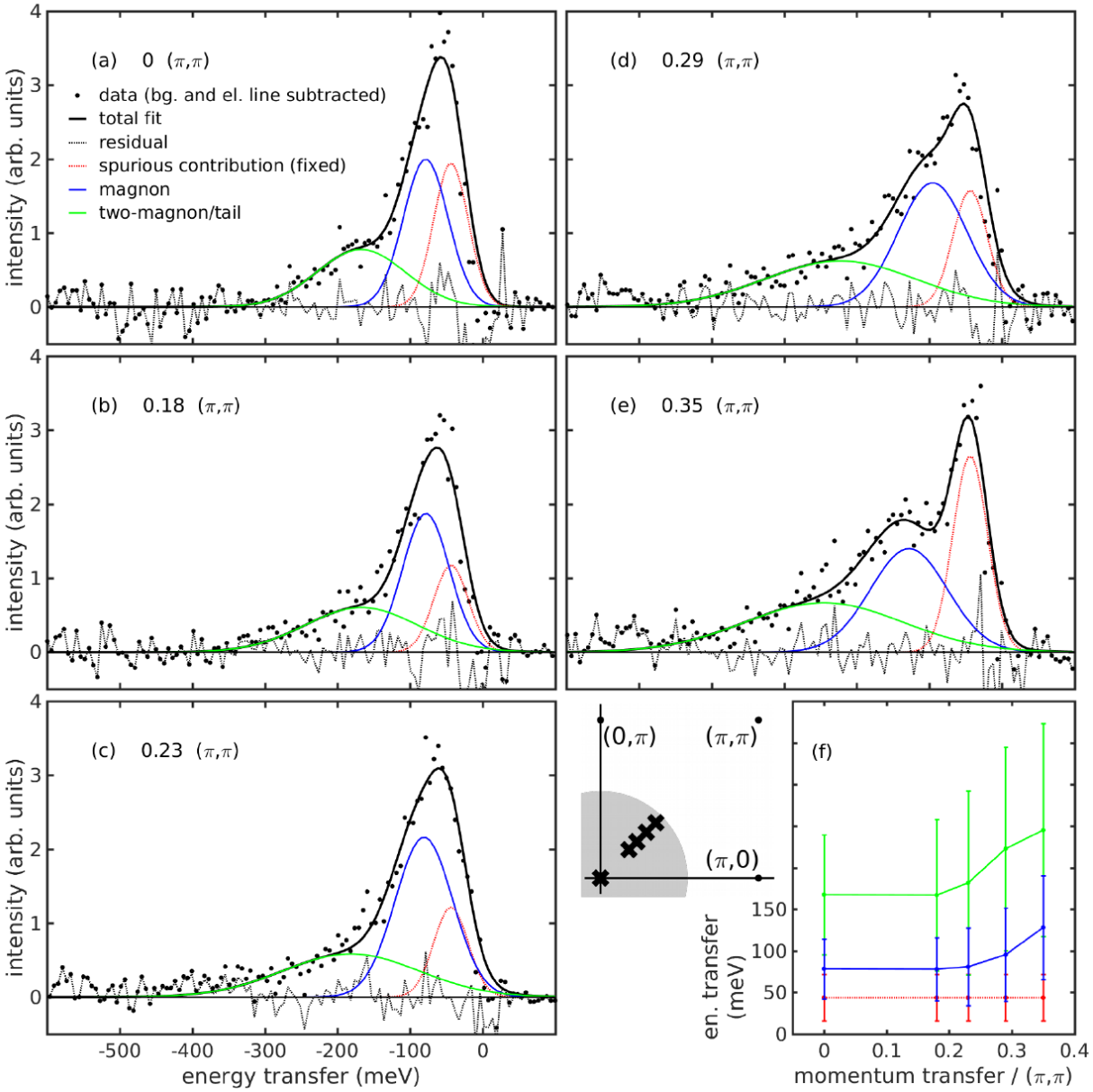

Figure 3.12: (a-e) Background-subtracted β-FeSe L_3 RIXS spectra for momentum transfers along the (π,π) direction (black markers). A phenomenological fit by three Gaussian peaks is indicated by red, green and blue lines. (f) The energy of and widths at half-maximum of these contributions, indicated in corresponding colours. The inset shows a map of the $(HK0)$ plane of reciprocal space with markers et the momenta $Q_{||}$ measured here.

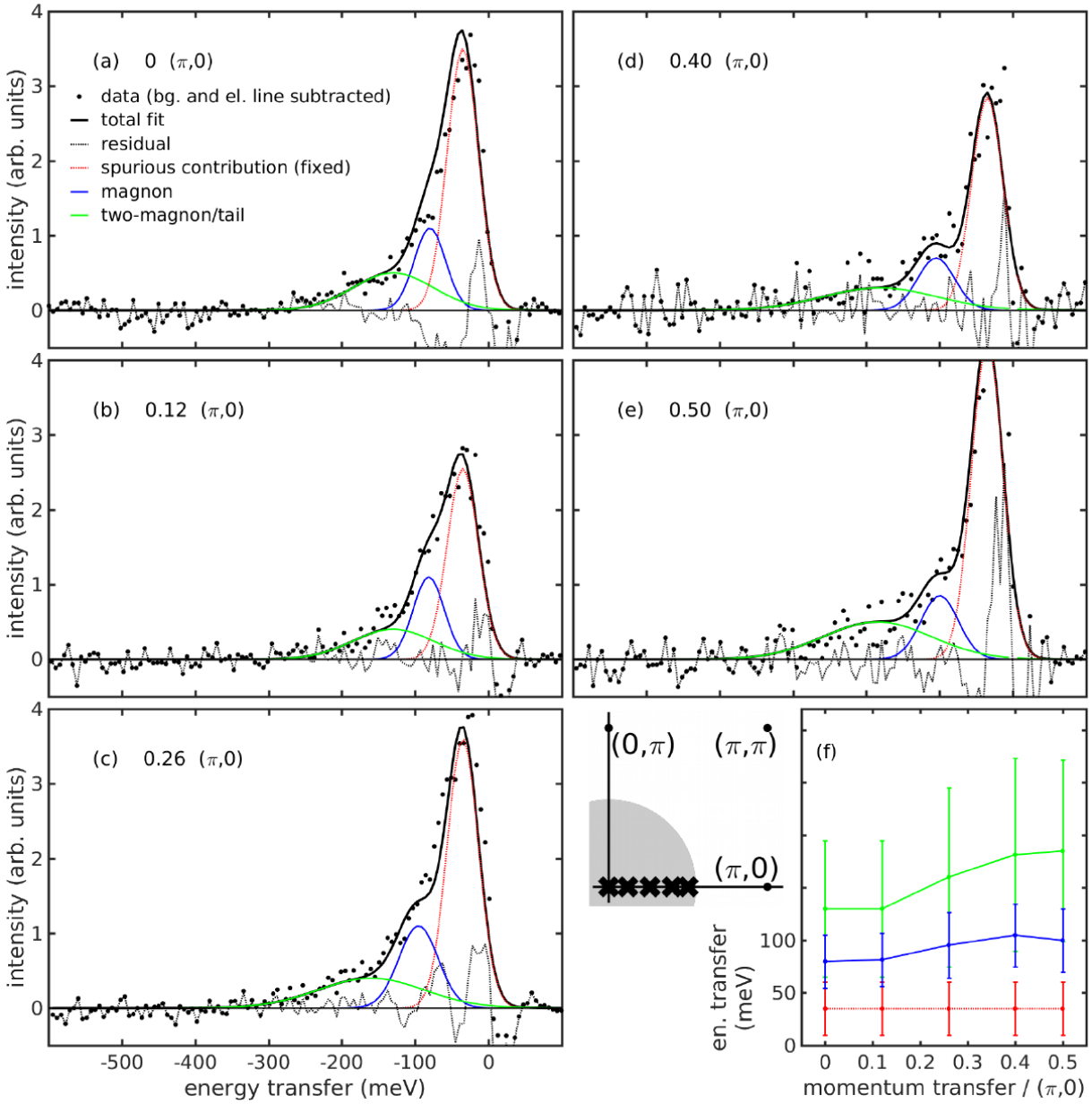

Figure 3.13: Background-subtracted β-FeSe L_3 RIXS spectra for momentum transfers along the $(\pi,0)$ presented as in Fig. 3.12.

therefore performed in a second experimental session[6], using a different crystallite. In this follow-up experiment, the beam position was moved in steps along a straight trajectory on the sample surface after every 10 minutes of irradiation. Due to the minute vertical beam dimension ($\approx 4\,\mu$m), this is feasible even for small sample dimensions. TEY spectra recorded every 10 minutes did not show indications of deterioration. This confirms that Fe^{2+} states were probed throughout this second experiment.

Such reference measurements were obtained for $Q_{\parallel}$ =0, 0.18 and 0.35 (π,π). In these spectra, the dispersive feature around 150 meV, with a broad tail up to $\approx$ 300 meV was well reproduced. On the other hand, the low energy contributions peaked around 40–50 meV (marked by red lines in Figs. 3.12 and 3.13) are absent in the revised spectra. The clear separation of these contributions suggest that the higher-energy features (marked by blue and green lines) are intrinsic to pristine FeSe.

3.3.4 Discussion

Soft RIXS studies of cuprates are already well established, as recently reviewed by Dean [394]. By contrast, only a few such experiments have been reported for iron based superconductors (IBSCs) [50, 396, 399, 395]. Due to the lower resolution (≈200–700 meV FWHM) of the previous generation of spectrometers, these studies focused on eV-scale excitations, such as *dd* [50] transitions and the fluorescence peak [396]. Previous experiments avoided the complications of soft-xrays by studying the Fe K edge ($\approx$ 7 keV) [399, 395] or "suppressed" the fluorescence background by choosing the least itinerant IBSCs [395]. In terms of high-resolution Fe L_3 RIXS, only one study, of the (Ba,K)Fe_2As_2 system, has been reported, by Zhou *et al.* [400].

The experiment by Zhou *et al.* had been performed on a similar spectrometer, with a slightly inferior energy resolution (≈80 meV FWHM) [400]. Both the parent $BaFe_2As_2$ and the "optimally doped" (40% K doping, $T_c = 39$ K) compound were investigated. All key features of these results, reproduced in Fig. 3.14, resemble the present results on FeSe. The subtraction of background and quasielastic line leaves a broad peak around 150–200 meV with a tail extending up to 300 meV. As in FeSe, the features weakly disperse towards higher energies as $Q_{\parallel}$ increases. The magnetic RIXS response of $BaFe_2As_2$ shown in Fig. 3.14 just appears to be stronger and better defined than in the present dataset, as expected for a more localized system with static magnetic order.

The modelling of RIXS spectra is presently a theoretical challenge, and it is not straightforward to distinguish between a range of possible energy transfer mechanisms. For example, spectral weight in the present energy range of interest may also be due to tran-

[6] Courtesy of Dr. Kurt Kummer, ESRF

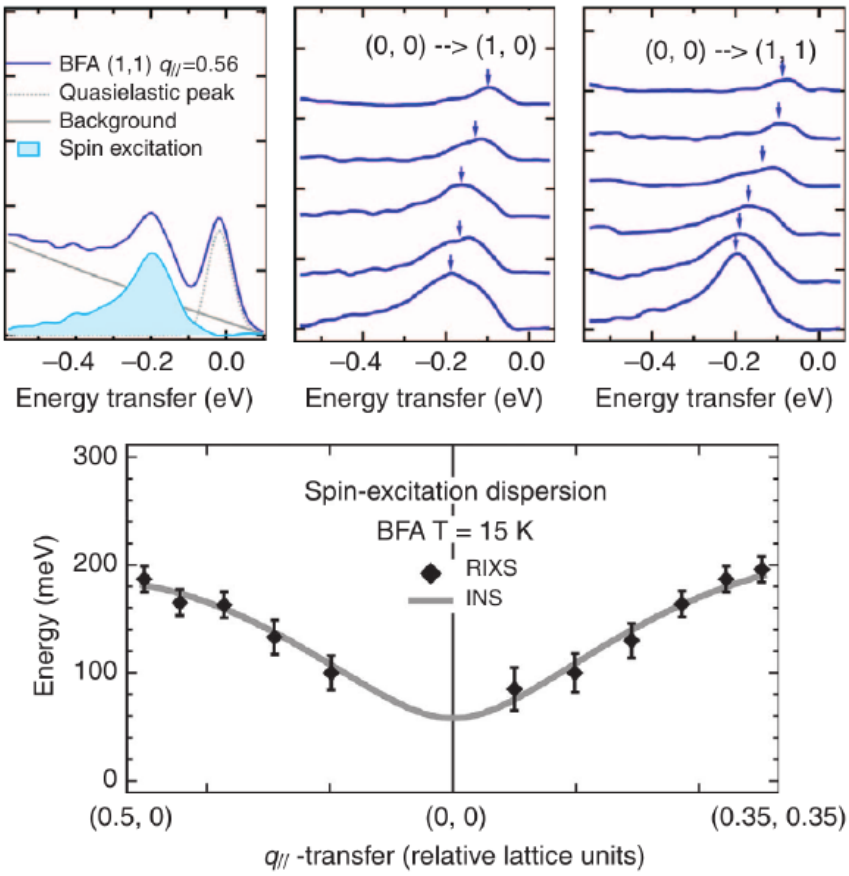

Figure 3.14: High resolution Fe L_3 RIXS spectra recorded in the low-temperature, magnetically ordered phase of the "122" parent compound $BaFe_2As_2$ (see Section 1.1), as reported by Zhou *et al.* [400]. The data closely resemble the present results on FeSe.

sitions between d-electron levels ("dd excitations") [50], as well as to higher harmonics of phonon scattering [303]. Zhou *et al.* confirmed the magnetic origin of this signal by its weakening above T_N and by direct comparison to the dispersion obtained from single crystal neutron spectroscopy (see Fig. 3.14, bottom panel). As FeSe does not order magnetically and high quality single crystal neutron data is not available for this range of momentum transfer, neither is possible in the present case.

In summary, the data presented in Figs. 3.12 and 3.13 is likely to describe dispersing high-energy paramagnon fluctuations. The observed line-width of these excitations (>100 meV) is much broader than the instrumental resolution, consistent with diffuse excitations in a broad Stoner continuum. Although the signal obtained from FeSe is much weaker, the resemblance with the results obtained in the magnetically ordered phase of the 122 parent compound $BaFe_2As_2$ is striking. Even though no static order is found in its magnetic phase diagram, the ground state of FeSe appears to feature short-range spin correlations of a similar bandwidth as in the more "conventional" arsenide family of IBSCs.

3.4 Conclusion

In the neutron part of this study, I established that the collective spin fluctuations in FeSe share many similarities with those in the high-T_c Fe arsenide superconductors, including a very steep dispersion and a low frequency response that is strongest at or very close to the square lattice wave vector $(\pi,0)$. I found no direct evidence for competing magnetic orders, although the highly anisotropic spin-wave velocity implies a greater tendency for transverse spin fluctuations.

Since the publication of these results [381], three single crystal INS studies have been reported [368, 401, 402]. To achieve a measurable magnetic response, up to 700 crystallites, equivalent to the sample used in my RIXS study, were co-aligned for these experiments [402]. With incident energies between 8 meV [368] and 475 meV [402], these studies complement the energy range of my powder experiment. Notably, the single crystal data confirm all information that I inferred from the powder data. This includes (1) the wave vector of the low energy spin fluctuations, $\boldsymbol{q}_m = (\pi,0)$, (2) the anisotropy of the magnetic dispersion, (3) the fact that the strength of the dynamic magnetic susceptibility of FeSe is of similar magnitude as in iron arsenide superconductors, and (4) the absence of significant renormalization of the dynamic magnetic susceptibility at the structural transition at $T_s = 90$ K.

One key additional insight gained from single crystals comes from the high-energy study by Wang *et al.* [401]. While the stripe-type $(\pi,0)$ fluctuations are dominant in this data, weak additional low-energy features centred at (π,π) were observed at high temperatures $T > T_s$ (see Fig. 3.15). This may indicate a competition between stripe- and Néel type correlations. The orthorhombic distortion at T_s may then play the role of favouring the stripe-like fluctuations (which also break C_4 symmetry). To confirm the relevance of the weak (π,π) instability to the superconducting mechanism, it would be of great interest to perform similar studies of samples that have been tuned to higher T_c, e.g. by application of pressure, or electron doping.

Secondly, by use of a high-flux triple-axis neutron spectrometer and a small incident energy of 8 meV, the same authors were able to distinguish a neutron magnetic resonance peak in the superconducting phase of FeSe [368]. This manifested as a re-distribution of low-energy $(\pi,0)$ spectral weight to a resonance peak centred at 4 meV $\approx 5.3\,k_B T_c$. As discussed in Section 1.1.4, this feature is associated with sign-changing $s_\pm$ symmetry of the superconducting gap function and is seen as strong evidence for spin-fluctuation mediated Cooper pairing.

If spin fluctuations are important for the pairing mechanism in IBSCs, then my results have shown that the ingredients for high-T_c are present in FeSe, and something other

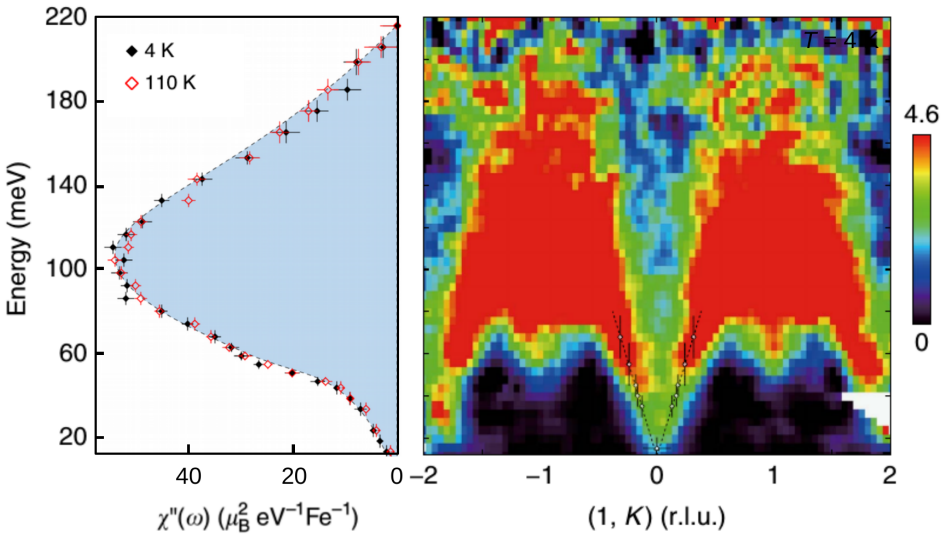

Figure 3.15: Results of the high energy single crystal neutron inelastic study of FeSe reported by Wang *et al.* [401]. The data confirm the steep dispersion inferred from my study of a polycrystalline sample. The energy-distribution of the dynamic magnetic susceptibility is reminiscent of the anomalous spectral weight observed in my RIXS experiment. Momenta are here stated in the 2-Fe unit cell, i.e. (1,0) corresponds to $(\pi,0)$ in the notation used in this thesis.

than conventional magnetic dipole fluctuations must compete with superconductivity. Several different nematic degrees of freedom that could suppress superconductivity have been discussed recently [74, 364, 365, 403, 367, 368, 369, 370], and experiments to search for possible orbital and spin nematic order parameters compatible with $(\pi,0)$ spin fluctuations will be an important next step.

The resonant x-ray data presented in this chapter marks the first time that RIXS has been able to resolve spin-flip excitations of such itinerant states as in the iron chalcogenides. This is encouraging, but also illustrates the limits of current experimental possibilities. The extreme counting times ($\approx 8\,\mathrm{h}$) needed to obtain the present spectra imply that in-depth RIXS studies of metallic correlated states are only beginning to be feasible. For example, higher count rates would have allowed me to infer information from the detailed line-shape of the excitations and to investigate their temperature- and incident-energy–dependence.

The present studies may thus create the impression that INS is the superior technique. By choice of low incident energies, INS can achieve sub-meV resolution and its momentum transfer is not constrained by fixed resonant energies. Moreover, successful studies of co-aligned crystallites suggest that the issue of sample dimensions can be avoided. However, it must be taken into account that this is only possible in favourable cases and under considerable experimental effort. It is easily underestimated that, relative to the probed sample volume, RIXS is actually $\approx 10^{11}$ times more sensitive to magnetism [394].

Most importantly, the complexity of the resonant exchange scattering cross section (see Section 2.4.4) harbours potential which is not being fully realized in current experiments. For example, very few RIXS studies have yet exploited the polarization analysis of the scattered beam [340]. The record RIXS photon count and energy resolution will already increase as new beamlines are being commissioned within the next year [394]. Nevertheless, even with significant instrumental and theoretical advances expected for the coming decade, RIXS is unlikely to become an alternative to neutron scattering — instead its merit will be to probe *qualitatively* new information encoded in the energy, orbital and momentum dependence of electronic and magnetic excitations.

Chapter 4

Spin dispersion in the anisotropic Dirac semimetals AMnBi$_2$ (A=Ca,Sr)

In this chapter I present a triple-axis inelastic neutron scattering study of the anisotropic Dirac semimetals SrMnBi$_2$ and CaMnBi$_2$, as also reported in Physical Review B **95**, 134405 (2017). The AMnBi$_2$ system attracts special interest because it features topologically protected band crossings, as well as electronic correlations. The antiferromagnetism (AFM) and Dirac fermions in these materials are highly two-dimensional and occur in distinct layers. Nevertheless, previous studies had indicated that the Dirac states may play a special role in mediating additional exchange interactions between the magnetically ordered layers [404].

By mapping the complete magnon dispersion in these two materials I was able to determine all relevant magnetic exchange interactions within small error margins. I found no evidence for anomalies due to coupling between magnetism and Dirac physics. Notably, these results call into question the interpretation of a recent Raman scattering study [405]. I show that INS is a more direct probe of magnetism and likely rules out the relevance of the present compounds in the search for magnetically tuned Dirac transport. Instead, I point to recent discoveries of closely related materials which may hold more promise in this regard [406].

Structurally, the AMnBi$_2$ class of ternary bismuthides bears close resemblance to iron based superconductors (IBSCs). It is therefore interesting to compare the ground states arising from corresponding square layers of Fe^{2+} and Mn^{2+} ions. The present chapter thus connects the topics of unconventional superconductivity (see Chapters 1.1 and 3) and Dirac physics (see Chapters 1.2 and 5).

Contents

4.1 Introduction 97
4.2 Characterization 101
4.3 Inelastic neutron scattering at IN8 (ILL) 102
4.4 Results and analysis 104
4.5 Discussion 109
4.6 Conclusion 112

4.1 Introduction

There is presently an intense interest in materials which combine topologically non-trivial electronic states with electronic correlations. As reviewed in Section 1.2, Dirac fermions in condensed matter were originally discovered in graphene [147], which then led to proposals and realizations of 3D topological insulators [202, 407] and Weyl semimetals [408, 232]. The two-spinor character of Dirac states in such materials originates from structural symmetries and the effects of spin orbit coupling. Although the number of known Dirac materials is constantly growing [409], none of these novel electronic phases feature strong interactions between electrons. For example, there has so far been no report of materials where Dirac fermions couple to magnetic correlations. The search for such compounds is motivated by the prospect of being able to use external fields as a handle on charge transport in future "Dirac-electronic devices".

The current interest in AMnBi$_2$ ternary bismuthides is mainly due to the Dirac points in their electronic dispersion. Nevertheless, it is relevant to note that these materials were re-discovered in the search for novel high-temperature superconductors. As parent compounds of high-temperature superconductors, the "122" class of iron arsenides such as SrFe$_2$As$_2$ and BaFe$_2$As$_2$ belong to the most-researched compounds of the last decade. Shortly after the original discovery of iron-based superconductivity in 2008 [32], a computational study by Shim *et al.* suggested that, apart from the known "122" iron based superconductors, a family of related "112" compounds should also be chemically stable [412].

It was predicted that compounds of either stoichiometry would share the tetragonal symmetry and the basic structural motif of layers of edge-sharing transition-metal–pnictide tetrahedra (see Fig. 4.1). In both 122 and 112 materials, these antifluorite layers would be spaced by insulating "blocking layers" acting as charge reservoirs (see Fig. 4.1). Special interest in the hypothetical 112 superconductors was due to additional *metallic* pnictogen layers. This would have allowed to study the interaction of superconductivity with additional *itinerant* states.

Although efforts to synthesize the computationally predicted BaFeAs$_2$ compound have not been successful to date, they led to the re-discovery of the ternary bismuthides AMnBi$_2$ (A = Ca, Sr) [413, 414, 410]. The transition-metal–pnictide layers in these compounds indeed form the same basic structural motif as in IBSCs (compare Figs. 4.1 and 1.1). In analogy to the Fe^{2+} ($3d^6$) state in IBSCs, the Mn^{2+} ($3d^5$) ions in these MnBi layers strongly interact. As discussed below, the resulting ground state is however different, and overall the correlations are stronger. This leads to antiferromagnetic order below $T_N \approx 260$–290 K.

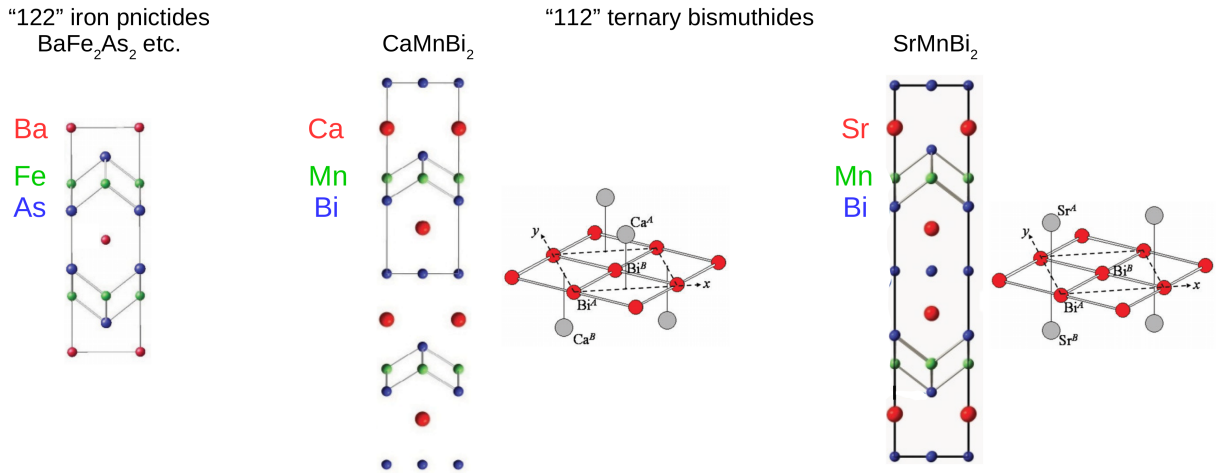

Figure 4.1: (adapted from [410, 411]). Crystal structures of ternary transition metal pnictides. The “122” family of iron based superconductors (space group $I4/mmm$) and the two compounds investigated in this project, $CaMnBi_2$ ($P4/nmm$) and $SrMnBi_2$ ($I4/mmm$), share the same structural motif of transition-metal–pnictide *antifluorite* layers. The structures of the Ca and Sr compounds differ only by the symmetry element in the Bi layer (a glide plane and a mirror plane, respectively). This effectively doubles the unit cell in the case of $SrMnBi_2$.

The key difference from IBSCs lies in the additional square pnictogen layers. The two compounds $CaMnBi_2$ and $SrMnBi_2$ differ only by the symmetry element in the Bi layer (a glide plane and a mirror plane, respectively). This effectively doubles the unit cell (along the c axis) in the case of $SrMnBi_2$. In both materials, the staggering of cations in the adjacent layers leads to a doubling of the unit cell (relative to the *one-Bi* lattice) along the a and b axes. Several first principles band calculations realized that the corresponding back-folding of the bismuth $2p_x$ and $2p_y$ bands entails linear band crossings close to the Fermi surface [415, 411] (see Fig. 4.2 a,b). A little later, direct evidence of these Dirac-points along the (110) direction in reciprocal space was found by angle-resolved photoemission spectroscopy (ARPES), see Fig. 4.2 c–f [415, 416].

The Dirac dispersion in these materials has the unprecedented property of being highly anisotropic: The Fermi velocity varies by up to an order of magnitude, depending on the direction of the charge transport (parallel or perpendicular to the $\langle 110 \rangle$ or “Γ–M” direction of reciprocal space). In view of potential technological applications, there had previously been efforts to engineer such a situation, e.g. by inducing strain in graphene [417]. In the present case, the Dirac anisotropy occurs naturally, due to a weak hybridization of Bi states with their environment (i.e. with the adjacent A cation layers).

Notably, it was found that, as these materials order magnetically, the Mn bands are spin-split away from the Fermi level. In effect, the density of states (DOS) at the Fermi surface is then dominated by the strongly spin-orbit-coupled square Bi planes. The macroscopic properties therefore share the unusual transport characteristics of graphene or topologi-

cal insulators [178, 181, 179, 409]: Due to the suppression of backscattering processes, the electronic and thermal conductivities are enhanced, and the large separation of Landau levels produces a large linear magnetoresistance.

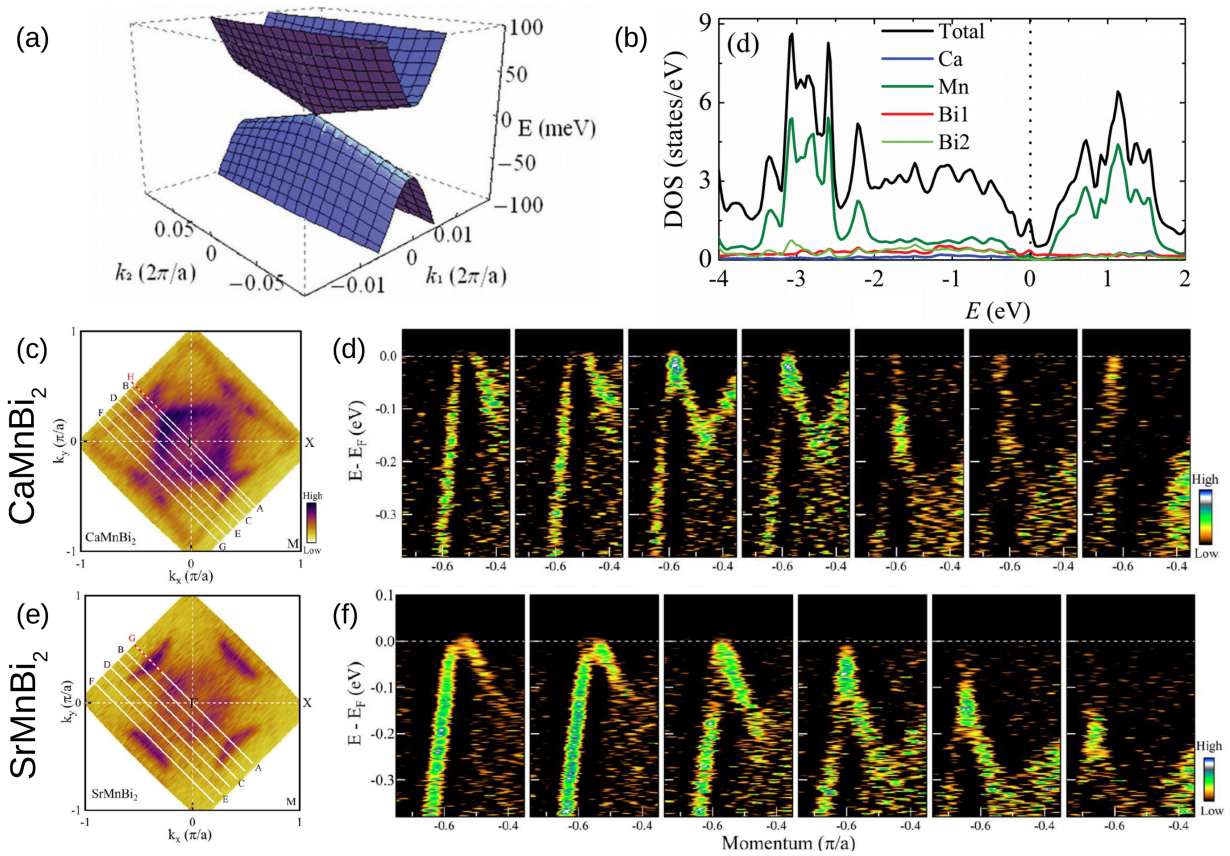

Figure 4.2: (adapted from [411, 416]). (a) Highly anisotropic linear band crossing at the Fermi surface as predicted from first principles calculations. (b) In the ordered magnetic state, the calculated electronic density of states at the Fermi surface is dominated by the $6p_{x,y}$ states of the square Bi layers (case of $CaMnBi_2$ shown). (c,e) Experimental Fermi surfaces and (d,f) energy–momentum-space slices of the electronic dispersion of $CaMnBi_2$ and $SrMnBi_2$ measured by angle-resolved photoemission spectroscopy.

To determine whether the magnetic moments of Mn ions may couple to this behaviour, Guo *et al.* characterized the magnetic order in the adjacent MnBi layers [404]. By neutron diffraction of powder and single-crystalline samples, the authors showed that below $T_N^{Sr} \approx 290\,K$ and $T_N^{Ca} \approx 265\,K$, the Mn^{2+} ($3d^5$, $S = 5/2$) magnetic moments align parallel to the c axis and form AFM structures with an ordered moment of $\approx 3.7\mu_B$ [404]. The two compounds were found to differ in the sign of their interlayer coupling, which results in ferro- and antiferromagnetic stacking of Néel-ordered layers in $CaMnBi_2$ and $SrMnBi_2$, respectively [404].

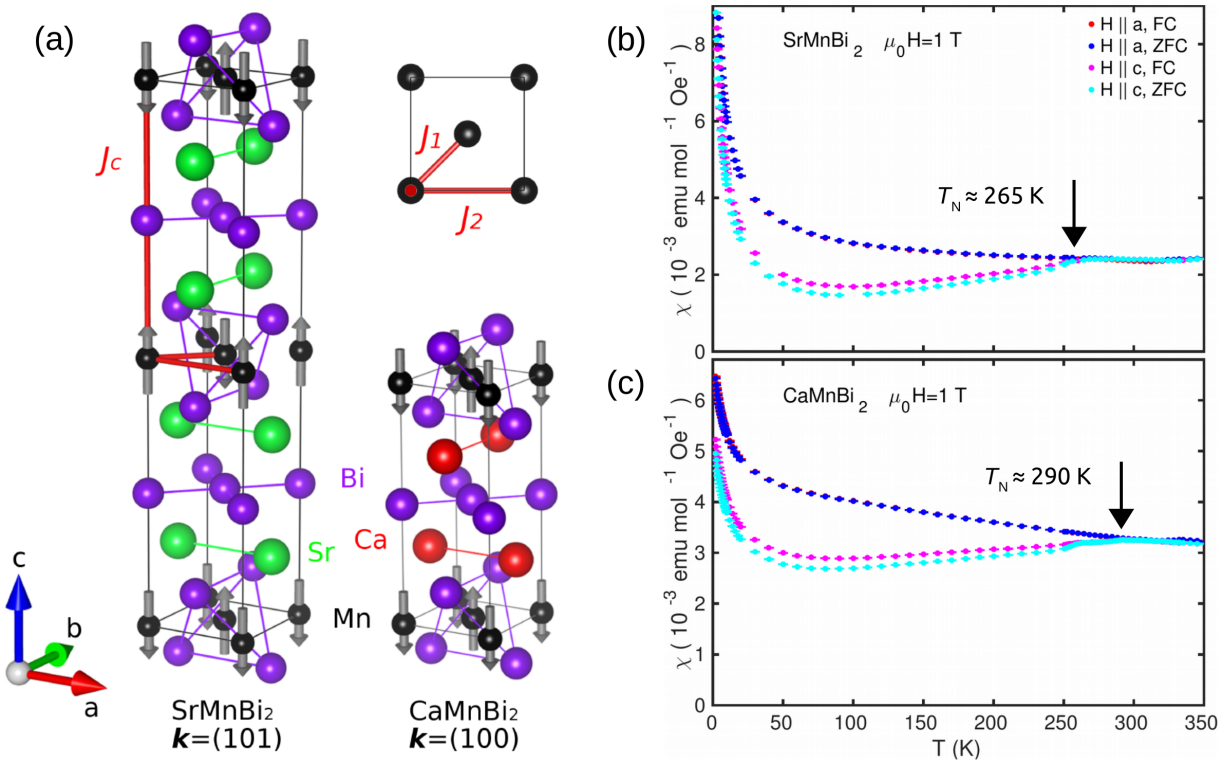

Figure 4.3: Magnetic properties of $CaMnBi_2$ and $SrMnBi_2$. (a) Néel-type ("checkerboard") magnetic structures of the two compounds, as determined by neutron diffraction in [404]. The compounds differ in the (anti-)ferromagnetic stacking of the spins along the c axis. (b) Magnetic susceptibility of the samples used in my neutron study. A weak splitting of the data obtained under zero-field-cooled (ZFC) vs. field-cooled (FC) condition reveals the onset of magnetic order at the indicated Néel temperatures.

An interpretation based on first-principles calculations suggests that in the ferromagnetically stacked case ($CaMnBi_2$), the Dirac bands may provide an itinerant interlayer exchange path and thus directly couple to the magnetic ground state [404]. In particular, this exchange path would be allowed by the non-symmorphic (*i.e.*, glide plane) symmetry of the Bi layers in the Ca compound (which corresponds to the "crossed" orientation of the adjacent cations illustrated in Fig. 4.3(a)). This appeared to be supported by a weak resistivity anomaly observed at T_N in $CaMnBi_2$, but not in $SrMnBi_2$ [404]. Earlier transport studies, however, had not registered such an anomaly in either $SrMnBi_2$ [410] or $CaMnBi_2$ [418, 419].

In metallic magnets, a coupling between the ordered magnetic moments and conduction electron states can reveal itself in the magnetic excitation spectrum. For example, there can be damping due to spin-wave decay into the Stoner continuum, anomalies in the magnon dispersion due to modifications of the exchange interactions by conduction electron states, or a gap could form due to an additional Kondo energy scale.

In the following sections I report a single-crystal inelastic neutron scattering (INS) study of $SrMnBi_2$ and $CaMnBi_2$ in the magnetically ordered state. My analysis shows that the

magnon spectrum in both materials can be accurately reproduced from a Heisenberg model describing a local-moment, quasi-two-dimensional (2D) antiferromagnet. The model includes nearest- and next-nearest-neighbour in-plane exchange interactions and a weak interlayer exchange interaction, together with an easy-axis anisotropy. I did not find any anomalies that would suggest significant coupling between the magnons and conduction electron states. The interlayer coupling is smaller than found in the reference compound $BaMn_2Bi_2$, consistent with the larger separation of the Mn spins along the c axis in AMnBi$_2$.

4.2 Characterization

The single crystals of $CaMnBi_2$ and $SrMnBi_2$ were prepared by my collaborators Youguo Shi[1] and Yanfeng Guo[2], as previously reported [404]. Polycrystalline AMnBi$_2$ was first synthesized by solid-state reaction of the elements. Single crystals of several grams were then grown from self-flux in an alumina crucible. Electron-probe microanalysis confirmed near-ideal stoichiometry, with a small ($\approx 2\,\%$) Bi deficiency in the Sr compound (for details, see Ref. [404]). Laboratory x-ray-diffraction measurements confirmed the originally reported tetragonal crystal structures [413, 414], with space groups $I4/mmm$ ($SrMnBi_2$) and $P4/nmm$ ($CaMnBi_2$) (see Fig. 4.3).

To check for consistency with previous studies, I measured the thermal variation of the magnetic properties of the batch of samples that I investigated by INS (see Fig. 4.3(b,c)). I first aligned these single crystals on a four-circle x-ray diffractometer (Mo K_α radiation). I then measured the magnetic susceptibility using a SQUID magnetometer (see Section 2.1), with a magnetic field of 1 T applied either in-plane or out-of-plane. The key characteristics (Fig. 4.3(b,c)) are qualitatively consistent with earlier results [404]. The samples used in my experiments have a larger Curie contribution, which may be attributed to paramagnetic impurities induced by sample decay. Since the magnon dispersion is a coherent response of the main crystal phase, such impurities are not of relevance to inelastic neutron scattering, apart from a possible small contribution to the diffuse background scattering.

[1]Beijing National Laboratory for Condensed Matter Physics, Institute of Physics, Chinese Academy of Sciences, Beijing 100190, China

[2]School of Physical Science and Technology, ShanghaiTech University, Shanghai 201210, China and CAS Center for Excellence in Superconducting Electronics (CENSE), Shanghai 200050, China

4.3 Inelastic neutron scattering at IN8 (ILL)

I performed the neutron inelastic measurements at the Institut Laue–Langevin on the triple-axis neutron spectrometer IN8 [420], using the FlatCone detector array [421]. This scattering geometry is illustrated in Figs. 4.5 and 4.6 (in real and reciprocal space, respectively). By keeping the outgoing energy fixed and recording rocking scans at various incident energies, this setup allows an efficient collection of constant energy-transfer maps covering a wide range of reciprocal space.

The FlatCone array of analyzer crystals and helium tube detectors consists of 31 channels spaced by 2.5°, thus covering a 75° range of scattering angle 2θ. Throughout the study, the FlatCone was used with its Si (111) analyzer crystals selecting a fixed outgoing wave vector of $k_f = 3\,\text{Å}^{-1}$ ($E_f = 18.6\,\text{meV}$). For energy transfers below and above 40 meV (E_i =58.6 meV), the double-focusing Si (111) and pyrolitic graphite (002) monochromators were used, respectively.

In four separate experiments, I investigated the scattering from the $SrMnBi_2$ and $CaMnBi_2$ single crystals (of mass 3.3 and 1.6 g, respectively) in the $(HK0)$ (*ab* orientation) and $(H0L)$ (*ac* orientation) scattering planes[3]. The samples were mounted in a standard top-loading liquid helium cryostat. I recorded all spectra at a sample temperature of approximately 5 K.

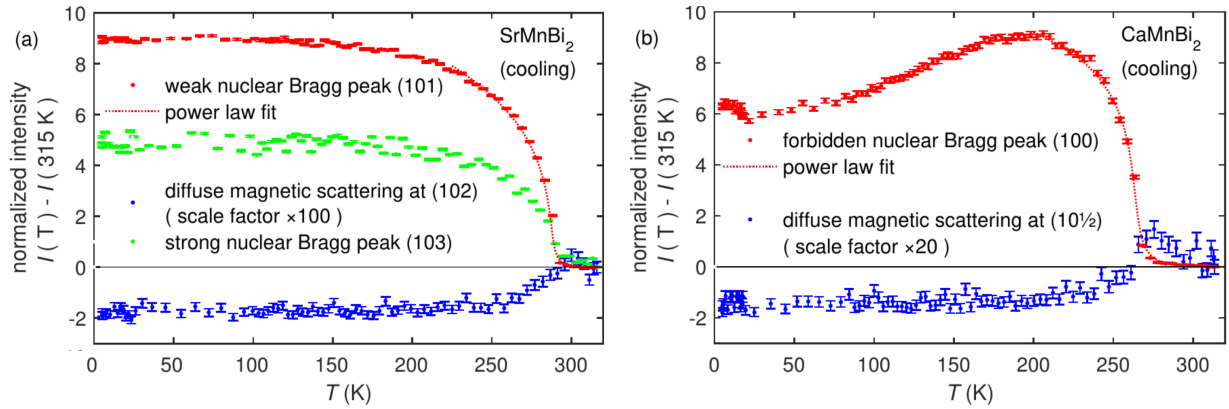

Figure 4.4: Temperature dependence of the intensity difference $I(T) - I(315\,\text{K})$ at selected wave vectors (see legend), recorded while cooling (a) $SrMnBi_2$ and (b) $CaMnBi_2$. Power law fits to the Bragg intensities yield transition temperatures of $T_N^{Sr} = 287(5)\,\text{K}$ and $T_N^{Ca} = 264(2)\,\text{K}$. Above T_N, incipient in-plane correlations contribute diffuse rods of magnetic scattering along $(10L)$. These fluctuations are enhanced towards T_N (critical scattering) and then freeze out with the onset of inter-plane order (blue symbols). The decrease in intensity of the (100) reflection of $CaMnBi_2$ below 200 K is not consistent with previous data and should be disregarded (see main text).

[3]Throughout this section, I give wave vectors in reciprocal lattice units (r.l.u.) $\mathbf{Q} = (H,K,L) \equiv (H \times 2\pi/a, K \times 2\pi/b, L \times 2\pi/c)$

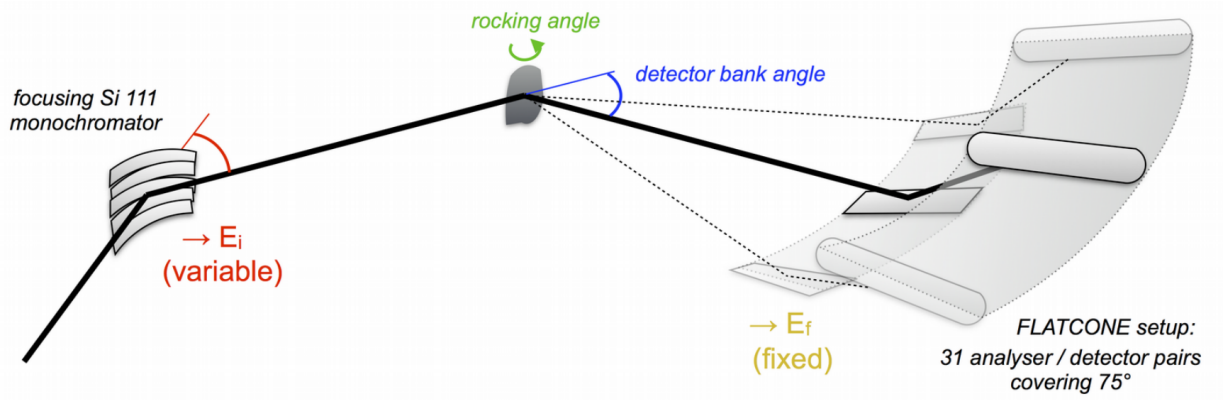

Figure 4.5: Illustration of the triple-axis inelastic neutron scattering technique using the FlatCone detector at instrument IN8 (Institut Laue-Langevin). The outgoing neutron energy is fixed by the setting of 31 Si (111) analyzer crystals inside the FlatCone assembly. The energy transfer to the sample is controlled by the monochromator angle. The detector bank is then positioned to cover a range of suitable scattering angles.

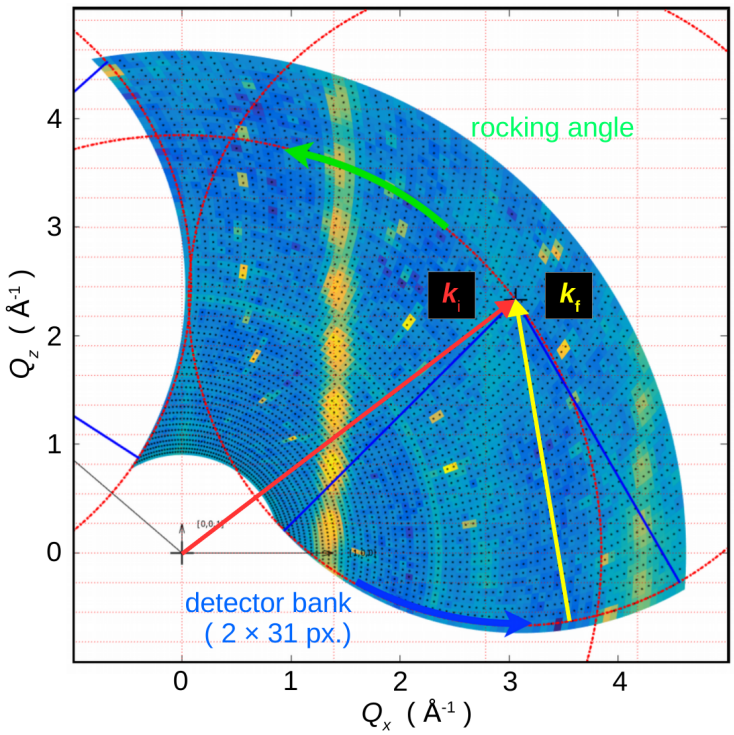

Figure 4.6: Reciprocal space view of Figure 4.5, illustrated on a raw dataset in the $(H0L)$ plane of $SrMnBi_2$. (HKL) coordinates are indicated by a dashed grid. The FlatCone detector bank corresponds to an arc of 31 measurement points in reciprocal space. Two scans, with an offset of half the detector spacing ($\Delta 2\theta = 1.25^{o}$), are combined to effectively double this number of *pixels*. In a rocking scan, a wide ring-section of momentum space is traced out, which covers several Brillouin zones.

4.4 Results and analysis

While cooling the samples in the *ac* orientation, I tracked the intensities at selected positions in the $(H0L)$ plane of reciprocal space. Figure 4.4 shows the resulting temperature dependences for $SrMnBi_2$ and $CaMnBi_2$. This includes the magnetic Bragg contribution at (101) and (103) (for Sr) and (100) (for Ca), as well as the diffuse magnetic scattering at another position along the $(10L)$ direction away from the Bragg condition. The data, here represented as the change in intensity relative to the paramagnetic phase, demonstrate the order-parameter characteristics of magnetic Bragg scattering at the antiferromagnetic transitions. I note that the decrease of the $CaMnBi_2$ (100) magnetic scattering below 200 K is not consistent with the previous powder neutron-diffraction data [404], which could be due to a shift of the peak between two detector channels as the crystal contracted.

Above the ordering temperature, incipient in-plane magnetic correlations form diffuse rods of magnetic scattering along the c direction of reciprocal space, which is seen at those $(10L)$ positions where Bragg scattering is extinct. When cooling towards T_N, this diffuse scattering initially intensifies and then subsides when the weaker interlayer correlations set in and neutron spectral weight is confined to the Bragg peaks. Fits of a power law to the thermal variation of the (101) (Sr) and (100) (Ca) peaks yield Néel temperatures of $T_N^{Sr} = 287(5)$ K and $T_N^{Ca} = 264(2)$ K. These values are consistent with previous single-crystal bulk measurements of transport and ARPES samples [410, 415, 419, 418], but differ slightly from the values found in the earlier neutron powder diffraction study [404]. This difference is likely due to small structural or compositional variations among the samples.

The critical exponents $\beta^{Sr} = 0.15(3)$ and $\beta^{Ca} = 0.11(2)$ obtained from the power-law fit are much smaller than the value $\beta = 0.365$ of the three-dimensional Heisenberg model. This indicates the reduced dimensionality of the magnetism in these systems. Due to the additional bismuth layers in the unit cells, the magnetism is more two-dimensional in $AMnBi_2$ than in the related (122) manganese arsenide $BaMn_2As_2$, $\beta = 0.35(2)$ [68]. Instead, the interlayer correlations compare well to the parent compounds of (122) iron-based superconductors, e.g. $\beta = 0.098(1)$ for $SrFe_2As_2$ [422] and $\beta = 0.125$ for $BaFe_2As_2$ [423].

The measured neutron spectra are summarized in Figure 4.7. Due to the periodicity of the antiferromagnetic order, the magnetic zone centres are located at (HKL) positions with $(H+K)$ and L both odd integers for $SrMnBi_2$, and at positions with $(H+K)$ odd and L any integer for $CaMnBi_2$. For both compounds, the spectra reveal a well-defined magnon dispersion above spin gaps of approximately 10 meV (Sr) and 8 meV (Ca). The magnons are highly dispersive parallel to the layers, but only weakly dispersive perpen-

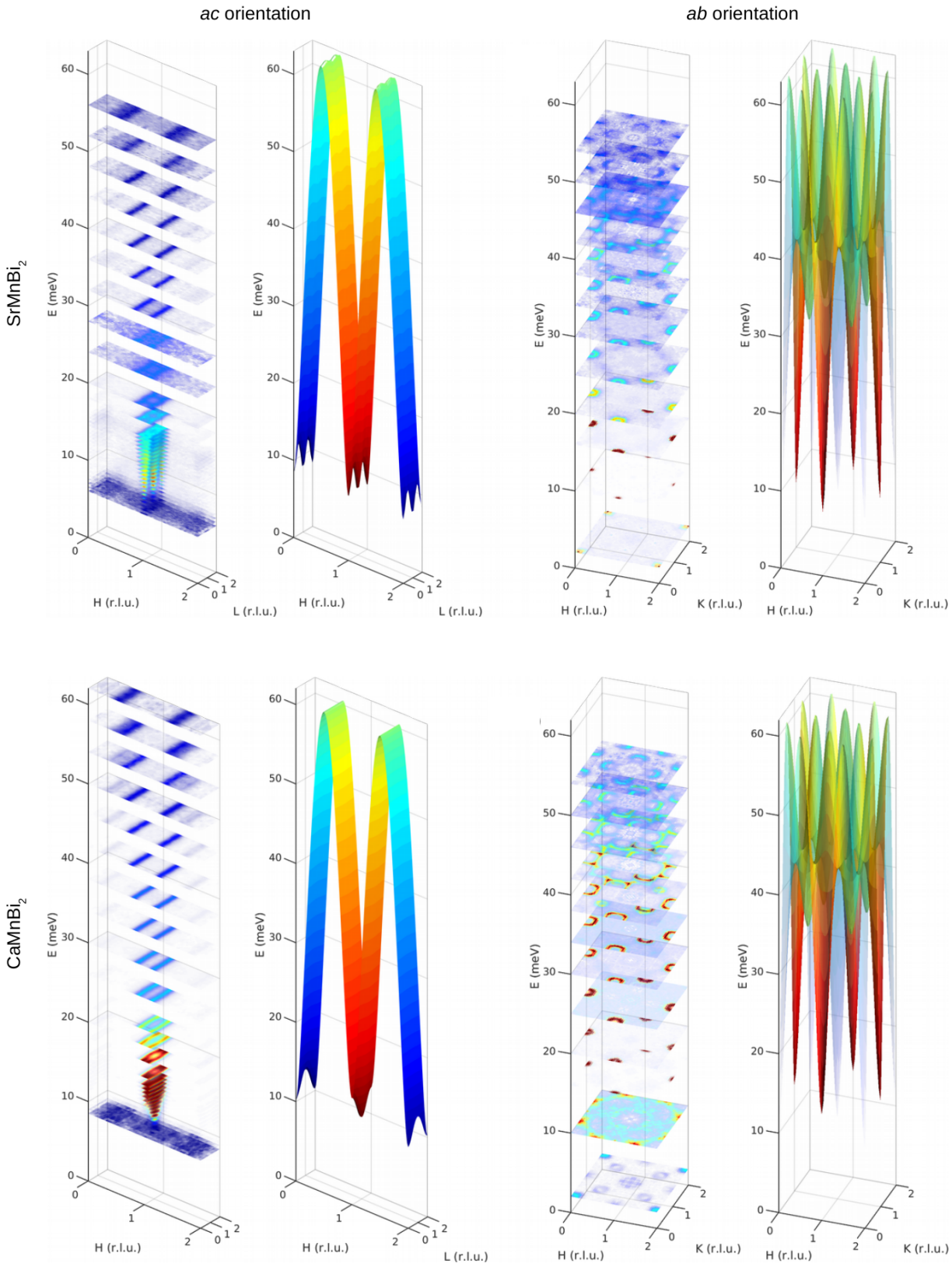

Figure 4.7: Magnon spectrum of $SrMnBi_2$ (top) and $CaMnBi_2$ (bottom) in the $(H0L)$ (left) and $(HK0)$ (right) planes in reciprocal space. The data are illustrated by a stacking plot of constant-energy slices (left panels), and the best-fit spin-wave model is represented by the corresponding dispersion surface (right panels).

dicular to the layers. For both samples, the magnon bandwidth is around 50 meV for spin waves propagating in the $(HK0)$ plane and 3–4 meV along $(10L)$. Figures 4.8(a,b) represent more quantitatively the magnon dispersion in the $(HK0)$ plane as obtained from Gaussian fits to constant-energy cuts, and the left-hand panels of Figs. 4.8(c,d) illustrate the out-of-plane dispersion by energy-wave-vector slices of the data along the $(10L)$ direction.

To obtain quantitative information on the magnetic couplings, I have compared the data with the linear spin-wave spectrum calculated from an effective spin Hamiltonian that includes a Heisenberg coupling term and an Ising-like single- ion anisotropy:

$$\hat{\mathcal{H}} = \sum_{\langle i,j \rangle} J_{ij}\, \hat{\mathbf{S}}_i \cdot \hat{\mathbf{S}}_j - \sum_i D\,(\hat{S}_i^z)^2 \quad . \tag{4.1}$$

Here I include nearest-neighbour (J_1) and next-nearest-neighbour (J_2) exchange constants, an interlayer exchange interaction J_c , and the anisotropy constant D. The exchange paths are shown in Fig. 4.3(a). In Appendix B, I outline how the magnon dispersion can be derived from this Hamiltonian by linear spin wave theory. By use of the Holstein-Primakoff transformation of two interacting Bose fields, which correspond to the two collinear antiferromagnetic sublattices, one obtains the relation

$$E(\mathbf{Q}) = \sqrt{A(\mathbf{Q})^2 - B(\mathbf{Q})^2} \tag{4.2}$$

where $\mathbf{Q}$ is the magnon wavevector,

$$\begin{aligned} A(\mathbf{Q}) &= S\,[\mathcal{J}_{\mathrm{AF}}(0) - \mathcal{J}_{\mathrm{F}}(0) + \mathcal{J}_{\mathrm{F}}(\mathbf{Q}) + 2D] \\ B(\mathbf{Q}) &= S\,\mathcal{J}_{\mathrm{AF}}(\mathbf{Q}) \end{aligned}$$

and

$$\mathcal{J}(\mathbf{Q}) = \sum_n J_n\, \mathrm{e}^{2\pi \mathrm{i}\, \mathbf{Q}\cdot\mathbf{r}_n} \tag{4.3}$$

are Fourier transforms of the exchange interactions. The subscripts F and AF refer to summation over ferromagnetically and antiferromagnetically aligned pairs of spins, respectively. The resulting differential scattering cross section for single-magnon creation is (see also, Eq. B.27)

$$\frac{\mathrm{d}\sigma}{\mathrm{d}\Omega \mathrm{d}\omega} = \frac{k_{\mathrm{f}}}{k_{\mathrm{i}}} \left(\frac{\gamma r_0\, g}{2}\right)^2 F(\mathbf{Q})^2\, \left(1 + \hat{Q}_z^2\right) N S \frac{A(\mathbf{Q}) - B(\mathbf{Q})}{E(\mathbf{Q})} \frac{1}{1 - e^{-\beta\hbar\omega}}\, \delta(\hbar\omega - E(\mathbf{Q})) \tag{4.4}$$

where $\hbar\omega$ is the neutron energy transfer, k_{f} and $k_{\mathbf{i}}$ are the outgoing and incoming neutron wave vectors, $\gamma = 1.913$, r_0 is the classical electron radius, g the Landé g-factor, N the

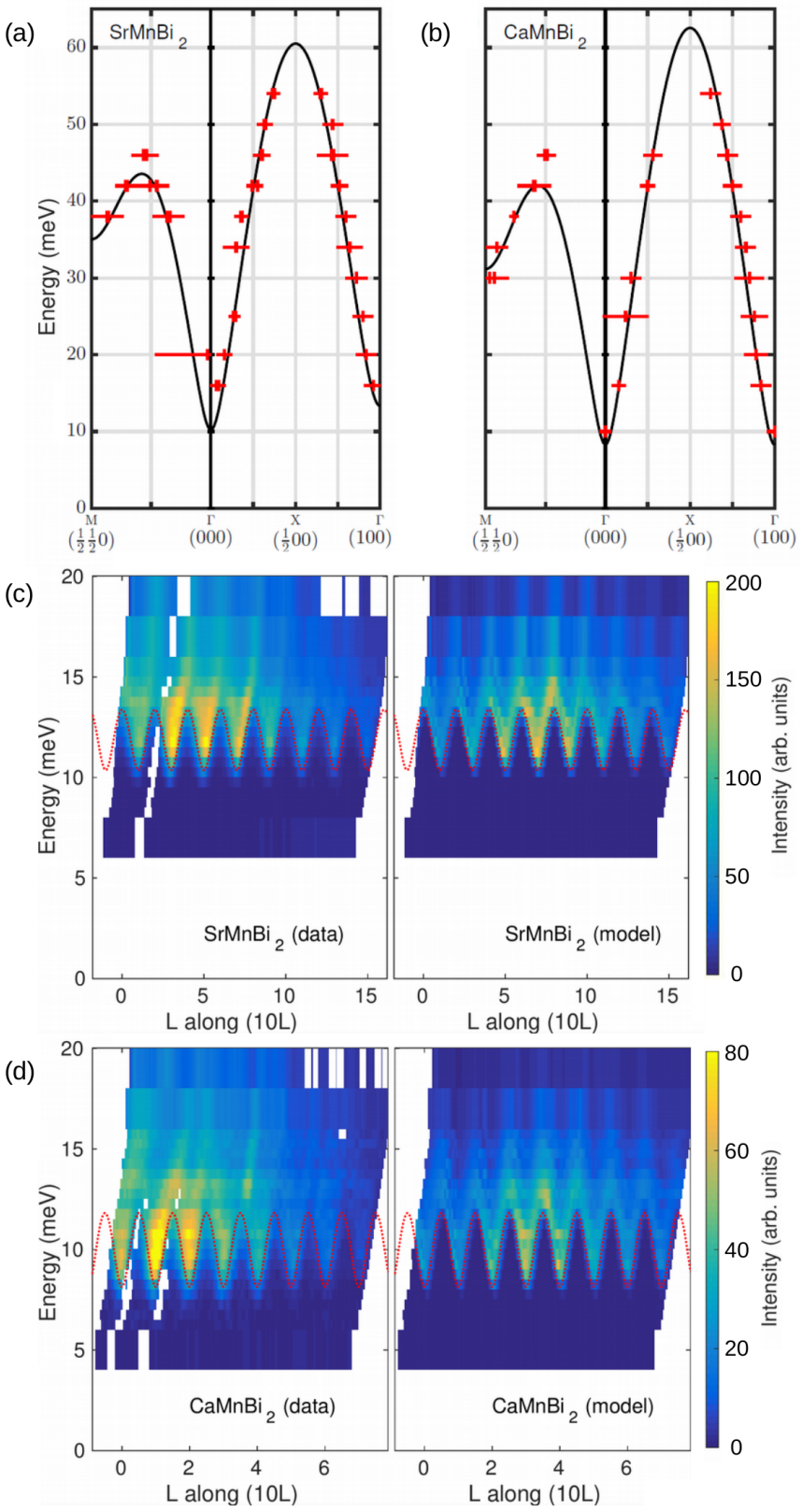

Figure 4.8: Fits to the magnon spectrum of $SrMnBi_2$ and $CaMnBi_2$. (a,b) Dispersion in the $(HK0)$ plane of reciprocal space. (c,d) Dispersion along $(10L)$, comparing the interpolated data (left) and the model convoluted with the numerically simulated resolution function. The analytical dispersion is indicated as a red dashed line.

number of magnetic ions per sublattice, S the spin quantum number, and $(e^{\hbar\omega/k_B T}-1)^{-1}$ is the boson occupation number. With the magnetic structures and exchange paths as defined in Fig. 4.3(a), the explicit Fourier exchange terms for the case of $SrMnBi_2$ are

$$\begin{aligned}\mathcal{J}_{\mathrm{AF}}^{\mathrm{Sr}}(\mathbf{Q}) &= 2J_1\,[\cos(\pi H+\pi K)+\cos(\pi H-\pi K)]+\\ &\quad+2J_c\cos(\pi L)\\ \mathcal{J}_{\mathrm{F}}^{\mathrm{Sr}}(\mathbf{Q}) &= 2J_2\,[\cos(2\pi H)+\cos(2\pi K)]\end{aligned}$$

and, in the case of $CaMnBi_2$,

$$\begin{aligned}\mathcal{J}_{\mathrm{AF}}^{\mathrm{Ca}}(\mathbf{Q}) &= 2J_1\,[\cos(\pi H+\pi K)+\cos(\pi H-\pi K)]\\ \mathcal{J}_{\mathrm{F}}^{\mathrm{Ca}}(\mathbf{Q}) &= 2J_2\,[\cos(2\pi H)+\cos(2\pi K)]+2J_c\cos(2\pi L).\end{aligned}$$

This allows an analytical description of the spin gaps:

$$\Delta^{\mathrm{Sr}}\approx\Delta^{\mathrm{Ca}}\approx 4\sqrt{SJ_1}\sqrt{SD}, \tag{4.5}$$

where I have applied the appropriate approximations for the present case ($J_1\gg J_c$, $J_1\gg D$). Complete expressions for these terms and their explicit derivation are given in Appendix B.

Similarly, the band width W of the dispersion along $(10L)$ is given by

$$W^{\mathrm{Sr}}\approx W^{\mathrm{Ca}}\approx 4\sqrt{SJ_1}\left(\sqrt{SD+2|SJ_c|}-\sqrt{SD}\right). \tag{4.6}$$

If J_1 is the dominant exchange, as is found to be the case here, then the maximum of the in-plane dispersion is $\approx 4SJ_1$. Given J_1 , one sees from Eqs. (4.5) and (4.6) that in the relevant parameter regime, D and J_c are determined by the size of the gap $\Delta^{\mathrm{Sr/Ca}}$ and bandwidth of the out-of-plane modulation $W^{\mathrm{Sr/Ca}}$, respectively. On the other hand, the balance between the parameters J_1 and J_2 determines details of the dispersion at higher energies in the $(HK0)$ plane. For example, a local minimum of the dispersion at the M point, $(\frac{1}{2},\frac{1}{2},0)$, as observed in both materials, will only occur for positive J_2. This indicates a competition (frustration) between nearest- and next-nearest-neighbour exchange.

Thus, I found that the above model is able to reproduce very well all features in the data. For a quantitative comparison, I folded and averaged the raw constant-energy maps of reciprocal space into tiles of 2×2 r.l.u.. With the data in this reduced form, I could compare it to the model after convolution of the theoretical spectrum, Eqs. (4.4)–(4.2), with an energy- and wave- vector-dependent broadening function to take into account the instrumental resolution. A phenomenological Gaussian broadening of the analytical

dispersion proved insufficient to achieve a consistent global fit to the data, particularly for the low-energy part of the magnetic dispersion in the *ac* plane.

Instead, it was necessary to take into account the resolution of the triple-axis spectrometer, which was calculated with the RESTRAX ray-tracing algorithm [424, 425]. My procedure to determine the parameters of the spin Hamiltonian J_1, J_2, J_c, and D comprised three steps. First, a global fit of all data, using phenomenological Gaussian broadening of the dispersion, produced rough estimates of all parameters. Using these as starting values and fixing the in-plane exchange interactions J_1 and J_2, I obtained precise bounds on the interlayer exchange J_c and anisotropy D by fitting the resolution-convoluted spectrum for low energies (0–20 meV) to an energy–wave-vector slice with wave vector along $(10L)$, as illustrated in Figs. 4.8(c,d). Finally, I refined J_1 and J_2 by fitting the in-plane (ab) dispersion at high energies (3–44 meV) using Gaussian broadening.

4.5 Discussion

The exchange parameters for $SrMnBi_2$ and $CaMnBi_2$ obtained from the fits are summarized in Table 4.1. Apart from the opposite sign of the interlayer exchange J_c, there are no significant differences between the parameters of $SrMnBi_2$ and $CaMnBi_2$. The absolute values of J_1 and J_2 are slightly larger in the case of $CaMnBi_2$, which is consistent with the smaller nearest-neighbour spacing (d_{NN}). The magnitudes of J_c for the two compounds, which are the same to within the error, are much smaller than J_1 and J_2. This confirms the quasi-2D character of the magnetism in these materials. Notably, these results are in good agreement with previous estimations based on first-principles calculations of the electronic structure, which gave an average in-plane exchange of $SJ_{ab} \approx 30$ meV and $|SJ_c| \approx 0.3$ meV [404].

Regarding the magnetocrystalline anisotropy, I observe that D is enhanced by a factor 1.8 in $SrMnBi_2$ compared with $CaMnBi_2$. According to the initial structure determinations at room temperature [413, 414], the local environment of the Mn ion is similar in both compounds: The $MnBi_4$ tetrahedra are elongated by $\approx 14\,\%$ along c and the ligand distances are $d^{Ca}_{Mn-Bi} = 2.87(1)$ Å and $d^{Sr}_{Mn-Bi} = 2.89(1)$ Å. The significant difference in anisotropy may therefore point to unknown structural distortions at 5 K (at present, no full refinement of crystallographic parameters at low temperatures is available). The anisotropy is in good agreement with the result of the density functional prediction by Guo *et al.* ($SD^{Ca}_{DFT} = 0.3$ meV [404]), as was also the case with the exchange constants.

It is instructive to compare the present results to two available inelastic neutron scattering studies of the related compounds $BaMn_2Bi_2$ [426] and $BaMn_2As_2$ [427]. The corresponding parameters for these materials are also quoted in Table 4.1. The pnictide-

Table 4.1: Exchange parameters, magnetocrystalline anisotropy constants and spin gaps of $SrMnBi_2$ and $CaMnBi_2$ obtained from a fit of the linear spin-wave model, as described in the text. The parameters can be related to the nearest-neighbour (d_{NN}) and interlayer (d_c) Mn–Mn atomic spacings, the ordered magnetic moment μ, and the ordering temperature T_N [404]. The corresponding values for two related Mn pnictides are reproduced below [426, 427].

	$SrMnBi_2$	$CaMnBi_2$	$BaMn_2Bi_2$ [426]	$BaMn_2As_2$ [427]
SJ_1 (meV)	21.3(2)	23.4(6)	21.7(1.5)	33(3)
SJ_2 (meV)	6.39(15)	7.9(5)	7.85(1.4)	9.5(1.3)
SJ_c (meV)	0.11(2)	-0.10(5)	1.26(2)	3.0(6)
SD (meV)	0.31(2)	0.18(3)	0.87(15)*	
Δ (meV)	10.2(2)	8.3(8)	16.29(26)	
d_{NN} (Å)	3.24	3.18	3.18	2.95
d_c (Å)	11.57	11.07	7.34	6.73
$\mu(\mu_B)$	3.75(5)	3.73(5)	3.83(4)	3.88(4)
T_N (K)	290.2(3)	267.0(1.6)	387.2(4)	625(1)

* The value of SD for $BaMn_2Bi_2$ was misquoted in Ref. [426]. Here I give the correct value [428].

coordinated magnetic Mn^{2+} layers in $BaMn_2Bi_2$ and $BaMn_2As_2$ ("122 materials") are analogous to those in the 112 materials investigated in this thesis. On the other hand, the $I4/mmm$ 122 compounds do not feature additional pnictide layers (which carry the Dirac bands in the present case). Hence, while the in-plane Mn–Mn spacing is very similar, the spacing of the magnetic layers in the 122 compounds is only 58–66% of that in $CaMnBi_2$ and $SrMnBi_2$. Both $BaMn_2Bi_2$ and $BaMn_2As_2$ form antiferromagnetically stacked layers of Néel-type order, in analogy to $SrMnBi_2$.

As may be expected from these circumstances, I find that the in-plane exchange interactions in 122 compounds are similar or identical to those in 112 compounds. On the other hand, in the present 112 materials the inter-plane exchange is significantly reduced. This is consistent with the much higher transition temperatures and the smaller separation of the Mn layers in the 122 materials compared with the 112 compounds.

I find no evidence that the additional Bi layers in 112 materials, which host the Dirac fermions, cause any qualitative changes in the magnon spectrum, such as anomalous broadening or dispersion. The instrument's simulated energy resolution provides an upper bound on the influence of such effects. The characteristics of the Bragg (0.5–1.0 meV) and vanadium (1–4 meV) widths of energy resolution are illustrated in Figure 4.9. By contrast, neutron inelastic measurements of many iron-based superconductors, as discussed in Chapters 1.1.4 and 3, show obvious signatures of a strong hybridization of magnetic and itinerant states.

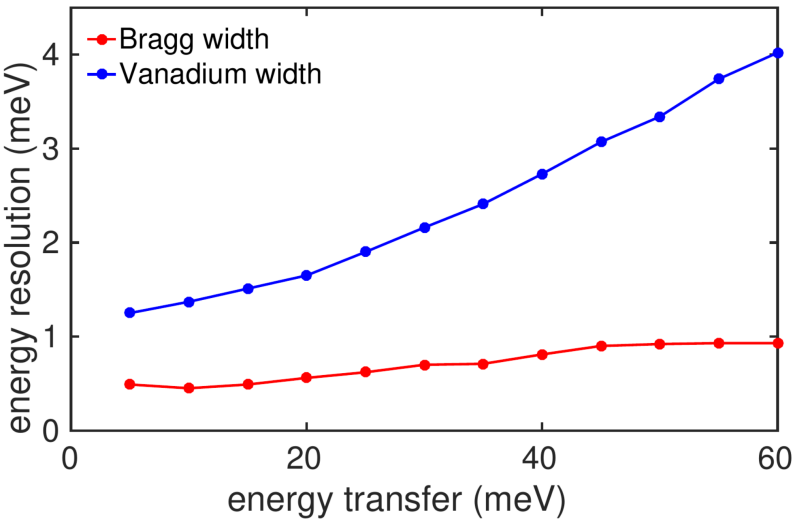

Figure 4.9: Simulated energy resolution of the IN8 spectrometer calculated using the RESTRAX raytracing algorithm for the experimental conditions of the present study. Calculations were performed for Si(111) monochromator and Si(111) analyzer crystals. The energy dimension of the resolution ellipsoid is only weakly dependent on the momentum transfer and was here sampled at an arbitrary position in reciprocal space.

A typical example is $SrFe_2As_2$ [102], which shows a crossover into the regime of itinerant (*Stoner*) spin fluctuations. This manifests as an increased dampening of spin fluctuations (i.e. a broadening of the neutron spectrum) above a characteristic energy of approximately 80 meV.

As in the 122 compounds, both J_1 and J_2 are positive (antiferromagnetic) in $SrMnBi_2$ and $CaMnBi_2$, resulting in frustration between nearest- and next-nearest-neighbour interactions. The theoretical phase diagram of the frustrated J_1–J_2 model on a square lattice has been investigated extensively in the context of iron-based superconductors [429, 430, 431]. There is special interest in this phase diagram owing to a possible quantum critical point and spin-liquid phase around $J_2/J_1 \approx \frac{1}{2}$. This regime separates two distinct ordered magnetic phases, with Néel-type order for $J_2/J_1 < \frac{1}{2}$ and stripe antiferromagnetic order for $J_2/J_1 > \frac{1}{2}$. Both 112 and 122 Mn-based compounds exhibit dominant nearest-neighbour exchange, with $J_2/J_1 \approx 0.3$. According to one study, the exchange and anisotropy parameters for AMnBi$_2$ place these materials close to the phase boundary between Néel-ordered and frustrated paramagnetic phases [431]. The resulting quantum fluctuations could explain some of the observed reduction in ordered magnetic moment ($\simeq 3.7\,\mu_B$) compared to the ideal local-moment value of $5\,\mu_B$ [427]. By contrast, in parent compounds of iron-based superconductors such as $BaFe_2As_2$ and $SrFe_2As_2$, J_1 and J_2 are of similar magnitude, resulting in stripe-antiferromagnetic order.

4.6 Conclusion

In summary, I have performed a comprehensive triple-axis neutron-scattering study of the anisotropic Dirac materials $SrMnBi_2$ and $CaMnBi_2$, with the aim of searching for possible influences of the unusual band topology at their Fermi surfaces on their magnetism. In particular, for $CaMnBi_2$ previous findings had indicated that the Bi $6p_{x,y}$ bands may play a role in mediating the magnetic exchange between Mn layers.

In both compounds, I observed well-defined magnon spectra consistent with local-moment, semiclassical antiferromagnetism. By use of linear spin-wave theory to describe the neutron spectra, I have identified and quantified all relevant exchange and anisotropy parameters of a Heisenberg model for the two compounds. In both cases, all details of the dispersion are well reproduced by the model and there is no indication of anomalous broadening or dispersion to within experimental precision. The absolute values of the exchange parameters indicate no substantive differences between the compounds (aside from opposite interlayer coupling).

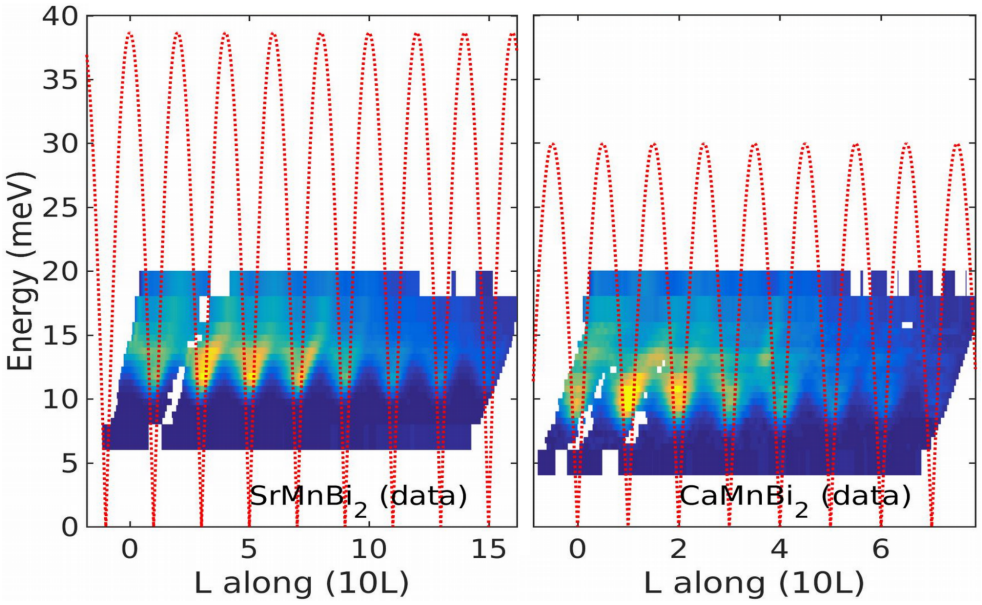

Figure 4.10: Magnon dispersion along the $(10L)$ direction in $SrMnBi_2$ (left) and $CaMnBi_2$ (right), as shown in Figure 4.8 (c,d). The dispersion corresponding to the parameters obtained from the Raman spectroscopy study by Zhang *et al.* [405] are superimposed as a red dashed line.

After completion of this work, a Raman spectroscopic study of $SrMnBi_2$ and $CaMnBi_2$ was reported by Zhang *et al.* [405]. Raman spectroscopy probes the spin dynamics through a small number of characteristic frequencies which are associated with van-Hove singularities in the two-magnon density of states. The authors of Ref. [405] interpret their data using a similar spin Hamiltonian as in this thesis chapter, but without the magnetocrystalline anisotropy term (D in my study). Their analysis yields values for

the spin-exchange parameters J_1 and J_2 that are similar to my results, but produces anomalously large values of the interlayer exchange J_c for both materials (one order of magnitude larger than in my study or in other related materials).

The authors of Ref. [405] suggest that this enhanced coupling is caused by the Bi Dirac bands. I draw attention to the fact that the parameters J_1, J_c, and D are strongly correlated in modelling key features of the magnon dispersion (see Eqs. 4.5 and 4.6), so the neglect of D in the Raman analysis could significantly affect the obtained values of J_c. In Fig. 4.10, I illustrate that the Raman value of J_c would imply a stronger interlayer dispersion of the one-magnon spectrum than that found here directly by neutron spectroscopy, by a factor of 11 (Sr) or 7 (Ca) (see Eq. 4.6). It seems likely, therefore, that the analysis of the Raman spectra has produced erroneously large values for J_c.

I conclude that different routes have to be found to achieve an entanglement of magnetic order and nontrivial band topology. One very promising option is the substitution of magnetic rare-earth ions on the A site, providing a more direct interaction with the relevant Bi layers. In particular, a strong response of the transport properties to rare-earth magnetic order has recently been observed in $EuMnBi_2$ [432], along with the trademark signatures of Dirac transport [433]. Furthermore, recent high-resolution ARPES results and first-principles calculations identify $YbMnBi_2$ as a type-2 Weyl semimetal and postulate canted antiferromagnetic order (see Fig. 4.11) [406]. The latter study further suggests that this state would be tuned to a Dirac metal by spin alignment. Naturally, it would be of great interest to perform analogous inelastic neutron studies of the magnetic ground states in those materials.

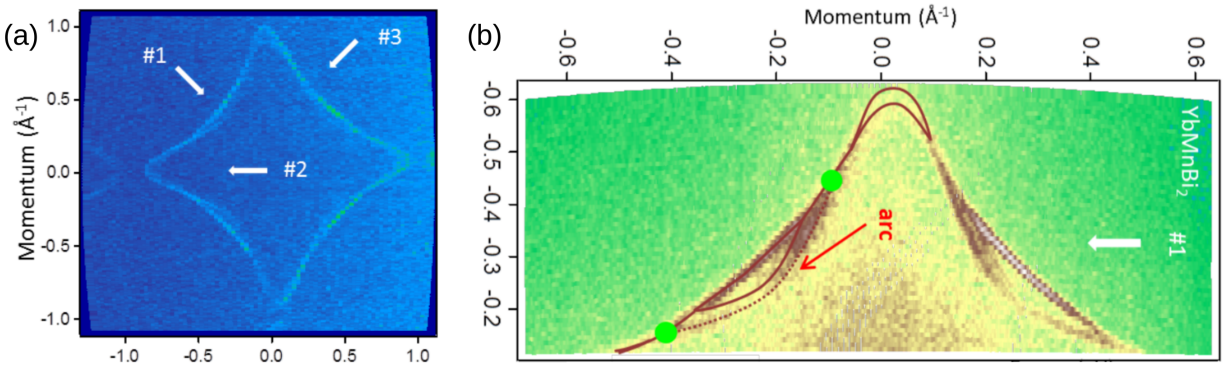

Figure 4.11: (adapted from [406]): High resolution ARPES study of $YbMnBi_2$, which is structurally identical to $CaMnBi_2$. (a) The diamond-shaped Fermi surface is reminiscent of the materials investigated in this thesis. (b) The authors identify a Fermi arc surface state consistent with Weyl nodes that have been predicted in this compound.

Chapter 5

Magnetic ground state of Dirac semimetal candidate $EuCd_2As_2$

$EuCd_2As_2$ is a magnetic semimetal with unusual transport properties. Renewed interest in this material is due to the recent discovery of a bulk Dirac semimetallic state in the related material Cd_3As_2 [254, 259] (see Chapter 1.2.6). The present compound features similar networks of edge-sharing $CdAs_4$ tetrahedra, albeit not in a three-dimensional, but layered configuration. These Cd_2As_2 planes in $EuCd_2As_2$ are separated by trigonal planes of magnetic Eu ions.

Even though preliminary first principles studies indicate the possibility of unusual linear band crossings close to the Fermi surface of $EuCd_2As_2$, experimental evidence is still lacking. In analogy to the preceding Chapter 4 on Mn magnetism in bismuth-based Dirac metals, there is a special interest in the possibility of coupling Dirac fermions to the large Eu^{2+} magnetic moment. The situation in $EuCd_2As_2$ is particularly encouraging as it exhibits a strong resistivity anomaly at the magnetic ordering temperature, $T_N \approx 9.5\,K$, as well as a large negative magnetoresistance.

Since $EuCd_2As_2$ is a strong neutron absorber, it is not feasible to investigate this material by neutron techniques. I have therefore used hard resonant elastic x-ray scattering (REXS) at the Eu L_3 edge to determine the magnetic ground state as well as its evolution in applied magnetic fields. Thus I demonstrate that REXS can be a complex, but powerful alternative to neutron diffraction. Notably, my results contradict previous models of the magnetic state that had been inferred from bulk measurements [401]. My findings will form the basis for an in-depth first principles search for non-trivial band-topology in $EuCd_2As_2$.

Contents

5.1 Introduction 117
5.2 Structural, transport and magnetic measurements 118
5.3 Resonant x-ray scattering at P09 (PETRA-III) 124
5.4 Results 129
5.5 Discussion 132
5.6 Conclusion 139

5.1 Introduction

$EuCd_2As_2$ was first synthesized in polycrystalline form by Artmann *et al.* [434], in the search for novel pnictides with 122 stoichiometry. As in the iron based superconductors discussed in preceding chapters, such materials often crystallize in tetragonal ($I4/mma$) symmetry. By contrast, the so-called *Zintl phases* with a trigonal $CaAl_2Si_2$-type structure ($P\bar{3}m1$) are less common. Magnetometry of these powders revealed ferromagnetic correlations (a positive Curie-Weiss temperature $\Theta_{CW} = 9.3\,K$) and a large effective magnetic moment of $7.7\,\mu_B$, close to the free-ion value of $7.94\,\mu_B$ expected for the divalent state of Eu [434]. An unusual magnetic transition at low temperatures was interpreted as a successive ferromagnetic (16 K) and then antiferromagnetic (9.5 K) ordering of these $S = 7/2$, $L = 0$ magnetic moments in the triangular layers. In a Mössbauer study of single-crystalline $EuCd_2As_2$ [435], a ferromagnetic phase was later ruled out and attributed to Eu^{3+} impurities introduced by oxidation of previous polycrystalline samples.

The present investigation of the material was motivated by the 2014 discovery of a first bulk Dirac semimetallic state in the material Cd_3As_2 [257, 259] (see Section 1.2.6). In analogy to the investigation of $AMnBi_2$ compounds presented in Chapter 4, it would be of great interest to couple 3D topological transport properties of Cd_3As_2, such as giant negative magnetoresistance, to magnetism [436, 256]. With this motivation, my collaborator Dr. Youguo Shi[1] synthesized the present $EuCd_2As_2$ crystals [437]. In the characterization of these samples, an unusual resistivity anomaly was discovered, which is associated with the magnetic phase transition. Within the ordered state, a sizeable negative magnetoresistance effect is observed (albeit in *perpendicular* fields).

Preliminary first principles band structure calculations in the paramagnetic state have indeed indicated the possibility of topologically protected linear crossings of Cd and As bands, in proximity to the Fermi surface [438]. Although Cd_3As_2 features a complex tetragonal superstructure (space group $I4_1cd$) with ordered vacancies and distortions of the fundamental structural motif, the three-dimensional network of edge-sharing $CdAs_4$ tetrahedra is structurally reminiscent of the corresponding Cd-As layers in $EuCd_2As_2$, as illustrated in Fig. 5.1.

Nevertheless, there are several alternative mechanisms which could potentially explain the observed charge transport anomalies, such as (1) the scattering of charge carriers from magnetic fluctuations, (2) the relative shift of Fermi surface pockets, associated with changes in the carrier density of states and mobility and also (3) a Kondo-like mechanism in which itinerant spins become localized in the vicinity of the large local rare earth moments [437].

[1]Beijing National Laboratory for Condensed Matter Physics, Institute of Physics, Chinese Academy of Sciences, Beijing 100190, China

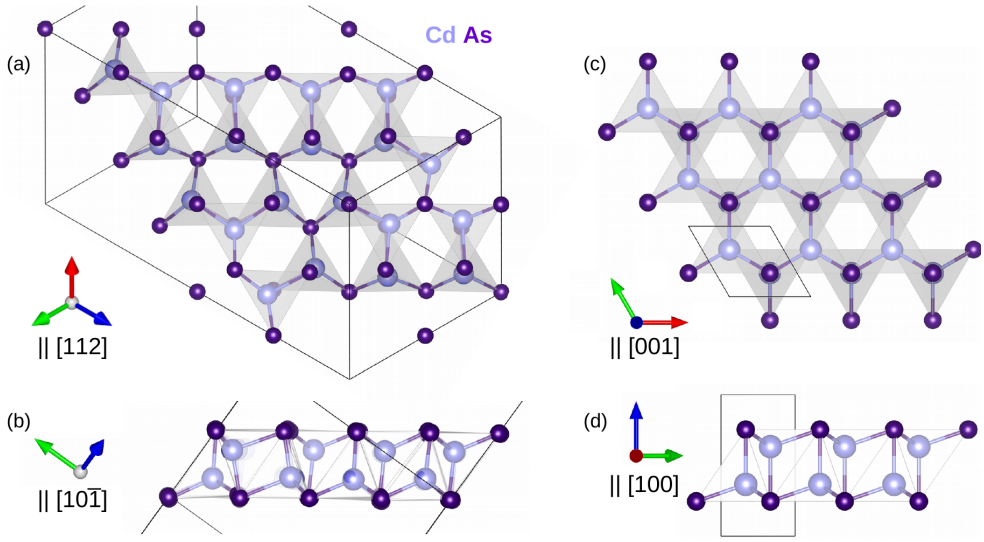

Figure 5.1: Views of Cd–As networks, (a,b) parallel to the [112] planes of Cd_3As_2 and (c,d) in the layers of $EuCd_2As_2$. The two materials share the structural motif of edge-sharing $CdAs_4$ tetrahedra. By comparison to $EuCd_2As_2$, the Cd_3As_2 structure is distorted and features ordered Cd vacancies.

The key to understanding the ground state of this material and to assess a potential relevance of topological anomalies in its electronic band structure is to determine its magnetic ordering mechanism. In fact, a neutron diffraction study had been called for [437], but is not feasible due to the overwhelming thermal neutron absorption cross sections of both Eu (4530 barn) and Cd (2520 barn). On the other hand, the magnetic moments of rare earth ions are known to couple to L edge resonant dipole ($2p \rightarrow 5d$) transitions (see Section 2.4.4). Resonant elastic x-ray scattering (REXS) in the hard x-ray regime (≈ 7 keV) is therefore a promising alternative for magnetic structure determination in this material.

5.2 Structural, transport and magnetic measurements

Single crystals of $EuCd_2As_2$ were prepared by my collaborators Youguo Shi[2] and Yanfeng Guo[3], using the NaCl/KCl flux method previously reported by Schellenberg *et al.* [435]. This yields shiny metallic platelets (c axis surface normal) with dimensions up to ≈ 2 mm and $\approx 500\,\mu$m thickness.

I used Mo K_α x-ray diffraction (at room temperature / see also Section 2.1.3) to confirm the trigonal (space group $P\bar{3}m1$) crystal structure that had been originally determined

[2]Beijing National Laboratory for Condensed Matter Physics, Institute of Physics, Chinese Academy of Sciences, Beijing 100190, China

[3]School of Physical Science and Technology, ShanghaiTech University, Shanghai 201210, China and CAS Center for Excellence in Superconducting Electronics (CENSE), Shanghai 200050, China

	Wyck.	x	y	z	B	occ. (%)
Eu	1a	0	0	0	1.08(6)	100
Cd	2d	1/3	2/3	0.6333(3)	1.27(7)	100
As	2d	1/3	2/3	0.2463(5)	1.09(7)	100

Table 5.1: Results of the refinement of integrated single crystal x-ray diffraction intensities of $EuCd_2As_2$ (as illustrated in Fig. 5.2): Wyckoff sites of space group $P\bar{3}m1$, atomic positions, thermal parameters and site occupations. The observed peaks were indexed in a trigonal cell with lattice parameters $a \approx 4.44$ Å and $c \approx 7.33$ Å.

by Artmann *et al.* [434], and is shown in Fig. 5.2(c,d). The dataset comprised 1077 Bragg reflections, which were indexed in the cell $[a,a,c,90,90,120]$ with $a \approx 4.44$ Å and $c \approx 7.33$ Å. Once this reference system has been assigned, the data can be integrated over a margin perpendicular to selected high symmetry planes of reciprocal space, shown in Fig. 5.2(b). In all directions, the average mosaicity was smaller than the instrumental resolution ($\approx 0.6^o$–0.9^o), which proves the high crystalline quality of these samples.

I also performed a Rietveld refinement of the integrated Bragg intensities (FullProf algorithm [382]). The best fit to the data is shown in Fig. 5.2(a). Due to the heavy elements, absorption effects are strong and the comparison factor of equivalent reflections is high, $R_{\text{int}} = 14\%$. Nevertheless, a satisfactory refinement ($R_F = 3.74$) was achieved. The obtained atomic parameters, listed in Table 5.1, are consistent with literature [434, 435]. The refinement of atomic occupation factors also confirmed the ideal stoichiometry of the sample.

Magnetic measurements had been previously reported for polycrystalline samples [434], and on single crystals with the field applied along an arbitrary direction [435]. I complemented these results with detailed SQUID magnetometry (see Section 2.1.1), with a magnetic field applied either along the a or c axis, as summarized in Fig. 5.3. The temperature sweeps reveal a magnetic ordering transition with unusual characteristics. A Curie-Weiss divergence of the magnetization is seen around 16 K. However, this ferromagnetic-like transition is arrested at $T_N = 9.5$ K, where antiferromagnetism sets in.

This behaviour is consistent with previous studies [434, 435], and had been interpreted as two distinct consecutive ferro- and antiferromagnetic phases by some authors [434]. However, these earlier studies had not been direction-selective. In the left and right panels of Fig. 5.3(a) I compare data obtained with the magnetic field parallel to the a and c axes, respectively. This reveals that the magnetic state is strongly anisotropic, with an in-plane susceptibility ≈ 7 times larger than the out-of-plane susceptibility. The in-plane response is also *qualitatively* different, in that it appears to saturate (around 12 K, see 5 mT data) and form a plateau, 2–3 K before onset of antiferromagnetism.

The comparison of temperature sweeps recorded in field-cooled (FC) and zero-field-

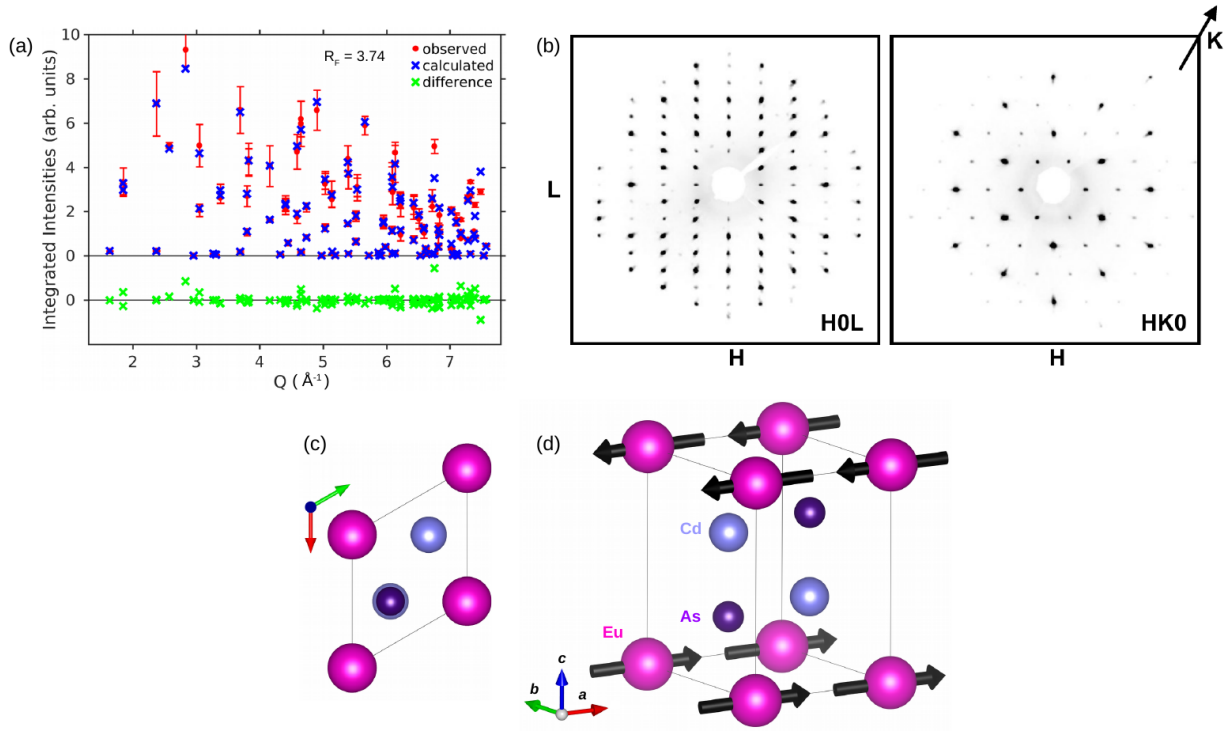

Figure 5.2: Room temperature Mo K_α four circle x-ray diffraction of a $\approx 200\,\mu$m $EuCd_2As_2$ crystallite. (a) Integrated intensities sorted by momentum transfer Q, along with the refined values (FullProf [382]) and the corresponding differences. (b) Integration of the dataset over a small margin perpendicular to the $(H0L)$ and $(HK0)$ reciprocal lattice planes. (c,d) Top and perspective view of the trigonal structure of $EuCd_2As_2$. A model of the $\boldsymbol{q}_\mathrm{m} = (0,0,1/2)$ antiferromagnetic order inferred from the REXS experiment is also drawn.

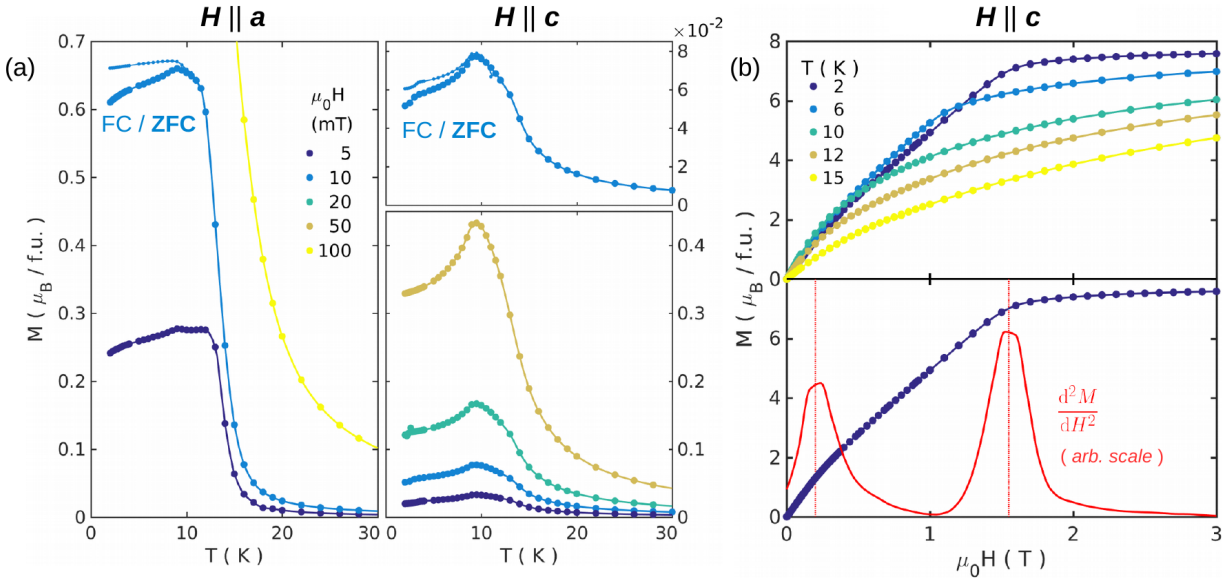

Figure 5.3: Direction-resolved SQUID magnetization measurements of $EuCd_2As_2$. (a) Low-temperature thermal variation of the magnetization in magnetic fields between 5 and 100 mT applied along the a axis (left panel) and c axis (right panels). (b) Field sweeps of the magnetization at temperatures between 2 and 15 K, in a field oriented almost parallel to the c axis. The lower panel indicates two changes in slope (at 0.2 and 1.55 T), emphasized by the second derivative of the 2 K $M(H)$ curve (arbitrary scale).

cooled (ZFC) conditions shows a splitting, which is more significant for $\boldsymbol{H} \parallel \boldsymbol{c}$ ($\approx 10\%$). For very low applied fields, $\mu_0 H < 50$ mT, an additional transition appears in the out-of-plane susceptibility, seen as an additional decrease of the signal (reaching ≈ 3 K at the lowest field, 5 mT).

Field sweeps of the out-of-plane magnetization are shown in Fig. 5.3(b). As reported earlier, the saturation magnetization approaches the value of $7.94\,\mu_B$ expected for an ideal Eu^{2+} ($4f^7$, $S = 7/2$, $L = 0$) state [434, 435]. At base temperature (2 K), this saturation is achieved already in a relatively low field of 1.55 T. This data of spin-alignment along the c axis shows no indication of a spin-flop transition. Instead, only a weak change in slope is observed at 200 mT (at 2 K), as indicated by the second derivative curve in the bottom panel of Fig. 5.3(b).

A detailed explanation of all the subtle magnetometry features noted above is provided in the context of the REXS data in Section 5.5.

In order to characterize the electronic transport properties of $EuCd_2As_2$, I performed alternating current transport (ACT) measurements using the six-point sample contacting geometry discussed in Section 2.1.2. The sample used in this measurement is shown in Fig. 2.1(a). The field was applied along the c axis throughout. In the top and bottom panels of Fig. 5.4, I summarize the low temperature characteristics of the longitudinal resistivity ρ_{xx} and transversal (Hall) resistivity ρ_{xy}, respectively.

Above $\approx 80\,\mathrm{K}$, the thermal variation of the resistivity shows a weak semimetallic behaviour (Fig. 5.4(a) and inset). However, at lower temperatures, the resistivity increases by up to 100% and forms an acute peak at $T_\mathrm{N} = 9.5\,\mathrm{K}$. This is reminiscent of the corresponding magnetization characteristics (Fig. 5.3(a)), although the anomalous resistive contributions set in at even higher temperatures $\approx 50\,\mathrm{K} \approx 5\,T_\mathrm{N}$. When a magnetic field is applied (out-of-plane), this resistivity peak splits into two broad features: (1) One with a leading edge that moves to higher temperatures in higher fields and (2) Another contribution separated by a dip (minimum) of ρ_{xx}. By comparison with the magnetization data, it can be inferred that this minimum corresponds to the magnetic phase boundary, and, accordingly, disappears with the complete spin-alignment at $1.55\,\mathrm{T}$.

The field sweeps of this resistivity signal (Fig. 5.4(c)) emphasize a strong negative magnetoresistance, corresponding to a $\approx 75\%$ reduction of the measured signal. Within the magnetically ordered phase, the negative magnetoresistance is clearly associated with the spin-alignment, as it abruptly saturates at the upper phase boundary at $1.55\,\mathrm{T}$. Notably, the observed minimum resistivity of $2\,\mathrm{m\Omega cm}$ is significantly lower than the minimum in resistivity that one would extrapolate from the high-temperature slope ($\approx 3\,\mathrm{m\Omega cm}$, see inset of Fig. 5.4(a)). This implies that the negative magnetoresistance inside the ordered phase is not merely due to the suppression of additional scattering processes associated with antiferromagnetic order. Another magnetoresistive feature is observed at temperatures *above* the ordering transition. It does not set in continuously, but is delineated by a clear kink in the field sweep (see data for $20\,\mathrm{K}$ in Fig. 5.4(c) and inset).

The features discussed above can all be recognized in the phase diagram of interpolated resistivity data presented in Fig. 5.4(e). Here, the magnetically ordered phase corresponds to a bright patch with a white-to-red gradient. The regime of strong negative magnetoresistance appears as a dark-red-to-black gradient and forms a diagonal phase line from the ordered phase towards high fields and high temperatures.

The characteristics of the Hall resistivity are summarized in the corresponding lower panels (b,d,f) of Fig. 5.4 and are governed by a similar phase diagram. In particular, the effective charge transport is electron-like and is superposed by *two* anomalous contributions: (1) One which is confined to the magnetically ordered phase and (2) a distinct Hall contribution associated with the spin-polarized state, which is clearly delineated by a diagonal phase line.

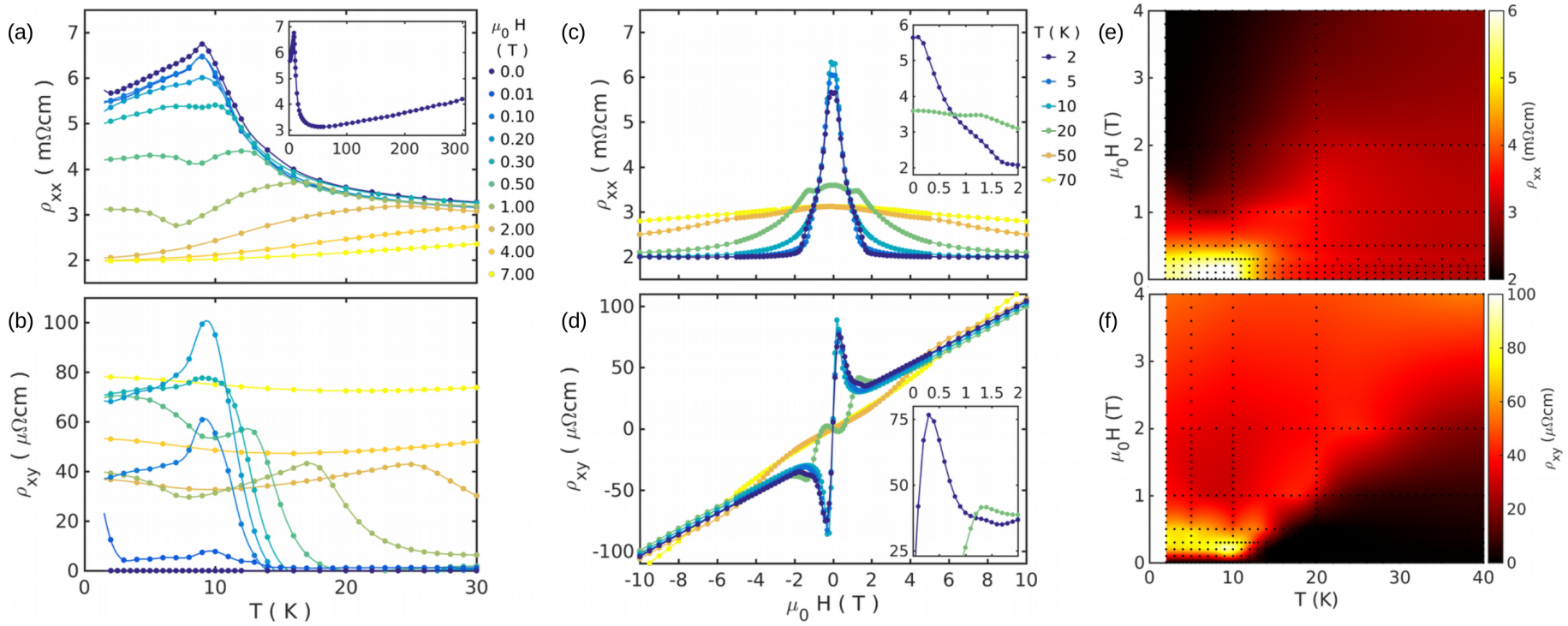

Figure 5.4: Alternating current six-point transport data of $EuCd_2As_2$, recorded with a 5 mA, 30 Hz excitation and magnetic fields applied along the c axis. The characteristics of the longitudinal resistivity ρ_{xx}, and transversal (Hall) resistivity ρ_{xy} are summarized in the top and bottom panels, respectively. (a,b) Thermal variation at magnetic fields between 0 and 7 T, applied along the c axis. (c,d) Field sweeps at temperatures between 2 and 70 K. The insets give a magnified view of subtle features in the low temperature data. (e,f) Phase diagrams created by colour maps of interpolated data. Black markers indicate the actual location of data points.

5.3 Resonant x-ray scattering at P09 (PETRA-III)

With the aim to determine the magnetic structure of $EuCd_2As_2$, I performed two REXS experiments in the second experimental hutch (EH2) of beamline P09 [439] at PETRA-III (DESY, Hamburg). In these experiments, single crystals of $EuCd_2As_2$ were probed with a magnetic field applied perpendicular and parallel to the c axis, respectively. EH2 has three unique advantages for the present study: (1) Up to high energies (3.2–14 keV), the angle of the incident linear x-ray polarization can be rotated using a pair of diamond phase plates [440]. (2) The diffractometer holds a cryomagnet for vertical applied fields up to 14 T (Fig. 5.5(d)). (3) By contrast to commonly used closed cycle refrigerators, the sample space of the top-loading liquid helium cryostat is filled with exchange gas, which reduces the effects of beam heating and allows base temperatures of ≈ 2.3 K.

The scattering geometry and sample environment of EH2 is illustrated in Fig. 5.5. The experiment is performed in horizontal scattering. The hard x-ray beam penetrates the cryostat through thin beryllium windows, which imposes constraints on the detector angles 2θ (azimuth) and γ (elevation). To avoid a tilting of the heavy cryostat (χ axis), the instrument is effectively used as a two-circle diffractometer (with scattering angle 2θ and a parallel sample rotation axis ω). Small misalignments of the sample can be compensated by an elevation of the detector out of the horizontal plane ($-5^\circ < \gamma < 5^\circ$). In principle, this tilts the scattering plane away from that shown in Fig. 5.5(a,b), which complicates the polarization analysis. However, as only peaks with $\gamma < 1.5^\circ$ were investigated, I neglect this effect in the data analysis. Since the incident energy is fixed in a REXS experiment, a constraint in 2θ (see inset of Fig. 5.5(d)) also implies strict limits on the accessible ranges of momentum transfer Q.

For these reasons, the sample must be oriented and mounted strategically (details of this procedure are noted in Section 2.1.3). Fig. 5.6 illustrates such planning of the scattering geometry in the case of the $\boldsymbol{H} \parallel \boldsymbol{c}$ sample. In this case, it was desirable to access a $(H,0,-1/2)$-type magnetic Bragg peak with largest possible index H. A crystal was first polished with a surface parallel to the $[100]$ crystal planes (which do not grow naturally / see Fig. 5.6(a)). A dedicated brass (non-magnetic) sample holder was then micro-machined with a 5° offset, such that the $(4,0,-1/2)$ direction is in the scattering plane and the field is applied only 5° from the c axis, see Fig. 5.6(a,b). As shown in Fig. 5.6(d), this left a narrow margin in reciprocal space in which $(H,K,-1/2)$-type peaks were accessible, delineated by the constraints in γ and 2θ.

To study the magnetic x-ray scattering from Eu^{2+} magnetic ions, the undulator energy was tuned to the Eu L_3 edge at $\hbar\omega \approx 6.972$ keV ($\lambda = 1.778$ Å). At this energy, the estimated x-ray penetration depth in $EuCd_2As_2$ is $\approx 6.3\,\mu$m, and the observed signal is therefore dominated by the bulk of the sample. The polarization of the scattered beam can be

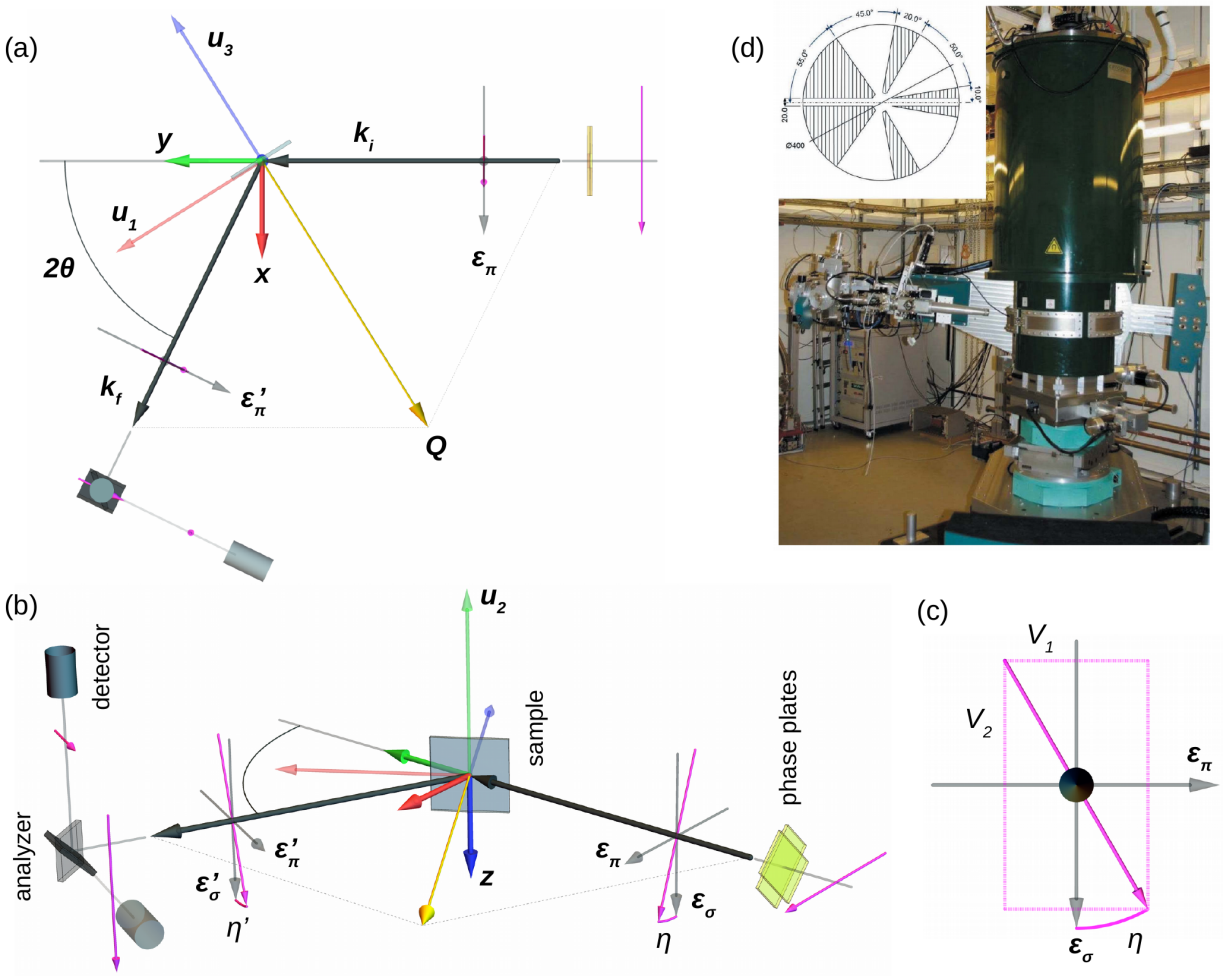

Figure 5.5: (a) Schematic of the horizontal scattering setup in the second experimental hutch of instrument P09, PETRA-III. The scattering triangle ($\boldsymbol{k}_i$, $\boldsymbol{k}_f$, $\boldsymbol{Q}$) for an arbitrary scattering angle 2θ is shown, along with the definitions of the laboratory reference frame $(\boldsymbol{x},\boldsymbol{y},\boldsymbol{z})$ and the conventional scattering reference frame $(\hat{\boldsymbol{u}}_1,\hat{\boldsymbol{u}}_2,\hat{\boldsymbol{u}}_3)$. (b) Perspective view of (a), illustrating the orientation of the incident ($\hat{\varepsilon}_\sigma$, $\hat{\varepsilon}_\pi$) and scattered ($\hat{\varepsilon}'_\sigma$, $\hat{\varepsilon}'_\pi$) polarization vectors as well as the corresponding polarization angles η and η'. (c) Definition of the amplitudes of the linearly polarized light, parallel (V_1) and perpendicular (V_2) to the scattering plane (view towards the beam). (d) (from [439]) Photograph of the diffractometer carrying the heavy cryomagnet. The inset indicates which ranges of 2θ are accessible through the beryllium windows of the cryostat (blocked range shaded). Out of plane, the accessible detector elevation is $\gamma \approx \pm 5^{\circ}$, if the sample is vertically centred with respect to the windows.

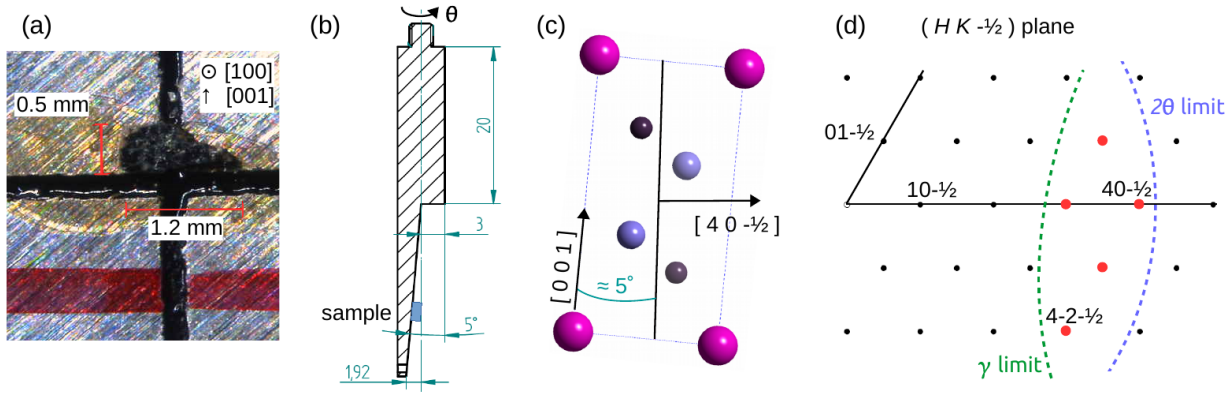

Figure 5.6: (a) Photograph of the crystal that was aligned and polished for $\boldsymbol{H} \parallel \boldsymbol{c}$-measurements. A surface parallel to the $[1,0,0]$ crystallographic planes has been prepared. (2) Technical drawing of a micro-machined sample holder for horizontal scattering with a 5° offset from the sample surface. (c) Unit cell of $EuCd_2As_2$ viewed along the (100) direction. The $[4,0,-1/2]$ crystallographic plane is indicated by a black line. (d) View of the $(H,K,-1/2)$ plane of reciprocal space investigated in this sample. The dashed lines mark the constraints imposed by the maximum scattering angle (2θ) and the vertical aperture of the Be windows (γ). Accessible $\boldsymbol{q}_m = (0,0,1/2)$ magnetic peaks are indicated by red markers.

determined by inserting an evacuated rotating analyzer arm into the beam path [439]. Inside the polarization analyzer arm, the outgoing beam was scattered from the $[110]$ planes of a polished Cu crystal. At the magnetic resonance, the Cu (110) scattering angle is $2\theta = 89.4°$. Thus, only $\cos^2 2\theta = 0.01\%$ of the components of the scattered light that are linearly polarized in the polarization analyzer scattering plane are transmitted. A scan of the analyzer arm from $-15°$ to $105°$ therefore corresponds to a scan of the outgoing linear polarization angle η' from $105°$ to $-15°$ (see definitions in Fig. 5.5(b)).

The relevant polarization directions and angles and reference frames are defined in Fig. 5.5(a–c). By convention, the REXS scattering process is described in the reference system $(\hat{\boldsymbol{u}}_1, \hat{\boldsymbol{u}}_2, \hat{\boldsymbol{u}}_3)$, as introduced in Section 2.4.4:

$$\begin{aligned} \hat{\boldsymbol{u}}_1 &= (\hat{\boldsymbol{k}}_i + \hat{\boldsymbol{k}}_f)/(2\cos\theta) \\ \hat{\boldsymbol{u}}_2 &= (\hat{\boldsymbol{k}}_i \times \hat{\boldsymbol{k}}_f)/(2\sin 2\theta) \\ \hat{\boldsymbol{u}}_3 &= (\hat{\boldsymbol{k}}_i - \hat{\boldsymbol{k}}_f)/(2\sin\theta) \end{aligned} \tag{5.1}$$

Linear polarization vectors are labelled π and σ for polarization parallel and perpendicular to the scattering plane, respectively. Since the undulator radiation is highly linearly polarized in the horizontal plane, in the present horizontal scattering geometry the default incoming polarization is $\hat{\boldsymbol{\varepsilon}}_\pi$ ($\eta = 90°$).

The scattered polarization vectors are labelled by π' and σ'. In the $\hat{\mathbf{u}}_i$ reference frame, these orthogonal polarization vectors are given by

$$\begin{aligned}\hat{\boldsymbol{\varepsilon}}_{\sigma} &= \hat{\boldsymbol{\varepsilon}}_{\sigma'} = -\hat{\boldsymbol{u}}_2 \\ \hat{\boldsymbol{\varepsilon}}_{\pi} &= \sin\theta\,\hat{\boldsymbol{u}}_1 - \cos\theta\,\hat{\boldsymbol{u}}_3 \\ \hat{\boldsymbol{\varepsilon}}_{\pi'} &= -\sin\theta\,\hat{\boldsymbol{u}}_1 - \cos\theta\,\hat{\boldsymbol{u}}_3\end{aligned} \tag{5.2}$$

As introduced in Section 2.4.4, x-ray scattering amplitudes can be be expressed as a 2×2-matrix in this (π/σ) basis. The scattering amplitude for arbitrary incoming and outgoing linear polarization angles η and η' is then given by the matrix product

$$F \propto \hat{\boldsymbol{\varepsilon}}_f \cdot \begin{pmatrix} \sigma\sigma' & \pi\sigma' \\ \sigma\pi' & \pi\pi' \end{pmatrix} \cdot \hat{\boldsymbol{\varepsilon}}_i \quad \text{, with} \quad \hat{\boldsymbol{\varepsilon}}_i = \begin{pmatrix} \cos\eta \\ \sin\eta \end{pmatrix} \quad \text{and} \quad \hat{\boldsymbol{\varepsilon}}_f = \begin{pmatrix} \cos\eta' \\ \sin\eta' \end{pmatrix} \tag{5.3}$$

As introduced in Chapter 2, the REXS amplitude has a complex dependence on the relative orientations of the magnetic moments, x-ray polarization and wave vectors. In the case of dominant electric dipole (E1) excitations, it takes the following form [338]:

$$\begin{aligned} F_{E1} \propto \left(\hat{\boldsymbol{\varepsilon}}_f \times \hat{\boldsymbol{\varepsilon}}_i\right) \cdot \hat{\boldsymbol{M}}_{\hat{\mathbf{u}}} &= \begin{pmatrix} 0 & \hat{\boldsymbol{k}}_i \\ -\hat{\boldsymbol{k}}_f & \hat{\boldsymbol{k}}_f \times \hat{\boldsymbol{k}}_i \end{pmatrix} \cdot \hat{\boldsymbol{M}}_{\hat{\mathbf{u}}} \\ &= \begin{pmatrix} 0 & M_1^{\hat{\mathbf{u}}}\cos\theta + M_3^{\hat{\mathbf{u}}}\sin\theta \\ M_3^{\hat{\mathbf{u}}}\sin\theta - M_1^{\hat{\mathbf{u}}}\cos\theta & -M_2^{\hat{\mathbf{u}}}\sin 2\theta \end{pmatrix} , \end{aligned} \tag{5.4}$$

where $\hat{\boldsymbol{M}}_{\hat{\mathbf{u}}}$ refers to the magnetic structure factor vector in the $\hat{\boldsymbol{u}}_i$ reference frame defined in Eq. 5.1. As discovered in this experiment, the antiferromagnetic state of $EuCd_2As_2$ has a magnetic propagation vector $\boldsymbol{q}_\mathrm{m} = (0,0,1/2)$ and its magnetic unit cell therefore contains only two, antiparallel, magnetic moments $\boldsymbol{m}$ at $\boldsymbol{r}_1 = (0,0,0)$ and $-\boldsymbol{m}$ at $\boldsymbol{r}_2 = (0,0,c)$. The magnetic structure factor vector in the reference frame of the crystal is therefore

$$\boldsymbol{M}_\mathrm{cryst} = \sum_i \boldsymbol{m}_i\, e^{i\,\boldsymbol{q}_\mathrm{m}\cdot\boldsymbol{r}_i} \to 2\,\boldsymbol{m} \quad . \tag{5.5}$$

With the knowledge of $\boldsymbol{q}_\mathrm{m}$, the determination of the magnetic structure thus reduces to the determination of the orientation of $\boldsymbol{m}$. For convenience, I parametrized the direction of this antiferromagnetic orientation by the azimuth ψ_m and elevation α_m:

$$\hat{\boldsymbol{M}}_\mathrm{cryst} = \begin{pmatrix} \cos\alpha_\mathrm{m}\cos\psi_\mathrm{m} \\ \cos\alpha_\mathrm{m}\sin\psi_\mathrm{m} \\ \sin\alpha_\mathrm{m} \end{pmatrix} \tag{5.6}$$

This vector can be transformed to the diffractometer-, laboratory-, and finally to the

$\hat{\boldsymbol{u}}_i$–reference-frame, as follows [441]:

$$\hat{\boldsymbol{M}}_{\hat{\mathbf{u}}} = \mathrm{A} \cdot \hat{\boldsymbol{M}}_{\mathrm{lab}} = \mathrm{A} \cdot \Omega \cdot \hat{\boldsymbol{M}}_{\mathrm{diff}} = \mathrm{A} \cdot \Omega \cdot \mathrm{U} \cdot \hat{\boldsymbol{M}}_{\mathrm{cryst}} \tag{5.7}$$

with unitary orientation matrix U and the rotation matrices

$$\mathrm{A} = \begin{pmatrix} \sin\theta & \cos\theta & 0 \\ 0 & 0 & -1 \\ -\cos\theta & \sin\theta & 0 \end{pmatrix} \quad \text{and} \quad \Omega = \begin{pmatrix} \cos\omega & \sin\omega & 0 \\ -\sin\omega & \cos\omega & 0 \\ 0 & 0 & 1 \end{pmatrix} \tag{5.8}$$

The transformation A is specific to the definition of the laboratory reference frame $(\hat{\boldsymbol{x}}, \hat{\boldsymbol{y}}, \hat{\boldsymbol{z}})$ shown in Fig. 5.5. The unitary matrix U describes the orientation of the crystal relative to the sample holder and is obtained from the indexing of two Bragg reflections [441].

To characterize the tensor properties of the magnetic scattering cross section in more detail, I used the full polarization analysis (FPA) method. To perform a FPA scan, a pair of phase retarding $\lambda/2$ diamond planes (300 μm thickness, $\approx 48\,\%$ transmission) is inserted in the incoming beam [440, 439]. This allows a continuous rotation of the angle η of the incident linear polarization (indicated in Fig. 5.5(c)).

The FPA method is described in detail in Appendix C. First, a given magnetic reflection was centred in the detector. The incoming polarization was then rotated in steps between $\eta = -90^{\circ}$ and 90°. For each incoming polarization, the polarization analyzer was then moved in steps over a similar angular range. For each selected outgoing linear polarization angle η', a rocking scan (θ_{P}) of the polarization analyzer crystal was performed. For each incident polarization η, one thus obtains a sinusoidal curve (of integrated intensities from Lorentzian fits to θ_{P} scans), as a function of η'.

The polarization state of the scattered x-ray beam is described by the Poincaré-Stokes parameters (P_1', P_2', P_3'), as defined in Eq. C.3 of Appendix C. In effect, these parameters measure whether the linear polarization is parallel to the main polarization axes ($|P_1'|$), rotated by 45° from a main polarization axis ($|P_2'|$), or whether it contains circularly polarized components ($|P_3'|$). By definition, the η' curve of integrated θ_{P} scans will therefore be cosine-like for $P1'$ scattered polarization and sine-like for $P2'$:

$$I_{\eta'} = I_0 \left(1 + P1' \cos\left(2\eta'\right) + P2' \sin\left(2\eta'\right)\right) \tag{5.9}$$

In Fig. C.1, Appendix C, I illustrate these characteristics for a FPA scan of the direct beam as rotated by the P09 phase plate device [440]. The evaluation of FPA scans can be complicated by varying conventions of reference frames, and some care must be taken since one sign error will significantly influence the inferred information. On the other hand, this method has the great advantage that no diffractometer angle is moved

throughout the scan. This precludes several possible sources of systematic errors, such as drifting alignment, a varying beam cross section on the sample and self-absorption.

As an alternative to FPA, the polarization dependence of the scattering cross section can also be probed in *azimuthal (ψ) scans*, i.e. by rotation of the sample around the momentum transfer axis. In the course of my thesis I have also used this type of technique [150]. Since ψ is not normally a physical axis, it is usually required to re-align the sample position and orientation after each azimuthal step. Even so, the ψ scans may be complicated by other azimuth-dependent phenomena such as multiple scattering. P09 is presently the only hard REXS instrument that offers the thick diamond phase plate setup necessary for FPA at hard x-ray energies [440].

5.4 Results

After aligning and cooling the sample to base temperature ($\approx 2.3\,\mathrm{K}$), I first determined that the magnetic propagation vector in $EuCd_2As_2$ is $\boldsymbol{q}_\mathrm{m} = (0,0,1/2)$. This is consistent with other magnetic materials of the same structural family for which neutron studies have been possible, such as $EuMn_2P_2$ [442] and $EuAl_2Si_2$ [443]. The magnetic character of these peaks was confirmed by scanning the incident energy over the resonance, while keeping $\boldsymbol{Q}$ fixed. In Fig. 5.7(a) I compare such an energy scan of the $(0,0,3.5)$ reflection (measured without polarization analysis) with the x-ray fluorescence background. In addition to the fluorescence, the observed reflection contains a strong Lorentzian peak centred in the pre-edge region at 6972 eV. This undulator energy was selected for the remainder of the experiment.

After locating the magnetic Bragg peaks, I tracked the field and temperature dependence of integrated magnetic intensities in the $\pi\sigma'$ and $\pi\pi'$ polarization channels. Given the form of the scattering amplitude, Eq. 5.4 (with reference to the $\hat{\boldsymbol{u}}_i$ reference frame shown in Fig. 5.5), these channels probe magnetic Fourier components parallel and perpendicular to the scattering plane, respectively. Fig. 5.7(b) shows the thermal variation of these intensities for the $(4,0,-1/2)$ peak, for zero field and for 0.5 T applied 5° from the c axis.

The $\pi\sigma'$ channel shows a clear order parameter behaviour, which I fitted with a power law. The obtained Néel temperatures are $T_\mathrm{N} = 8.43(3)\,K$ (0 T) and 8.08(2) K (0.5 T). By attenuating the beam, I confirmed that the reduction by $\approx 1\,\mathrm{K}$ from the expected value is due to beam heating. Notably, beam heating did *not* affect the FPA scans (discussed below), since the beam is attenuated by insertion of the phase plates. The critical exponent obtained from the power-law fit is $\beta = 0.34(1)$ (0 T). This agrees with the values expected for the 3D Ising model ($\beta = 0.3250$) or 3D xy-antiferromagnet ($\beta = 0.3460$). This points

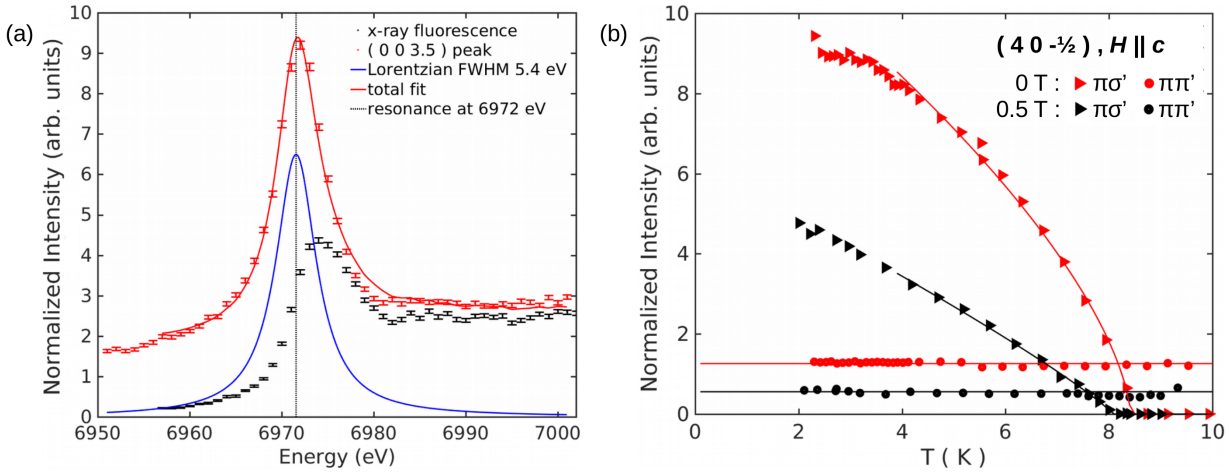

Figure 5.7: (a) Energy scans at the Eu L_3 resonance, recorded without polarization analysis of the scattered beam. The magnetic resonance at the $(0,0,3.5)$ reflection can be decomposed into a contribution due to x-ray fluorescence (black markers) and a Lorentzian peak centred in the pre-edge region, at 6972 eV. (b) Temperature dependence of the $(4,0,-1/2)$ peak, recorded at zero field (red) and 0.5 T applied along the c axis (black). The solid lines indicate power law fits to the data ($T_N = 8.43(3)$, $\beta = 0.34(1)$ for $\pi\sigma'$ at 0 T). The $\pi\pi'$ channel contains a strong fluorescence background, but no magnetic contribution (see text).

to a three-dimensional character of the antiferromagnetic state in $EuCd_2As_2$ [444], although β may also be altered by beam heating.

The $\pi\pi'$ intensity of the $(4,0,-1/2)$ peak in Fig. 5.7(b) shows no thermal variation, which indicates that there are no sizeable $\boldsymbol{q}_m$ magnetic Fourier components perpendicular to the scattering plane, i.e. parallel to the c-axis. Instead, the $\pi\pi'$ channel contains a strong x-ray fluorescence background signal proportional to $|\cos 2\theta|^2$ (see Section 2.4).

The field dependences of three magnetic peaks at base temperature (2.3 K) are shown in Fig. 5.8. Again, the $(0,0,4.5)$ and $(1,0,4.5)$ peaks correspond to an in-plane magnetic field, whereas for $(4,0,-1/2)$, the c axis is directed 5° away from the magnet axis. Both $\boldsymbol{H} \perp \boldsymbol{c}$-type peaks show a transition at a low field of ≈ 50 mT, where magnetically scattered intensity changes abruptly form the $\pi\pi'$ to the $\pi\sigma'$ channel. As noted above, this implies a switching of antiferromagnetic Fourier components, which are initially perpendicular to the scattering plane, into the scattering plane. By 0.5 T applied in-plane, the $\pi\sigma'$ intensity has also completely subsided. At this point the sample is fully spin-polarized, i.e. all magnetic intensity would be located at the Γ point of the Brillouin zone.

A very different behaviour is observed for the almost $\boldsymbol{H} \parallel \boldsymbol{c}$-like situation shown in Fig. 5.8(c). Here, the $\pi\pi'$ channel is flat (no component perpendicular to the scattering plane). The intensity in the $\pi\sigma'$ channel varies little up to ≈ 0.4 T and then decreases monotonically. By contrast to panels (a) and (b), a much larger field of ≈ 1.5 T is required

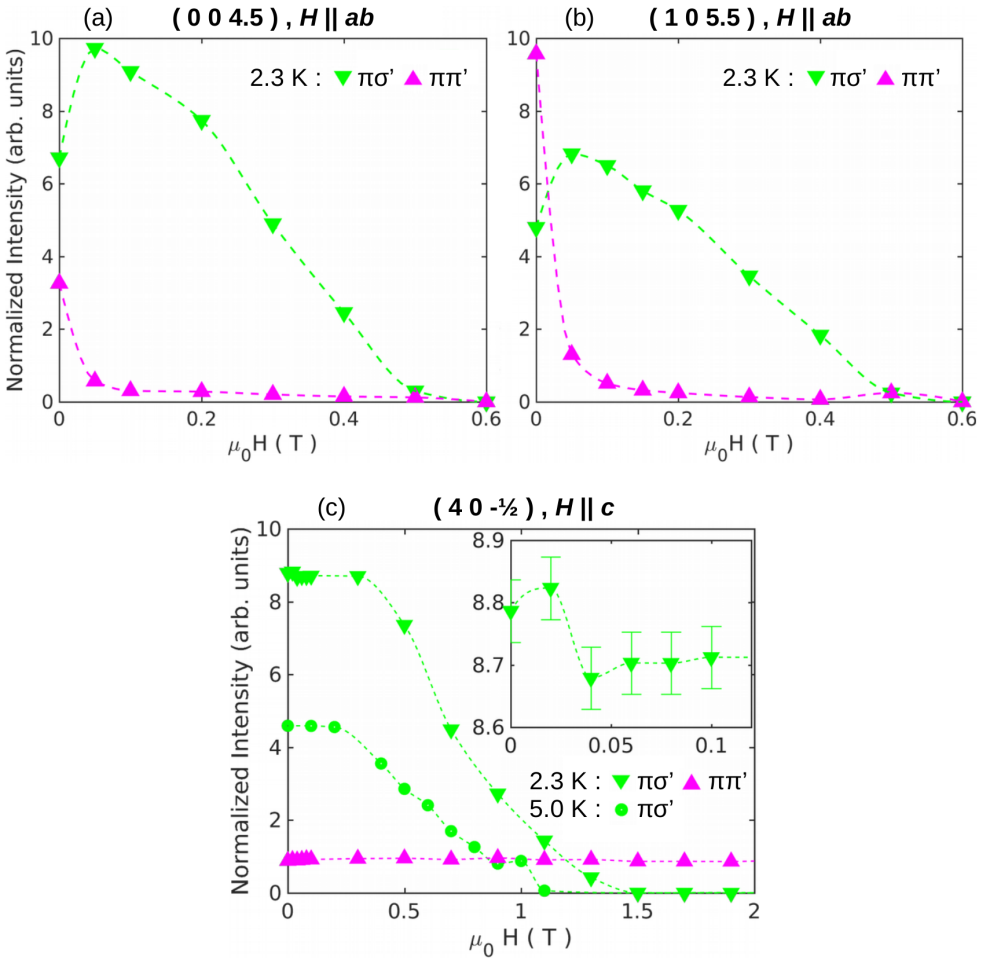

Figure 5.8: Field dependence of $EuCd_2As_2$ resonant magnetic x-ray scattering observed in the $\pi\sigma'$ and $\pi\pi'$ polarization channels. (a) For fields applied in the a-b plane of the crystal, the scattered intensity abruptly switches from $\pi\pi'$ to $\pi\sigma'$ character at $\approx 50\,\mathrm{mT}$ and is then fully suppressed at $\approx 0.5\,\mathrm{T}$. (b) When a magnetic field is applied parallel to the c-axis, $\approx 1.5\,\mathrm{T}$ is required to spin-polarize the sample. The anomaly at 50 mT is seen as a small decrease in $\pi\sigma'$ intensity (inset, explanation in the main text). Dashed lines are intended as visual guides.

to spin-polarize the material (at 2.3 K), which is consistent with the magnetization field sweeps shown above in Fig. 5.3(b). In the inset of Fig. 5.8(c), I draw attention to an abrupt $\approx 1\%$ decrease in $\pi\sigma'$ intensity at $\approx 40\,\mathrm{mT}$. This very subtle feature is also captured by the picture of the magnetic ground state established in Section 5.5.

For the purpose of FPA scans, I selected and probed two peaks in either experimental setting. In particular, in the first experiment ($\boldsymbol{H} \perp \boldsymbol{c}$ setting), I characterized the $(0,0,4.5)$ and $(1,0,5.5)$ peaks in zero field as well as in applied fields of 50 and 300 mT. In the second experiment ($\boldsymbol{H} \parallel \boldsymbol{c}$ setting, cf. Fig. 5.6), I investigated the $(4,0,-1/2)$ and $(4,-2,-1/2)$, in zero field and in applied fields of 0.5 and 1.0 T.

For each case, I determined the Poincaré-Stokes parameters (P_1', P_2') of the scattered beam as described in Appendix C. For each situation (field direction and magnitude), I then performed simultaneous least squares fits of the polarization characteristics of the corresponding pair of magnetic reflections. The results of this procedure are summarized in Figs. 5.9 ($\boldsymbol{H} \perp \boldsymbol{c}$) and 5.10 ($\boldsymbol{H} \parallel \boldsymbol{c}$).

5.5 Discussion

As a first observation, several datasets (Fig. 5.9(a) and 5.10(a,d,g)) show a significant reduction in the degree of linear polarization of the scattered beam ($P'_{\mathrm{lin}} = \sqrt{P_1'^2 + P_2'^2}$, see green markers). In the corresponding η' curves (cf. Eq. 5.9, and Fig. C.1), this manifests as a non-vanishing residual intensity in the minimum of the curve. I considered several factors that may cause this effect:

1. Due to an improper alignment of the phase retarder setup, the incoming beam may not be perfectly linearly polarized. This can be ruled out given the characterization of the direct beam shown in Appendix C, Fig. C.1. For any angle of incoming polarization η, the beam had an excellent $P_{\mathrm{lin}} > 97\%$.

2. Linearly polarized light can acquire circular components by scattering from helical spin structures. Such a long-range modulated structure would correspond to an incommensurate magnetic propagation vector, which is clearly at odds with the present case of $\boldsymbol{q}_{\mathrm{m}} = (0, 0, 1/2)$.

3. Circular components may also arise from the higher order term in the electric dipole (E1) part or from the electric quadrupole (E2) resonances in the REXS scattering amplitude. For the L_3 edge of Eu^{2+}, direct excitations of the magnetic shells ($2p_{\frac{3}{2}} \rightarrow 4f$) are actually of quadrupolar character, while the (stronger) E1 transition excites electrons the unoccupied $5d$ shell and thus couples only indirectly to $4f$ magnetic moments. The relevance of quadrupolar contributions at rare earth L_3 edges has been noted in the literature [338], and the interference of E1 and E2 contributions as been investigated by Mazzoli *et al.* [445] at the Cr K edge. However, the dipolar and quadrupolar contributions should be separated in energy, and this is not observed in the present fluorescence scan (see Fig. 5.7). Even when including the intricate quadrupolar terms in the scattering cross section (and thus adding five additional fit parameters) I was not able to reproduce the present data.

4. The effective observed Stokes parameters may also vary if the signal contains sizeable contributions from charge scattering or fluorescence background. These contributions may interfere coherently or occur independently (i.e. added intensities).

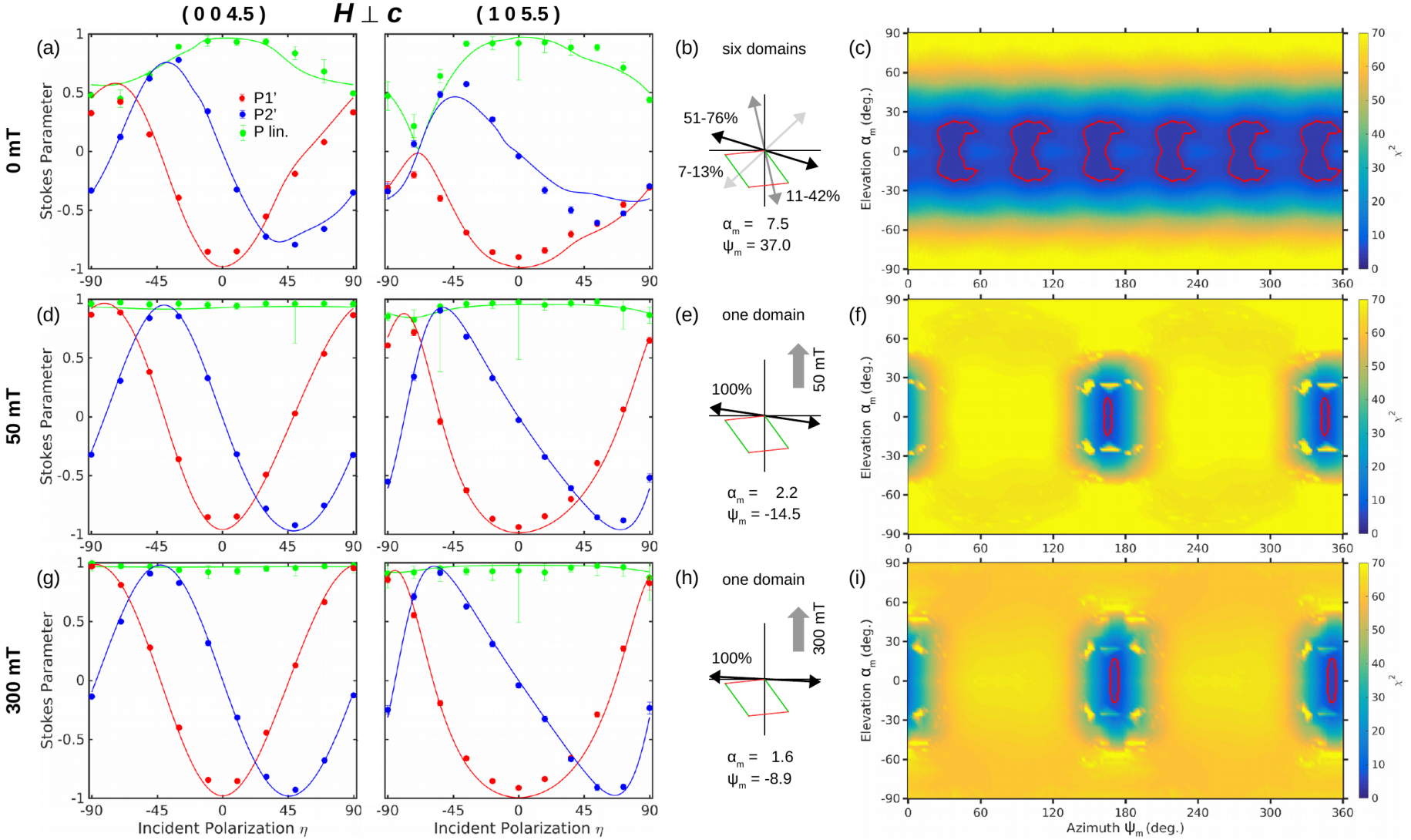

Figure 5.9: Full polarization analysis of the (0,0,4.5) and (1,0,5.5) magnetic reflections of $EuCd_2As_2$, in zero field (top row) and with magnetic fields of 50 and 300 mT applied within the *ab* plane (middle and bottom rows). Panels (a,d,g) show the best fits (lines) to the Stokes parameters P_1', P_2' and $P_{\rm lin} = \sqrt{P_1'^2 + P_2'^2}$ extracted from the polarization scans. Panels (b,e,h) illustrate the orientations of the unit cell (*a*/*b* axes red/green), the best fit orientations of the magnetic moments (azimuthal orientation ψ_M, elevation angle α_M), and corresponding domain populations. Panels (c,f,i) show χ^2 maps of least squares fits performed with the angles (ψ_M, α_M) held fixed (discussion cf. main text).

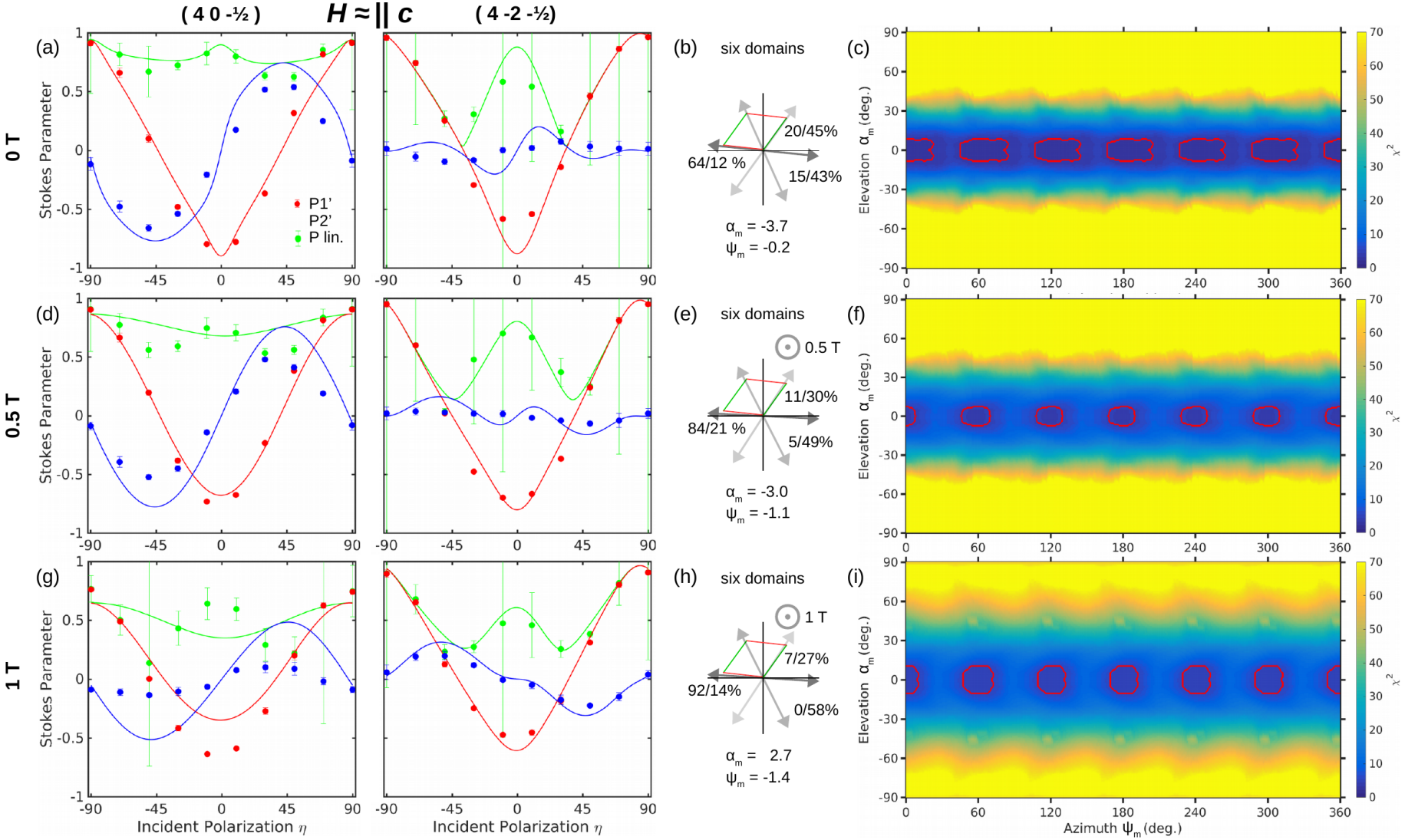

Figure 5.10: Full polarization analysis of the (4,0,-1/2) and (4,-2,-1/2) magnetic reflections of $EuCd_2As_2$, in zero field and with magnetic fields of 0.5 and 1 T applied almost parallel to the c axis. The figure is organized in analogy to Fig. 5.9. In all cases, fits using six domains were superior to models using a single domain or an isotropic distribution of azimuthal moment orientations. In applied fields, the magnetic intensity subsides and interference terms between x-ray fluorescence and magnetic scattering become substantial. Increasing relative background ($\pi\pi'$, $\sigma\sigma$) contributions deteriorate the Stokes parameter fit quality at higher fields.

This is a key issue in non-resonant magnetic x-ray scattering, where charge background is often dominating the magnetic signal.

5. In general, it must be expected that a zero-field–cooled sample will contain all symmetry-equivalent magnetic domains, whose scattered intensities add. Antiphase signals from different domains will introduce circular components to the beam. For trigonal $EuCd_2As_2$, six equivalent magnetic domains would be expected if the magnetic moments are not aligned strictly along the c axis.

In the present data, I found that effect (4), the interference of x-ray fluorescence and magnetic scattering, is indeed significant in certain cases. In particular, the effect becomes important for peaks at large scattering angles when the sample is almost spin-polarized and antiferromagnetic scattering is weak. This can be gleaned from the field sweep of the $(4,0,-1/2)$ peak shown in Fig. 5.8(c): At 1 T (corresponding to the FPA shown in 5.10(g)) the background intensity in the $\pi\pi'$ channel is about $\approx 50\%$ of the magnetic signal seen in $\pi\sigma'$. In fact, when considering the panels (a,d,g) of Fig. 5.10, it can be recognized that the Stokes parameter P_1' continuously becomes more "$\cos 2\eta$-like" and P_2' becomes more "$-\sin 2\eta$-like" as the magnetic field is applied. In effect, these antiphase contributions decrease the amplitudes of both P_1' and P_2', and so $P'_{\mathrm{lin}} = \sqrt{P_1'^2 + P_2'^2}$ is no longer unity.

Nevertheless, this interference with the Eu L_3 fluorescence does not account for the decrease in P'_{lin} in the case of 5.10(a), where the magnetic intensity is strongly dominating the observed signal. This points to the relevance of the effect (5), and indeed it was possible to precisely reproduce the observed η dependence of P'_{lin} by imposing the six-fold domain structure expected for $EuCd_2As_2$.

Taking into account these considerations, all results can be explained as follows (see Fig. 5.11). The magnetic structure of $EuCd_2As_2$ is defined by ferromagnetic layers which are stacked antiferromagnetically, in other words, an A-type antiferromagnet. Even though the Eu^{2+} state has no angular momentum, the magnetic moments experience a weak magnetocrystalline anisotropy which favours an alignment in the a-b plane, as already illustrated in Fig. 5.2. The six magnetic domains (in-plane moment orientations separated by 60°) are smaller than the probed sample volume. In this experiment I measured the sum of their magnetic intensities. For each pair of FPA scans in Figs. 5.9 and 5.10, I indicate the best fit moment-directions and domain populations in panels (b,e,h) and show a χ^2 map of least squares fits with fixed magnetic moment directions in panels (c,f,i) (azimuth ψ_{m} and elevation α_{m} as defined in Eq. 5.6). Red contours imposed onto these χ^2 maps delineate the parameter range corresponding to one standard deviation from the best fit parameters.

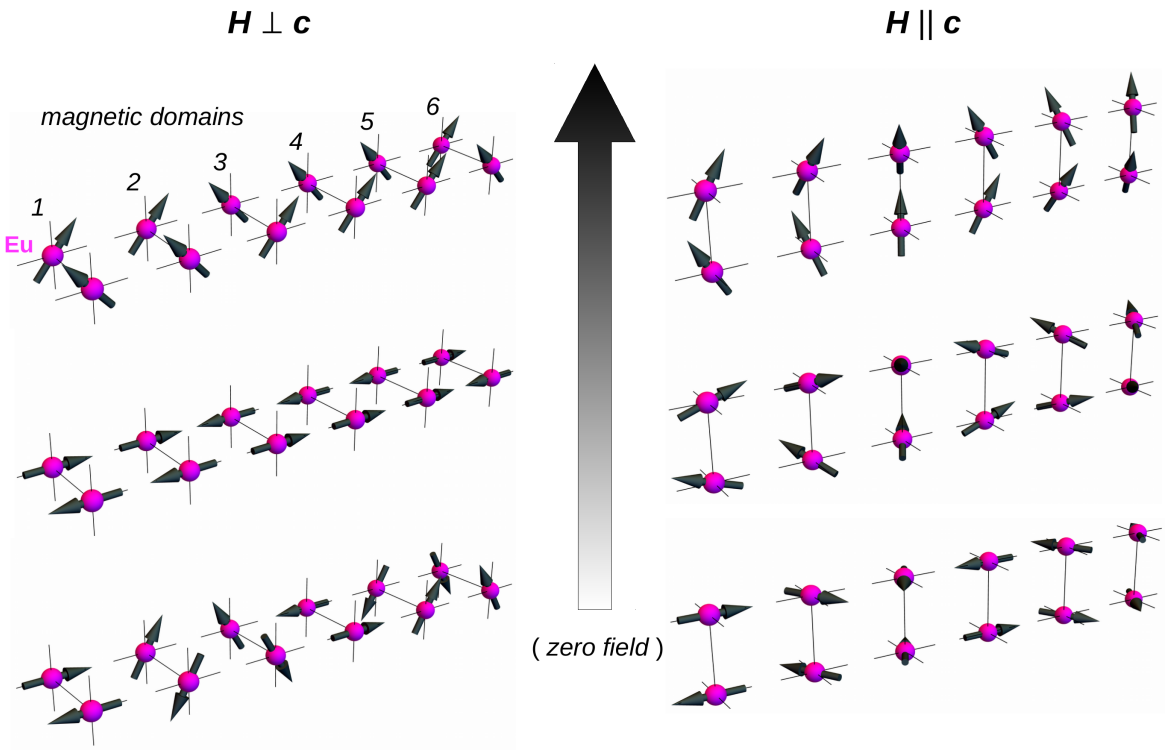

Figure 5.11: Model of the magnetization process in $EuCd_2As_2$. For in-plane (left) and out-of-plane (right) applied magnetic fields $\boldsymbol{H}$, three stages of the spin alignment are shown, from the zero-field situation (bottom) to an almost spin-polarized state (top). In each situation, the magnetic structure in the six domain is shown. Each is, the trigonal planes are symbolized by the two Eu ions in the magnetic unit cell (at $\boldsymbol{r} = (0,0,0)$ and $(0,0,c)$). For $\boldsymbol{H} \perp \boldsymbol{c}$, this process entails the elimination of four less favourable domains (intermediate step), before the moments can cant continuously into the field direction.

For zero applied field, in both cases (Figs. 5.9(a) and 5.10(a)) the obtained fits were superior when imposing an arbitrary six-fold domain population. The fits allow a definite exclusion that the magnetic moments have a significant out-of-plane antiferromagnetic component. On the other hand, the fit is rather degenerate regarding the azimuthal orientation ψ_m. In fact, the two crystals investigated favour different orientations, with best fits at $\psi_\mathrm{m} \approx 37^\mathrm{o}$ and $\psi_\mathrm{m} \approx 0^\mathrm{o}$ for the $\boldsymbol{H} \perp \boldsymbol{c}$ and $\boldsymbol{H} \parallel \boldsymbol{c}$ samples, respectively. This may indicate that there is no strong in-plane anisotropy, or a dependence on sample history. Nevertheless, in all cases, it was *not* possible to reproduce the data by assuming a continuous (i.e., not six-fold but random) distribution of azimuthal moment direction.

When a 50 mT in-plane magnetic field is applied (Fig. 5.9(d,e,f)), P'_lin is restored to unity throughout and the Stokes parameters can be perfectly reproduced by a two-domain model with the magnetic moments aligned almost perpendicular to the applied field (which happens to be close to the a axis in this experiment). This behaviour corresponds to a spin-flop–like re-distribution of domain populations, before all moments can be continuously canted into the field direction. The small magnitude of the magnetic

field which effects this domain-flop corresponds to the weakness of the dipolar coupling between antiferromagnetic domains. This model also naturally explains the $\boldsymbol{H} \perp \boldsymbol{c}$ field sweeps shown in Fig. 5.8(a,b) and discussed above. Increasing the in-plane field to 300 mT (Fig. 5.9(g,h,i)) only suppresses the antiferromagnetic Bragg peaks (as the moments cant, intensity is redistributed to the Brillouin zone centre), but the Stokes scans are hardly changed. I illustrate these spin-polarization processes in Fig. 5.11.

As expected in this model, the selection of a single domain does not occur if the field does not break the six-fold symmetry. Accordingly, all results shown in Fig. 5.10 were better modelled by imposing the six-fold domain structure. However, since this crystal was actually mounted with a 5° tilt from the magnet axis, one domain (the only direction in which the magnetic moments lie both in the a-b plane and in the scattering plane) is clearly favoured by the fits. As the out-of-plane field is successively increased to 0.5 and 1 T, the favoured moment direction (close to the a axis) does not change. Instead, the continuous change in Stokes-scan characteristics is attributed to the increasing relevance of interference terms between magnetic scattering and x-ray fluorescence, as the magnetic intensity subsides.

The subtle downward step of $(4,0,-1/2)$ $\pi\sigma'$ intensity shown in the inset of Fig. 5.8 could also be understood in this picture. According to Eq. 5.4, the $\pi\sigma'$ the $(4,0,-1/2)$ scattering cross section is proportional to

$$\left(\frac{\mathrm{d}\sigma}{\mathrm{d}\Omega}\right)_{\pi\sigma} \propto \; |M_1 \cos\theta + M_3 \sin\theta\,|^2 \quad \overset{(4,0,-\frac{1}{2})}{\rightarrow} \quad |\,0.37\,M_1 + 0.92\,M_3\,|^2$$

The observed intensity is therefore dominated by the Fourier components parallel to $\hat{\mathbf{u}}_3$, i.e. (anti-)parallel to the momentum transfer Q, see Fig. 5.5. As illustrated in Figure 5.6, this sample was mounted with a 5° offset between the c axis and the field direction, corresponding to a 5° tilt between the ab plane and $\hat{\mathbf{u}}_3$. For any distribution of magnetic domains with magnetic moments lying in the ab plane, some domains will lie at an angle (of up to 5°) to the scattering plane. Similar to the $\boldsymbol{H} \perp \boldsymbol{c}$ situation, a very small applied field then suffices to select the only in-plane moment direction which is also perpendicular to the field (i.e., $\hat{\mathbf{u}}_1$). This is seen at ≈ 50 mT in the inset of Fig. 5.8(b). Since moments aligned parallel to $\hat{\mathbf{u}}_1$ have a smaller weight scattering cross section, a small downward step in intensity is expected.

Going back to the $\boldsymbol{H} \parallel \boldsymbol{c}$ magnetization data shown in Fig. 5.3, it is likely that the SQUID sample had similar or worse mis-alignment from the field direction. The additional "phase line" observed as a decrease in susceptibility below ≈ 50 mT and 3 K could then be attributed to the same effect, i.e. the magnetic state shows a larger resilience to spin-canting (a smaller susceptibility), if domains are locked-in with magnetic moments oriented at an angle to the field direction.

The in-plane ferromagnetic correlations are expected to be much stronger than the inter-plane antiferromagnetic exchange interactions (six in-plane ferromagnetic nearest neighbours vs. two further antiferromagnetic neighbours along c). This explains the continuous onset of short-range in-plane ferromagnetic correlations that sets in at $T \gg T_N$ and leads to an incipient ferromagnetic-like transition, before the pre-formed ferromagnetic planes lock into an antiferromagnetic stacking at T_N.

It is interesting to discuss the resistivity and Hall resistivity characteristics in the light of this model. For small applied fields, anomalous Hall effect (AHE) contributions in the multi-domain state will cancel. On the other hand, once the 2D ferromagnetic domains are aligned out-of plane, a sizeable anomalous Hall effect would expected, also above the (3D-) magnetic ordering temperature [446]. The out-of-plane polarization of pre-formed 2D ferromagnetic correlations will cost more energy for increasing temperatures, which explains the diagonal phase line observed in 5.4(f). AHE contributions can also be understood at low temperatures and high fields (i.e. where the initially antiferromagnetic order has been fully spin-polarized).

If the full spin alignment reduces the scattering of charge carriers from magnetic fluctuations, the above ρ_{xy} argument simultaneously explains the corresponding "inverse" ρ_{xx} phase diagram of Fig. 5.4(e). On the other hand, this explanation does *not* encompass the transport characteristics *within* the antiferromagnetically ordered phase. In particular, the insets of Figs. 5.4(c) and (d) show both large longitudinal and transversal resistivity contributions that are effectively proportional to the antiferromagnetic component measured by REXS, see 5.8(c). This implies a more subtle coupling between the magnetic state and the electronic state.

Optical reflectivity measurements suggest that $EuCd_2As_2$ is a semimetal with almost compensated electron- and hole pockets [437]. Whether electronic states in the vicinity of the Fermi surface form topologically protected states or not, it is plausible that a coupling of the antiferromagnetic order parameter with the Cd and As states could shift the electronic bands. This would would have the potential to tune the charge carrier density of states and mobility. It would also explain why very similar characteristic are observed in both longitudinal and transversal transport.

5.6 Conclusion

In conclusion, by comprehensive REXS experiments in applied magnetic fields, I have formed a consistent picture of the magnetic ground state of $EuCd_2As_2$, which naturally explains subtle features of the bulk measurements that were previously not understood. The relation of the magnetic structure to resistivity and Hall effect measurements suggests a coupling between the Eu^{2+} antiferromagnetic order parameter and the charge transport within the heavily spin-orbit–coupled Cd-As states at the Fermi surface.

This study also demonstrates a successful application of REXS, in a material where neutron diffraction had been called for in the literature [437], but would not be feasible without isotopic enrichment with both Eu-153 and Cd-114. Furthermore, the results discussed in this chapter illustrate the inherent ambiguities of bulk techniques and show how the "conventional interpretations" of magnetization and resistivity data may lead to wrong conclusions.

For example, I have shown that the magnetic susceptibility of $EuCd_2As_2$ is about 7 times larger if the magnetic field is applied in the *a*-*b* plane. For a conventional antiferromagnet, it is expected that the magnetic state is *softer* for magnetic fields applied perpendicular to the moment direction. One would therefore infer an out-of-plane alignment. However, in the present case, the magnetic moments are actually lying in-plane, and due to the six-fold domain structure, $EuCd_2As_2$ can avoid a true spin-flop transition irrespective of the field direction. Instead, the anisotropy of the susceptibility is mainly a measure of in-plane vs. out-of-plane magnetocrystalline anisotropy. Due to the lack of orbital angular momentum, neither is expected to be significant, but this does not contradict a 1:7 ratio. This is also reflected by the fact that the saturation fields (0.5 T vs. 1.5 T) are small along both directions, but smaller for an in-plane field. In fact, this also justifies why in all cases where REXS was used to probe a multi-domain state, the FPA fit quality was almost degenerate along the azimuthal direction (cf. Figs. 5.9 and 5.10).

Very recently, Wang *et al.* have reported an electrical and optical conductivity study of $EuCd_2As_2$, in which, based on resistivity measurements, an out-of-plane magnetic moment direction is postulated [437]. The present findings contradict this model and call into question whether the unusual transport properties of $EuCd_2As_2$ can be purely ascribed to the magnetic scattering of the charge carriers. As a next step, it will be of great interest to perform photoemission and quantum oscillation experiments and establish an accurate picture of the Fermi surface. In-depth density-functional studies are also underway, which will verify which states form the electron and hole pockets and how they may couple to the antiferromagnetic order parameter.

Chapter 6

Varying degrees of magnetic frustration in two polymorphs of $Ca_2Os_2O_7$

The heavy transition metal oxide calcium osmate $Ca_2Os_2O_7$ forms two chemically stable polymorphs. Depending on synthesis conditions, the compound crystallizes in a *pyrochlore* (cubic) or *weberite* (orthorhombic) structure. In this chapter, I present an in-depth investigation of these materials by magnetization and resistivity measurements, x-ray and neutron diffraction, as well as muon spin rotation and relaxation experiments.

The present interest in these materials arose in the context of other heavy transition metal oxides (TMOs). As laid out in Section 1.3, it has recently been realized that this family of materials features effects of both strong spin-orbit coupling (SOC) and electronic correlation (EC). A number of emergent phenomena have been predicted to arise from the interplay of these interactions. In analogy to perovskite and pyrochlore iridates ($5d^5$), an unusual metal-to-insulator–like transition has been reported at the magnetic ordering transition of ($5d^3$) weberite $Ca_2Os_2O_7$ [447], even though it must be of different origin.

In this *half frustrated* material, I discovered a complex magnetic ordering transition and determined the magnetic order at low temperatures. This is the first step towards an understanding of the charge gap in this state. Beyond SOC and EC, the parallel study of the pyrochlore compound emphasized the importance of magnetic frustration. For this *fully frustrated* modification of $Ca_2Os_2O_7$, I was able rule out static magnetic order at temperatures down to 40 mK.

Contents

6.1 Introduction 143

6.2 Structural, transport and magnetic measurements 146

6.3 Neutron diffraction and MuSR experiments 153

6.4 Results and analysis 154

6.4.1 Pyrochlore $Ca_2Os_2O_7$ 154

6.4.2 Weberite $Ca_2Os_2O_7$ 156

6.5 Discussion 163

6.6 Conclusion 166

6.1 Introduction

Systematic synthesis studies of $3d$ transition metal compounds with the composition $A_2(B1)(B2)C_{6,7}$ ($B1$, $B2$: transition metals, C: O or F) indicate that the crystal chemistry of these materials depends largely on the electronegativity and ionic radius of the A cation [448, 449]. In particular, it has been shown that for A=Ca, the compounds are poised at the interface between the pyrochlore and weberite structural phases. As in the present case, two polymorphs may then be chemically stable.

The pyrochlore and weberite crystal structures (see Fig. 6.1) are derivatives of the *fluorite* structure and their structural properties have been reviewed in depth in the context of $3d$ transition metal oxides and fluorides [277, 449]. Starting from the face-centred cubic fluorite (CaF_2, $Fm\bar{3}m$) structure, the pyrochlore is obtained by an ordering of anion vacancies (one per fluorite unit cell). This breaks the fluorite's mirror symmetry and reduces its four-fold rotation symmetry to a screw-axis perpendicular to a diamond glide plane. This effectively doubles the unit cell in each dimension and lowers the symmetry to subgroup $Fd\bar{3}m$. In turn, the orthorhombic *weberite* structure is related to the pyrochlore by an angular transformation that further lowers the symmetry to the orthorhombic subgroup $Imma$ [449]. The true symmetry of the weberite structure has been subject to intense debate. A definite structural determination was achieved due to the experimental efforts of Knop *et al.* [450, 451]. However, this is not of immediate relevance in the present context of magnetism.

For the study of magnetic ground states, it is sufficient to consider these fluorite-related oxides as networks of corner-sharing BO_6 (B: transition metal) octahedra, with superexchange interactions mediated through the oxygen ions on connecting vertices. I illustrate this in Fig. 6.1 with a comparison of the pyrochlore and weberite unit cells and the corresponding transition metal environments. In the pyrochlore structure, all transition metal sites are equivalent (Wyckoff site $16c$ of $Fd\bar{3}m$) and all BO_6 octahedra are fully connected, which yields a network of regular transition metal tetrahedra. Panels (b,e,f) of Fig. 6.1 compare the connection of these tetrahedra along the (111)-direction of the cubic cell with the corresponding situation in the orthorhombic weberite variant. Here, transition metal ions occupy two distinct Wyckoff-sites $4b$ and $4c$ (of $Imma$). While the full connectivity of weberite $4c$ sites (to two $4c$ sites and four $4b$ sites) resembles the situation in the pyrochlore, the $4b$ sites only feature four superexchange paths (all to $4c$ sites) and two disconnected vertices with "dangling" anions.

The pyrochlore is thus *fully* magnetically frustrated, while the weberite has been christened a *half-frustrated* structure by Zheng *et al.* [447]. In the present case of $Ca_2Os_2O_7$, density functional calculations have indicated that both osmium ions in the weberite (Os1 at $4c$ and Os2 at $4b$) are pentavalent (Os^{5+}, $5d^3$), as they are in the pyrochlore. Any

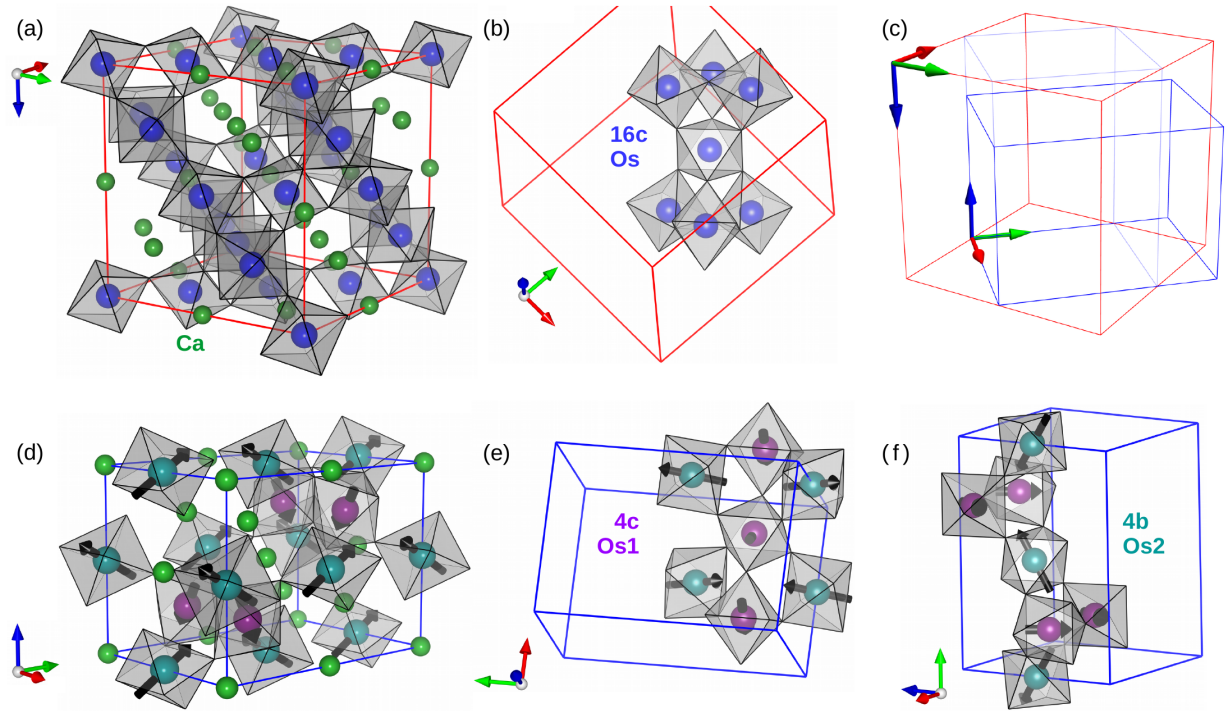

Figure 6.1: Crystal structures of $Ca_2Os_2O_7$ (oxygen ions not shown). (a) The cubic ($Fd\bar{3}m$) pyrochlore phase, forming a three-dimensional network of fully connected OsO_6 octahedra. (b) Detailed view of the resulting three-dimensional triangular network of osmium ions at the 16*c* Wyckoff sites. (c) The relation of the pyrochlore (red) and weberite (blue) unit cells. (d) Crystal structure of weberite $Ca_2Os_2O_7$, with a model of the low-temperature magnetic structure inferred in this chapter. Due to the orthorhombic (*Imma*) symmetry, the osmium ions occupy two distinct crystallographic sites. (e,f) Views of the Os1 (4*c*, frustrated) and Os2 (4*b*, not frustrated) environments in the weberite, corresponding to panel (b). Due to the relative "distortion" along the weberite *b* axis, the $(Os2)O_6$ octahedra are disconnected along this direction, which partially relieves the magnetic frustration at these sites.

difference between the respective magnetic ground states must therefore be attributed to the frustrating geometric arrangement of the ions or subtle structural modifications of the superexchange paths between osmium sites.

The bulk properties of weberite $Ca_2Os_2O_7$ had previously attracted interest. Resistivity and magnetization measurements indicated a metal–insulator-like transition, concomitant with a continuous magnetic ordering transition above room temperature ($T_N \approx 320\,K$) [452]. The opening of a charge gap of $\approx 240\,meV$ had also been reproduced in density functional calculations, consistent with optical reflectivity experiments [447]. However, the character of the magnetically ordered state was not known at the time.

In the case of the pyrochlore phase, little is known beyond initial crystal chemistry studies. In particular, magnetometry or other bulk data have not been reported. The pyrochlore structure is common in ternary heavy transition metal oxides. In the search for new members of this family, pyrochlore $Ca_2Os_2O_7$ powders were originally synthesized by thermal composition of osmium hydroxides [453]. Around the same time, the same phase was also synthesized by reacting CaO and OsO_2 powders at moderate pressure (0.3 GPa) [454]. It was found that the compound actually forms with a 15% anion deficiency, $Ca_{1.7}Os_2O_7$, as is frequently the case in pyrochlores [454]. For simplicity, in the rest of this chapter I frequently omit explicit reference to this non-stoichiometry. Single crystals of this compound have not been previously reported.

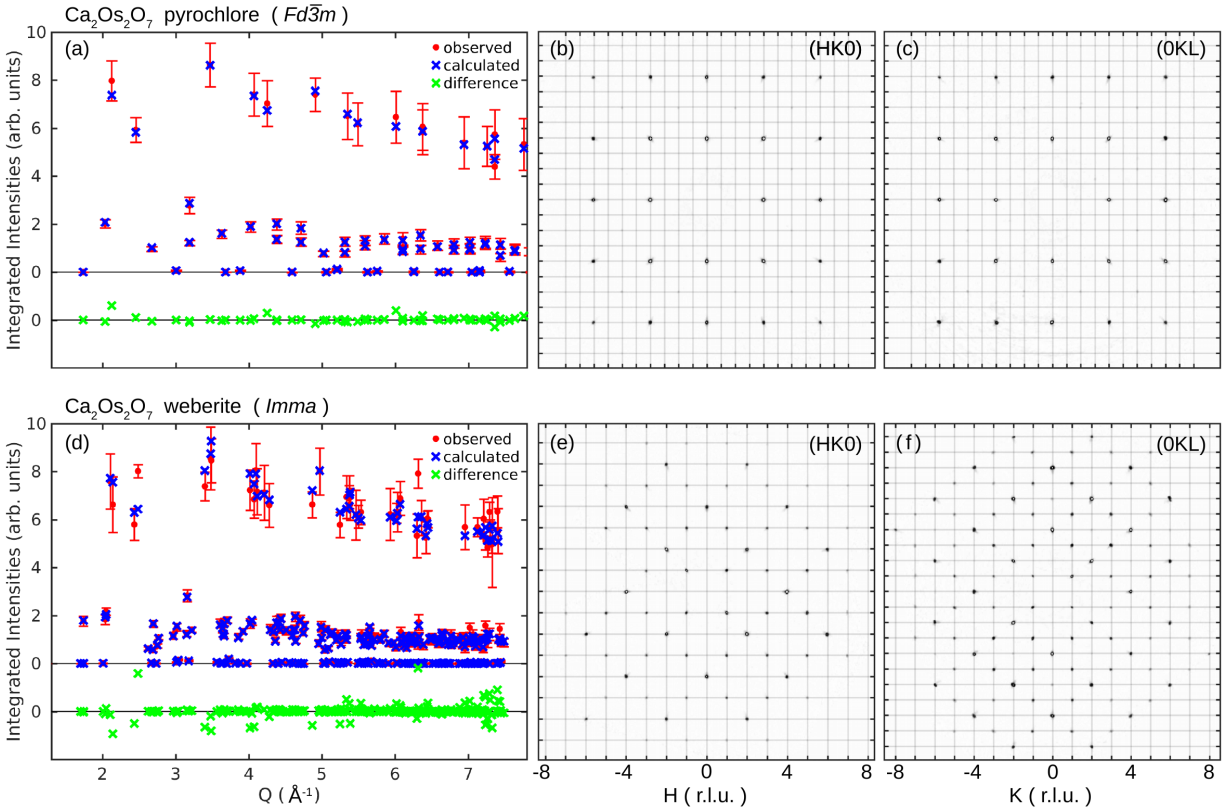

Figure 6.2: Single crystal Mo K_α x-ray diffraction of the pyrochlore (top) and weberite (bottom) phases. (a,d) Results of a refinement (FullProf program [382]) of integrated Bragg intensities (sorted by momentum transfer Q), corresponding to the structures show in Fig. 6.1. (b,c/e,f) Intensity maps of the $(HK0)$ and $(0KL)$ planes of reciprocal space, illustrating the high crystalline quality of these samples.

6.2 Structural, transport and magnetic measurements

Single crystals and powders of pyrochlore and weberite $Ca_2Os_2O_7$ were prepared by my collaborators Prof. Kazunari Yamaura[1], Dr. Yanfeng Guo[2] and Dr. Youguo Shi[3], using a belt-type high pressure apparatus at the National Institute for Materials Science (NIMS, Tsukuba, Japan). The synthesis of the weberite phase, at 3 GPa and 1500°C, has already been reported by Zheng *et al.* [447].

First, I confirmed the structural properties of pyrochlore and weberite $Ca_2Os_2O_7$ single crystals by Mo K_α x-ray diffraction (see Section 2.1.3). The corresponding datasets, along with a refinement of the observed integrated intensities is illustrated in Fig. 6.2. The inferred structural parameters, which are consistent with all previous reports [453, 454, 452, 447], are listed in Table 6.1.

Pyrochlore ($Fd\bar{3}m$, $a = 10.22537(1)$ Å)
3129 reflections, 96% indexed, $R_{\rm int} = 11.61\%$, $R_{\rm F} = 2.89$

	Wyck.	x	y	z	B	occ. (%)
Ca	16d	1/2	1/2	1/2	0.7(4)	85.2(8.4)
Os	16c	0	0	0	0.05(1)	100
O1	48f	0.32049(8)	1/8	1/8	0.7(3)	100
O2	8b	3/8	3/8	3/8	2(1)	100

Weberite ($Imma$, $a = 7.2094(1)$ Å, $b = 10.1169(2)$ Å, $c = 7.3926(1)$ Å)
2942 reflections, 98% indexed, $R_{\rm int} = 10.25\%$, $R_{\rm F} = 3.81$

	Wyck.	x	y	z	B	occ. (%)
Ca1	4a	0	0	0	0.8(2)	100
Ca2	4d	1/4	1/4	3/4	0.8(2)	100
Os1	4c	1/4	1/4	1/4	0.1(1)	100
Os2	4b	0	0	1/2	0.0(5)	100
O1	4e	0	1/4	0.15693(47)	0.1(5)	100
O2	8h	0	0.40633(28)	0.72901(38)	0.7(4)	100
O3	16j	0.20374(26)	0.38266(19)	0.43599(23)	0.7(3)	100

Table 6.1: Room temperature structural parameters of pyrochlore and weberite $Ca_2Os_2O_7$, inferred from the single crystal x-ray diffraction illustrated in Fig. 6.2. The corresponding structural models are shown in Fig. 6.1. For lattice parameters and oxygen positions, the more precise results of neutron powder diffraction (see below) are given. All results, including the $\approx 15\%$ Ca deficiency, are consistent for both single- and polycrystalline samples and across various diffraction techniques.

[1]Superconducting Properties Unit, National Institute for Material Science, 1-1 Namiki, Tsukuba, 305-0044 Ibaraki, Japan
[2]School of Physical Science and Technology, ShanghaiTech University, Shanghai 201210, China and CAS Center for Excellence in Superconducting Electronics (CENSE), Shanghai 200050, China
[3]Beijing National Laboratory for Condensed Matter Physics, Institute of Physics, Chinese Academy of Sciences, Beijing 100190, China

The mosaicity of both samples was smaller than the experimental resolution (0.6–0.9°) along all crystal directions. This is demonstrated by the reciprocal space intensity maps in Fig. 6.2(b,c) and (e,f). Notably, this measurement confirmed the ≈ 15% Ca deficiency of the pyrochlore phase, which had already been reported for powder samples [454].

To understand the nature of the unusual phase transition at $T_N \approx 325\,K$ in weberite $Ca_2Os_2O_7$, it is relevant to quantify to what extent this phase transition couples to the lattice. To search for structural anomalies at T_N, my colleague Christian Donnerer[4] performed a high resolution x-ray powder diffraction experiment at instrument I11 (DIAMOND Light Source). By use of a highly monochromated beam and five arrays of multiple-analyzer-crystal (MAC) scintillation detectors, the powder diffractometer I11 achieves an extreme structural (d-spacing) resolution of $\Delta d/d = 10^{-5}$–10^{-6} [455, 456]. The instrument is therefore ideally suited to detect minute variations in the lattice constant. This experiment was however affected by the strong x-ray absorption of osmium ($Z = 76$, calculated attenuation coefficient $\mu R \approx 25$ [457]). In the histogram of Fig 6.3(a), this is recognized as a rapid suppression of Bragg intensities with momentum transfer. Since such strong absorption ($\mu R > 1$) cannot be reliably corrected by analytical models, I did not attempt to determine atomic positions from this data. Instead, I used a LeBail (*peak matching*) algorithm to refine the lattice and profile parameters only [458].

In Fig. 6.3(b–f), I present the thermal variation of the lattice constants and the resulting Os-Os spacing in the weberite phase, together with structural refinements of time-of-flight neutron powder diffraction (TOF NPD) data discussed in Section 6.4.2. No structural transition is observed over the complete temperature range (3–350 K). Upon cooling from 350 K to 100 K, the lattice constants b and c contract by ≈ 0.02 Å (0.2%) and ≈ 0.01 Å(0.1%), respectively, while a is almost constant. Below ≈ 100 K, the weak thermal contraction appears to be abruptly arrested. A tiny anomaly in the a lattice constant (on the order of 0.001 Å) aside, a structural coupling of the magnetic ordering mechanism can be ruled out. Figure 6.3(g) shows the corresponding thermal variation of the Os-O-Os bond angles inferred from the oxygen atomic positions refined from NPD data. This reveals a weak (up to 1.5°) continuous counter-rotation of (Os1)O_6 octahedra, which sets in below T_N. This is also consistent with the shown contraction of the Os1–Os2 spacing d_{12} (while d_{11} stays constant). As discussed in Section 6.5, the absence of any symmetry breaking structural transition would be consistent with the scenarios of Slater or Lifshitz transitions, which have been proposed for several $5d^3$ osmates.

Next, I measured the thermal variation of the resistivity of both cubic and orthorhombic $Ca_2Os_2O_7$ by the four-point AC transport method described in Section 2.1.2. Sample dimensions obtained from the high pressure synthesis method do not exceed ≈ 500 μm.

[4]London Centre for Nanotechnology and Department of Physics and Astronomy, University College London, London WC1E 6BT, United Kingdom

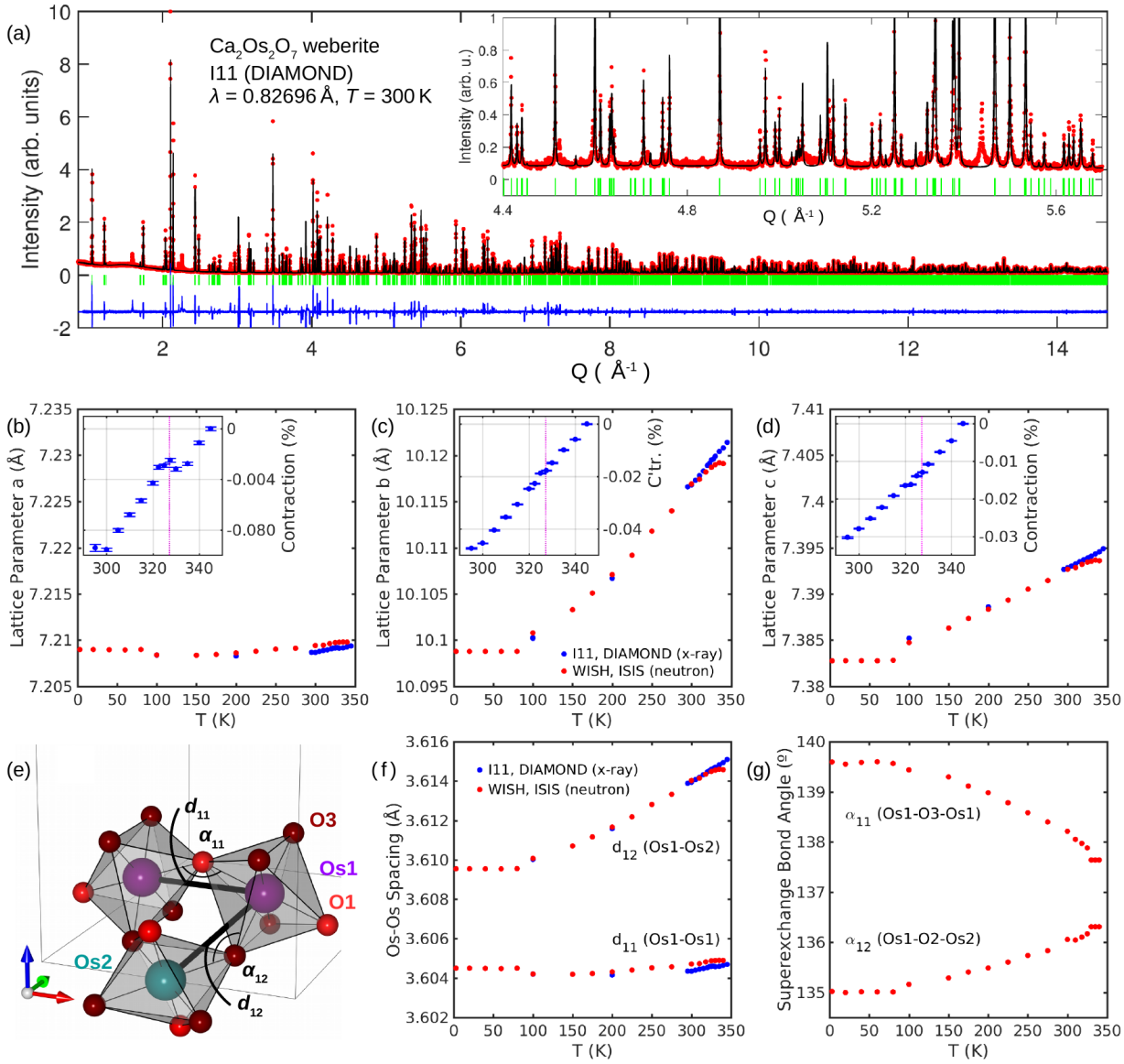

Figure 6.3: Structural properties of the polycrystalline weberite sample. (a) High resolution x-ray powder diffraction pattern obtained at I11, DIAMOND light source (300 K dataset shown). The black and blue lines indicate a LeBail refinement and the difference, respectively. (b,c,d) Thermal variation of the orthorhombic lattice parameters. The results of both synchrotron x-ray (I11, blue markers) and neutron (WISH, ISIS, red markers) powder diffraction are shown. All panels are plotted on the same scale. The insets give the contraction relative to the room temperature value. (e) Definition of inter-atomic distances (d_{11}, d_{12}) and bond angles (α_{11}, α_{12}). (f,g) Thermal variation of these quantities.

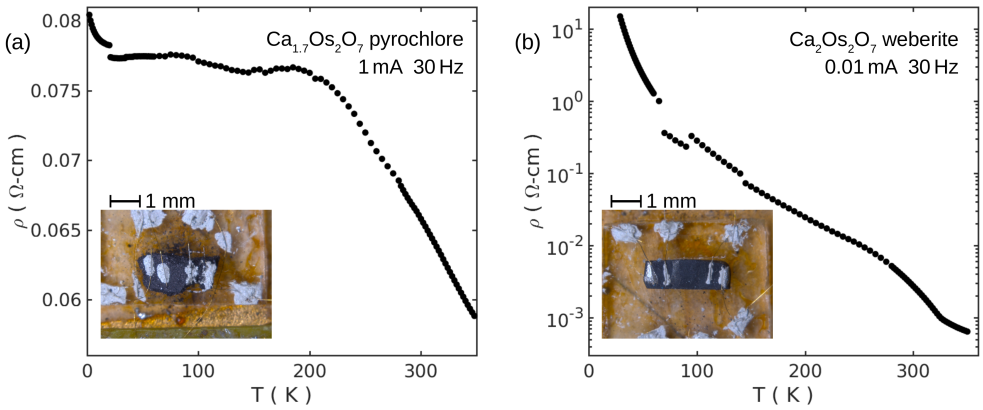

Figure 6.4: 30 Hz AC resistivity of pyrochlore and weberite $Ca_2Os_2O_7$, measured on polycrystalline pellets (insets). (a) The cubic phase shows insulating or semiconducting behaviour, with a plateau of resistivity between 20–200 K. The overall increase in resistivity between 350 and 2 K is $\approx 30\%$. (b) (Note log scale) In the orthorhombic polymorph, a charge gap opens at the magnetic ordering temperature $T_N \approx 325$ K. Due to the limited temperature range, this measurement does not reveal the character of charge transport in the high temperature ($T > T_N$) phase. Discontinuities in the measured curves are systematic errors of the lock-in amplifiers.

A quantitative resistivity measurement on these single crystals is therefore not feasible by standard methods. Instead, I used a hydraulic press to obtain polycrystalline pellets (≈ 2 mm, see insets to Fig. 6.4) from the powders. The resulting resistivity curves are shown in Fig. 6.4. For the pyrochlore phase, no transport data has been published, but it had been noted that the resistivity of polycrystalline samples were "roughly temperature independent at about one Ohm-cm" [454]. My measurement confirms that resistivity is not very temperature dependent over the temperature range probed (2–350 K), but has weak insulating or semiconducting behaviour between 200 and 350K, constant resistivity between 20K and 200K, and a small upturn below 20K.

By contrast, the weberite phase shows a marked transition in its resistive behaviour at $T_N \approx 327$ K. This observation has been interpreted as a metal–insulator transition by Zheng *et al.* [447]. However, the high-temperature state is actually not well characterized due to the limited temperature range of these measurements. In the present data, the incipient $T > T_N$ phase does not appear metallic. Instead, it is more likely that there is still a small band gap or semimetallic state at high temperatures. Below T_N, the resistivity first increases by 2–3 orders of magnitude and then diverges below ≈ 50 K. Notably, the charge transport in this orthorhombic phase is likely to be *anisotropic* and the present results are effectively a powder-average of this behaviour.

Inspired by the neutron powder diffraction results presented below (Section 6.4.2), I performed detailed direction-dependent SQUID magnetization measurements of weberite $Ca_2Os_2O_7$ (see Section 2.1.1). The results of these experiments are summarized in

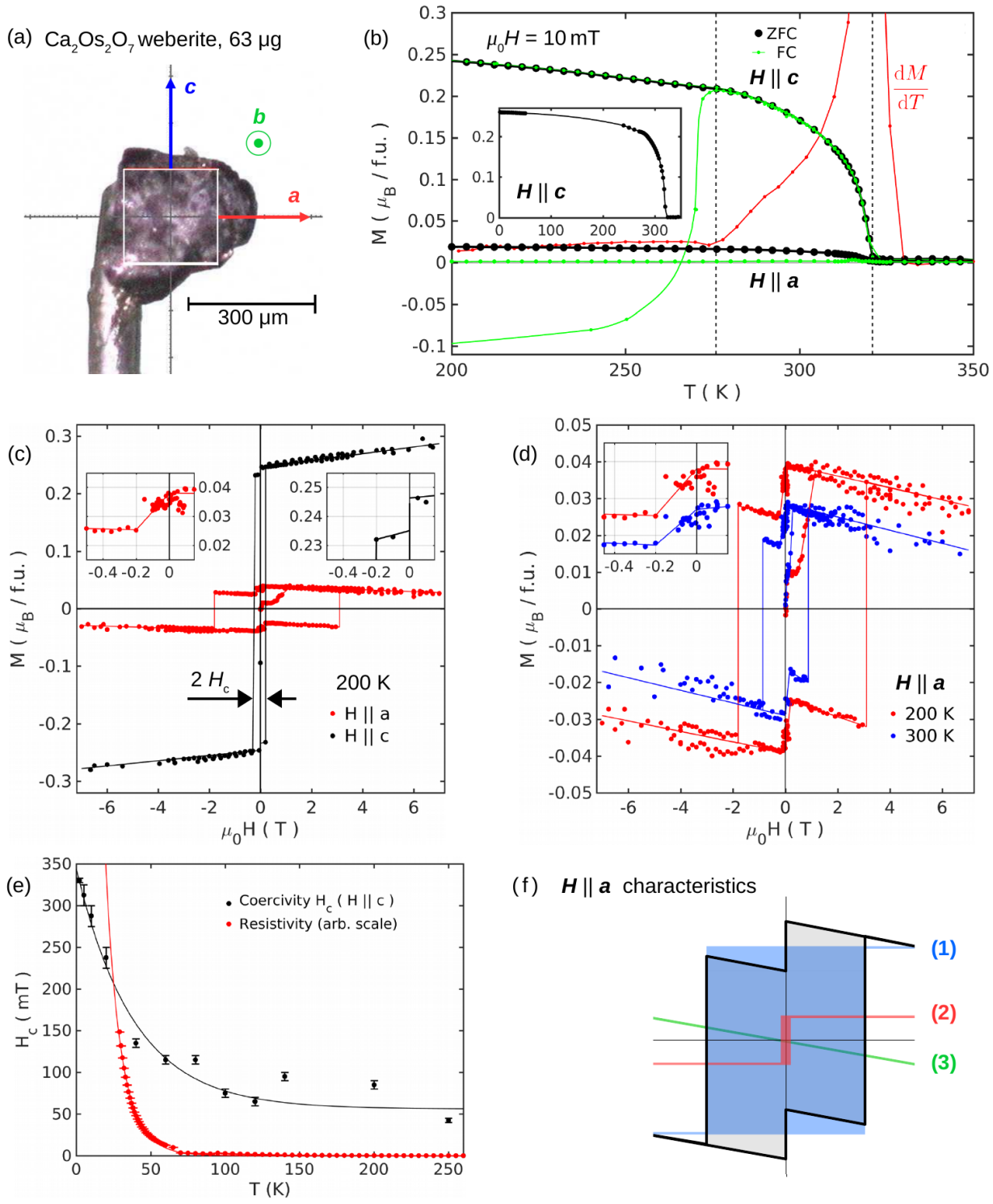

Figure 6.5: Single crystal SQUID magnetometry of weberite $Ca_2Os_2O_7$ (all lines are guides to the eye). (a) View of the sample, mounted on a quartz capillary and aligned by four-circle x-ray diffraction. (b) Field cooled (black markers) and zero field cooled (green markers) temperature dependence of the magnetization, in a field of 10 mT aligned parallel to the c or a axes. The gradient of the FC $\boldsymbol{H} \parallel \boldsymbol{c}$ data is also shown (red markers). All curves were measured upon warming the sample. (c,d) Comparison of hysteresis curves, $\boldsymbol{H} \parallel \boldsymbol{a}$ and $\boldsymbol{H} \parallel \boldsymbol{c}$ at 200 and 300 K. (e) Thermal variation of the c axis coercivity H_c, compared to the polycrystal resistivity also shown in Fig. 6.4. (f) Illustration of three components in the observed $\boldsymbol{H} \parallel \boldsymbol{a}$ hystereses (explanation cf. text).

Fig. 6.5. The weberite phase single crystals do not grow with facets parallel to specific crystallographic directions. These magnetization measurements therefore also required a sample-alignment by laboratory x-ray diffraction. Fig. 6.5(a) shows an aligned crystal with the assigned until cell and crystallographic main axes. Panel (b) shows the temperature dependence of the magnetization M of this crystal, recorded upon warming the sample in an external field of 10 mT applied either along the a or c crystallographic axes. Field cooled (FC) and zero field cooled (ZFC) data are indicated by black and green markers, respectively. The data have the characteristics of a ferromagnetic-like transition at $T_N = 321$ K, followed by an abrupt drop in $M(T)$ curvature at $T_2 = 276$ K. The deviation of Néel temperatures observed in single- and polycrystalline samples ($T_N = 321$ K / 327 K) may well be due to a small oxygen deficiency or anion site mixing, which is frequently observed in fluorite-related structures.

The second transition at $T_2 = 276$ K is seen more clearly in the derivative of the $\boldsymbol{H} \parallel \boldsymbol{c}$ FC data, which is shown in red (on an arbitrary scale). At low temperatures, the $\boldsymbol{H} \parallel \boldsymbol{c}$ FC magnetization reaches $\approx 0.26\,\mu_B$ per formula unit (f.u.), which is one order of magnitude larger than the corresponding $\boldsymbol{H} \parallel \boldsymbol{a}$ signal. Notably, this is only $\approx 3\%$ of single-ion value of Os^{5+} single-ion value in the absence of interactions with the environment and assuming weak spin-orbit coupling ($5d^3$, $L = 3$, $S = 3/2$, $3.87\,\mu_B$). In a previous study, an effective magnetic moment of $2.59\,\mu_B$ per Os ion had been inferred from a Curie-Weiss fit to high temperature ($T < 550$ K) susceptibility data [447].

For the case of $\boldsymbol{H} \parallel \boldsymbol{c}$, two ZFC curves are shown in Fig. 6.5(b), which represent situations in which magnetic domains either aligned in a FC-like configuration, or with a net moment opposed to the field axis. This behaviour is due to residual fields in the magnet coils and reveals that the domain orientation "softens" as the systems approaches T_2 (upon warming). At this temperature, the small measuring field suffices to align all domains and reproduce FC-like characteristics.

In Fig. 6.5(c,d) I compare hysteresis curves of weberite $Ca_2Os_2O_7$, measured at 200 K with a field directed along the a and c axes (panel c) and in the $\boldsymbol{H} \parallel \boldsymbol{a}$ configuration at 200 and 300 K (panel d). As noted above, the c-axis magnetization is clearly dominant, but much smaller than expected for a ferromagnetic alignment of Os^{5+} ions. At 200 K, a small coercive field on the order of ≈ 100 mT is enough to force this alignment of domains. However, the magnetic order appears very hard against a further spin alignment. This is recognized by the shallow slope of $M(H)$, with a net magnetic moment that does not reach $0.3\,\mu_B$/f.u. in an applied field of 7 T.

I have also tracked the thermal evolution of the $\boldsymbol{H} \parallel \boldsymbol{c}$ coercivity (Fig. 6.5(e)). Below ≈ 50 K, this quantity appears to increase exponentially. In Section 6.5, I speculate on a potential indirect relation of this effect to charge transport in the sample, as suggested by the superimposed polycrystalline resistivity curve (data as in Fig. 6.4(b), but on an

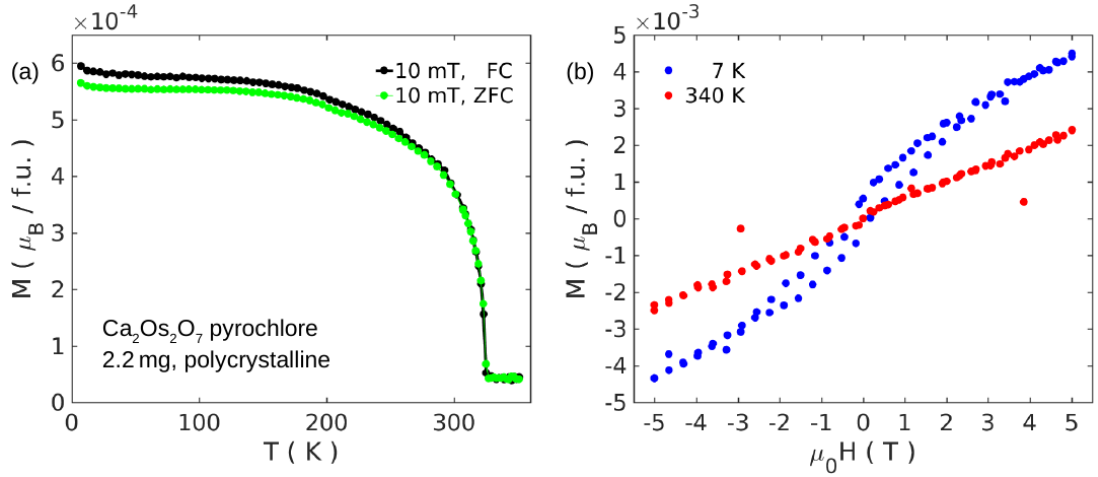

Figure 6.6: SQUID magnetometry of polycrystalline pyrochlore $Ca_2Os_2O_7$. (a) Zero field and field cooled temperature sweeps of the magnetization at 10 mT (recorded upon warming the sample). The curves show a order-parameter behaviour at the Néel temperature of the weberite polymorph, $T_N \approx 327\,K$. The net magnetic moment at base temperature is only $\approx 5.8 \times 10^{-4}\,\mu_B$/f.u. (b) Hysteresis curves indicate paramagnetic behaviour, superimposed by a weak hysteresis at low temperatures.

arbitrary linear scale).

If the magnetic field is applied along the a axis (Figs. 6.5(c,d,f)), the magnetic hysteresis shows an intricate two-step behaviour. I propose that this can be understood in terms of three components, as illustrated in panel (f): (1) The strongest component, with the largest coercive field, can be attributed to a parasitic $\boldsymbol{H} \parallel \boldsymbol{c}$-like contribution due to a small misalignment of the sample. The magnitude of this component, $\approx 0.03\,\mu_B$/f.u.$= 0.25 \sin\alpha$ may be explained by a sample tilt of $\alpha < 7°$. The coercivity of this component is expected to be inversely proportional to the net moment in the field direction. This component therefore appears much wider than that of the corresponding $\boldsymbol{H} \parallel \boldsymbol{c}$ measurement. (2) This spurious signal is superimposed on a small ($\approx 0.01\,\mu_B$/f.u.) constant component with vanishing coercivity < 200 mT (see also insets of panels c and d). This second contribution does not show a marked temperature dependence and, on closer inspection, is also observed in the $\boldsymbol{H} \parallel \boldsymbol{c}$ data. (3) Lastly, the additional diamagnetic signal (negative slope) is likely a spurious contribution from the glue or quartz capillary, which becomes noticeable only on this small scale of $0.01\,\mu_B$/f.u. .

SQUID magnetization data for a polycrystalline sample of the pyrochlore polymorph is shown in Fig. 6.6. The temperature dependence at 10 mT (panel a) resembles that of the weberite phase (Fig. 6.5(b)), but with a magnetization of only $5.8 \times 10^{-4}\,\mu_B$ at base temperature. The field sweep in the low temperature phase (panel b) appears to be dominated by paramagnetic behaviour, with only a weak hysteresis at 7 K. A signal of this magnitude and with this transition temperature could be explained by a small

0.22% weberite impurity. Indeed, the refinement of constant wavelength neutron powder diffraction data (D2B, ILL) of the pyrochlore phase revealed a weberite impurity of 0.43(22)% (see Section 6.4.1, Fig. 6.7). The present magnetization data therefore points to the fact that pyrochlore $Ca_2Os_2O_7$ does not feature a magnetically ordered phase in this temperature range (2–350 K).

6.3 Neutron diffraction and MuSR experiments

In order to determine the magnetic order in weberite $Ca_2Os_2O_7$, and to further characterize the magnetic ground state of the pyrochlore polymorph, I performed neutron powder diffraction (NPD) and muon spin relaxation and rotation (MuSR) studies of both compounds.

I used two neutron powder diffractometers. For an initial screening of the nuclear structure and to search for magnetic Bragg scattering, I used the high resolution instrument D2B at the reactor source ILL. At this beamline, a vertically focusing Ge (335) monochromator is used to select a wavelength of $\lambda = 1.594$ Å from the thermal neutrons coming from a liquid D_2O moderator. The choice of a high monochromator take-off angle (135°) minimizes the wavelength spread $\Delta\lambda/\lambda$. Thus a d-spacing resolution of $\Delta d/d = 10^{-4}$ is achieved at large momentum transfers Q. Notably, this instrument is not designed for high flux and good resolution at low Q, as is most relevant for magnetic scattering. Powders of weberite and pyrochlore $Ca_2Os_2O_7$ were filled into standard vanadium sample cans and cooled in a top-loading ILL *Orange* liquid helium cryostat. The diffracted neutrons are detected on a bank of 128 ^{3}He detector tubes, covering a range of $5° < 2\theta < 165°$ in scattering angle (see Fig. 6.7(b)). The tubes are spaced by 1.25°, and a complete NPD histogram is obtained by scanning the detector bank over this range in 0.05° steps [459, 460].

For a dedicated study of the magnetic Bragg scattering in weberite $Ca_2Os_2O_7$, I used the WISH (Wide angle In a Single Histogram) instrument. This is a state-of-the-art neutron time-of-flight (TOF) diffractometer at the second target station of the ISIS spallation source. With a low repetition rate of 10 Hz and a solid methane (40 K) moderator, this setup is optimized for the production of long-wavelength neutrons and the investigation of the low-momentum transfer regime [461]. The instrument reaches its peak flux at $\lambda = 2.8$ Å and a frame-width of $\Delta\lambda = 8$ Å is diffracted by the sample after each pulse. In contrast to constant-wavelength instruments, the resolution of TOF instruments is not determined by a monochromator take-off angle, and depends only weakly on the scattering angle. The high flux and good resolution in the low momentum transfer regime proved critical in distinguishing the weak magnetic signal from the sample-intrinsic back-

ground. Since the large detector vessel at WISH is fully boron-shielded, the extrinsic background at this beamline is negligible [462].

The WISH instrument features two gap-less $10^{o} < 2\theta < 170^{o}$ arrays of 760 ^{3}He detector tubes each [461]. As shown in Fig. 6.8, the detectors are grouped into ten banks. For the present powder diffraction study, the neutron events recorded on opposite banks were combined. The best resolution is achieved at large TOF. As shown in the following section, magnetic Bragg peaks were observed in the Q =1–1.25 Å^{-1} regime, which was best resolved on banks 3 and 8. The powder was loaded in a vanadium sample can and cooled in a top-loading liquid helium cryostat. I obtained NPD histograms at temperatures between 3 and 350 K.

To clarify an ambiguity of the weberite TOF NPD dataset and to rule out static magnetic order in the pyrochlore, I performed muon spin rotation experiments of both compounds on the instrument MuSR (ISIS). As shown in Fig. 6.7(d), the instrument features two circular arrays of 32+32 positron detector tubes, up- and downstream of sample position. As described in Section 2.5, the time-resolved variation between forward- and backward detector events is stated in terms of the asymmetry ratio (Eq. 2.70). To determine the detector constant α in Eq. 2.70, reference measurements were performed in the paramagnetic state of each sample, in applied transversal fields of 20 Oe. α is then determined by the condition that the time-integrated asymmetry-ratio should vanish for a constant muon Larmor precession in the horizontal plane. Samples of both compounds were packed in thin Ag-foil sachets. The evolution of the magnetic order in the weberite phase was investigated between 350 and 3 K using a standard liquid helium cryostat. Test measurements of the pyrochlore sample were first performed in the same setting (down to 1.4 K). In a separate experiment, I used a dilution refrigerator to track the MuSR anisotropy of pyrochlore $Ca_2Os_2O_7$ down to 40 mK.

6.4 Results and analysis

6.4.1 Pyrochlore $Ca_2Os_2O_7$

Constant wavelength neutron diffraction data of pyrochlore $Ca_2Os_2O_7$, measured at instrument D2B (ILL) is presented in Fig. 6.7(a,b). Room temperature structural parameters obtained from a Rietveld refinement of this data (FullProf program [382]) have been given in Table 6.1. As noted above, the refinement of this data confirmed a 14.8% Ca deficiency and 0.42(22)% weberite impurity. Conventional crystallographic R_F-factors between 2–7 were achieved in the refinement [382]. The comparison of 350 and 3 K histograms in Fig. 6.7(a) illustrates that there is no evidence of additional contributions at

low temperature. Nevertheless, the background at low momentum transfer $Q < 1.5\,\text{Å}$ is significant, and a very weak magnetic signal would not necessarily be resolved.

Even though muon spin rotation and relaxation is a *bulk* probe and does not allow a direct magnetic structure determination, it is more sensitive to weak magnetic fields in the sample (i.e. to small ordered magnetic moments) than neutron diffraction. MuSR results for pyrochlore $Ca_2Os_2O_7$ are shown in Fig 6.7(c). Down to 1.4 K, only a weak slowing down of the spin fluctuations is observed, which was modelled by the phenomenological fit of the MuSR asymmetry ratio with a stretched exponential function,

$$A(t) = A_0\, e^{-(\lambda t)^{\beta}} \tag{6.1}$$

The best fit parameters ($\lambda = 0.09\,\text{MHz}$, $\beta = 0.99$) did not show any variation at temperatures down to 40 mK. This observation rules out any static order or significant slowing down of the paramagnetic fluctuations in the pyrochlore phase down to this temperature.

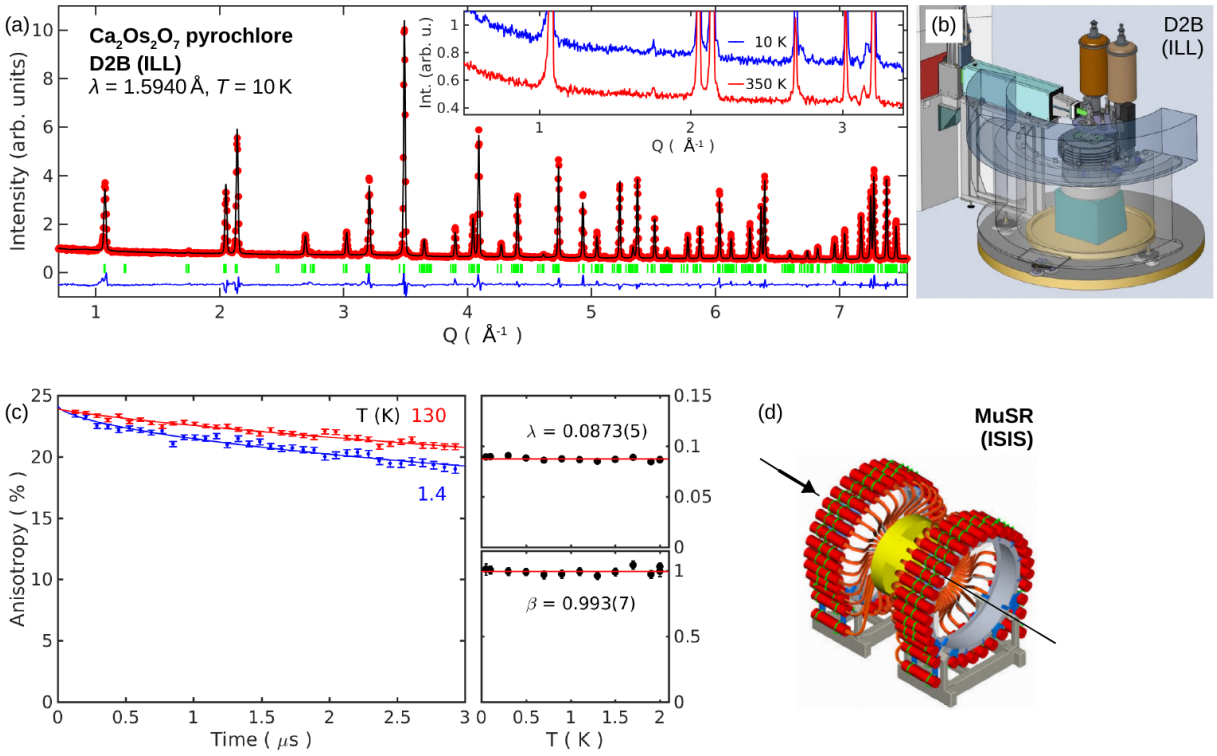

Figure 6.7: Constant wavelength neutron powder diffraction (D2B, ILL) of pyrochlore $Ca_2Os_2O_7$. (a) Rietveld refinement (black line) of the 10 K dataset (red markers). The inset shows a comparison of 350 K and 10 K histograms in the low momentum transfer regime. (b) (from [463]) Perspective technical drawing of the D2B instrument. (c) Muon decay anisotropy in pyrochlore $Ca_2Os_2O_7$, at 130 and 1.4 K (markers). Fits of stretched exponentials are indicated by lines. The right hand panels demonstrates the absence of thermal variation down to 40 mK in the fit parameters (λ, β). (d) (from [464]) Perspective technical drawing of the MuSR instrument, which features two circular arrays of 32+32 positron detector tubes, up- and downstream of the sample position.

6.4.2 Weberite $Ca_2Os_2O_7$

Neutron time-of-flight powder diffraction data (WISH, ISIS) of weberite $Ca_2Os_2O_7$ is shown in Fig. 6.8. The left hand panels (a,b,c) show the results of a simultaneous refinement of the base temperature (3 K) dataset of banks 3–8, grouped into three pairs. It can be seen that the instrument allows a good resolution of nuclear Bragg peaks over a wide range of momentum transfer and the observed background signal is negligible. Room temperature structural parameters inferred from such datasets have been listed in Table 6.1, and the thermal variation of these parameters has been shown and discussed in the context of Fig. 6.3 (red markers).

The Os^{5+} magnetic form factor (plotted in Fig. 2.5) decreases rapidly with momentum transfer [321]. At $Q \approx 1.5\,\text{Å}^{-1}$, magnetic intensities are expected to be suppressed by 50%. Indeed, within the ordered phase, several weak magnetic Bragg scattering contributions appear at integer Bragg positions with $Q < 1.25\,\text{Å}^{-1}$. The magnetic order in weberite $Ca_2Os_2O_7$ is therefore described by a magnetic propagation vector $\boldsymbol{q}_\text{m} = (0,0,0)$ (also denoted as "$\boldsymbol{q}_\text{m} = 0$").

The (011) and (101) Bragg positions of the weberite phase are strong nuclear reflections and and the small additional magnetic contributions at low temperatures are barely resolved within the statistics of this experiment. For this reason, the determination $\boldsymbol{q}_\text{m} = 0$ magnetic structures can be challenging. However, due to its orthorhombic symmetry, weberite $Ca_2Os_2O_7$ features two Bragg positions that are dominated by the magnetic contributions. The thermal variations of the integrated intensities at these (110) and (020) peaks is shown in 6.8(e). Both reflections show an order-parameter-like temperature dependence at transition temperatures $T_\text{N} \approx 331\,\text{K}$ and $T_2 = 278\,\text{K}$. As noted above, small variations in T_N between polycrystalline batches ($T_\text{N} = 325$–$327\,\text{K}$ observed in magnetization and transport measurements) may be due to a small oxygen deficiency or cation mixing. Enlarged views of diffraction patterns showing the (110) and (020) peaks are also found below, in Fig. 6.10.

First, at $T_\text{N} \approx 331\,\text{K}$, magnetic intensity appears at the (020) position. The (020) reflection is symmetry allowed in the *Imma* space group, but has no contributions from the Ca or Os sites and the nuclear scattering contributions from the three oxygen Wyckoff sites of the weberite structure ($4e$, $8h$ and $16j$, see Table 6.1) nearly cancel. On the other hand, the reflection (110) is extinct by the a and b-glide planes $(x, y, \frac{1}{4})$ and $(x, y, 0)$ (symmetry operation 6 in space group *Imma*, which results in the reflection condition $HK0 : H, K \stackrel{!}{=} 2n$).

Thus, the consecutive appearance of magnetic intensity at these two positions implies the following two-step process: First, at T_N, the magnetic moments order with the full symmetry of the nuclear structure, i.e. the moments must be aligned collinearly. Then, at

the intermediate transition at T_2, the magnetic moments cant, whereby the glide plane symmetry of the underlying nuclear structure is broken and intensity appears at the "nuclear-forbidden" peak (110).

A $\boldsymbol{q}_\mathrm{m} = 0$-type spin structure is consistent with the magnetization measurements presented in Section 6.2, which suggest a net magnetic moment along the c axis. However, the neutron data is ambiguous regarding the distribution of this net magnetic moment over the two osmium sites (Os1 at 4*c* and Os2 at 4*b*). In the intermediate phase ($T_2 < T < T_\mathrm{N}$), the moments could (1) align parallel (ferromagnetically) or (2) antiparallel (ferrimagnetically) and, notably, (3) not both sites must necessarily carry an ordered moment.

As noted in Section 6.1, the weberite structure has been described as magnetically *half frustrated*. In other words, antiferromagnetic exchange interactions between nearest neighbour osmium ions do not favour a unique ground state at the Os1 (4*c*) site. For the Os2 (4*b*) site, this frustration is lifted (see Fig. 6.1). I therefore propose that the two sites do not order simultaneously. Instead, there may be only a small or vanishing ordered magnetic moment at the Os1 site in the intermediate phase. In this picture, the observed canting of the spin arrangement below T_2 follows naturally from the increasing interaction between the two sites as the fluctuating frustrated moment at Os1 begins to freeze out.

In order to test this hypothesis, I performed the MuSR experiment summarized in Fig. 6.9. The variation of the MuSR anisotropy (see Eq. 2.70) up to 3 μs after the muon pulse, for sample temperatures between 351.5 and 3.5 K, is shown in panel (a). The data (markers) are approximated by the following phenomenological model (lines):

$$A(t) = C + A_0 \cdot R \cdot e^{-(\lambda t)^\beta} + A_0 \cdot (1-R) \cdot \left(\frac{1}{3} + \frac{2}{3} \cos(\omega t)\, e^{-\lambda_2 t} \right) \tag{6.2}$$

Here, $A_0 = 25.23\%$ is the initial anisotropy, which was held constant. The parameter $0 < R < 1$ models the changeover between two types of behaviour that have been illustrated in Fig. 2.9 (Section 2.5): (1) Either, the local fields are dominated by fluctuating magnetic moments. This leads to a fast relaxation of the muons, described by a stretched exponential decay with parameters λ and β. Or, (2), the muons experience sizeable *static* components of the local fields, which lead to Larmor precession. Due to the polycrystalline character of the sample, the muon anisotropy component due to this precession does not decay completely, but only to a fraction of one third. The constant baseline $C = 5.25\%$ is a background contribution attributed to $1/6$ of the muons stopping outside the sample, e.g. in the Ag sachet. As expected for (non-magnetic) Ag, this effect is temperature-independent and does not affect the intrinsic signal of the sample.

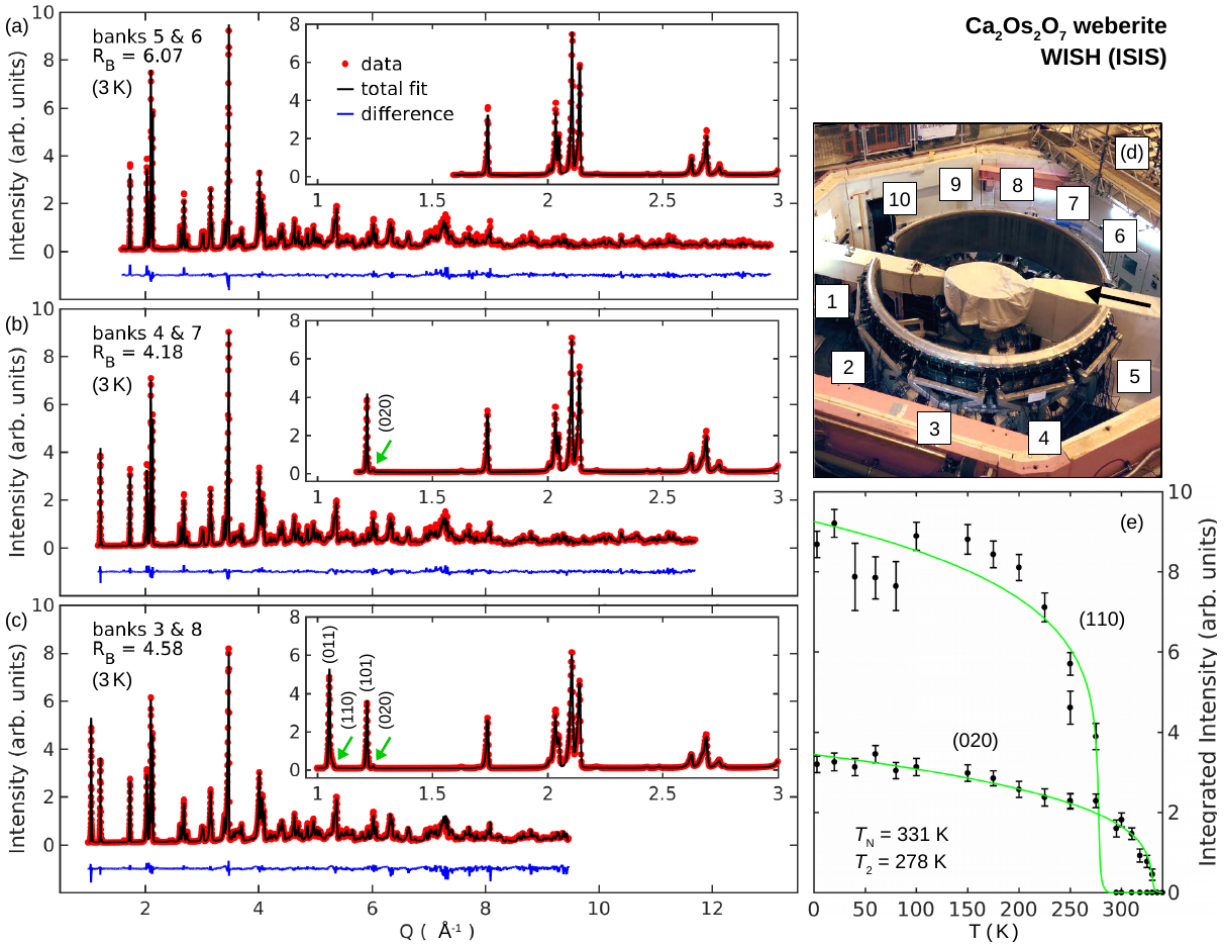

Figure 6.8: Time-of-flight neutron powder diffraction (WISH, ISIS) of weberite $Ca_2Os_2O_7$. (a,b,c) Simultaneous Rietveld refinement (FullProf algorithm [382], black line) of data (red markers) from six detector banks, grouped into three pairs. The insets show detail views of the low momentum transfer regimes. Magnetic Bragg intensities are indicated by green arrows. (d) Assembly of the WISH instrument, with labels of the ten detector banks. The beam direction is indicated by a black arrow (from [465]). (e) Temperature dependence of the magnetic intensities at the (110) and (020) Bragg reflections. The green lines are guides to the eye.

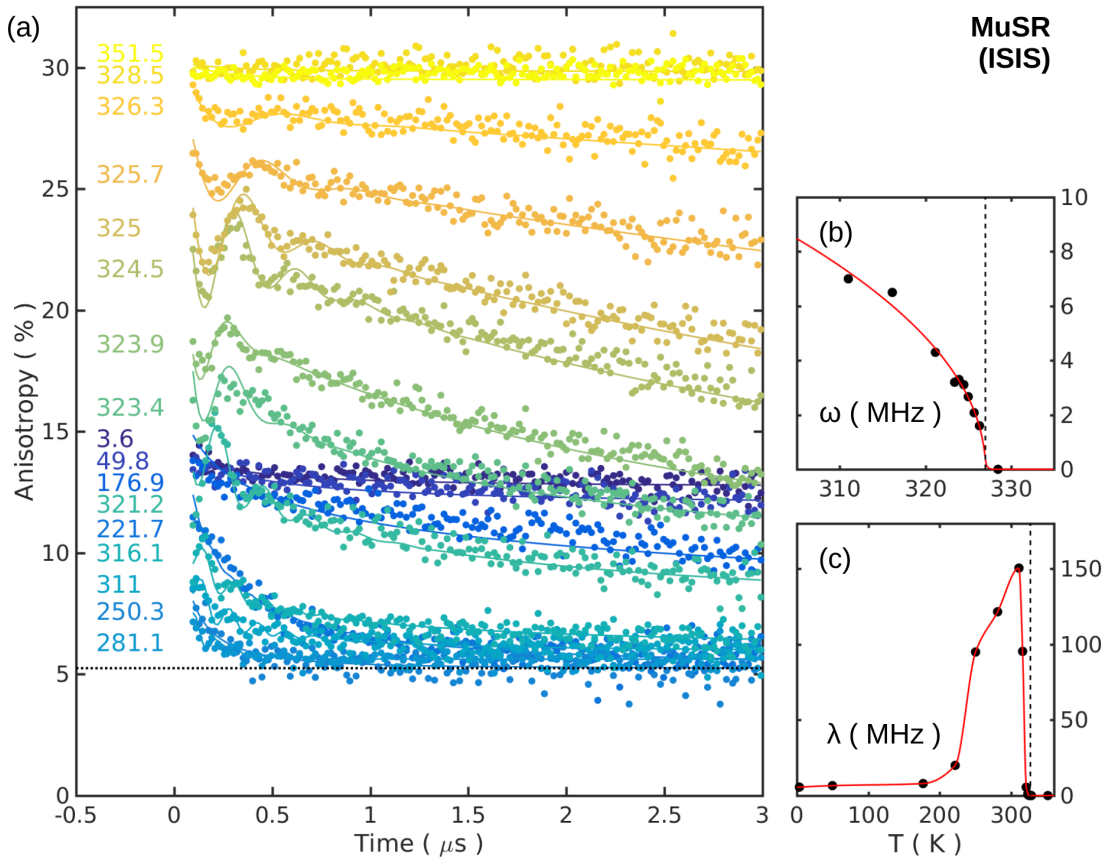

Figure 6.9: Muon spin rotation and relaxation (MuSR) in weberite $Ca_2Os_2O_7$. (a) Muon decay anisotropy (markers) between 351.5 and 3.6 K, and the phenomenological model of Eq. 6.2 (solid lines). The baseline $C = 5.25\%$ is indicated by a dashed black line. (b,c) Corresponding thermal variation of the model parameters λ and ω.

The temperature dependence of the model parameters λ and ω corresponding to the lines in Fig. 6.9(a) are summarized in panels (b,c). The ratio R is close to unity above the ordering transition and in the intermediate range of 150–250 K. Immediately below T_N, as well as at low temperatures $T < 150$ K, R is reduced down to 10–30%. In the relevant regime, β was largely constant at 0.2–0.3.

It should be noted that the above model is not uniquely determined over the full temperature range. Instead, the *fits* presented here should be understood merely as the simplest model which can account for all features in the data. The muon rotation frequency (panel (b)) reveals the characteristic order parameter behaviour at $T_N = 327$ K. Below ≈ 305 K, the precession grows too fast to be resolved by the MuSR instrument. When cooling below 315 K, fluctuating fields dominate ($R \to 1$) and λ diverges. In the data, this is seen as a sharp drop down to the baseline C (indicated as a black dashed line) at intermediate temperatures. At lower temperatures, static field components become more important again and the muon anisotropy relaxes to the "1/3-tail" of $C + A_0/3 \approx 14$ %.

The above observations lend strong support to the picture that the magnetic moment at the two osmium sites of weberite $Ca_2Os_2O_7$ do *not* order simultaneously. Instead, the non-monotonic changeover between two types of muon relaxation characteristics can be explained more naturally by two separate components of the magnetic order. First, the Os2 magnetic moments order in a c axis ferromagnetic arrangement. Due to the antiferromagnetic interactions, this frustrates the Os1 neighbours. In the intermediate state $T_2 < T < T_N$, the Os1 ions therefore remain in a "cooperative paramagnetic" state [466], with diverging fluctuations of the magnetic moments at T_2. A detailed view of the Rietveld refinement of the 300 K WISH TOF neutron data, and a illustration of this magnetic state is shown in Fig. 6.10(a,b)

More detailed information on the low-temperature, canted magnetic order in weberite $Ca_2Os_2O_7$ can be gained from representational analysis [467]. The space group *Imma* yields four irreducible representations (irreps) Γ_1, Γ_3, Γ_5 and Γ_7 (see Table 6.2) for a $\boldsymbol{q}_m = 0$ magnetic structure with a finite magnetic moment at both osmium sites. The possible magnetic structures can be further constrained by comparing the magnetic structure factors for the magnetic basis vectors corresponding to each irreducible representation with experiment.

In particular, a magnetic structure corresponding to Γ_1 cannot yield a Bragg peak at (020) (which is observed). Conversely, Γ_3 or Γ_5 magnetic order would generally scatter at (002), but I observe no magnetic intensity at this position. The magnetic basis vectors of the remaining choice Γ_7 implies a net magnetic moment along the c-axis, which I confirmed by direction-dependent single crystal magnetization measurements (see Fig. 6.5). Similarly, Γ_3 and Γ_5-type structures would be "weakly ferromagnetic" along the a- and b-axes, respectively, which is not observed in magnetometry. Since the magnetic moments

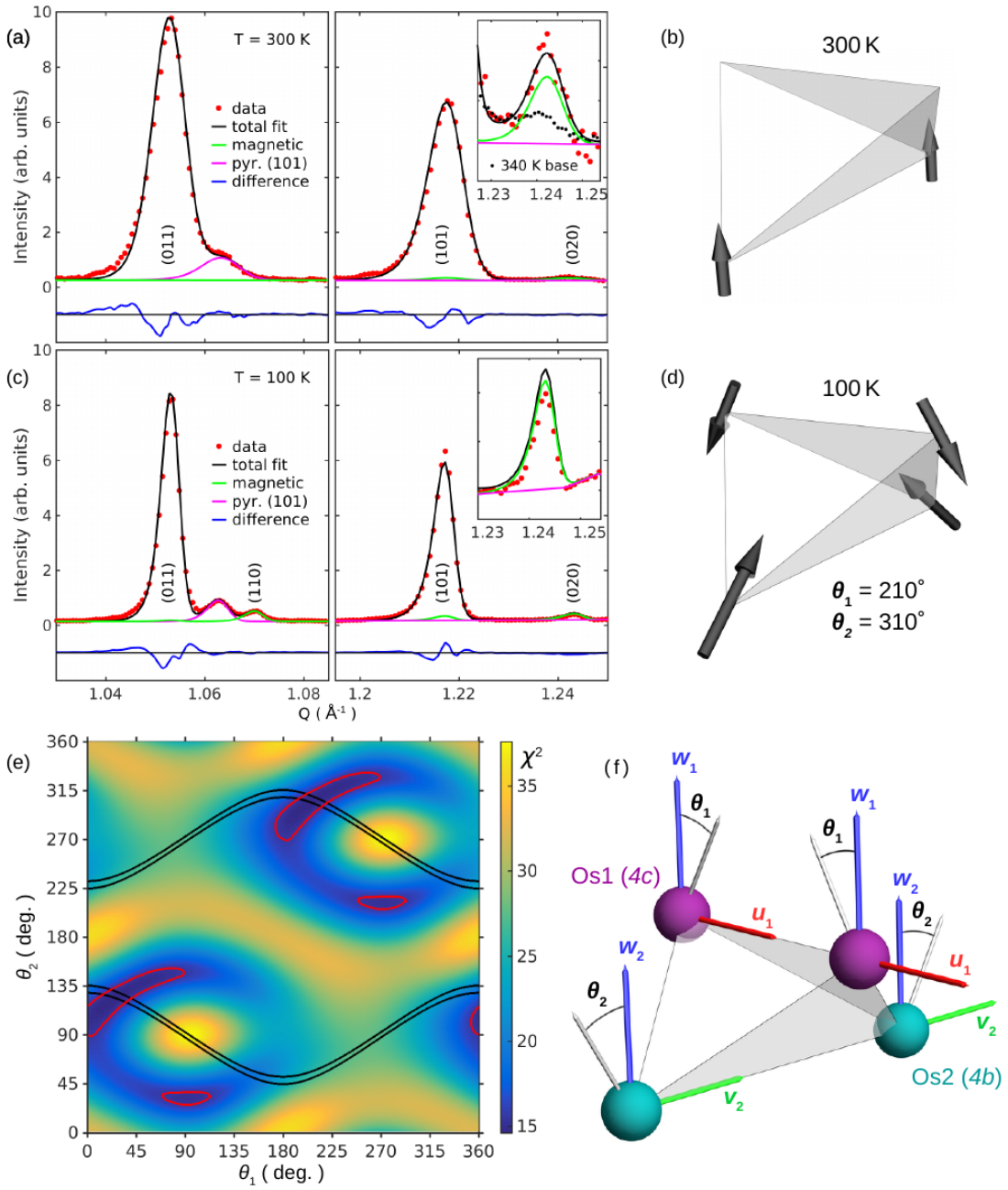

Figure 6.10: Magnetic structure determination of weberite $Ca_2Os_2O_7$. (a) Detailed view of 300 K time-of-flight neutron powder diffraction data obtained at WISH (compare Fig. 6.8). The refined scattering contributions of the pyrochlore impurity and weberite magnetic order are indicated by separate lines. (b) Model of ferromagnetic order at 300 K at the Os2 site. (c,d) Corresponding data, refinement and model of the canted magnetic structure at 100 K. (e) χ^2 map of refinements of the data shown in panel (c), with fixed angles (θ_1, θ_2) of the magnetic moments ($m_1 = 2\,\mu_B$, $m_2 = 3\,\mu_B$). The red contour delineates one standard deviation from the best fit. The black lines bound the narrow region for which the net magnetic moment almost vanishes ($m_{net} = \pm 0.26\,\mu_B$/f.u. margins indicated). (f) Definition of the basis vectors $(\boldsymbol{u}, \boldsymbol{v}, \boldsymbol{w})$ of the magnetic structure at the two osmium sites (Os1/Os2). The angles θ_1 and θ_2, along with the magnitudes of the ordered moments are the only degrees of freedom in the Γ_7 irreducible representation.

Table 6.2: Representational analysis of the propagation vector $\boldsymbol{k} = (0,0,0)$ in the space-group *Imma* with magnetic moments at the Osmium positions Os1 (4*c* site) and Os2 (4*b* site). The positions are listed explicitly in unit cell fractions below the table. For each irreducible representation, the magnetic basis vectors are noted in terms of the fundamental modes F and G, as defined below the table.

irr. rep.	basis vectors Os1			Os2			comment
Γ_1		G_y			G_y		$I_{(020)} = 0$
Γ_3	F_x		G_z	F_x			$I_{(002)} \neq 0$
Γ_5		F_y			F_y	G_z	$I_{(002)} \neq 0$
Γ_7	G_x		F_z		G_y	F_z	FiM. $\|\|\, \boldsymbol{c}$

Os1 (4*c*):	$(1/4\ 1/4\ 1/4)$	$(3/4\ 1/4\ 1/4)$	$(3/4\ 3/4\ 3/4)$	$(1/4\ 3/4\ 3/4)$
Os2 (4*b*):	$(0\ 0\ 1/2)$	$(0\ 1/2\ 1/2)$	$(1/2\ 1/2\ 0)$	$(1/2\ 0\ 0)$
"F"	+	+	+	+
"G"	+	−	+	−

order above room temperature ($T_N = 47^{\circ}$ C), the correct irrep can also be determined using a permanent magnet: Single crystals align with their c axis along the field-lines, which confirms the more quantitative experiment of Fig. 6.5.

The irreducible representation Γ_7 yields magnetic basis vectors

$$\left.\begin{array}{ll} \text{Os1} & (\frac{1}{4}\frac{1}{4}\frac{1}{4}) \\ \text{(4c site,} & : \\ \text{frustrated)} & (\frac{3}{4}\frac{3}{4}\frac{3}{4}) \end{array}\right\} \begin{pmatrix} u_1 \\ 0 \\ w_1 \end{pmatrix} \text{ and } \left.\begin{array}{l} (\frac{3}{4}\frac{1}{4}\frac{1}{4}) \\ \\ (\frac{1}{4}\frac{3}{4}\frac{3}{4}) \end{array}\right\} \begin{pmatrix} -u_1 \\ 0 \\ w_1 \end{pmatrix}$$

and

$$\left.\begin{array}{ll} \text{Os2} & (00\frac{1}{2}) \\ \text{(4b site,} & : \\ \text{un-frust.)} & (\frac{1}{2}\frac{1}{2}0) \end{array}\right\} \begin{pmatrix} 0 \\ v_2 \\ w_2 \end{pmatrix} \text{ and } \left.\begin{array}{l} (0\frac{1}{2}\frac{1}{2}) \\ \\ (\frac{1}{2}00) \end{array}\right\} \begin{pmatrix} 0 \\ -v_2 \\ w_2 \end{pmatrix}$$

Thus, the magnetic moments of the Os1 and Os2 sites are restricted to lie in the a–c and b–c planes, respectively, and the refinement of the magnetic structure can be restricted to the magnitudes (m_1, m_2) and canting angles (θ_1, θ_2) of the magnetic moments at the two sites. The definitions of these angles and magnetic basis vectors are also shown in Fig. 6.10. As noted above, magnetic intensities are observed at four integer (HKL) positions at $Q < 1.25\,\text{Å}^{-1}$. For a refinement of the magnetic structure parameters (100 K dataset), I fixed the structural parameters and constrained the Rietveld algorithm to the Q-range shown in the panels of Fig. 6.10(c).

By writing out the magnetic structure factors of the four reflections, one obtains the following relationships between magnetic Bragg intensities and basis vectors of Γ_7:

$$I_{(011)} \propto (2v_2 - 3w_1)^2/13 \qquad I_{(101)} \propto (u_1 - 3w_2)^2/10$$
$$I_{(110)} \propto (u_1 + 2v_2)^2/5 \qquad I_{(020)} \propto (w_1 - w_2)^2$$

This confirms that the $I_{(020)}$ integrated intensity effectively measures the "staggered" c axis magnetization, while $I_{(110)}$ is determined by the canting due to transversal (u_1, v_2) components. An additional constraint comes from the SQUID magnetometry results (Fig. 6.5(b–d)): The net c axis magnetization must be $w1 + w2 \approx \pm 0.26\,\mu_B$. Taken together, these constraints still do not unambiguously define the structure. To quantify these constrains I performed systematic refinements of the data shown in Fig. 6.10(c).

In Fig 6.10(e), I show a χ^2-map as a function of the magnetic moment angles (θ_1, θ_2). To obtain this map, I fixed the magnitudes of the magnetic moments at $m_1 = 2\,\mu_B$ and $m_2 = 3\,\mu_B$. Although the magnitudes are only weakly constrained, I calculated χ^2 maps for several values of (m_1, m_2) and obtained the best results in this setting. The red contours in Fig. 6.10(e) delineate the regime of one standard deviation from the best fit. The black lines bound the narrow region in which the net moment (per f.u.) is smaller than $\pm 0.26\,\mu_B$. Acceptable configurations are thus confined to narrow regions around (θ_1, θ_2) =(30°, 130°) or (210°, 310°), which corresponds to the spin structure illustrated in Fig. 6.10(d). This double degeneracy of the fit results corresponds to spin inversion (i.e. time-reversal), and cannot be avoided due to the *phase problem* in scattering techniques. The two choices also correspond to two magnetic domains, which would necessarily both be realized in the sample.

6.5 Discussion

The present study has revealed very different results for the magnetism in pyrochlore and weberite $Ca_2Os_2O_7$. The cubic material appears to be a semimetal, in which the full frustration of Os^{5+} magnetic moments prevents even a sizeable slowing down of spin fluctuation, down to 40 mK. The local environments and magnetic superexchange interactions are not expected to be dissimilar for the orthorhombic polymorph. It is therefore impressive that the partial relief of frustration suffices for the formation of magnetic order above room temperature.

Magnetic order in weberite materials has been previously investigated for several 3*d* transition metal fluorides $A_2^{1+}(B1)^{2+}(B2)^{3+}F_7$, as well as fluoro-hydrates $(B1)^{2+}(B2)^{3+}F_5(H_2O)_2$ (*A*: alkali metal, *B*1 and *B*2: 3*d* transition metal) [468, 469, 470, 471]. In cases where

neutron diffraction data is available, similar two-step magnetic ordering transition as in the present case have been observed [472, 473, 474]. In these materials, these intricate magnetic ordering transitions were generally discussed in terms of competing exchange interactions between the *different* $B1$ and $B2$ magnetic ions. A number of scenarios was investigated, either (1) with different elements ($Ni^{2+}Fe^{3+}$), or (2) with the same element in mixed valency ($Fe^{2+}Fe^{3+}$), or (3) with one site occupied by a non-magnetic ion ($Cu^{2+}In^{3+}$). Cooperative paramagnetism or *idle spin* behaviour has also been reported in mixed valent materials of the hexagonal tungsten bronze structure, which is also based on the fluorite structural motif [475].

There exist far fewer studies of magnetism in weberite *oxides* [449]. To my knowledge, magnetic properties have only been reported for certain rare-earth based materials, which are not directly relevant in the present context [476, 477, 478]. Notably, first principles calculations of weberite $Ca_2Os_2O_7$ indicate a strict pentavalence at both sites [447]. If the transition at T_2 is driven by a crossover in superexchange interactions, this must then be due to the variations in exchange paths, which I have quantified in panels (e,f,g) of Fig. 6.3 (Section 6.2). This is surprising, since these structural parameters vary only weakly. Nevertheless, the in-ward counter-rotation of the $(Os1)O_6$ octahedra (in reference to 6.3(e)) is clearly coupled to T_N and is arrested at lower temperatures, $T < 100\,\mathrm{K}$. It is debatable whether this very subtle effect is responsible for tipping the scale towards a spin freeze-out at the Os1 site.

As introduced in Chapter 1.3, the driving motivation for the present study has been the unusual physics of strongly spin-orbit coupled heavy transition metal oxides (TMOs) with electronic correlations. Indeed, the poor-metal- or semimetal-to-insulator transition observed in weberite $Ca_2Os_2O_7$ (see Fig. 6.4) cannot be explained by the traditional Mott-Hubbard scenario. Instead, it is reminiscent of the metal-insulator-transitions (MITs) which have recently attracted great interest $5d$ TMOs. This includes several families of iridates as well as the osmates $NaOsO_3$ and $Cd_2Os_2O_7$ (see discussion in Section 1.3).

The magnetization and resistivity measurements presented in this chapter (see Figs. 6.4, 6.5 and 6.6) suggest that the charge transport transition observed in weberite $Ca_2Os_2O_7$ is induced by the evolution of magnetic order. This is also consistent with the fact that no such transition is observed in the *paramagnetic* pyrochlore phase. Os^{5+} in the octahedral environment is in a $5d^3$ state with quantum numbers $S = 1$ and $L = 0$ (see level scheme in Fig. 1.11). The $J_{\mathrm{eff}} = 1/2$ scenario of a spin-orbit–assisted MIT does therefore not apply in the present case (see Section 1.3). Two alternative candidate mechanisms are the Slater [298] and Lifshitz [297] transitions.

A metal-insulator transition driven by the Slater scenario has recently been evidenced in the $5d^3$ compound $NaOsO_3$ [293, 294]. Resistive characteristics of this material are indeed similar to the present results [293]. Simple antiferromagnetic order implies a

doubling (or generally, increase) of the primitive unit cell along the propagation direction of the magnetic structure. In momentum space, this corresponds to a reduction of the effective primitive Brillouin zone, which entails a back-folding of electronic bands. If the parent band structure features a band crossing at the *new* Brillouin zone boundary, these states will hybridize and open a gap. If the gapped bands have been half-filled (as expected for the Os^{5+} t_{2g} manifold), this results in a MIT [298]. The Slater MIT is expected to occur continuously, and does not directly couple to the lattice. I have shown by bulk measurements and high resolution x-ray diffraction[5] that both requirements are satisfied in weberite $Ca_2Os_2O_7$. On the other hand, my neutron diffraction study revealed no sizeable antiferromagnetic component of the magnetic structure in the intermediate magnetic phase. Within the accuracy of the measurement, this rules out the Slater mechanism.

In another $5d^3$ compound, the pyrochlore $Cd_2Os_2O_7$, a metal insulator transition has been interpreted as a Lifshitz transition [479]. This is a general term applied to any transition which changes the topology of the electronic band structure, i.e. by creation or destruction of electron or hole pockets [297]. In the case of $Cd_2Os_2O_7$, it is attributed to the coupling of Os bands to the all-in/all-out magnetic order [479, 480]. I have shown that weberite $Ca_2Os_2O_7$ forms a similar $\boldsymbol{q}_\mathrm{m} = 0$ ground state. The Lifshitz opening of the charge gap would be expected to occur continuously, which is also consistent with the observed second order transition.

Preliminary first principles band structure calculations have demonstrated that collinear magnetic order in weberite $Ca_2Os_2O_7$ have the potential to split the Os2 (4*b* site) t_{2g} manifold away from the Fermi surface [447]. On the other hand, a canting of magnetic structure was required to split the remaining Os1 (4*c*) states. The two-step ordering process and character of the low temperature magnetic order was not known at the time of this study.

In this chapter, I have noted that the charge gap in weberite $Ca_2Os_2O_7$ appears to open in two steps. Although the transition sets in at T_N, the resistivity of the polycrystalline sample shows an inflection after increasing by 2–3 orders of magnitude, before it diverges at much lower temperatures $T < 50\,\mathrm{K}$. The present results therefore do seem compatible with a two-step Lifshitz transition, meaning a consecutive destruction of Os2 Fermi pockets (at T_N) and Os1 Fermi pockets (at T_2).

In their study of the Lifshitz transition in $Cd_2Os_2O_7$, Hiroi *et al.* have emphasized the importance of metallic antiferromagnetic domain walls in the interpretation of the transport characteristics. The presence of these all-in/all-out – all-out/all-in interfaces has also been evidenced by resonant magnetic x-ray micro-diffraction [481].

[5] Experiment performed by Christian Donnerer, London Centre for Nanotechnology and Department of Physics and Astronomy, University College London, London WC1E 6BT, United Kingdom

In my magnetization measurements, I observed an exponential increase in coercivity in the temperature regime where the resistivity the material diverges (see Fig. 6.5(e)). This could be attributed to a growth of the magnetic domains, or, inversely, a reduction in domain wall density. I therefore speculate that conductive magnetic walls could also play an important role in the effective charge transport properties of weberite $Ca_2Os_2O_7$. It would be of great interest to investigate the anisotropy of the resistivity and Hall effect in single crystal magnetotransport experiments, and to compare field cooled and zero-field cooled characteristics.

6.6 Conclusion

In this chapter, I have presented an in-depth transport, magnetization, MuSR, and x-ray and neutron powder diffraction study of the magnetism in cubic and orthorhombic polymorphs of the 5*d* TMO $Ca_2Os_2O_7$. The orthorhombic phase is of special interest, because it features the unconventional opening of a charge gap, simultaneously with magnetic ordering, above room temperature. Although the cubic polymorph does not exhibit such a transition, its study is of interest since its physical properties have not been previously reported.

Taken together, the chemical stability of both phases also affords a fortuitous opportunity to assess the impact of magnetic frustration. In the fully frustrated, cubic phase, magnetic order is completely suppressed, and the material therefore also forgoes any transport anomalies. By contrast, for the orthorhombic material, I was able to establish a consistent picture of a multi-axial spin structure with a net ferrimagnetic moment, which is preceded by an intermediate state with *idle spin* behaviour on one site.

My observations in weberite $Ca_2Os_2O_7$ would be consistent with a two-step Lifshitz transition due consecutive diffraction of distinct Fermi pockets. It will be interesting to perform first principle calculations of the electronic structure at the Fermi surface, as in Ref. [447], but based on the two-step magnetic ordering process that I discovered. Ideally, such results could also be verified by photoemission and quantum oscillation measurements. As noted in Section 6.5, a magnetotransport study of oriented single crystals would also aid the understanding of this transition.

Metal-insulator transitions in the room temperature regime also deserve attention in view of technological application. Very little is presently known about heavy transition metal oxides of the weberite structure. As fluorite-related structures are flexible with regards to ionic substitution, the synthesis of new compounds in this family seems promising [449].

From an experimental point of view, I have intended to demonstrate how subtle microscopic information can be extracted from *powder-averaged* neutron and x-ray diffraction data. In the present case of a magnetic structure that is commensurate with the nuclear structure, the information obtained from neutron powder diffraction is necessarily ambiguous. However, additional information from symmetry analysis and bulk properties (e.g. single crystal magnetization and MuSR data) are often enough to obtain tight constraints on possible magnetic structures.

Chapter 7

Summary and conclusion

In this thesis I have presented investigations of magnetism in several unusual materials, using state-of-the-art neutron and x-ray scattering techniques.

To this end, I first provided a broad overview of emergent phenomena in quantum materials, which includes the topics of unconventional superconductivity (1.1), topologically non-trivial band structures (1.2) and heavy transition metal oxides (1.3). In the last decade, each of these topics has experienced a surge of scientific activity. This was sparked by the discoveries of iron-based high temperature superconductors [32], Dirac fermions in condensed matter [146], and spin-orbit assisted metal–insulator transitions [262], respectively. Taken together, these discoveries have broadened the focus of the field, from strong electronic correlations, to *quantum materials* in general [13].

The exploration of these complex electronic states requires experimental tools that can probe the bulk of materials on atomic length- and energy scales. This is achieved uniquely by the coherent interference of radiation that is *scattered* from electrons and nuclei. In chapter 2, I explained how the different properties of neutron and x-ray radiation each provide access to specific attributes of condensed matter, including charge, magnetic and nuclear order and excitations. The subsequent four chapters then served as examples of successful applications of these elastic and inelastic neutron- and x-ray scattering techniques. In each case, I demonstrated the state-of-the-art of experimental capabilities.

In Chapters 3 and 4, I reported *inelastic* scattering experiments, i.e. studies of magnetic *excitations*.

By use of time-of-flight neutron spectroscopy, I was able to determine the wave vector of paramagnon excitations in the unusual superconductor FeSe (Chapter 3). I compared the dispersion of these fluctuations with several theoretical models that had been proposed [482]. This data demonstrated the advantage of high-flux neutron chopper spectrometers as a simultaneous probe of a wide regime in momentum and energy-transfer–space. A special feature of this technique is that intensities can be measured in absolute units, which allowed a quantitative comparison with other iron-based superconductors. My analysis of this data also showed that, even though much information is lost in the powder average, a careful consideration of selected features can lead to correct conclusions (as later corroborated by single crystal studies). I also complemented my neutron powder study with a single crystal resonant x-ray spectroscopic experiment. RIXS measurements with such energy resolution had only become possible few months before this experiment. Although the results yield only little information on the magnetic state of the material, it marks the first time that this technique has produced evidence of such weak magnetic fluctuations of such itinerant states. The modelling of this data will provide a touchstone for computational models of the magnetic RIXS process that are currently being developed.

In the following chapter (4), I presented another inelastic neutron scattering study, in a rather different context. In this case, I used a triple-axis spectrometer at a reactor source and determined the energy transfer with a special multi-analyzer device. The subject of this study was a pair of bismuthides AMnBi$_2$ (A=Ca, Sr). These were promising to be the first materials in which a coupling of electronic correlations and Dirac fermions is shaping the magnetic ground state. I obtained high resolution spectra of the magnetic excitations in both materials and quantified their magnetic anisotropy and exchange interactions. Within the small errors of this measurement, my results rule out the elusive *correlated topological state* in these compounds [482]. This finding will play an important role in steering future experimental efforts towards more promising candidate materials. This chapter demonstrated several great advantages of single crystal inelastic neutron scattering: With a relatively small experimental effort, it is possible to map a large four-dimensional volume of momentum- and energy-transfer, with good resolution in all dimensions. In the analysis of this data (see also Appendix B), I showed that in favourable cases, it can be straightforward to construct an analytical model of the neutron spectroscopic response from linear spin wave theory.

In Chapters 5 and 6, the focus of this thesis shifted to *elastic* scattering, i.e. studies of magnetic *order*. I used two very different experimental approaches to obtain this information: In Chapter 5, I exploited the intricate polarization-dependence of resonant elastic x-ray scattering from a single crystal. By contrast, in Chapter 6, I refined details of a magnetic ordering process in a polycrystalline sample from cold neutron chopper diffraction data.

My measurements of the magnetic and charge transport properties of $EuCd_2As_2$ (Chapter 5) showed that it is a promising candidate for unusual band topology — and a possible coupling of these bands to large Eu^{2+} magnetic moments. $EuCd_2As_2$ is also the ideal example to point out a strong limitation of neutron scattering: Cadmium is commonly used for neutron shielding, and the absorption cross section of europium is even almost twice as large. In the case of $EuCd_2As_2$, resonant x-ray scattering at the Eu L_3 edge proved to be an excellent alternative probe of magnetic order. I was able to construct a coherent picture of the magnetic state and its evolution in a magnetic field. Notably, these results contradict the previous perception of the magnetic order in this material. Based on my findings, in-depth computational and photoemission spectroscopy studies are now underway to determine the potential relevance of a topologically protected band crossing in this material. My analysis of the full x-ray polarization scans shows that the interpretation of such data is rather involved, even under the favourable circumstances of this experiment. On the other hand, the complexity of the REXS scattering cross section is proportional to the amount of information that is potentially encoded in a single scan.

The neutron powder diffraction experiments of weberite and pyrochlore $Ca_2Os_2O_7$ (Chapter 6) echoed the limitations of neutron powder techniques that were already evident in Chapter 3. The disparate results for the orthorhombic and cubic polymorphs are exemplary for the effects of *magnetic frustration* — an extrinsic factor which increases the complexity of these 5*d* electron states. Pyrochlore $Ca_2Os_2O_7$ turned out to be a paramagnet down to very low temperatures. By contrast, weberite $Ca_2Os_2O_7$ is magnetically ordered at room temperature — but the suppression of magnetic scattering due to the neutron magnetic form factor and the commensurability of the magnetic and nuclear structure complicated the powder diffraction experiment. The few observed magnetic reflections would have likely been obscured on instruments that are not optimized for low momentum transfer, high resolution and low background. I analysed the ambiguities of this neutron data in detail and showed how some of the missing information can be substituted by symmetry analysis and targeted bulk magnetic measurements. In particular, I used both direction-dependent SQUID magnetometry and muon spin rotation and relaxation. My model of the ordering process in weberite $Ca_2Os_2O_7$ suggests that the partial release of magnetic frustration has a striking indirect consequence: It results in a

two-step Lifshitz metal–insulator-like transition that sets in above room temperature.

In conclusion, the research presented in this thesis provides a cross section of the most relevant topics in current quantum materials physics. On the background of these topics I have attempted to showcase and contrast the impressive capabilities — but also the limitations — of a wide scope of modern x-ray and neutron scattering techniques. By choice of the appropriate scattering technique, method of data analysis and supporting bulk measurements, I have been able to make an important scientific contribution with each of these four case studies.

Bibliography

[1] P. W. Anderson, "More is different," *Science*, vol. 177, no. 4047, pp. 393–396, 1972. 2

[2] P. Chandra, P. Coleman, G. Kotliar, P. Ong, S. D. L., and C. Yu, eds., *PWA90: A Lifetime of Emergence*. World Scientific, 2016. 2

[3] J. Goldstein, "Emergence as a construct: History and issues," *Emergence: Complexity and Organization*, vol. 1, no. 1, pp. 49–72, 1999. 2

[4] P. A. Corning, "The re-emergence of "emergence": A venerable concept in search of a theory," *Complexity*, vol. 7, no. 6, pp. 18–30, 2002. 2

[5] C. Darwin, *The Descent of Man and selection in relation to sex*. John Murray, Albemarle Street., London, 1871. 2

[6] J. S. Mill, *A System of Logic, Ratiocinative and Inductive, Being a Connected View of the Principles of Evidence and the Methods of Scientific Investigation*. John W. Parker, West Strand., London, 1843. 2

[7] G. H. Lewes, *Problems of life and mind*. Trübner & co., London, 1874. 2

[8] M. Gu, C. Weedbrook, A. Perales, and M. A. Nielsen, "More really is different," *Physica D*, vol. 238, no. 9, pp. 835–839, 2009. 2

[9] J. G. Bednorz and K. A. Müller, "Über mögliche Hochtemeratur der Supraleitung im System Ba-La-Cu-O," *Z. Phys.*, vol. 64, pp. 189–193, 1986. 2

[10] M. N. Baibich, J. M. Broto, A. Fert, F. N. Van Dau, F. Petroff, P. Etienne, G. Creuzet, A. Friederich, and J. Chazelas, "Giant magnetoresistance of (001)Fe/(001)Cr magnetic superlattices," *Phys. Rev. Lett.*, vol. 61, pp. 2472–2475, 1988. 2

[11] M. Sagawa, S. Fujimura, N. Togawa, H. Yamamoto, and Y. Matsuura, "New material for permanent magnets on a base of Nd and Fe (invited)," *J. Appl. Phys.*, vol. 55, no. 6, pp. 2083–2087, 1984. 2

[12] T. Wehling, A. Black-Schaffer, and A. Balatsky, "Dirac materials," *Adv. Phys.*, vol. 63, no. 1, pp. 1–76, 2014. 2, 11, 12, 14, 16, 17

[13] Editorial, "The rise of quantum materials," *Nat. Phys.*, vol. 12, no. 2, p. 105, 2016. 2, 169

[14] J. Paglione and R. L. Greene, "High-temperature superconductivity in iron-based materials," *Nat. Phys.*, vol. 6, no. 9, pp. 645–658, 2010. 4

[15] I. I. Mazin, "Superconductivity gets an iron boost," *Nature*, vol. 464, no. 7286, pp. 183–186, 2010. 3, 4

[16] J. D. Thompson and Z. Fisk, "Progress in heavy-fermion superconductivity: Ce115 and related materials," *J. Phys. Soc. Jpn.*, vol. 81, no. 1, p. 011002, 2012. 3, 14

[17] C. C. Tsuei and J. R. Kirtley, "Pairing symmetry in cuprate superconductors," *Rev. Mod. Phys.*, vol. 72, pp. 969–1016, 2000. 3, 14

[18] H. Hosono and K. Kuroki, "Iron-based superconductors: Current status of materials and pairing mechanism," *Physica C*, vol. 514, pp. 399–422, 2015. Superconducting Materials: Conventional, Unconventional and Undetermined. 3

[19] H. Hosono, H. Fukuyama, and H. Akai, "Iron-based superconductors are entering a new stage: Actors are ready," *Solid State Commun.*, vol. 152, no. 8, p. 631, 2012. Special Issue on Iron-based Superconductors. 3

[20] P. J. Hirschfeld, M. M. Korshunov, and I. I. Mazin, "Gap symmetry and structure of Fe-based superconductors," *Rep. Prog. Phys.*, vol. 74, no. 12, p. 124508, 2011. 3, 6, 8, 67

[21] L. Malavasi and S. Margadonna, "Structure-properties correlations in Fe chalcogenide superconductors," *Chem. Soc. Rev.*, vol. 41, pp. 3897–3911, 2012. 3

[22] T. Shibauchi, A. Carrington, and Y. Matsuda, "A quantum critical point lying beneath the superconducting dome in iron pnictides," *Annu. Rev. Cond. Mat. Phys.*, vol. 5, no. 1, pp. 113–135, 2014. 3

[23] J. E. Hoffman, "Spectroscopic scanning tunneling microscopy insights into Fe-based superconductors," *Rep. Prog. Phys.*, vol. 74, no. 12, p. 124513, 2011. 3

[24] E. Dagotto, "Colloquium: The unexpected properties of alkali metal iron selenide superconductors," *Rev. Mod. Phys.*, vol. 85, pp. 849–867, 2013. 3

[25] X. Chen, P. Dai, D. Feng, T. Xiang, and F.-C. Zhang, "Iron-based high transition temperature superconductors," *National Science Review*, vol. 1, no. 3, p. 371, 2014. 3

[26] A. A. Kordyuk, "Iron-based superconductors: Magnetism, superconductivity, and electronic structure (review article)," *Low Temp. Phys.*, vol. 38, no. 9, pp. 888–899, 2012. 3

[27] A. Chubukov, "Pairing mechanism in Fe-based superconductors," *Annu. Rev. Cond. Mat. Phys.*, vol. 3, no. 1, pp. 57–92, 2012. 3, 67

[28] G. R. Stewart, "Superconductivity in iron compounds," *Rev. Mod. Phys.*, vol. 83, pp. 1589–1652, 2011. 3

[29] K. Ishida, Y. Nakai, and H. Hosono, "To what extent iron-pnictide new superconductors have been clarified: A progress report," *J. Phys. Soc. Jpn.*, vol. 78, no. 6, p. 062001, 2009. 3

[30] D. C. Johnston, "The puzzle of high temperature superconductivity in layered iron pnictides and chalcogenides," *Adv. Phys.*, vol. 59, no. 6, pp. 803–1061, 2010. 3

[31] Y. Kamihara, H. Hiramatsu, M. Hirano, R. Kawamura, H. Yanagi, T. Kamiya, and H. Hosono, "Iron-based layered superconductor: LaOFeP," *J. Am. Chem. Soc.*, vol. 128, no. 31, pp. 10012–10013, 2006. 3

[32] Y. Kamihara, T. Watanabe, M. Hirano, and H. Hosono, "Iron-based layered superconductor $La[O_{1-x}F_x]FeAs$ (x =0.05–0.12) with $T_c = 26$ K," *J. Am. Chem. Soc.*, vol. 130, no. 11, pp. 3296–3297, 2008. 3, 97, 169

[33] H. Takahashi, K. Igawa, K. Arii, Y. Kamihara, M. Hirano, and H. Hosono, "Superconductivity at 43 K in an iron-based layered compound $LaO_{1-x}F_xFeAs$," *Nature*, vol. 453, no. 7193, pp. 376–378, 2008. 3

[34] R. Zhi-An, L. Wei, Y. Jie, Y. Wei, S. Xiao-Li, Zheng-Cai, C. Guang-Can, D. Xiao-Li, S. Li-Ling, Z. Fang, and Z. Zhong-Xian, "Superconductivity at 55 K in iron-based F-doped layered quaternary compound $Sm[O_{1-x}F_x]FeAs$," *Chin. Phys. Lett.*, vol. 25, no. 6, p. 2215, 2008. 3

[35] C. Wang, L. Li, S. Chi, Z. Zhu, Z. Ren, Y. Li, Y. Wang, X. Lin, Y. Luo, S. Jiang, X. Xu, G. Cao, and Z. Xu, "Thorium-doping–induced superconductivity up to 56 K in $Gd_{1-x}Th_xFeAsO$," *Europhys. Lett.*, vol. 83, no. 6, p. 67006, 2008. 3

[36] M. Rotter, M. Tegel, and D. Johrendt, "Superconductivity at 38 K in the iron arsenide $(Ba_{1-x}K_x)Fe_2As_2$," *Phys. Rev. Lett.*, vol. 101, p. 107006, 2008. 3

[37] C. Chu, F. Chen, M. Gooch, A. Guloy, B. Lorenz, B. Lv, K. Sasmal, Z. Tang, J. Tapp, and Y. Xue, "The synthesis and characterization of LiFeAs and NaFeAs," *Physica C: Superconductivity*, vol. 469, no. 9–12, pp. 326–331, 2009. Superconductivity in Iron-Pnictides. 3

[38] F.-C. Hsu, J.-Y. Luo, K.-W. Yeh, T.-K. Chen, T.-W. Huang, P. M. Wu, Y.-C. Lee, Y.-L. Huang, Y.-Y. Chu, D.-C. Yan, and M.-K. Wu, "Superconductivity in the PbO-type structure α-FeSe," *Proc. Natl. Acad. Sci. USA*, vol. 105, no. 38, pp. 14262–14264, 2008. 3, 67, 69, 71

[39] P. C. W. Chu, A. Koshelev, W. Kwok, I. Mazin, U. Welp, and H.-H. Wen, eds., *Superconductivity in Iron Pnictides*, vol. 469. Physica C, 2009. 5

[40] P. A. Lee, N. Nagaosa, and X.-G. Wen, "Doping a Mott insulator: Physics of high-temperature superconductivity," *Rev. Mod. Phys.*, vol. 78, pp. 17–85, 2006. 5, 11

[41] R. M. Fernandes and A. V. Chubukov, "Low-energy microscopic models for iron-based superconductors: a review," *Rep. Prog. Phys.*, vol. 80, no. 1, p. 014503, 2017. 5, 6, 7

[42] D. J. Van Harlingen, "Phase-sensitive tests of the symmetry of the pairing state in the high-temperature superconductors—evidence for $d_{x^2-y^2}$ symmetry," *Rev. Mod. Phys.*, vol. 67, pp. 515–535, 1995. 5, 8, 14

[43] I. Mazin and J. Schmalian, "Pairing symmetry and pairing state in ferropnictides: Theoretical overview," *Physica C*, vol. 469, no. 9–12, pp. 614–627, 2009. Superconductivity in Iron-Pnictides. 6, 8, 9

[44] D. Singh, "Electronic structure of Fe-based superconductors," *Physica C*, vol. 469, no. 9–12, pp. 418–424, 2009. Superconductivity in Iron-Pnictides. 5

[45] V. Cvetkovic and Z. Tesanovic, "Multiband magnetism and superconductivity in Fe-based compounds," *Europhys. Lett.*, vol. 85, no. 3, p. 37002, 2009. 5

[46] H. Eschrig and K. Koepernik, "Tight-binding models for the iron-based superconductors," *Phys. Rev. B*, vol. 80, p. 104503, 2009. 5

[47] O. Andersen and L. Boeri, "On the multi-orbital band structure and itinerant magnetism of iron-based superconductors," *Annalen der Physik*, vol. 523, no. 1-2, pp. 8–50, 2011. 5

[48] K. Haule and G. Kotliar, "Coherence–incoherence crossover in the normal state of iron oxypnictides and importance of Hund's rule coupling," *New J. Phys.*, vol. 11, no. 2, p. 025021, 2009. 5

[49] V. Anisimov, E. Kurmaev, A. Moewes, and I. Izyumov, "Strength of correlations in pnictides and its assessment by theoretical calculations and spectroscopy experiments," *Physica C: Superconductivity*, vol. 469, no. 9–12, pp. 442–447, 2009. 5

[50] W. L. Yang, A. P. Sorini, C.-C. Chen, B. Moritz, W.-S. Lee, F. Vernay, P. Olalde-Velasco, J. D. Denlinger, B. Delley, J.-H. Chu, J. G. Analytis, I. R. Fisher, Z. A. Ren, J. Yang, W. Lu, Z. X. Zhao, J. van den Brink, Z. Hussain, Z.-X. Shen, and T. P. Devereaux, "Evidence for weak electronic correlations in iron pnictides," *Phys. Rev. B*, vol. 80, p. 014508, 2009. 5, 6, 84, 89, 90

[51] W.-G. Yin, C.-C. Lee, and W. Ku, "Unified picture for magnetic correlations in iron-based superconductors," *Phys. Rev. Lett.*, vol. 105, p. 107004, 2010. 5

[52] A. Georges, L. de' Medici, and J. Mravlje, "Strong correlations from Hund's coupling," *Annual Review of Condensed Matter Physics*, vol. 4, no. 1, pp. 137–178, 2013. 5

[53] S. Graser, T. A. Maier, P. J. Hirschfeld, and D. J. Scalapino, "Near-degeneracy of several pairing channels in multiorbital models for the Fe pnictides," *New J. Phys.*, vol. 11, no. 2, p. 025016, 2009. 5

[54] K. Kuroki, S. Onari, R. Arita, H. Usui, Y. Tanaka, H. Kontani, and H. Aoki, "Unconventional pairing originating from the disconnected fermi surfaces of superconducting $LaFeAsO_{1-x}F_x$," *Phys. Rev. Lett.*, vol. 101, p. 087004, 2008. 5

[55] H. Ikeda, R. Arita, and J. Kuneš, "Phase diagram and gap anisotropy in iron-pnictide superconductors," *Phys. Rev. B*, vol. 81, p. 054502, 2010. 5

[56] J.-P. Reid, M. A. Tanatar, X. G. Luo, H. Shakeripour, N. Doiron-Leyraud, N. Ni, S. L. Bud'ko, P. C. Canfield, R. Prozorov, and L. Taillefer, "Nodes in the gap structure of the iron arsenide superconductor $Ba(Fe_{1-x}Co_x)_2as_2$ from c-axis heat transport measurements," *Phys. Rev. B*, vol. 82, p. 064501, 2010. 5

[57] M. D. Watson, T. K. Kim, A. A. Haghighirad, N. R. Davies, A. McCollam, A. Narayanan, S. F. Blake, Y. L. Chen, S. Ghannadzadeh, A. J. Schofield, M. Hoesch, C. Meingast, T. Wolf, and A. I. Coldea, "Emergence of the nematic electronic state in FeSe," *Phys. Rev. B*, vol. 91, p. 155106, 2015. 5, 7, 69

[58] A. I. Coldea, J. D. Fletcher, A. Carrington, J. G. Analytis, A. F. Bangura, J.-H. Chu, A. S. Erickson, I. R. Fisher, N. E. Hussey, and R. D. McDonald, "Fermi surface of superconducting LaFePO determined from quantum oscillations," *Phys. Rev. Lett.*, vol. 101, p. 216402, 2008. 5

[59] J. G. Analytis, J.-H. Chu, R. D. McDonald, S. C. Riggs, and I. R. Fisher, "Enhanced Fermi-surface nesting in superconducting $BaFe_2(As_{1-x}P_x)_2$ revealed by the de Haas–van Alphen effect," *Phys. Rev. Lett.*, vol. 105, p. 207004, 2010. 5

[60] Z. Tesanovic, "Viewpoint: Are iron pnictides new cuprates?," *Physics*, vol. 2, p. 60, 2009. 6

[61] V. Brouet, M. Marsi, B. Mansart, A. Nicolaou, A. Taleb-Ibrahimi, P. Le Fèvre, F. Bertran, F. Rullier-Albenque, A. Forget, and D. Colson, "Nesting between hole and electron pockets in $Ba(Fe_{1-x}Co_x)_2as_2$ ($x = 0$–0.3) observed with angle-resolved photoemission," *Phys. Rev. B*, vol. 80, p. 165115, 2009. 7

[62] K. Terashima, Y. Sekiba, J. H. Bowen, K. Nakayama, T. Kawahara, T. Sato, P. Richard, Y.-M. Xu, L. J. Li, G. H. Cao, Z.-A. Xu, H. Ding, and T. Takahashi, "Fermi surface nesting induced strong pairing in iron-based superconductors," *Proc. Natl. Acad. Sci. USA*, vol. 106, no. 18, pp. 7330–7333, 2009. 7

[63] H. Ding, P. Richard, K. Nakayama, K. Sugawara, T. Arakane, Y. Sekiba, A. Takayama, S. Souma, T. Sato, T. Takahashi, Z. Wang, X. Dai, Z. Fang, G. F. Chen, J. L. Luo, and N. L. Wang, "Observation of fermi-surface-dependent nodeless superconducting gaps in $Ba_{0.6}K_{0.4}Fe_2As_2$," *Europhys. Lett.*, vol. 83, no. 4, p. 47001, 2008. 7

[64] C. Liu, G. D. Samolyuk, Y. Lee, N. Ni, T. Kondo, A. F. Santander-Syro, S. L. Bud'ko, J. L. McChesney, E. Rotenberg, T. Valla, A. V. Fedorov, P. C. Canfield, B. N. Harmon, and A. Kaminski, "K-Doping dependence of the Fermi surface of the iron-arsenic $Ba_{1-x}K_xFe_2As_2$ superconductor using angle-resolved photoemission spectroscopy," *Phys. Rev. Lett.*, vol. 101, p. 177005, 2008. 7

[65] M. Yi, D. H. Lu, J. G. Analytis, J.-H. Chu, S.-K. Mo, R.-H. He, M. Hashimoto, R. G. Moore, I. I. Mazin, D. J. Singh, Z. Hussain, I. R. Fisher, and Z.-X. Shen, "Unconventional electronic reconstruction in undoped $(Ba,Sr)Fe_2As_2$ across the spin density wave transition," *Phys. Rev. B*, vol. 80, p. 174510, 2009. 7

[66] T. Kondo, A. F. Santander-Syro, O. Copie, C. Liu, M. E. Tillman, E. D. Mun, J. Schmalian, S. L. Bud'ko, M. A. Tanatar, P. C. Canfield, and A. Kaminski, "Momentum dependence of the superconducting gap in $NdFeAsO_{0.9}F_{0.1}$ single crystals measured by angle resolved photoemission spectroscopy," *Phys. Rev. Lett.*, vol. 101, p. 147003, 2008. 7

[67] C. Utfeld, J. Laverock, T. D. Haynes, S. B. Dugdale, J. A. Duffy, M. W. Butchers, J. W. Taylor, S. R. Giblin, J. G. Analytis, J.-H. Chu, I. R. Fisher, M. Itou, and Y. Sakurai, "Bulk electronic structure of optimally doped $Ba(Fe_{1-x}Co_x)_2As_2$," *Phys. Rev. B*, vol. 81, p. 064509, 2010. 7

[68] Y. Singh, M. A. Green, Q. Huang, A. Kreyssig, R. J. McQueeney, D. C. Johnston, and A. I. Goldman, "Magnetic order in $BaMn_2As_2$ from neutron diffraction measurements," *Phys. Rev. B*, vol. 80, p. 100403, 2009. 7, 104

[69] T. Yildirim, "Origin of the 150-K anomaly in LaFeAsO: Competing antiferromagnetic interactions, frustration, and a structural phase transition," *Phys. Rev. Lett.*, vol. 101, p. 057010, 2008. 7, 9

[70] C. de la Cruz, Q. Huang, J. W. Lynn, J. Li, W. R. II, J. L. Zarestky, H. A. Mook, G. F. Chen, J. L. Luo, N. L. Wang, and P. Dai, "Magnetic order close to superconductiv-

ity in the iron-based layered $LaO_{1-x}F_xFeAs$ systems," *Nature*, vol. 453, no. 7197, pp. 899–902, 2008. 7, 9

[71] M. D. Lumsden and A. D. Christianson, "Magnetism in Fe-based superconductors," *J. Phys. Condens. Matter*, vol. 22, no. 20, p. 203203, 2010. 7, 9, 10

[72] A. Jesche, C. Krellner, M. de Souza, M. Lang, and C. Geibel, "Coupling between the structural and magnetic transition in CeFeAsO," *Phys. Rev. B*, vol. 81, p. 134525, 2010. 7

[73] S. Kasahara, H. J. Shi, K. Hashimoto, S. Tonegawa, Y. Mizukami, T. Shibauchi, K. Sugimoto, T. Fukuda, T. Terashima, A. H. Nevidomskyy, and Y. Matsuda, "Electronic nematicity above the structural and superconducting transition in $BaFe_2(As_{1-x}P_x)_2$," *Nature*, vol. 486, no. 7403, pp. 382–385, 2012. 7

[74] S.-H. Baek, D. V. Efremov, J. M. Ok, J. S. Kim, J. van den Brink, and B. Büchner, "Orbital-driven nematicity in FeSe," *Nat. Mater.*, vol. 14, no. 2, pp. 210–214, 2015. 7, 67, 92

[75] H.-J. Grafe, D. Paar, G. Lang, N. J. Curro, G. Behr, J. Werner, J. Hamann-Borrero, C. Hess, N. Leps, R. Klingeler, and B. Büchner, "^{75}As NMR studies of superconducting $LaFeAsO_{0.9}F_{0.1}$," *Phys. Rev. Lett.*, vol. 101, p. 047003, 2008. 7

[76] K. Matano, Z. A. Ren, X. L. Dong, L. L. Sun, Z. X. Zhao, and G. qing Zheng, "Spin-singlet superconductivity with multiple gaps in $PrFeAsO_{0.89}F_{0.11}$," *Europhys. Lett.*, vol. 83, no. 5, p. 57001, 2008. 7

[77] F. Ning, K. Ahilan, T. Imai, A. S. Sefat, R. Jin, M. A. McGuire, B. C. Sales, and D. Mandrus, "^{59}Co and ^{75}As NMR investigation of electron-doped high T_c superconductor $BaFe_{1.8}Co_{0.2}As_2$ ($T_c = 22$ K)," *J. Phys. Soc. Jpn.*, vol. 77, no. 10, p. 103705, 2008. 7

[78] Y. Shimizu, T. Yamada, T. Takami, S. Niitaka, H. Takagi, and M. Itoh, "Pressure-induced antiferromagnetic fluctuations in the pnictide superconductor $FeSe_{0.5}Te_{0.5}$: ^{125}Te NMR study," *J. Phys. Soc. Jpn.*, vol. 78, no. 12, p. 123709, 2009. 7

[79] C. W. Hicks, T. M. Lippman, M. E. Huber, Z.-A. Ren, J. Yang, Z.-X. Zhao, and K. A. Moler, "Limits on the superconducting order parameter in $NdFeAsO_{1-x}F_y$ from scanning SQUID microscopy," *J. Phys. Soc. Jpn.*, vol. 78, no. 1, p. 013708, 2009. 8

[80] X. Zhang, Y. S. Oh, Y. Liu, L. Yan, K. H. Kim, R. L. Greene, and I. Takeuchi, "Observation of the Josephson effect in $Pb/Ba_{1-x}K_xFe_2As_2$ single crystal junctions," *Phys. Rev. Lett.*, vol. 102, p. 147002, 2009. 8

[81] C.-T. Chen, C. C. Tsuei, M. B. Ketchen, Z.-A. Ren, and Z. X. Zhao, "Integer and half-integer flux-quantum transitions in a niobium-iron pnictide loop," *Nat. Phys.*, vol. 6, no. 4, pp. 260–264, 2010. 8

[82] T. Hanaguri, S. Niitaka, K. Kuroki, and H. Takagi, "Unconventional s-wave superconductivity in Fe(Se,Te)," *Science*, vol. 328, no. 5977, pp. 474–476, 2010. 8

[83] I. I. Mazin, D. J. Singh, M. D. Johannes, and M. H. Du, "Unconventional superconductivity with a sign reversal in the order parameter of $LaFeAsO_{1-x}F_x$," *Phys. Rev. Lett.*, vol. 101, p. 057003, 2008. 8, 9

[84] D. Singh, M.-H. Du, L. Zhang, A. Subedi, and J. An, "Electronic structure, magnetism and superconductivity of layered iron compounds," *Physica C*, vol. 469, no. 15–20, pp. 886–889, 2009. Proceedings of the 21st International Symposium on Superconductivity (ISS 2008). 8

[85] A. Chubukov, "Renormalization group analysis of competing orders and the pairing symmetry in Fe-based superconductors," *Physica C: Superconductivity*, vol. 469, no. 9–12, pp. 640–650, 2009. Superconductivity in Iron-Pnictides. 8

[86] K. Kuroki and H. Aoki, "Unconventional pairing originating from disconnected Fermi surfaces in the iron-based superconductor," *Physica C*, vol. 469, no. 9–12, pp. 635–639, 2009. Superconductivity in Iron-Pnictides. 8

[87] D. Scalapino, "Superconductivity and spin fluctuations," *J. Low Temp. Phys.*, vol. 117, no. 3, pp. 179–188, 1999. 8

[88] W. L. Roth, "Magnetic structures of MnO, FeO, CoO, and NiO," *Phys. Rev.*, vol. 110, pp. 1333–1341, 1958. 9

[89] D. Fruchart, P. Convert, P. Wolfers, R. Madar, J. Senateur, and R. Fruchart, "Structure antiferromagnetique de $Fe_{1.125}Te$ accompagnee d'une deformation monoclinique," *Mat. Res. Bull.*, vol. 10, no. 3, pp. 169–174, 1975. 9

[90] Q. Huang, Y. Qiu, W. Bao, M. A. Green, J. W. Lynn, Y. C. Gasparovic, T. Wu, G. Wu, and X. H. Chen, "Neutron-diffraction measurements of magnetic order and a structural transition in the parent $BaFe_2As_2$ compound of FeAs-based high-temperature superconductors," *Phys. Rev. Lett.*, vol. 101, p. 257003, 2008. 9

[91] J. Zhao, W. Ratcliff, J. W. Lynn, G. F. Chen, J. L. Luo, N. L. Wang, J. Hu, and P. Dai, "Spin and lattice structures of single-crystalline $SrFe_2As_2$," *Phys. Rev. B*, vol. 78, p. 140504, 2008. 9

[92] A. I. Goldman, D. N. Argyriou, B. Ouladdiaf, T. Chatterji, A. Kreyssig, S. Nandi, N. Ni, S. L. Bud'ko, P. C. Canfield, and R. J. McQueeney, "Lattice and magnetic

instabilities in $CaFe_2As_2$: A single-crystal neutron diffraction study," *Phys. Rev. B*, vol. 78, p. 100506, 2008. 9

[93] M. Ishikado, R. Kajimoto, S. ichi Shamoto, M. Arai, A. Iyo, K. Miyazawa, P. M. Shirage, H. Kito, H. Eisaki, S. Kim, H. Hosono, T. Guidi, R. Bewley, and S. M. Bennington, "Two-dimensional spin density wave state in LaFeAsO," *J. Phys. Soc. Jpn.*, vol. 78, no. 4, p. 043705, 2009. 9, 72

[94] S. Iikubo, M. Fujita, S. Niitaka, and H. Takagi, "Antiferromagnetic fluctuations in $Fe(Se_{1-x}Te_x)_{0.92}$ ($x = 0.75,\ 1$) observed by inelastic neutron scattering," *J. Phys. Soc. Jpn.*, vol. 78, no. 10, p. 103704, 2009. 9

[95] R. A. Ewings, T. G. Perring, R. I. Bewley, T. Guidi, M. J. Pitcher, D. R. Parker, S. J. Clarke, and A. T. Boothroyd, "High-energy spin excitations in $BaFe_2As_2$ observed by inelastic neutron scattering," *Phys. Rev. B*, vol. 78, p. 220501, 2008. 9, 72

[96] K. Matan, R. Morinaga, K. Iida, and T. J. Sato, "Anisotropic itinerant magnetism and spin fluctuations in $BaFe_2As_2$: A neutron scattering study," *Phys. Rev. B*, vol. 79, p. 054526, 2009. 9

[97] R. J. McQueeney, S. O. Diallo, V. P. Antropov, G. D. Samolyuk, C. Broholm, N. Ni, S. Nandi, M. Yethiraj, J. L. Zarestky, J. J. Pulikkotil, A. Kreyssig, M. D. Lumsden, B. N. Harmon, P. C. Canfield, and A. I. Goldman, "Anisotropic three-dimensional magnetism in $CaFe_2As_2$," *Phys. Rev. Lett.*, vol. 101, p. 227205, 2008. 9

[98] S. O. Diallo, V. P. Antropov, T. G. Perring, C. Broholm, J. J. Pulikkotil, N. Ni, S. L. Bud'ko, P. C. Canfield, A. Kreyssig, A. I. Goldman, and R. J. McQueeney, "Itinerant magnetic excitations in antiferromagnetic $CaFe_2As_2$," *Phys. Rev. Lett.*, vol. 102, p. 187206, 2009. 9

[99] J. Zhao, D. T. Adroja, D.-X. Yao, R. Bewley, S. Li, X. F. Wang, G. Wu, X. H. Chen, J. Hu, and P. Dai, "Spin waves and magnetic exchange interactions in $CaFe_2As_2$," *Nat. Phys.*, vol. 5, no. 8, pp. 555–560, 2009. 9

[100] S. O. Diallo, D. K. Pratt, R. M. Fernandes, W. Tian, J. L. Zarestky, M. Lumsden, T. G. Perring, C. L. Broholm, N. Ni, S. L. Bud'ko, P. C. Canfield, H.-F. Li, D. Vaknin, A. Kreyssig, A. I. Goldman, and R. J. McQueeney, "Paramagnetic spin correlations in $CaFe_2As_2$ single crystals," *Phys. Rev. B*, vol. 81, p. 214407, 2010. 9

[101] J. Zhao, D.-X. Yao, S. Li, T. Hong, Y. Chen, S. Chang, W. Ratcliff, J. W. Lynn, H. A. Mook, G. F. Chen, J. L. Luo, N. L. Wang, E. W. Carlson, J. Hu, and P. Dai, "Low energy spin waves and magnetic interactions in $SrFe_2As_2$," *Phys. Rev. Lett.*, vol. 101, p. 167203, 2008. 9

[102] R. A. Ewings, T. G. Perring, J. Gillett, S. D. Das, S. E. Sebastian, A. E. Taylor, T. Guidi, and A. T. Boothroyd, "Itinerant spin excitations in $SrFe_2As_2$ measured by inelastic neutron scattering," *Phys. Rev. B*, vol. 83, p. 214519, 2011. 9, 111

[103] M. A. Kastner, R. J. Birgeneau, G. Shirane, and Y. Endoh, "Magnetic, transport, and optical properties of monolayer copper oxides," *Rev. Mod. Phys.*, vol. 70, pp. 897–928, 1998. 9

[104] K. Matan, S. Ibuka, R. Morinaga, S. Chi, J. W. Lynn, A. D. Christianson, M. D. Lumsden, and T. J. Sato, "Doping dependence of spin dynamics in electron-doped $Ba(Fe_{1-x}Co_x)_2As_2$," *Phys. Rev. B*, vol. 82, p. 054515, 2010. 9

[105] J. Dong, H. J. Zhang, G. Xu, Z. Li, G. Li, W. Z. Hu, D. Wu, G. F. Chen, X. Dai, J. L. Luo, Z. Fang, and N. L. Wang, "Competing orders and spin-density-wave instability in $La(O_{1-x}F_x)FeAs$," *Europhys. Lett.*, vol. 83, no. 2, p. 27006, 2008. 9

[106] D. J. Singh and M.-H. Du, "Density functional study of $LaFeAsO_{1-x}F_x$: A low carrier density superconductor near itinerant magnetism," *Phys. Rev. Lett.*, vol. 100, p. 237003, 2008. 9

[107] F. Ma, Z.-Y. Lu, and T. Xiang, "Arsenic-bridged antiferromagnetic superexchange interactions in LaFeAsO," *Phys. Rev. B*, vol. 78, p. 224517, 2008. 9

[108] Q. Si and E. Abrahams, "Strong correlations and magnetic frustration in the high t_c iron pnictides," *Phys. Rev. Lett.*, vol. 101, p. 076401, 2008. 9

[109] M. D. Johannes and I. I. Mazin, "Microscopic origin of magnetism and magnetic interactions in ferropnictides," *Phys. Rev. B*, vol. 79, p. 220510, 2009. 9

[110] A. E. Taylor, R. A. Ewings, T. G. Perring, J. S. White, P. Babkevich, A. Krzton-Maziopa, E. Pomjakushina, K. Conder, and A. T. Boothroyd, "Spin-wave excitations and superconducting resonant mode in $Cs_xFe_{2-y}Se_2$," *Phys. Rev. B*, vol. 86, p. 094528, 2012. 9, 10, 68

[111] W. Bao, Y. Qiu, Q. Huang, M. A. Green, P. Zajdel, M. R. Fitzsimmons, M. Zhernenkov, S. Chang, M. Fang, B. Qian, E. K. Vehstedt, J. Yang, H. M. Pham, L. Spinu, and Z. Q. Mao, "Tunable $(\delta\pi, \delta\pi)$-type antiferromagnetic order in α-Fe(Te,Se) superconductors," *Phys. Rev. Lett.*, vol. 102, p. 247001, 2009. 9

[112] J. Wen, G. Xu, Z. Xu, Z. W. Lin, Q. Li, W. Ratcliff, G. Gu, and J. M. Tranquada, "Short-range incommensurate magnetic order near the superconducting phase boundary in $Fe_{1+\delta}Te_{1-x}Se_x$," *Phys. Rev. B*, vol. 80, p. 104506, 2009. 9

[113] H. A. Mook, M. D. Lumsden, A. D. Christianson, B. C. Sales, R. Jin, M. A. McGuire, A. Sefat, D. Mandrus, S. E. Nagler, T. Egami, and C. de la Cruz, "Neutron scat-

tering patterns show superconductivity in $FeTe_{0.5}Se_{0.5}$ likely results from itinerant electron fluctuations," *arXiv:0904.2178*, 2009. 9, 11

[114] Y. Qiu, W. Bao, Y. Zhao, C. Broholm, V. Stanev, Z. Tesanovic, Y. C. Gasparovic, S. Chang, J. Hu, B. Qian, M. Fang, and Z. Mao, "Spin gap and resonance at the nesting wave vector in superconducting $FeSe_{0.4}Te_{0.6}$," *Phys. Rev. Lett.*, vol. 103, p. 067008, 2009. 9, 11, 68

[115] B. Vignolle, S. M. Hayden, D. F. McMorrow, H. M. Ronnow, B. Lake, C. D. Frost, and T. G. Perring, "Two energy scales in the spin excitations of the high-temperature superconductor $La_{2-x}Sr_xCuO_4$," *Nat. Phys.*, vol. 3, no. 3, pp. 163–167, 2007. 9, 10

[116] A. Subedi, L. Zhang, D. J. Singh, and M. H. Du, "Density functional study of FeS, FeSe, and FeTe: Electronic structure, magnetism, phonons, and superconductivity," *Phys. Rev. B*, vol. 78, p. 134514, 2008. 9, 69

[117] Y. Xia, D. Qian, L. Wray, D. Hsieh, G. F. Chen, J. L. Luo, N. L. Wang, and M. Z. Hasan, "Fermi surface topology and low-lying quasiparticle dynamics of parent $Fe_{1+x}Te/Se$ superconductor," *Phys. Rev. Lett.*, vol. 103, p. 037002, 2009. 9

[118] P. Dai, J. Hu, and E. Dagotto, "Magnetism and its microscopic origin in iron-based high-temperature superconductors," *Nat. Phys.*, vol. 8, no. 10, pp. 709–718, 2012. 10

[119] L. W. Harriger, H. Q. Luo, M. S. Liu, C. Frost, J. P. Hu, M. R. Norman, and P. Dai, "Nematic spin fluid in the tetragonal phase of $BaFe_2As_2$," *Phys. Rev. B*, vol. 84, p. 054544, 2011. 10

[120] D. S. Inosov, J. T. Park, P. Bourges, D. L. Sun, Y. Sidis, A. Schneidewind, K. Hradil, D. Haug, C. T. Lin, B. Keimer, and V. Hinkov, "Normal-state spin dynamics and temperature-dependent spin-resonance energy in optimally doped $BaFe_{1.85}Co_{0.15}As_2$," *Nat. Phys.*, vol. 6, no. 3, pp. 178–181, 2010. 9

[121] J. Rossat-Mignod, L. Regnault, C. Vettier, P. Bourges, P. Burlet, J. Bossy, J. Henry, and G. Lapertot, "Neutron scattering study of the $YBa_2Cu_3O_{6+x}$ system," *Physica C*, vol. 185, pp. 86–92, 1991. 9

[122] H. A. Mook, M. Yethiraj, G. Aeppli, T. E. Mason, and T. Armstrong, "Polarized neutron determination of the magnetic excitations in $YBa_2Cu_3O_7$," *Phys. Rev. Lett.*, vol. 70, pp. 3490–3493, 1993. 9

[123] H. F. Fong, P. Bourges, Y. Sidis, L. P. Regnault, A. Ivanov, G. D. Gu, N. Koshizuka, and B. Keimer, "Neutron scattering from magnetic excitations in $Bi_2Sr_2CaCu_2O_{8+\delta}$," *Nature*, vol. 398, no. 6728, pp. 588–591, 1999. 9

[124] P. Dai, H. A. Mook, G. Aeppli, S. M. Hayden, and F. Dogan, "Resonance as a measure of pairing correlations in the high-T_c superconductor $YBa_2Cu_3O_{6.6}$," *Nature*, vol. 406, no. 6799, pp. 965–968, 2000. 9

[125] N. K. Sato, N. Aso, K. Miyake, R. Shiina, P. Thalmeier, G. Varelogiannis, C. Geibel, F. Steglich, P. Fulde, and T. Komatsubara, "Strong coupling between local moments and superconducting heavy electrons in UPd_2Al_3," *Nature*, vol. 410, no. 6826, pp. 340–343, 2001. 9

[126] C. Stock, C. Broholm, J. Hudis, H. J. Kang, and C. Petrovic, "Spin resonance in the *d*-wave superconductor $CeCoIn_5$," *Phys. Rev. Lett.*, vol. 100, p. 087001, 2008. 9, 11

[127] A. D. Christianson, E. A. Goremychkin, R. Osborn, S. Rosenkranz, M. D. Lumsden, C. D. Malliakas, I. S. Todorov, H. Claus, D. Y. Chung, M. G. Kanatzidis, R. I. Bewley, and T. Guidi, "Unconventional superconductivity in $Ba_{0.6}K_{0.4}Fe_2As_2$ from inelastic neutron scattering," *Nature*, vol. 456, no. 7224, pp. 930–932, 2008. 11, 72

[128] M. D. Lumsden, A. D. Christianson, D. Parshall, M. B. Stone, S. E. Nagler, G. J. MacDougall, H. A. Mook, K. Lokshin, T. Egami, D. L. Abernathy, E. A. Goremychkin, R. Osborn, M. A. McGuire, A. S. Sefat, R. Jin, B. C. Sales, and D. Mandrus, "Two-dimensional resonant magnetic excitation in $BaFe_{1.84}Co_{0.16}As_2$," *Phys. Rev. Lett.*, vol. 102, p. 107005, 2009. 11

[129] S. Chi, A. Schneidewind, J. Zhao, L. W. Harriger, L. Li, Y. Luo, G. Cao, Z. Xu, M. Loewenhaupt, J. Hu, and P. Dai, "Inelastic neutron-scattering measurements of a three-dimensional spin resonance in the FeAs-based $BaFe_{1.9}Ni_{0.1}As_2$ superconductor," *Phys. Rev. Lett.*, vol. 102, p. 107006, 2009. 11

[130] A. D. Christianson, M. D. Lumsden, S. E. Nagler, G. J. MacDougall, M. A. McGuire, A. S. Sefat, R. Jin, B. C. Sales, and D. Mandrus, "Static and dynamic magnetism in underdoped superconductor $BaFe_{1.92}Co_{0.08}As_2$," *Phys. Rev. Lett.*, vol. 103, p. 087002, 2009. 11

[131] H. A. Mook, M. D. Lumsden, A. D. Christianson, S. E. Nagler, B. C. Sales, R. Jin, M. A. McGuire, A. S. Sefat, D. Mandrus, T. Egami, and C. dela Cruz, "Unusual relationship between magnetism and superconductivity in $FeTe_{0.5}Se_{0.5}$," *Phys. Rev. Lett.*, vol. 104, p. 187002, 2010. 11

[132] S.-H. Lee, G. Xu, W. Ku, J. S. Wen, C. C. Lee, N. Katayama, Z. J. Xu, S. Ji, Z. W. Lin, G. D. Gu, H.-B. Yang, P. D. Johnson, Z.-H. Pan, T. Valla, M. Fujita, T. J. Sato, S. Chang, K. Yamada, and J. M. Tranquada, "Coupling of spin and orbital excitations in the iron-based superconductor $FeSe_{0.5}Te_{0.5}$," *Phys. Rev. B*, vol. 81, p. 220502, 2010. 11

[133] J. Wen, G. Xu, Z. Xu, Z. W. Lin, Q. Li, Y. Chen, S. Chi, G. Gu, and J. M. Tranquada, "Effect of magnetic field on the spin resonance in $FeTe_{0.5}Se_{0.5}$ as seen via inelastic neutron scattering," *Phys. Rev. B*, vol. 81, p. 100513, 2010. 11

[134] D. N. Argyriou, A. Hiess, A. Akbari, I. Eremin, M. M. Korshunov, J. Hu, B. Qian, Z. Mao, Y. Qiu, C. Broholm, and W. Bao, "Incommensurate itinerant antiferromagnetic excitations and spin resonance in the $FeTe_{0.6}Se_{0.4}$ superconductor," *Phys. Rev. B*, vol. 81, p. 220503, 2010. 11

[135] P. Monthoux and D. J. Scalapino, "Self-consistent $d_{x^2-y^2}$ pairing in a two-dimensional Hubbard model," *Phys. Rev. Lett.*, vol. 72, pp. 1874–1877, 1994. 11

[136] H. F. Fong, B. Keimer, P. W. Anderson, D. Reznik, F. Doğan, and I. A. Aksay, "Phonon and magnetic neutron scattering at 41 meV in $YBa_2Cu_3O_7$," *Phys. Rev. Lett.*, vol. 75, pp. 316–319, 1995. 11

[137] C. D. Batista, G. Ortiz, and A. V. Balatsky, "Unified description of the resonance peak and incommensuration in high-T_c superconductors," *Phys. Rev. B*, vol. 64, p. 172508, 2001. 11

[138] J. Chang, I. Eremin, P. Thalmeier, and P. Fulde, "Theory of magnetic excitons in the heavy-fermion superconductor UPd_2Al_3," *Phys. Rev. B*, vol. 75, p. 024503, 2007. 11

[139] M. R. Norman, "Linear response theory and the universal nature of the magnetic excitation spectrum of the cuprates," *Phys. Rev. B*, vol. 75, p. 184514, 2007. 11

[140] R. Osborn, S. Rosenkranz, E. Goremychkin, and A. Christianson, "Inelastic neutron scattering studies of the spin and lattice dynamics in iron arsenide compounds," *Physica C*, vol. 469, no. 9–12, pp. 498–506, 2009. Superconductivity in Iron-Pnictides. 11

[141] J. Zhao, L.-P. Regnault, C. Zhang, M. Wang, Z. Li, F. Zhou, Z. Zhao, C. Fang, J. Hu, and P. Dai, "Neutron spin resonance as a probe of the superconducting energy gap of $BaFe_{1.9}Ni_{0.1}As_2$ superconductors," *Phys. Rev. B*, vol. 81, p. 180505, 2010. 11

[142] W. Bao, A. T. Savici, G. E. Granroth, C. Broholm, K. Habicht, Y. Qiu, J. Hu, T. Liu, and Z. Q. Mao, "A triplet resonance in superconducting $FeSe_{0.4}Te_{0.6}$," *arXiv:1002.1617*, 2010. 11

[143] S. Onari, H. Kontani, and M. Sato, "Structure of neutron-scattering peaks in both s_{++}-wave and $s_{\pm}$-wave states of an iron pnictide superconductor," *Phys. Rev. B*, vol. 81, p. 060504, 2010. 11

[144] S. Hüfner, M. A. Hossain, A. Damascelli, and G. A. Sawatzky, "Two gaps make a high-temperature superconductor?," *Rep. Prog. Phys.*, vol. 71, no. 6, p. 062501, 2008. 11

[145] A. Mourachkine, "The order parameters for pairing and phase coherence in cuprates; the magnetic origin of the coherent gap. the MCS model of high-T_c superconductivity," *Journal of Low Temperature Physics*, vol. 117, no. 3, pp. 401–405, 1999. 11

[146] K. S. Novoselov, A. K. Geim, S. V. Morozov, D. Jiang, Y. Zhang, S. V. Dubonos, I. V. Grigorieva, and A. A. Firsov, "Electric field effect in atomically thin carbon films," *Science*, vol. 306, no. 5696, pp. 666–669, 2004. 11, 12, 169

[147] K. S. Novoselov, A. K. Geim, S. V. Morozov, D. Jiang, M. I. Katsnelson, I. V. Grigorieva, S. V. Dubonos, and A. A. Firsov, "Two-dimensional gas of massless Dirac fermions in graphene," *Nature*, vol. 438, no. 7065, pp. 197–200, 2005. 11, 12, 97

[148] P. A. M. Dirac, "The quantum theory of the electron," *Proc. R. Soc. London, Ser. A*, vol. 117, no. 778, pp. 610–624, 1928. 12, 16

[149] M. I. Katsnelson, "Graphene: carbon in two dimensions," *Materials Today*, vol. 10, no. 1–2, pp. 20–27, 2007. 12, 13

[150] C. Donnerer, M. C. Rahn, M. M. Sala, J. G. Vale, D. Pincini, J. Strempfer, M. Krisch, D. Prabhakaran, A. T. Boothroyd, and D. F. McMorrow, "All-in–all-out magnetic order and propagating spin waves in $Sm_2Ir_2O_7$," *Phys. Rev. Lett.*, vol. 117, p. 037201, 2016. 12, 18, 26, 57, 129

[151] A. H. Castro Neto, F. Guinea, N. M. R. Peres, K. S. Novoselov, and A. K. Geim, "The electronic properties of graphene," *Rev. Mod. Phys.*, vol. 81, pp. 109–162, 2009. 13

[152] M. Wilson, "Electrons in atomically thin carbon sheets behave like massless particles," *Phys. Today*, vol. 59, no. 1, p. 21, 2006. 13

[153] Y. Yao, F. Ye, X.-L. Qi, S.-C. Zhang, and Z. Fang, "Spin-orbit gap of graphene: First-principles calculations," *Phys. Rev. B*, vol. 75, p. 041401, 2007. 13, 15

[154] P. R. Wallace, "The band theory of graphite," *Phys. Rev.*, vol. 71, pp. 622–634, 1947. 12, 13

[155] J. C. Slonczewski and P. R. Weiss, "Band structure of graphite," *Phys. Rev.*, vol. 109, pp. 272–279, 1958. 12

[156] G. W. Semenoff, "Condensed-matter simulation of a three-dimensional anomaly," *Phys. Rev. Lett.*, vol. 53, pp. 2449–2452, 1984. 12

[157] F. D. M. Haldane, “Model for a quantum Hall effect without Landau levels: Condensed-matter realization of the "Parity Anomaly",” *Phys. Rev. Lett.*, vol. 61, pp. 2015–2018, 1988. 12, 14

[158] M. I. Katsnelson, *Graphene: Carbon in Two Dimensions*. Cambridge University Press, 2012. 13

[159] J. L. Mañes, F. Guinea, and M. A. H. Vozmediano, “Existence and topological stability of Fermi points in multilayered graphene,” *Phys. Rev. B*, vol. 75, p. 155424, 2007. 13

[160] Y. Zhang, Y.-W. Tan, H. L. Stormer, and P. Kim, “Experimental observation of the quantum Hall effect and Berry’s phase in graphene,” *Nature*, vol. 438, no. 7065, pp. 201–204, 2005. 13

[161] M. Sprinkle, D. Siegel, Y. Hu, J. Hicks, A. Tejeda, A. Taleb-Ibrahimi, P. Le Fèvre, F. Bertran, S. Vizzini, H. Enriquez, S. Chiang, P. Soukiassian, C. Berger, W. A. de Heer, A. Lanzara, and E. H. Conrad, “First direct observation of a nearly ideal graphene band structure,” *Phys. Rev. Lett.*, vol. 103, p. 226803, 2009. 13

[162] M. I. Katsnelson, K. S. Novoselov, and A. K. Geim, “Chiral tunnelling and the Klein paradox in graphene,” *Nat. Phys.*, vol. 2, no. 9, pp. 620–625, 2006. 13

[163] M. Y. Han, B. Özyilmaz, Y. Zhang, and P. Kim, “Energy band-gap engineering of graphene nanoribbons,” *Phys. Rev. Lett.*, vol. 98, p. 206805, 2007. 13

[164] X. Fan, W. Peng, Y. Li, X. Li, S. Wang, G. Zhang, and F. Zhang, “Deoxygenation of exfoliated graphite oxide under alkaline conditions: A green route to graphene preparation,” *Adv. Mater.*, vol. 20, no. 23, pp. 4490–4493, 2008. 13

[165] S. Cahangirov, M. Topsakal, E. Aktürk, H. Şahin, and S. Ciraci, “Two- and one-dimensional honeycomb structures of silicon and germanium,” *Phys. Rev. Lett.*, vol. 102, p. 236804, 2009. 14

[166] M. E. Dávila, L. Xian, S. Cahangirov, A. Rubio, and G. L. Lay, “Germanene: a novel two-dimensional germanium allotrope akin to graphene and silicene,” *New J. Phys.*, vol. 16, no. 9, p. 095002, 2014. 14

[167] N. Schroeter, M. Watson, L. Duffy, M. Hoesch, Y. Chen, T. Hesjedal, and T. Kim, “Emergence of Dirac-like bands in the monolayer limit of epitaxial Ge films on Au(111),” *2D Materials*, 2017. Accepted manuscript. 14

[168] M. Polini, F. Guinea, M. Lewenstein, H. C. Manoharan, and V. Pellegrini, “Artificial honeycomb lattices for electrons, atoms and photons,” *Nat. Nano*, vol. 8, no. 9, pp. 625–633, 2013. 14

[169] C.-H. Park and S. G. Louie, "Making massless Dirac fermions from a patterned two-dimensional electron gas," *Nano Letters*, vol. 9, no. 5, pp. 1793–1797, 2009. 14

[170] B. Wunsch, F. Guinea, and F. Sols, "Dirac-point engineering and topological phase transitions in honeycomb optical lattices," *New J. Phys*, vol. 10, no. 10, p. 103027, 2008. 14

[171] M. Sutherland, D. G. Hawthorn, R. W. Hill, F. Ronning, S. Wakimoto, H. Zhang, C. Proust, E. Boaknin, C. Lupien, L. Taillefer, R. Liang, D. A. Bonn, W. N. Hardy, R. Gagnon, N. E. Hussey, T. Kimura, M. Nohara, and H. Takagi, "Thermal conductivity across the phase diagram of cuprates: Low-energy quasiparticles and doping dependence of the superconducting gap," *Phys. Rev. B*, vol. 67, p. 174520, 2003. 14

[172] F. Steglich, J. Aarts, C. D. Bredl, W. Lieke, D. Meschede, W. Franz, and H. Schäfer, "Superconductivity in the presence of strong Pauli paramagnetism: $CeCu_2Si_2$," *Phys. Rev. Lett.*, vol. 43, pp. 1892–1896, 1979. 14

[173] T. Arai, K. Ichimura, K. Nomura, S. Takasaki, J. Yamada, S. Nakatsuji, and H. Anzai, "Tunneling spectroscopy on the organic superconductor $\kappa-(\mathrm{BEDT-TTF})_2\mathrm{Cu(NCS)}_2$ using STM," *Phys. Rev. B*, vol. 63, p. 104518, 2001. 14

[174] K. Ichimura, M. Takami, and K. Nomura, "Direct observation of d-wave superconducting gap in κ-$(\mathrm{BEDT\text{-}TTF})_2\mathrm{Cu[N(CN)}_2]\mathrm{Br}$ with scanning tunneling microscopy," *J. Phys. Soc. Jpn.*, vol. 77, no. 11, p. 114707, 2008. 14

[175] J. Orenstein and A. J. Millis, "Advances in the physics of high-temperature superconductivity," *Science*, vol. 288, no. 5465, pp. 468–474, 2000. 14

[176] S. H. Simon and P. A. Lee, "Scaling of the quasiparticle spectrum for d-wave superconductors," *Phys. Rev. Lett.*, vol. 78, pp. 1548–1551, 1997. 14

[177] P. W. Anderson, "Anomalous magnetothermal resistance of high-T_c superconductors: Anomalous cyclotron orbits at a Dirac point," *arXiv:cond-mat/9812063v1*, 1998. 14

[178] Y. Ran, F. Wang, H. Zhai, A. Vishwanath, and D.-H. Lee, "Nodal spin density wave and band topology of the FeAs-based materials," *Phys. Rev. B*, vol. 79, p. 014505, 2009. 14, 99

[179] T. Morinari, E. Kaneshita, and T. Tohyama, "Topological and transport properties of Dirac fermions in an antiferromagnetic metallic phase of iron-based superconductors," *Phys. Rev. Lett.*, vol. 105, p. 037203, 2010. 14, 99

[180] J. Knolle, I. Eremin, and R. Moessner, "Multiorbital spin susceptibility in a magnetically ordered state: Orbital versus excitonic spin density wave scenario," *Phys. Rev. B*, vol. 83, p. 224503, 2011. 14

[181] P. Richard, K. Nakayama, T. Sato, M. Neupane, Y.-M. Xu, J. H. Bowen, G. F. Chen, J. L. Luo, N. L. Wang, X. Dai, Z. Fang, H. Ding, and T. Takahashi, "Observation of Dirac cone electronic dispersion in $BaFe_2As_2$," *Phys. Rev. Lett.*, vol. 104, p. 137001, 2010. 14, 99

[182] N. Harrison and S. E. Sebastian, "Dirac nodal pockets in the antiferromagnetic parent phase of FeAs superconductors," *Phys. Rev. B*, vol. 80, p. 224512, 2009. 14

[183] Y. Ando, "Topological insulator materials," *Journal of the Physical Society of Japan*, vol. 82, no. 10, p. 102001, 2013. 15

[184] J. E. Moore, "The birth of topological insulators," *Nature*, vol. 464, no. 7286, pp. 194–198, 2010. 15, 16

[185] Y. Xia, D. Qian, D. Hsieh, L. Wray, A. Pal, H. Lin, A. Bansil, D. Grauer, Y. S. Hor, R. J. Cava, and M. Z. Hasan, "Observation of a large-gap topological-insulator class with a single Dirac cone on the surface," *Nat. Phys.*, vol. 5, no. 6, pp. 398–402, 2009. 15, 16

[186] D. Hsieh, Y. Xia, D. Qian, L. Wray, J. H. Dil, F. Meier, J. Osterwalder, L. Patthey, J. G. Checkelsky, N. P. Ong, A. V. Fedorov, H. Lin, A. Bansil, D. Grauer, Y. S. Hor, R. J. Cava, and M. Z. Hasan, "A tunable topological insulator in the spin helical Dirac transport regime," *Nature*, vol. 460, no. 7259, pp. 1101–1105, 2009. 15

[187] K. von Klitzing, G. Dorda, and M. Pepper, "New method for high-accuracy determination of the fine-structure constant based on quantized Hall resistance," *Phys. Rev. Lett.*, vol. 45, pp. 494–497, 1980. 14

[188] C. L. Kane and E. J. Mele, "Z_2 topological order and the quantum spin Hall effect," *Phys. Rev. Lett.*, vol. 95, p. 146802, 2005. 14

[189] C. L. Kane and E. J. Mele, "Quantum spin Hall effect in graphene," *Phys. Rev. Lett.*, vol. 95, p. 226801, 2005. 14

[190] S. Murakami, N. Nagaosa, and S.-C. Zhang, "Spin-Hall insulator," *Phys. Rev. Lett.*, vol. 93, p. 156804, 2004. 14

[191] J. E. Moore and L. Balents, "Topological invariants of time-reversal-invariant band structures," *Phys. Rev. B*, vol. 75, p. 121306, 2007. 15

[192] L. Fu and C. L. Kane, "Topological insulators with inversion symmetry," *Phys. Rev. B*, vol. 76, p. 045302, 2007. 15, 16

[193] X.-L. Qi, T. L. Hughes, and S.-C. Zhang, "Topological field theory of time-reversal invariant insulators," *Phys. Rev. B*, vol. 78, p. 195424, 2008. 15

[194] B. A. Bernevig, T. L. Hughes, and S.-C. Zhang, "Quantum spin Hall effect and topological phase transition in HgTe quantum wells," *Science*, vol. 314, no. 5806, pp. 1757–1761, 2006. 15

[195] M. König, S. Wiedmann, C. Brüne, A. Roth, H. Buhmann, L. W. Molenkamp, X.-L. Qi, and S.-C. Zhang, "Quantum spin Hall insulator state in HgTe quantum wells," *Science*, vol. 318, no. 5851, pp. 766–770, 2007. 15

[196] M. Z. Hasan and C. L. Kane, "Colloquium: Topological insulators," *Rev. Mod. Phys.*, vol. 82, pp. 3045–3067, 2010. 15

[197] X.-L. Qi and S.-C. Zhang, "Topological insulators and superconductors," *Rev. Mod. Phys.*, vol. 83, pp. 1057–1110, 2011. 15

[198] L. Müchler, H. Zhang, S. Chadov, B. Yan, F. Casper, J. Kübler, S.-C. Zhang, and C. Felser, "Topological insulators from a chemist's perspective," *Angew. Chem. Int. Ed.*, vol. 51, no. 29, pp. 7221–7225, 2012. 15

[199] C. Kane and J. Moore, "Topological insulators," *Physics World*, vol. 24, no. 02, p. 32, 2011. 15

[200] J. Moore, "Topological insulators: The next generation," *Nat. Phys.*, vol. 5, no. 6, pp. 378–380, 2009. 15, 16

[201] D. Hsieh, Y. Xia, L. Wray, D. Qian, A. Pal, J. H. Dil, J. Osterwalder, F. Meier, G. Bihlmayer, C. L. Kane, Y. S. Hor, R. J. Cava, and M. Z. Hasan, "Observation of unconventional quantum spin textures in topological insulators," *Science*, vol. 323, no. 5916, pp. 919–922, 2009. 15, 16

[202] D. Hsieh, D. Qian, L. Wray, Y. Xia, Y. S. Hor, R. J. Cava, and M. Z. Hasan, "A topological Dirac insulator in a quantum spin Hall phase," *Nature*, vol. 452, no. 7190, pp. 970–974, 2008. 16, 97

[203] L. Fu, C. L. Kane, and E. J. Mele, "Topological insulators in three dimensions," *Phys. Rev. Lett.*, vol. 98, p. 106803, 2007. 16, 21

[204] H. Zhang, C.-X. Liu, X.-L. Qi, X. Dai, Z. Fang, and S.-C. Zhang, "Topological insulators in Bi_2Se_3, Bi_2Te_3 and Sb_2Te_3 with a single Dirac cone on the surface," *Nat. Phys.*, vol. 5, no. 6, pp. 438–442, 2009. 16

[205] I. Garate and M. Franz, "Inverse spin-galvanic effect in the interface between a topological insulator and a ferromagnet," *Phys. Rev. Lett.*, vol. 104, p. 146802, 2010. 16

[206] R. Ramesh and N. A. Spaldin, "Multiferroics: progress and prospects in thin films," *Nat. Mater.*, vol. 6, no. 1, pp. 21–29, 2007. 16

[207] L. Fu and C. L. Kane, "Superconducting proximity effect and Majorana fermions at the surface of a topological insulator," *Phys. Rev. Lett.*, vol. 100, p. 096407, 2008. 16

[208] R. Jackiw and P. Rossi, "Zero modes of the vortex-fermion system," *Nuc. Phys. B*, vol. 190, no. 4, pp. 681–691, 1981. 16

[209] G. P. Collins, "Computing with quantum knots," *Scientific American*, vol. 294, pp. 57–63, 2006. 16

[210] S. Murakami, "Phase transition between the quantum spin Hall and insulator phases in 3D: emergence of a topological gapless phase," *New J. Phys.*, vol. 9, no. 9, p. 356, 2007. 16

[211] X. Wan, A. M. Turner, A. Vishwanath, and S. Y. Savrasov, "Topological semimetal and Fermi-arc surface states in the electronic structure of pyrochlore iridates," *Phys. Rev. B*, vol. 83, p. 205101, 2011. 16, 17, 26

[212] C. Herring, "Accidental degeneracy in the energy bands of crystals," *Phys. Rev.*, vol. 52, pp. 365–373, 1937. 16, 17

[213] H. Weyl, "Elektron und Gravitation. I," *Z. Phys.*, vol. 56, no. 5, pp. 330–352, 1929. 16

[214] H. Nielsen and M. Ninomiya, "Absence of neutrinos on a lattice," *Nuc. Phys. B*, vol. 185, no. 1, pp. 20–40, 1981. 16

[215] H. Nielsen and M. Ninomiya, "A no-go theorem for regularizing chiral fermions," *Phys. Lett. B*, vol. 105, no. 2, pp. 219–223, 1981. 16

[216] D. Xiao, M.-C. Chang, and Q. Niu, "Berry phase effects on electronic properties," *Rev. Mod. Phys.*, vol. 82, pp. 1959–2007, 2010. 17

[217] M. Z. Hasan, S.-Y. Xu, I. Belopolski, and S.-M. Huang, "Discovery of Weyl fermion semimetal and topological Fermi arc states," *Annu. Rev. Cond. Mat. Phys.*, vol. 8, pp. 289–309, 2017. 17, 18, 19

[218] W. Witczak-Krempa, G. Chen, Y. B. Kim, and L. Balents, "Correlated quantum phenomena in the strong spin-orbit regime," *Annu. Rev. Cond. Mat. Phys.*, vol. 5, no. 1, pp. 57–82, 2014. 18, 22, 23, 24, 27, 28

[219] A. A. Burkov, M. D. Hook, and L. Balents, "Topological nodal semimetals," *Phys. Rev. B*, vol. 84, p. 235126, 2011. 18

[220] D. Bulmash, C.-X. Liu, and X.-L. Qi, "Prediction of a Weyl semimetal in $Hg_{1-x-y}Cd_xMn_yTe$," *Phys. Rev. B*, vol. 89, p. 081106, 2014. 18

[221] Z. K. Liu, L. X. Yang, Y. Sun, T. Zhang, H. Peng, H. F. Yang, C. Chen, Y. Zhang, Y. F. Guo, D. Prabhakaran, M. Schmidt, Z. Hussain, S.-K. Mo, C. Felser, B. Yan, and Y. L. Chen, "Evolution of the Fermi surface of Weyl semimetals in the transition metal pnictide family," *Nat Mater*, vol. 15, no. 1, pp. 27–31, 2016. 18, 19

[222] B. Singh, A. Sharma, H. Lin, M. Z. Hasan, R. Prasad, and A. Bansil, "Topological electronic structure and Weyl semimetal in the $TlBiSe_2$ class of semiconductors," *Phys. Rev. B*, vol. 86, p. 115208, 2012. 18

[223] G. B. Halász and L. Balents, "Time-reversal invariant realization of the Weyl semimetal phase," *Phys. Rev. B*, vol. 85, p. 035103, 2012. 18

[224] J. Liu and D. Vanderbilt, "Weyl semimetals from noncentrosymmetric topological insulators," *Phys. Rev. B*, vol. 90, p. 155316, 2014. 18

[225] S.-M. Huang, S.-Y. Xu, I. Belopolski, C.-C. Lee, G. Chang, B. Wang, N. Alidoust, G. Bian, M. Neupane, C. Zhang, S. Jia, A. Bansil, H. Lin, and M. Z. Hasan, "A Weyl fermion semimetal with surface Fermi arcs in the transition metal monopnictide TaAs class," *Nat. Commun.*, vol. 6, p. 7373, 2015. 18, 19

[226] H. Weng, C. Fang, Z. Fang, B. A. Bernevig, and X. Dai, "Weyl semimetal phase in noncentrosymmetric transition-metal monophosphides," *Phys. Rev. X*, vol. 5, p. 011029, 2015. 18, 19

[227] S.-Y. Xu, C. Liu, S. K. Kushwaha, R. Sankar, J. W. Krizan, I. Belopolski, M. Neupane, G. Bian, N. Alidoust, T.-R. Chang, H.-T. Jeng, C.-Y. Huang, W.-F. Tsai, H. Lin, P. P. Shibayev, F.-C. Chou, R. J. Cava, and M. Z. Hasan, "Observation of Fermi arc surface states in a topological metal," *Science*, vol. 347, no. 6219, pp. 294–298, 2015. 18

[228] S.-Y. Xu, I. Belopolski, N. Alidoust, M. Neupane, G. Bian, C. Zhang, R. Sankar, G. Chang, Z. Yuan, C.-C. Lee, S.-M. Huang, H. Zheng, J. Ma, D. S. Sanchez, B. Wang, A. Bansil, F. Chou, P. P. Shibayev, H. Lin, S. Jia, and M. Z. Hasan, "Discovery of a Weyl fermion semimetal and topological Fermi arcs," *Science*, vol. 349, no. 6248, pp. 613–617, 2015. 18

[229] B. Q. Lv, H. M. Weng, B. B. Fu, X. P. Wang, H. Miao, J. Ma, P. Richard, X. C. Huang, L. X. Zhao, G. F. Chen, Z. Fang, X. Dai, T. Qian, and H. Ding, "Experimental discovery of Weyl semimetal TaAs," *Phys. Rev. X*, vol. 5, p. 031013, 2015. 18

[230] S.-Y. Xu, N. Alidoust, I. Belopolski, Z. Yuan, G. Bian, T.-R. Chang, H. Zheng, V. N. Strocov, D. S. Sanchez, G. Chang, C. Zhang, D. Mou, Y. Wu, L. Huang, C.-C. Lee,

S.-M. Huang, B. Wang, A. Bansil, H.-T. Jeng, T. Neupert, A. Kaminski, H. Lin, S. Jia, and M. Zahid Hasan, "Discovery of a Weyl fermion state with Fermi arcs in niobium arsenide," *Nat. Phys.*, vol. 11, no. 9, pp. 748–754, 2015. 18

[231] S.-Y. Xu, I. Belopolski, D. S. Sanchez, C. Zhang, G. Chang, C. Guo, G. Bian, Z. Yuan, H. Lu, T.-R. Chang, P. P. Shibayev, M. L. Prokopovych, N. Alidoust, H. Zheng, C.-C. Lee, S.-M. Huang, R. Sankar, F. Chou, C.-H. Hsu, H.-T. Jeng, A. Bansil, T. Neupert, V. N. Strocov, H. Lin, S. Jia, and M. Z. Hasan, "Experimental discovery of a topological Weyl semimetal state in TaP," *Sci. Adv.*, vol. 1, no. 10, 2015. 18

[232] L. X. Yang, Z. K. Liu, Y. Sun, H. Peng, H. F. Yang, T. Zhang, B. Zhou, Y. Zhang, Y. F. Guo, M. Rahn, D. Prabhakaran, Z. Hussain, S.-K. Mo, C. Felser, B. Yan, and Y. L. Chen, "Weyl semimetal phase in the non-centrosymmetric compound TaAs," *Nat. Phys.*, vol. 11, no. 9, pp. 728–732, 2015. 19, 97

[233] I. Belopolski, S.-Y. Xu, D. S. Sanchez, G. Chang, C. Guo, M. Neupane, H. Zheng, C.-C. Lee, S.-M. Huang, G. Bian, N. Alidoust, T.-R. Chang, B. Wang, X. Zhang, A. Bansil, H.-T. Jeng, H. Lin, S. Jia, and M. Z. Hasan, "Criteria for directly detecting topological Fermi arcs in Weyl semimetals," *Phys. Rev. Lett.*, vol. 116, p. 066802, 2016. 19

[234] S.-M. Huang, S.-Y. Xu, I. Belopolski, C.-C. Lee, G. Chang, T.-R. Chang, B. Wang, N. Alidoust, G. Bian, M. Neupane, D. Sanchez, H. Zheng, H.-T. Jeng, A. Bansil, T. Neupert, H. Lin, and M. Z. Hasan, "New type of Weyl semimetal with quadratic double Weyl fermions," *Proc. Natl. Acad. Sci. USA*, vol. 113, no. 5, pp. 1180–1185, 2016. 19

[235] S.-Y. Xu, N. Alidoust, G. Chang, H. Lu, B. Singh, I. Belopolski, D. Sanchez, X. Zhang, G. Bian, H. Zheng, M.-A. Husanu, Y. Bian, S.-M. Huang, C.-H. Hsu, T.-R. Chang, H.-T. Jeng, A. Bansil, V. N. Strocov, H. Lin, S. Jia, and M. Zahid Hasan, "Discovery of Lorentz-violating Weyl fermion semimetal state in LaAlGe materials," *arXiv:1603.07318*, 2016. 19

[236] T.-R. Chang, S.-Y. Xu, G. Chang, C.-C. Lee, S.-M. Huang, B. Wang, G. Bian, H. Zheng, D. S. Sanchez, I. Belopolski, N. Alidoust, M. Neupane, A. Bansil, H.-T. Jeng, H. Lin, and M. Zahid Hasan, "Prediction of an arc-tunable Weyl fermion metallic state in $Mo_xW_{1-x}Te_2$," *Nat. Commun.*, vol. 7, p. 10639, 2016. 19

[237] Y. Sun, S.-C. Wu, M. N. Ali, C. Felser, and B. Yan, "Prediction of Weyl semimetal in orthorhombic $MoTe_2$," *Phys. Rev. B*, vol. 92, p. 161107, 2015. 19

[238] G. Autès, D. Gresch, M. Troyer, A. A. Soluyanov, and O. V. Yazyev, "Robust type-II Weyl semimetal phase in transition metal diphosphides XP_2 ($X =$ Mo, W)," *Phys. Rev. Lett.*, vol. 117, p. 066402, 2016. 19

[239] C.-C. Liu, J.-J. Zhou, Y. Yao, and F. Zhang, "Weak topological insulators and composite Weyl semimetals: $\beta-Bi_4X_4$ (X = Br, I)," *Phys. Rev. Lett.*, vol. 116, p. 066801, 2016. 19

[240] A. A. Soluyanov, D. Gresch, Z. Wang, Q. Wu, M. Troyer, X. Dai, and B. A. Bernevig, "Type-II Weyl semimetals," *Nature*, vol. 527, no. 7579, pp. 495–498, 2015. 19

[241] K. Koepernik, D. Kasinathan, D. V. Efremov, S. Khim, S. Borisenko, B. Büchner, and J. van den Brink, "$TaIrTe_4$: A ternary type-II Weyl semimetal," *Phys. Rev. B*, vol. 93, p. 201101, 2016. 19

[242] K. Deng, G. Wan, P. Deng, K. Zhang, S. Ding, E. Wang, M. Yan, H. Huang, H. Zhang, Z. Xu, J. Denlinger, A. Fedorov, H. Yang, W. Duan, H. Yao, Y. Wu, S. Fan, H. Zhang, X. Chen, and S. Zhou, "Experimental observation of topological Fermi arcs in type-II Weyl semimetal $MoTe_2$," *Nat. Phys.*, vol. 12, no. 12, pp. 1105–1110, 2016. 19

[243] H.-J. Kim, K.-S. Kim, J.-F. Wang, M. Sasaki, N. Satoh, A. Ohnishi, M. Kitaura, M. Yang, and L. Li, "Dirac versus Weyl fermions in topological insulators: Adler-Bell-Jackiw anomaly in transport phenomena," *Phys. Rev. Lett.*, vol. 111, p. 246603, 2013. 19

[244] A. A. Zyuzin and A. A. Burkov, "Topological response in Weyl semimetals and the chiral anomaly," *Phys. Rev. B*, vol. 86, p. 115133, 2012. 19

[245] P. Hosur and X. Qi, "Recent developments in transport phenomena in Weyl semimetals," *Comptes Rendus Physique*, vol. 14, no. 9–10, pp. 857–870, 2013. 19

[246] C. Zhang, E. Zhang, W. Wang, Y. Liu, Z.-G. Chen, S. Lu, S. Liang, J. Cao, X. Yuan, L. Tang, Q. Li, C. Zhou, T. Gu, Y. Wu, J. Zou, and F. Xiu, "Room-temperature chiral charge pumping in Dirac semimetals," *Nat. Commun.*, vol. 8, p. 13741, 2017. 19

[247] X. Huang, L. Zhao, Y. Long, P. Wang, D. Chen, Z. Yang, H. Liang, M. Xue, H. Weng, Z. Fang, X. Dai, and G. Chen, "Observation of the chiral-anomaly-induced negative magnetoresistance in 3D Weyl semimetal TaAs," *Phys. Rev. X*, vol. 5, p. 031023, 2015. 19

[248] J. L. Mañes, "Existence of bulk chiral fermions and crystal symmetry," *Phys. Rev. B*, vol. 85, p. 155118, 2012. 21

[249] S. M. Young, S. Zaheer, J. C. Y. Teo, C. L. Kane, E. J. Mele, and A. M. Rappe, "Dirac semimetal in three dimensions," *Phys. Rev. Lett.*, vol. 108, p. 140405, 2012. 21

[250] B. J. Wieder, Y. Kim, A. M. Rappe, and C. L. Kane, "Double Dirac semimetals in three dimensions," *Phys. Rev. Lett.*, vol. 116, p. 186402, 2016. 21

[251] B. Bradlyn, J. Cano, Z. Wang, M. G. Vergniory, C. Felser, R. J. Cava, and B. A. Bernevig, "Beyond Dirac and Weyl fermions: Unconventional quasiparticles in conventional crystals," *Science*, vol. 353, no. 6299, 2016. 21

[252] L. Li, J. G. Checkelsky, Y. S. Hor, C. Uher, A. F. Hebard, R. J. Cava, and N. P. Ong, "Phase transitions of Dirac electrons in bismuth," *Science*, vol. 321, no. 5888, pp. 547–550, 2008. 21

[253] Z. Wang, Y. Sun, X.-Q. Chen, C. Franchini, G. Xu, H. Weng, X. Dai, and Z. Fang, "Dirac semimetal and topological phase transitions in A_3Bi ($A = $ Na, K, Rb)," *Phys. Rev. B*, vol. 85, p. 195320, 2012. 21

[254] Z. K. Liu, B. Zhou, Y. Zhang, Z. J. Wang, H. M. Weng, D. Prabhakaran, S.-K. Mo, Z. X. Shen, Z. Fang, X. Dai, Z. Hussain, and Y. L. Chen, "Discovery of a three-dimensional topological Dirac semimetal, Na_3Bi," *Science*, vol. 343, no. 6173, pp. 864–867, 2014. 21, 115

[255] J. Xiong, S. K. Kushwaha, T. Liang, J. W. Krizan, W. Wang, R. J. Cava, and N. P. Ong, "Signature of the chiral anomaly in a Dirac semimetal: a current plume steered by a magnetic field," *arXiv:1503.08179*, 2015. 21

[256] Z. Wang, H. Weng, Q. Wu, X. Dai, and Z. Fang, "Three-dimensional Dirac semimetal and quantum transport in Cd_3As_2," *Phys. Rev. B*, vol. 88, p. 125427, 2013. 21, 117

[257] Z. K. Liu, J. Jiang, B. Zhou, Z. J. Wang, Y. Zhang, H. M. Weng, D. Prabhakaran, S.-K. Mo, H. Peng, P. Dudin, T. Kim, M. Hoesch, Z. Fang, X. Dai, Z. X. Shen, D. L. Feng, Z. Hussain, and Y. L. Chen, "A stable three-dimensional topological Dirac semimetal Cd_3As_2," *Nat. Mater.*, vol. 13, no. 7, pp. 677–681, 2014. 21, 117

[258] S. Borisenko, Q. Gibson, D. Evtushinsky, V. Zabolotnyy, B. Büchner, and R. J. Cava, "Experimental realization of a three-dimensional Dirac semimetal," *Phys. Rev. Lett.*, vol. 113, p. 027603, 2014. 21

[259] M. Neupane, S.-Y. Xu, R. Sankar, N. Alidoust, G. Bian, C. Liu, I. Belopolski, T.-R. Chang, H.-T. Jeng, H. Lin, A. Bansil, F. Chou, and M. Z. Hasan, "Observation of a three-dimensional topological Dirac semimetal phase in high-mobility Cd_3As_2," *Nat. Commun.*, vol. 5, p. 3786, 2014. 21, 115, 117

[260] P. J. W. Moll, N. L. Nair, T. Helm, A. C. Potter, I. Kimchi, A. Vishwanath, and J. G. Analytis, "Transport evidence for fermi-arc-mediated chirality transfer in the Dirac semimetal Cd_3As_2," *Nature*, vol. 535, no. 7611, pp. 266–270, 2016. 21

[261] C. Zhu, F. Wang, Y. Meng, X. Yuan, F. Xiu, H. Luo, Y. Wang, J. Li, X. Lv, L. He, Y. Xu, J. Liu, C. Zhang, Y. Shi, R. Zhang, and S. Zhu, "A robust and tuneable mid-

infrared optical switch enabled by bulk Dirac fermions," *Nat. Commun.*, vol. 8, p. 14111, 2017. 21

[262] G. Jackeli and G. Khaliullin, "Mott insulators in the strong spin-orbit coupling limit: From Heisenberg to a quantum compass and Kitaev models," *Phys. Rev. Lett.*, vol. 102, p. 017205, 2009. 22, 24, 25, 169

[263] S. Boseggia, *Magnetic order and excitations in perovskite iridates studied with resonant x-ray scattering techniques*. PhD thesis, University College London, 2014. 23

[264] J. G. Rau, E. K.-H. Lee, and H.-Y. Kee, "Spin-orbit physics giving rise to novel phases in correlated systems: Iridates and related materials," *Annu. Rev. Cond. Mat. Phys.*, vol. 7, pp. 195–221, 2016. 23, 25, 27

[265] Y. Maeno, H. Hashimoto, K. Yoshida, S. Nishizaki, T. Fujita, J. G. Bednorz, and F. Lichtenberg, "Superconductivity in a layered perovskite without copper," *Nature*, vol. 372, no. 6506, pp. 532–534, 1994. 25

[266] M. K. Crawford, M. A. Subramanian, R. L. Harlow, J. A. Fernandez-Baca, Z. R. Wang, and D. C. Johnston, "Structural and magnetic studies of Sr_2IrO_4," *Phys. Rev. B*, vol. 49, pp. 9198–9201, 1994. 25

[267] B. J. Kim, H. Jin, S. J. Moon, J.-Y. Kim, B.-G. Park, C. S. Leem, J. Yu, T. W. Noh, C. Kim, S.-J. Oh, J.-H. Park, V. Durairaj, G. Cao, and E. Rotenberg, "Novel $J_{\text{eff}} = 1/2$ Mott state induced by relativistic spin-orbit coupling in Sr_2IrO_4," *Phys. Rev. Lett.*, vol. 101, p. 076402, 2008. 25, 28

[268] B. J. Kim, H. Ohsumi, T. Komesu, S. Sakai, T. Morita, H. Takagi, and T. Arima, "Phase-sensitive observation of a spin-orbital Mott state in Sr_2IrO_4," *Science*, vol. 323, no. 5919, pp. 1329–1332, 2009. 25

[269] J. Kim, D. Casa, M. H. Upton, T. Gog, Y.-J. Kim, J. F. Mitchell, M. van Veenendaal, M. Daghofer, J. van den Brink, G. Khaliullin, and B. J. Kim, "Magnetic excitation spectra of Sr_2IrO_4 probed by resonant inelastic x-ray scattering: Establishing links to cuprate superconductors," *Phys. Rev. Lett.*, vol. 108, p. 177003, 2012. 25

[270] M. Ge, T. F. Qi, O. B. Korneta, D. E. De Long, P. Schlottmann, W. P. Crummett, and G. Cao, "Lattice-driven magnetoresistivity and metal-insulator transition in single-layered iridates," *Phys. Rev. B*, vol. 84, p. 100402, 2011. 25

[271] Z. Nussinov and J. van den Brink, "Compass models: Theory and physical motivations," *Rev. Mod. Phys.*, vol. 87, pp. 1–59, 2015. 25

[272] A. Kitaev, "Anyons in an exactly solved model and beyond," *Ann. Phys.*, vol. 321, no. 1, pp. 2–111, 2006. 25

[273] S. K. Choi, R. Coldea, A. N. Kolmogorov, T. Lancaster, I. I. Mazin, S. J. Blundell, P. G. Radaelli, Y. Singh, P. Gegenwart, K. R. Choi, S.-W. Cheong, P. J. Baker, C. Stock, and J. Taylor, "Spin waves and revised crystal structure of honeycomb iridate Na_2IrO_3," *Phys. Rev. Lett.*, vol. 108, p. 127204, 2012. 26, 29

[274] X. Liu, T. Berlijn, W.-G. Yin, W. Ku, A. Tsvelik, Y.-J. Kim, H. Gretarsson, Y. Singh, P. Gegenwart, and J. P. Hill, "Long-range magnetic ordering in Na_2IrO_3," *Phys. Rev. B*, vol. 83, p. 220403, 2011. 26

[275] H. Gretarsson, J. P. Clancy, X. Liu, J. P. Hill, E. Bozin, Y. Singh, S. Manni, P. Gegenwart, J. Kim, A. H. Said, D. Casa, T. Gog, M. H. Upton, H.-S. Kim, J. Yu, V. M. Katukuri, L. Hozoi, J. van den Brink, and Y.-J. Kim, "Crystal-field splitting and correlation effect on the electronic structure of A_2IrO_3," *Phys. Rev. Lett.*, vol. 110, p. 076402, 2013. 26, 29

[276] S. Hwan Chun, J.-W. Kim, J. Kim, H. Zheng, C. C. Stoumpos, C. D. Malliakas, J. F. Mitchell, K. Mehlawat, Y. Singh, Y. Choi, T. Gog, A. Al-Zein, M. M. Sala, M. Krisch, J. Chaloupka, G. Jackeli, G. Khaliullin, and B. J. Kim, "Direct evidence for dominant bond-directional interactions in a honeycomb lattice iridate Na_2IrO_3," *Nat. Phys.*, vol. 11, no. 6, pp. 462–466, 2015. 26, 29

[277] M. Subramanian, G. Aravamudan, and G. S. Rao, "Oxide pyrochlores: A review," *Prog. Solid State Chem.*, vol. 15, no. 2, pp. 55–143, 1983. 26, 143

[278] L. Balents, "Spin liquids in frustrated magnets," *Nature*, vol. 464, p. 199, 2010. 26

[279] D. Yanagishima and Y. Maeno, "Metal-nonmetal changeover in pyrochlore iridates," *J. Phys. Soc. Jpn.*, vol. 70, no. 10, pp. 2880–2883, 2001. 26

[280] K. Matsuhira, M. Wakeshima, R. Nakanishi, T. Yamada, A. Nakamura, W. Kawano, S. Takagi, and Y. Hinatsu, "Metal–insulator transition in pyrochlore iridates $Ln_2Ir_2O_7$ (Ln = Nd, Sm, and Eu)," *J. Phys. Soc. Jpn.*, vol. 76, no. 4, p. 043706, 2007. 26

[281] K. Matsuhira, M. Wakeshima, Y. Hinatsu, and S. Takagi, "Metal–insulator transitions in pyrochlore oxides $Ln_2Ir_2O_7$," *J. Phys. Soc. Jpn.*, vol. 80, no. 9, p. 094701, 2011. 26

[282] H.-J. Koo, M.-H. Whangbo, and B. Kennedy, "Similarities and differences in the structural and electronic properties of ruthenium and iridium pyrochlores $A_2M_2O_{7-y}$ (M =Ru, Ir)," *J. Solid State Chem.*, vol. 136, no. 2, pp. 269–273, 1998. 26

[283] W. Witczak-Krempa and Y. B. Kim, "Topological and magnetic phases of interacting electrons in the pyrochlore iridates," *Phys. Rev. B*, vol. 85, p. 045124, 2012. 26, 27

[284] A. Go, W. Witczak-Krempa, G. S. Jeon, K. Park, and Y. B. Kim, "Correlation effects on 3D topological phases: From bulk to boundary," *Phys. Rev. Lett.*, vol. 109, p. 066401, 2012. 26

[285] S. Calder, L. Li, S. Okamoto, Y. Choi, R. Mukherjee, D. Haskel, and D. Mandrus, "Spin-orbit driven magnetic insulating state with $J_{\text{eff}} = \frac{1}{2}$ character in a $4d$ oxide," *Phys. Rev. B*, vol. 92, p. 180413, 2015. 28

[286] S. Calder, G.-X. Cao, S. Okamoto, J. W. Kim, V. R. Cooper, Z. Gai, B. C. Sales, M. D. Lumsden, D. Mandrus, and A. D. Christianson, "$J_{\text{eff}} = \frac{1}{2}$ Mott spin-orbit insulating state close to the cubic limit in Ca_4IrO_6," *Phys. Rev. B*, vol. 89, p. 081104, 2014. 28

[287] G. Chen and L. Balents, "Spin-orbit coupling in d^2 ordered double perovskites," *Phys. Rev. B*, vol. 84, p. 094420, 2011. 28

[288] K.-W. Lee and W. E. Pickett, "Half semimetallic antiferromagnetism in the $Sr_2Cr\mathcal{T}O_6$ system $(\mathcal{T} = \text{Os}, \text{Ru})$," *Phys. Rev. B*, vol. 77, p. 115101, 2008. 28

[289] H. J. Xiang and M.-H. Whangbo, "Cooperative effect of electron correlation and spin-orbit coupling on the electronic and magnetic properties of Ba_2NaOsO_6," *Phys. Rev. B*, vol. 75, p. 052407, 2007. 28

[290] C. Svoboda, M. Randeira, and N. Trivedi, "Orbital and spin order in spin-orbit coupled d^1 and d^2 double perovskites," *arXiv:1507.04847*, 2017. 28

[291] G. Chen, R. Pereira, and L. Balents, "Exotic phases induced by strong spin-orbit coupling in ordered double perovskites," *Phys. Rev. B*, vol. 82, p. 174440, 2010. 28

[292] C. Svoboda, M. Randeria, and N. Trivedi, "Effective magnetic interactions in spin-orbit coupled d^4 mott insulators," *Phys. Rev. B*, vol. 95, p. 014409, 2017. 28

[293] Y. G. Shi, Y. F. Guo, S. Yu, M. Arai, A. A. Belik, A. Sato, K. Yamaura, E. Takayama-Muromachi, H. F. Tian, H. X. Yang, J. Q. Li, T. Varga, J. F. Mitchell, and S. Okamoto, "Continuous metal-insulator transition of the antiferromagnetic perovskite $NaOsO_3$," *Phys. Rev. B*, vol. 80, p. 161104, 2009. 28, 164

[294] S. Calder, V. O. Garlea, D. F. McMorrow, M. D. Lumsden, M. B. Stone, J. C. Lang, J.-W. Kim, J. A. Schlueter, Y. G. Shi, K. Yamaura, Y. S. Sun, Y. Tsujimoto, and A. D. Christianson, "Magnetically driven metal-insulator transition in $NaOsO_3$," *Phys. Rev. Lett.*, vol. 108, p. 257209, 2012. 28, 164

[295] D. Mandrus, J. R. Thompson, R. Gaal, L. Forro, J. C. Bryan, B. C. Chakoumakos, L. M. Woods, B. C. Sales, R. S. Fishman, and V. Keppens, "Continuous metal-insulator transition in the pyrochlore $Cd_2Os_2O_7$," *Phys. Rev. B*, vol. 63, p. 195104, 2001. 28

[296] W. J. Padilla, D. Mandrus, and D. N. Basov, "Searching for the Slater transition in the pyrochlore $Cd_2Os_2O_7$ with infrared spectroscopy," *Phys. Rev. B*, vol. 66, p. 035120, 2002. 28

[297] I. M. Lifshitz, "Anomalies of electron characteristics of a metal in the high pressure region," *Sov. Phys. JETP*, vol. 11, no. 5, pp. 1130–1135, 1960. 28, 164, 165

[298] J. C. Slater, "Magnetic effects and the Hartree-Fock equation," *Phys. Rev.*, vol. 82, pp. 538–541, 1951. 28, 164, 165

[299] E. Lefrançois, V. Simonet, R. Ballou, E. Lhotel, A. Hadj-Azzem, S. Kodjikian, P. Lejay, P. Manuel, D. Khalyavin, and L. C. Chapon, "Anisotropy-tuned magnetic order in pyrochlore iridates," *Phys. Rev. Lett.*, vol. 114, p. 247202, 2015. 29

[300] H. Guo, C. Ritter, and A. C. Komarek, "Direct determination of the spin structure of $Nd_2Ir_2O_7$ by means of neutron diffraction," *Phys. Rev. B*, vol. 94, p. 161102, 2016. 29

[301] P. G. Radaelli and S. S. Dhesi, "The contribution of Diamond Light Source to the study of strongly correlated electron systems and complex magnetic structures," *Philos. Trans. R. Soc. London, Ser. A*, vol. 373, no. 2036, 2015. 29, 59

[302] C. Vettier, "Resonant elastic x-ray scattering: Where from? where to?," *Eur. Phys. J. Special Topics*, vol. 208, no. 1, pp. 3–14, 2012. 29

[303] L. J. P. Ament, M. van Veenendaal, and J. van den Brink, "Determining the electron-phonon coupling strength from resonant inelastic x-ray scattering at transition metal L-edges," *Europhysics Letters*, vol. 95, no. 2, p. 27008, 2011. 29, 59, 60, 90

[304] Quantum Design, Inc., 10307 Pacific Center Court, San Diego, CA 92121, USA, Tel: +1858481440, Fax: +18584817410, info@qdusa.com. 33, 34

[305] Epoxy Technology, Inc., 14 Fortune Drive, Billerica, MA 01821, Tel: 978.667.3805, Fax: 978.663.9782, customerservice@epotek.com. 34

[306] Agilent Technologies XRD Products, "SuperNova X-ray Diffractometer System - User Manual (2014)." http://agilent.com/cs/ library/usermanuals/ public/ SuperNova_User_Manual.pdf – retrieved 13.6.2017. 35, 36

[307] Rigaku Corporation, 9009 New Trails Drive, The Woodlands, TX 77381-5209, USA, Tel: +1-281-362-2300. info@rigaku.com, https://www.rigaku.com/en/products/ xrd/smartlab — retrieved 14.7.2017. 37

[308] W. Friedrich, P. Knipping, and M. Laue, "Interferenzerscheinungen bei Röntgenstrahlen," *Ann. Phys.*, vol. 346, no. 10, pp. 971–988, 1913. 38

[309] W. H. Bragg and W. L. Bragg, "The reflection of x-rays by crystals," *Proc. R. Soc. London, Ser. A*, vol. 88, no. 605, pp. 428–438, 1913. 38, 40

[310] A. Authier, *Early Days of X-ray Crystallography*. Oxford University Press, 2013. 38

[311] J. Als-Nielsen and D. F. McMorrow, *Elements of Modern X-ray Physics*. John Wiley & Sons, Ltd., 2011. 38, 51, 59

[312] C. G. Shull and J. S. Smart, "Detection of antiferromagnetism by neutron diffraction," *Phys. Rev.*, vol. 76, pp. 1256–1257, 1949. 38

[313] J. S. Schwinger, "On the magnetic scattering of neutrons," *Phys. Rev.*, vol. 51, pp. 544–552, 1937. 38, 46

[314] J. D. Watson and F. H. C. Crick, "Molecular structure of nucleic acids: A structure for deoxyribose nucleic acid," *Nature*, vol. 171, no. 4356, pp. 737–738, 1953. 38

[315] J. Rodriguez-Carvajal, "Determination of magnetic structures and magnetic structure factors, magnetic structure determination workshop, Florida State University." https://conference.sns.gov/ event/22/picture/ 26.pdfRemove, 2016. 42

[316] G. L. Squires, *Thermal Neutron Scattering*. Cambridge University Press, 1978. 42, 43, 44, 45, 46, 48

[317] A. Furrer, J. Mesot, and T. Strässle, *Neutron Scattering in Condensed Matter Physics*. World Scientific, 2009. 42, 44, 45, 46, 48

[318] V. F. Sears, "Neutron scattering lengths and cross sections," *Neutron News*, vol. 3, no. 3, pp. 26–37, 1992. 44

[319] S. W. Lovesey, *Theory of neutron scattering from consdensed matter, vol. 2*. Clarendon Press, Oxford, 1984. 47

[320] P. J. Brown, *Magnetic form factors, chapter 4.4.5, p. 454*, vol. C. International Tables for Crystallography, 2006. 47

[321] K. Kobayashi, T. Nagao, and M. Ito, "Radial integrals for the magnetic form factor of 5*d* transition elements," *Acta Crystallogr. Sec. A*, vol. 67, no. 5, pp. 473–480, 2011. 47, 156

[322] T. Chatterji, *Neutron Scattering from Magnetic Materials*. Elsevier Science, 2006. 48

[323] Y. A. Izyumov and R. P. Ozerov, *Magnetic neutron diffraction*. Springer Science & Business Media, 2012. 48

[324] B. N. Brockhouse, "Structural dynamics of water by neutron spectrometry," *Il Nuovo Cimento*, vol. 9, no. 1, pp. 45–71, 1958. 50

[325] R. Lowde, "The principles of mechanical neutron-velocity selection," *J. Nuc. En. A*, vol. 11, no. 2, pp. 69–80, 1960. 50

[326] M. Blume, "Magnetic scattering of x rays (invited)," *J. Appl. Phys.*, vol. 57, no. 8, pp. 3615–3618, 1985. 52, 54, 55

[327] M. Altarelli, *Resonant X-ray Scattering: A Theoretical Introduction*, pp. 201–242. Berlin, Heidelberg: Springer Berlin Heidelberg, 2006. 52, 53, 54, 55, 59

[328] P. M. Platzman and N. Tzoar, "Magnetic scattering of x rays from electrons in molecules and solids," *Phys. Rev. B*, vol. 2, pp. 3556–3559, 1970. 55

[329] F. D. Bergevin and M. Brunel, "Observation of magnetic superlattice peaks by x-ray diffraction on an antiferromagnetic NiO crystal," *Phys. Lett. A*, vol. 39, no. 2, pp. 141–142, 1972. 55

[330] K. Namikawa, M. Ando, T. Nakajima, and H. Kawata, "X-ray resonance magnetic scattering," *J. Phys. Soc. Jpn.*, vol. 54, no. 11, pp. 4099–4102, 1985. 55

[331] D. Gibbs, D. R. Harshman, E. D. Isaacs, D. B. McWhan, D. Mills, and C. Vettier, "Polarization and resonance properties of magnetic x-ray scattering in holmium," *Phys. Rev. Lett.*, vol. 61, pp. 1241–1244, 1988. 55

[332] J. P. Hannon, G. T. Trammell, M. Blume, and D. Gibbs, "X-ray resonance exchange scattering," *Phys. Rev. Lett.*, vol. 61, pp. 1245–1248, 1988. 55, 56, 217

[333] M. Blume and D. Gibbs, "Polarization dependence of magnetic x-ray scattering," *Phys. Rev. B*, vol. 37, pp. 1779–1789, 1988. 55

[334] G. T. Trammell, "Elastic scattering at resonance from bound nuclei," *Phys. Rev.*, vol. 126, pp. 1045–1054, 1962. 56

[335] J. P. Hannon and G. T. Trammell, "Mössbauer Diffraction. II. dynamical theory of Mössbauer optics," *Phys. Rev.*, vol. 186, pp. 306–325, 1969. 56

[336] M. D. Hamrick, *Magnetic and Chemical Effects in X-ray Resonant Exchange Scattering in Rare Earths and Transition Metal Compounds*. PhD thesis, Rice University, 1994. 56, 57, 217, 218

[337] C. Detlefs, M. Sanchez del Rio, and C. Mazzoli, "X-ray polarization: General formalism and polarization analysis," *Eur. Phys. J. Special Topics*, vol. 208, no. 1, pp. 359–371, 2012. 58, 227, 229

[338] J. P. Hill and D. F. McMorrow, "Resonant exchange scattering: Polarization dependence and correlation function," *Acta Crystallogr. Sec. A*, vol. 52, no. 2, pp. 236–244, 1996. 58, 127, 132, 217

[339] L. Braicovich, N. B. Brookes, G. Ghiringhelli, M. Minola, G. Monaco, M. M. Sala, and L. Simonelli, "Resonant inelastic x-ray scattering at the ESRF: Hard and soft x-rays," *Synchrotron Radiation News*, vol. 25, no. 4, pp. 9–15, 2012. 59

[340] A. Amorese, *Complete characterization of the crystal electric field in Ce Kondo lattice with resonant inelastic soft x-ray scattering*. PhD thesis, European Synchrotron Radiation Facility (ESRF), 2017. 60, 81, 82, 93

[341] C. S. Wu, E. Ambler, R. W. Hayward, D. D. Hoppes, and R. P. Hudson, "Experimental test of parity conservation in beta decay," *Phys. Rev.*, vol. 105, pp. 1413–1415, 1957. 61

[342] S. J. Blundell, "Spin-polarized muons in condensed matter physics," *Contemp. Phys.*, vol. 40, no. 3, pp. 175–192, 1999. 61, 63, 64

[343] C. D. Anderson and S. H. Neddermeyer, "Cloud chamber observations of cosmic rays at 4300 meters elevation and near sea-level," *Phys. Rev.*, vol. 50, pp. 263–271, 1936. 61

[344] J. Möller, *Muon-spin relaxation and its application in the study of molecular quantum magnets*. PhD thesis, University of Oxford, 2013. 61, 64

[345] J. Chappert and R. Grynszpan, *Principles of the μSR technique*. North-Holland, 1984. 61

[346] R. L. Garwin, L. M. Lederman, and M. Weinrich, "Observations of the failure of conservation of parity and charge conjugation in meson decays: the magnetic moment of the free muon," *Phys. Rev.*, vol. 105, pp. 1415–1417, 1957. 62

[347] S. F. J. Cox, "Implanted muon studies in condensed matter science," *J. Phys. C: Solid State Physics*, vol. 20, no. 22, p. 3187, 1987. 64

[348] P. Dalmas de Réotier and A. Yaouanc, "Muon spin rotation and relaxation in magnetic materials," *J. Phys. Condens. Matter*, vol. 9, no. 43, p. 9113, 1997. 64

[349] E. Roduner, "Muon spin resonance — a variant of magnetic resonance," *Appl. Mag. Res.*, vol. 13, no. 1, pp. 1–14, 1997. 64

[350] A. Yaouanc and P. Dalmas De Réotier, *Muon Spin Rotation, Relaxation and Resonance - Applications to Condensed Matter*. Oxford University Press, 2011. 64

[351] A. Steele, *Quantum magnetism probed with muon-spin relaxation*. PhD thesis, University of Oxford, 2011. 64

[352] F. R. Foronda, F. Lang, J. S. Möller, T. Lancaster, A. T. Boothroyd, F. L. Pratt, S. R. Giblin, D. Prabhakaran, and S. J. Blundell, "Anisotropic local modification of crystal field levels in Pr-based pyrochlores: A muon-induced effect modeled using density functional theory," *Phys. Rev. Lett.*, vol. 114, p. 017602, 2015. 64

[353] S. Medvedev, T. M. McQueen, I. A. Troyan, T. Palasyuk, M. I. Eremets, R. J. Cava, S. Naghavi, F. Casper, V. Ksenofontov, G. Wortmann, and C. Felser, "Electronic and magnetic phase diagram of β-$Fe_{1.01}Se$ with superconductivity at 36.7 K under pressure," *Nat. Mater.*, vol. 8, no. 8, pp. 630–633, 2009. 67, 68

[354] J. Guo, S. Jin, G. Wang, S. Wang, K. Zhu, T. Zhou, M. He, and X. Chen, "Superconductivity in the iron selenide $K_xFe_2Se_2$ $(0 \leq x \leq 1.0)$," *Phys. Rev. B*, vol. 82, p. 180520(R), 2010. 67

[355] T. P. Ying, X. L. Chen, G. Wang, S. F. Jin, T. T. Zhou, X. F. Lai, H. Zhang, and W. Y. Wang, "Observation of superconductivity at 30 K–46 K in $A_xFe_2Se_2$ (A = Li, Na, Ba, Sr, Ca, Yb, and Eu)," *Sci. Rep.*, vol. 2, 2012. 67

[356] M. Burrard-Lucas, D. G. Free, S. J. Sedlmaier, J. D. Wright, S. J. Cassidy, Y. Hara, A. J. Corkett, T. Lancaster, P. J. Baker, S. J. Blundell, and S. J. Clarke, "Enhancement of the superconducting transition temperature of FeSe by intercalation of a molecular spacer layer," *Nat. Mater.*, vol. 12, no. 1, pp. 15–19, 2013. 67

[357] A. Krzton-Maziopa, E. V. Pomjakushina, V. Y. Pomjakushin, F. von Rohr, A. Schilling, and K. Conder, "Synthesis of a new alkali metal–organic solvent intercalated iron selenide superconductor with $T_c \approx 45$ K," *J. Phys. Condens. Matter*, vol. 24, no. 38, p. 382202, 2012. 67

[358] Q.-Y. Wang, Z. Li, W.-H. Zhang, Z.-C. Zhang, J.-S. Zhang, W. Li, H. Ding, Y.-B. Ou, P. Deng, K. Chang, J. Wen, C.-L. Song, K. He, J.-F. Jia, S.-H. Ji, Y.-Y. Wang, L.-L. Wang, X. Chen, X.-C. Ma, and Q.-K. Xue, "Interface-induced high-temperature superconductivity in single unit-cell FeSe films on $SrTiO_3$," *Chin. Phys. Lett.*, vol. 29, no. 3, pp. 37402–37402, 2012. 67

[359] J.-F. Ge, Z.-L. Liu, C. Liu, C.-L. Gao, D. Qian, Q.-K. Xue, Y. Liu, and J.-F. Jia, "Superconductivity above 100 K in single-layer FeSe films on doped $SrTiO_3$," *Nat. Mater.*, vol. 10, p. 4153, 2014. 67

[360] H. Sun, D. N. Woodruff, S. J. Cassidy, G. M. Allcroft, S. J. Sedlmaier, A. L. Thompson, P. A. Bingham, S. D. Forder, S. Cartenet, N. Mary, S. Ramos, F. R. Foronda, B. H. Williams, X. Li, S. J. Blundell, and S. J. Clarke, "Soft chemical control of superconductivity in lithium iron selenide hydroxides $Li_{1-x}Fe_x(OH)Fe_{1-y}Se$," *Inorg. Chem.*, vol. 54, no. 4, pp. 1958–1964, 2015. 67

[361] T. M. McQueen, Q. Huang, V. Ksenofontov, C. Felser, Q. Xu, H. Zandbergen, Y. S. Hor, J. Allred, A. J. Williams, D. Qu, J. Checkelsky, N. P. Ong, and R. J. Cava, "Extreme sensitivity of superconductivity to stoichiometry in $Fe_{1+\delta}Se$," *Phys. Rev. B*, vol. 79, p. 014522, 2009. 67, 71

[362] T. M. McQueen, A. J. Williams, P. W. Stephens, J. Tao, Y. Zhu, V. Ksenofontov, F. Casper, C. Felser, and R. J. Cava, "Tetragonal-to-orthorhombic structural phase transition at 90 K in the superconductor $Fe_{1.01}Se$," *Phys. Rev. Lett.*, vol. 103, p. 057002, 2009. 67, 71

[363] Y. Mizuguchi, T. Furubayashi, K. Deguchi, S. Tsuda, T. Yamaguchi, and Y. Takano, "Mössbauer studies on FeSe and FeTe," *Physica C*, vol. 470, pp. S338–S339, 2010. 67

[364] K. Nakayama, Y. Miyata, G. N. Phan, T. Sato, Y. Tanabe, T. Urata, K. Tanigaki, and T. Takahashi, "Reconstruction of band structure induced by electronic nematicity in an FeSe superconductor," *Phys. Rev. Lett.*, vol. 113, p. 237001, 2014. 67, 69, 92

[365] T. Shimojima, Y. Suzuki, T. Sonobe, A. Nakamura, M. Sakano, J. Omachi, K. Yoshioka, M. Kuwata-Gonokami, K. Ono, H. Kumigashira, A. E. Böhmer, F. Hardy, T. Wolf, C. Meingast, H. v. Löhneysen, H. Ikeda, and K. Ishizaka, "Lifting of xz/yz orbital degeneracy at the structural transition in detwinned FeSe," *Phys. Rev. B*, vol. 90, p. 121111, 2014. 67, 69, 92

[366] A. E. Böhmer, F. Hardy, F. Eilers, D. Ernst, P. Adelmann, P. Schweiss, T. Wolf, and C. Meingast, "Lack of coupling between superconductivity and orthorhombic distortion in stoichiometric single-crystalline FeSe," *Phys. Rev. B*, vol. 87, p. 180505, 2013. 67

[367] H.-Y. Cao, S. Chen, H. Xiang, and X.-G. Gong, "Antiferromagnetic ground state with pair-checkerboard order in FeSe," *Phys. Rev. B*, vol. 91, p. 020504, 2015. 67, 69, 92

[368] F. Wang, S. A. Kivelson, and D.-H. Lee, "Nematicity and quantum paramagnetism in FeSe," *Nat. Phys.*, vol. 11, no. 11, pp. 959–963, 2015. 67, 69, 91, 92

[369] J. K. Glasbrenner, I. I. Mazin, H. O. Jeschke, P. J. Hirschfeld, R. M. Fernandes, and R. Valenti, "Effect of magnetic frustration on nematicity and superconductivity in

iron chalcogenides," *Nat. Phys.*, vol. 11, no. 11, pp. 953–958, 2015. 67, 69, 92

[370] R. Yu and Q. Si, "Antiferroquadrupolar and Ising-nematic orders of a frustrated bilinear-biquadratic Heisenberg model and implications for the magnetism of FeSe," *Phys. Rev. Lett.*, vol. 115, p. 116401, 2015. 67, 69, 92

[371] D. J. Scalapino, "A common thread: The pairing interaction for unconventional superconductors," *Rev. Mod. Phys.*, vol. 84, pp. 1383–1417, 2012. 67

[372] G. Friemel, W. P. Liu, E. A. Goremychkin, Y. Liu, J. T. Park, O. Sobolev, C. T. Lin, B. Keimer, and D. S. Inosov, "Conformity of spin fluctuations in alkali-metal iron selenide superconductors inferred from the observation of a magnetic resonant mode in $K_xFe_{2-y}Se_2$," *Europhys. Lett.*, vol. 99, p. 67004, 2012. 68

[373] J. T. Park, G. Friemel, Y. Li, J.-H. Kim, V. Tsurkan, J. Deisenhofer, H.-A. Krug von Nidda, A. Loidl, A. Ivanov, B. Keimer, and D. S. Inosov, "Magnetic resonant mode in the low-energy spin-excitation spectrum of superconducting $Rb_2Fe_4Se_5$ single crystals," *Phys. Rev. Lett.*, vol. 107, p. 177005, 2011. 68

[374] A. E. Taylor, S. J. Sedlmaier, S. J. Cassidy, E. A. Goremychkin, R. A. Ewings, T. G. Perring, S. J. Clarke, and A. T. Boothroyd, "Spin fluctuations away from $(\pi,0)$ in the superconducting phase of molecular-intercalated FeSe," *Phys. Rev. B*, vol. 87, p. 220508(R), 2013. 68

[375] S. Margadonna, Y. Takabayashi, M. T. McDonald, K. Kasperkiewicz, Y. Mizuguchi, Y. Takano, A. N. Fitch, E. Suard, and K. Prassides, "Crystal structure of the new $FeSe_{1-x}$ superconductor," *Chem. Commun.*, vol. 43, pp. 5607–5609, 2008. 68, 71

[376] F. Essenberger, P. Buczek, A. Ernst, L. Sandratskii, and E. Gross, "Paramagnons in FeSe close to a magnetic quantum phase transition: *Ab initio* study," *Phys. Rev. B*, vol. 86, p. 060412, 2012. 69

[377] C. Heil, H. Sormann, L. Boeri, M. Aichhorn, and W. von der Linden, "Accurate bare susceptibilities from full-potential *ab initio* calculations," *Phys. Rev. B*, vol. 90, p. 115143, 2014. 69

[378] T. Terashima, N. Kikugawa, A. Kiswandhi, E.-S. Choi, J. S. Brooks, S. Kasahara, T. Watashige, H. Ikeda, T. Shibauchi, Y. Matsuda, T. Wolf, A. E. Böhmer, F. Hardy, C. Meingast, H. v. Löhneysen, M.-T. Suzuki, R. Arita, and S. Uji, "Anomalous fermi surface in FeSe seen by Shubnikov–de Haas oscillation measurements," *Phys. Rev. B*, vol. 90, p. 144517, 2014. 69

[379] J. Maletz, V. B. Zabolotnyy, D. V. Evtushinsky, S. Thirupathaiah, A. U. B. Wolter, L. Harnagea, A. N. Yaresko, A. N. Vasiliev, D. A. Chareev, A. E. Böhmer, F. Hardy, T. Wolf, C. Meingast, E. D. L. Rienks, B. Büchner, and S. V. Borisenko, "Unusual

band renormalization in the simplest iron-based superconductor $FeSe_{1-x}$," *Phys. Rev. B*, vol. 89, p. 220506, 2014. 69

[380] A. Audouard, F. Duc, L. Drigo, P. Toulemonde, S. Karlsson, P. Strobel, and A. Sulpice, "Quantum oscillations and upper critical magnetic field of the iron-based superconductor FeSe," *Europhysics Letters*, vol. 109, no. 2, p. 27003, 2015. 69

[381] M. C. Rahn, R. A. Ewings, S. J. Sedlmaier, S. J. Clarke, and A. T. Boothroyd, "Strong $(\pi,0)$ spin fluctuations in $\beta-$FeSe observed by neutron spectroscopy," *Phys. Rev. B*, vol. 91, p. 180501, 2015. 69, 91

[382] J. Rodriguez-Carvajal, "Recent advances in magnetic structure determination by neutron powder diffraction," *Physica B*, vol. 192, no. 1, pp. 55–69, 1993. 69, 119, 120, 145, 154, 158

[383] R. Bewley, R. Eccleston, K. McEwen, S. Hayden, M. Dove, S. Bennington, J. Treadgold, and R. Coleman, "MERLIN, a new high count rate spectrometer at ISIS," *Physica B*, vol. 385-386, pp. 1029–1031, 2006. 71

[384] D. Phelan, J. N. Millican, E. L. Thomas, J. B. Leão, Y. Qiu, and R. Paul, "Neutron scattering measurements of the phonon density of states of $FeSe_{1-x}$ superconductors," *Phys. Rev. B*, vol. 79, p. 014519, 2009. 72

[385] A. E. Taylor, M. J. Pitcher, R. A. Ewings, T. G. Perring, S. J. Clarke, and A. T. Boothroyd, "Antiferromagnetic spin fluctuations in LiFeAs observed by neutron scattering," *Phys. Rev. B*, vol. 83, p. 220514(R), 2011. 72, 79

[386] G. S. Tucker, R. M. Fernandes, H.-F. Li, V. Thampy, N. Ni, D. L. Abernathy, S. L. Bud'ko, P. C. Canfield, D. Vaknin, J. Schmalian, and R. J. McQueeney, "Magnetic excitations in underdoped $Ba(Fe_{1-x}Co_x)_2As_2$ with $x = 0.047$," *Phys. Rev. B*, vol. 86, p. 024505, 2012. 75, 78

[387] C. Lester, J.-H. Chu, J. G. Analytis, T. G. Perring, I. R. Fisher, and S. M. Hayden, "Dispersive spin fluctuations in the nearly optimally doped superconductor $Ba(Fe_{1-x}Co_x)_2As_2$ $(x = 0.065)$," *Phys. Rev. B*, vol. 81, p. 064505, 2010. 76, 77

[388] D. Chareev, E. Osadchii, T. Kuzmicheva, J.-Y. Lin, S. Kuzmichev, O. Volkova, and A. Vasiliev, "Single crystal growth and characterization of tetragonal $FeSe_{1-x}$ superconductors," *Cryst. Eng. Comm.*, vol. 15, pp. 1989–1993, 2013. 80

[389] W. Schuster, H. Mikler, and K. L. Komarek, "Transition metal-chalcogen systems, VII.: The iron-selenium phase diagram," *Monatshefte für Chemie / Chemical Monthly*, vol. 110, no. 5, pp. 1153–1170, 1979. 80

[390] L. Braicovich, L. J. P. Ament, V. Bisogni, F. Forte, C. Aruta, G. Balestrino, N. B. Brookes, G. M. De Luca, P. G. Medaglia, F. M. Granozio, M. Radovic, M. Salluzzo, J. van den Brink, and G. Ghiringhelli, "Dispersion of magnetic excitations in the cuprate La_2CuO_4 and $CaCuO_2$ compounds measured using resonant x-ray scattering," *Phys. Rev. Lett.*, vol. 102, p. 167401, 2009. 81

[391] L. Braicovich, J. van den Brink, V. Bisogni, M. M. Sala, L. J. P. Ament, N. B. Brookes, G. M. De Luca, M. Salluzzo, T. Schmitt, V. N. Strocov, and G. Ghiringhelli, "Magnetic excitations and phase separation in the underdoped $La_{2-x}Sr_xCuO_4$ superconductor measured by resonant inelastic x-ray scattering," *Phys. Rev. Lett.*, vol. 104, p. 077002, 2010. 81

[392] M. Le Tacon, G. Ghiringhelli, J. Chaloupka, M. M. Sala, V. Hinkov, M. W. Haverkort, M. Minola, M. Bakr, K. J. Zhou, S. Blanco-Canosa, C. Monney, Y. T. Song, G. L. Sun, C. T. Lin, G. M. De Luca, M. Salluzzo, G. Khaliullin, T. Schmitt, L. Braicovich, and B. Keimer, "Intense paramagnon excitations in a large family of high-temperature superconductors," *Nat. Phys.*, vol. 7, no. 9, pp. 725–730, 2011. 81, 84

[393] M. Le Tacon, M. Minola, D. C. Peets, M. Moretti Sala, S. Blanco-Canosa, V. Hinkov, R. Liang, D. A. Bonn, W. N. Hardy, C. T. Lin, T. Schmitt, L. Braicovich, G. Ghiringhelli, and B. Keimer, "Dispersive spin excitations in highly overdoped cuprates revealed by resonant inelastic x-ray scattering," *Phys. Rev. B*, vol. 88, p. 020501, 2013. 81

[394] M. Dean, "Insights into the high temperature superconducting cuprates from resonant inelastic x-ray scattering," *J. Magn. Magn. Mater.*, vol. 376, pp. 3–13, 2015. Pseudogap, Superconductivity and Magnetism. 81, 89, 92, 93

[395] H. Gretarsson, T. Nomura, I. Jarrige, A. Lupascu, M. H. Upton, J. Kim, D. Casa, T. Gog, R. H. Yuan, Z. G. Chen, N.-L. Wang, and Y.-J. Kim, "Resonant inelastic x-ray scattering study of electronic excitations in insulating $K_{0.83}Fe_{1.53}Se_2$," *Phys. Rev. B*, vol. 91, p. 245118, 2015. 84, 89

[396] J. N. Hancock, R. Viennois, D. van der Marel, H. M. Rønnow, M. Guarise, P.-H. Lin, M. Grioni, M. Moretti Sala, G. Ghiringhelli, V. N. Strocov, J. Schlappa, and T. Schmitt, "Evidence for core-hole-mediated inelastic x-ray scattering from metallic $Fe_{1.087}Te$," *Phys. Rev. B*, vol. 82, p. 020513, 2010. 84, 89

[397] P. A. van Aken, B. Liebscher, and V. J. Styrsa, "Quantitative determination of iron oxidation states in minerals using Fe 2,3-edge electron energy loss near-edge structure spectroscopy," *Phys. Chem. Miner.*, vol. 25, pp. 323–327, 1998. 85, 86

[398] P. S. Miedema and F. M. F. de Groot, "The iron L edges: Fe 2p x-ray absorption and electron energy loss spectroscopy," *Journal of Electron Spectroscopy and Related Phenomena*, no. 187, pp. 32–48, 2013. 86

[399] I. Jarrige, K. Ishii, M. Yoshida, T. Fukuda, K. Ikeuchi, M. Ishikado, N. Hiraoka, K. Tsuei, H. Kito, A. Iyo, H. Eisaki, and S. Shamoto, "Resonant inelastic x-ray scattering in single-crystal superconducting," *Physica C*, vol. 470, Supplement 1, pp. S377–S378, 2010. Proceedings of the 9th International Conference on Materials and Mechanisms of Superconductivity. 89

[400] K.-J. Zhou, Y.-B. Huang, C. Monney, X. Dai, V. N. Strocov, N.-L. Wang, Z.-G. Chen, C. Zhang, P. Dai, L. Patthey, J. van den Brink, H. Ding, and T. Schmitt, "Persistent high-energy spin excitations in iron-pnictide superconductors," *Nat. Commun.*, vol. 4, p. 1470, 2013. 89, 90

[401] Q. Wang, Y. Shen, B. Pan, X. Zhang, K. Ikeuchi, K. Iida, A. D. Christianson, H. C. Walker, D. T. Adroja, M. Abdel-Hafiez, X. Chen, D. A. Chareev, A. N. Vasiliev, and J. Zhao, "Magnetic ground state of FeSe," *Nat. Commun.*, vol. 7, p. 12182, 2016. 91, 92, 115

[402] S. Shamoto, K. Matsuoka, R. Kajimoto, M. Ishikado, Y. Yamakawa, T. Watashige, S. Kasahara, M. Nakamura, H. Kontani, T. Shibauchi, and Y. Matsuda, "Spin nematic susceptibility studied by inelastic neutron scattering in FeSe," *arXiv:1511.04267*, 2015. 91

[403] A. E. Böhmer, T. Arai, F. Hardy, T. Hattori, T. Iye, T. Wolf, H. v. Löhneysen, K. Ishida, and C. Meingast, "Origin of the tetragonal-to-orthorhombic phase transition in FeSe: a combined thermodynamic and NMR study of nematicity," *Phys. Rev. Lett.*, vol. 114, p. 027001, 2014. 92

[404] Y. F. Guo, A. J. Princep, X. Zhang, P. Manuel, D. Khalyavin, I. I. Mazin, Y. G. Shi, and A. T. Boothroyd, "Coupling of magnetic order to planar Bi electrons in the anisotropic Dirac metals AMnBi$_2$ (A = Sr, Ca)," *Phys. Rev. B*, vol. 90, p. 075120, 2014. 95, 99, 100, 101, 104, 109, 110

[405] A. Zhang, C. Liu, C. Yi, G. Zhao, T.-l. Xia, J. Ji, Y. Shi, R. Yu, X. Wang, C. Chen, and Q. Zhang, "Interplay of Dirac electrons and magnetism in CaMnBi$_2$ and SrMnBi$_2$," *Nat. Commun.*, vol. 7, p. 13833, 2016. 95, 112, 113

[406] S. Borisenko, D. Evtushinsky, Q. Gibson, A. Yaresko, T. Kim, M. N. Ali, B. Buechner, M. Hoesch, and R. J. Cava, "Time-reversal summetry breaking type-II Weyl state in YbMnBi$_2$," *arXiv:1507.04847*, 2016. 95, 113

[407] Y. L. Chen, J. G. Analytis, J.-H. Chu, Z. K. Liu, S.-K. Mo, X. L. Qi, H. J. Zhang, D. H. Lu, X. Dai, Z. Fang, S. C. Zhang, I. R. Fisher, Z. Hussain, and Z.-X. Shen, "Experimental realization of a three-dimensional topological insulator, Bi_2Te_3," *Science*, vol. 325, no. 5937, pp. 178–181, 2009. 97

[408] S.-Y. Xu, I. Belopolski, N. Alidoust, M. Neupane, G. Bian, C. Zhang, R. Sankar, G. Chang, Z. Yuan, C.-C. Lee, S.-M. Huang, H. Zheng, J. Ma, D. S. Sanchez, B. Wang, A. Bansil, F. Chou, P. P. Shibayev, H. Lin, S. Jia, and M. Z. Hasan, "Discovery of a Weyl fermion semimetal and topological Fermi arcs," *Science*, vol. 349, no. 6248, pp. 613–617, 2015. 97

[409] O. Vafek and A. Vishwanath, "Dirac fermions in solids: From high-t_c cuprates and graphene to topological insulators and Weyl semimetals," *Annu. Rev. Cond. Mat. Phys.*, vol. 5, no. 1, pp. 83–112, 2014. 97, 99

[410] J. K. Wang, L. L. Zhao, Q. Yin, G. Kotliar, M. S. Kim, M. C. Aronson, and E. Morosan, "Layered transition-metal pnictide $SrMnBi_2$ with metallic blocking layer," *Phys. Rev. B*, vol. 84, p. 064428, 2011. 97, 98, 100, 104

[411] G. Lee, M. A. Farhan, J. S. Kim, and J. H. Shim, "Anisotropic Dirac electronic structures of AMnBi$_2$ (A = Sr,Ca)," *Phys. Rev. B*, vol. 87, p. 245104, 2013. 98, 99

[412] J. H. Shim, K. Haule, and G. Kotliar, "Density-functional calculations of the electronic structures and magnetism of the pnictide superconductors $BaFeAs_2$ and $BaFeSb_2$," *Phys. Rev. B*, vol. 79, p. 060501, 2009. 97

[413] G. Cordier and H. Schäfer, "Darstellung und Kristallstruktur von $BaMnSb_2$, $SrMnBi_2$ und $BaMnBi_2$.," *Z. Naturforsch.*, vol. 32, no. B, p. 383, 1977. 97, 101, 109

[414] E. Brechtel, G. Cordier, and H. Schäfer, "On the preparation and crystal structure of $CaMnBi_2$," *Z. Naturforsch.*, vol. 35, p. 1, 1980. 97, 101, 109

[415] J. Park, G. Lee, F. Wolff-Fabris, Y. Y. Koh, M. J. Eom, Y. K. Kim, M. A. Farhan, Y. J. Jo, C. Kim, J. H. Shim, and J. S. Kim, "Anisotropic Dirac fermions in a Bi square net of $SrMnBi_2$," *Phys. Rev. Lett.*, vol. 107, p. 126402, 2011. 98, 104

[416] Y. Feng, Z. Wang, C. Chen, Y. Shi, Z. Xie, H. Yi, A. Liang, S. He, J. He, Y. Peng, X. Liu, Y. Liu, L. Zhao, G. Liu, X. Dong, J. Zhang, C. Chen, Z. Xu, X. Dai, Z. Fang, and X. J. Zhou, "Strong anisotropy of Dirac cones in $SrMnBi_2$ and $CaMnBi_2$ revealed by angle-resolved photoemission spectroscopy," *Sci. Rep.*, vol. 4, pp. 5385–, 2014. 98, 99

[417] C.-H. Park, L. Yang, Y.-W. Son, M. L. Cohen, and S. G. Louie, "Anisotropic behaviours of massless Dirac fermions in graphene under periodic potentials," *Nat. Phys.*, vol. 4, no. 3, pp. 213–217, 2008. 98

[418] K. Wang, D. Graf, L. Wang, H. Lei, S. W. Tozer, and C. Petrovic, "Two-dimensional Dirac fermions and quantum magnetoresistance in $CaMnBi_2$," *Phys. Rev. B*, vol. 85, p. 041101, 2012. 100, 104

[419] J. B. He, D. M. Wang, and G. F. Chen, "Giant magnetoresistance in layered manganese pnictide $CaMnBi_2$," *Appl. Phys. Lett.*, vol. 100, no. 11, p. 112405, 2012. 100, 104

[420] A. Hiess, M. Jiménez-Ruiz, P. Courtois, R. Currat, J. Kulda, and F. Bermejo, "ILL's renewed thermal three-axis spectrometer IN8: A review of its first three years on duty," *Physica B*, vol. 385-386, no. 2, pp. 1077–1079, 2006. 102

[421] M. Kempa, B. Janousova, J. Saroun, P. Flores, M. Boehm, F. Demmel, and J. Kulda, "The FlatCone multianalyzer setup for ILL's three-axis spectrometers," *Physica B*, vol. 385–386, no. 2, pp. 1080–1082, 2006. 102

[422] M. Tegel, M. Rotter, V. Weiss, F. M. Schappacher, R. Poettgen, and D. Johrendt, "Structural and magnetic phase transitions in the ternary iron arsenides $SrFe_2As_2$ and $EuFe_2As_2$," *J. Phys.: Cond. Mat.*, vol. 20, no. 45, p. 452201, 2008. 104

[423] S. D. Wilson, C. R. Rotundu, Z. Yamani, P. N. Valdivia, B. Freelon, E. Bourret-Courchesne, and R. J. Birgeneau, "Universal magnetic and structural behaviors in the iron arsenides," *Phys. Rev. B*, vol. 81, p. 014501, 2010. 104

[424] J. Saroun and J. Kulda, "RESTRAX - a program for TAS resolution calculation and scan profile simulation," *Physica B*, vol. 234, pp. 1102–1104, 1997. Proceedings of the First European Conference on Neutron Scattering. 109

[425] J. Saroun and J. Kulda, "Monte Carlo ray-tracing code for RESTRAX," *Neutron News*, vol. 13, no. 4, pp. 15–19, 2002. 109

[426] S. Calder, B. Saparov, H. B. Cao, J. L. Niedziela, M. D. Lumsden, A. S. Sefat, and A. D. Christianson, "Magnetic structure and spin excitations in $BaMn_2Bi_2$," *Phys. Rev. B*, vol. 89, p. 064417, 2014. 109, 110

[427] D. C. Johnston, R. J. McQueeney, B. Lake, A. Honecker, M. E. Zhitomirsky, R. Nath, Y. Furukawa, V. P. Antropov, and Y. Singh, "Magnetic exchange interactions in $BaMn_2As_2$: A case study of the J_1-J_2-J_c Heisenberg model," *Phys. Rev. B*, vol. 84, p. 094445, 2011. 109, 110, 111

[428] *private communication, S. Calder, Quantum Condensed Matter Division, Oak Ridge National Laboratory, Oak Ridge, Tennessee 37831, USA*. 110

[429] M. Mambrini, A. Läuchli, D. Poilblanc, and F. Mila, "Plaquette valence-bond crystal in the frustrated Heisenberg quantum antiferromagnet on the square lattice," *Phys. Rev. B*, vol. 74, p. 144422, 2006. 111

[430] J. Richter and J. Schulenburg, "The spin-1/2 J_1–J_2 Heisenberg antiferromagnet on the square lattice: Exact diagonalization for N=40 spins," *Eur. Phys. J. B*, vol. 73, no. 1, pp. 117–124, 2010. 111

[431] H.-Y. Wang, "Phase transition of square-lattice antiferromagnets at finite temperature," *Phys. Rev. B*, vol. 86, p. 144411, 2012. 111

[432] A. F. May, M. A. McGuire, and B. C. Sales, "Effect of Eu magnetism on the electronic properties of the candidate Dirac material $EuMnBi_2$," *Phys. Rev. B*, vol. 90, p. 075109, 2014. 113

[433] H. Masuda, H. Sakai, M. Tokunaga, Y. Yamasaki, A. Miyake, J. Shiogai, S. Nakamura, S. Awaji, A. Tsukazaki, H. Nakao, Y. Murakami, T.-H. Arima, Y. Tokura, and S. Ishiwata, "Quantum Hall effect in a bulk antiferromagnet $EuMnBi_2$ with magnetically confined two-dimensional Dirac fermions," *Sci. Adv.*, vol. 2, no. 1, p. e1501117, 2016. 113

[434] A. Artmann, A. Mewis, M. Roepke, and G. Michels, "AM_2X_2-Verbindungen mit $CaAl_2Si_2$-Struktur. XI. Struktur und Eigenschaften der Verbindungen ACd_2X_2 (A: Eu, Yb; X: P, As, Sb)," *Zeitschrift für anorganische und allgemeine Chemie*, vol. 622, no. 4, pp. 679–682, 1996. 117, 119, 121

[435] I. Schellenberg, U. Pfannenschmidt, M. Eul, C. Schwickert, and R. Pöttgen, "A ^{121}Sb and ^{151}Eu Mössbauer spectroscopic investigation of $EuCd_2X_2$ (x = P, As, Sb) and $YbCd_2Sb_2$," *Z. Anorg. Allg. Chem.s*, vol. 637, no. 12, pp. 1863–1870, 2011. 117, 118, 119, 121

[436] H. Li, H. He, H.-Z. Lu, H. Zhang, H. Liu, R. Ma, Z. Fan, S.-Q. Shen, and J. Wang, "Negative magnetoresistance in Dirac semimetal Cd_3As_2," *Nat. Commun.*, vol. 7, p. 10301, Li2016. 117

[437] H. P. Wang, D. S. Wu, Y. G. Shi, and N. L. Wang, "Anisotropic transport and optical spectroscopy study on antiferromagnetic triangular lattice $EuCd_2As_2$: An interplay between magnetism and charge transport properties," *Phys. Rev. B*, vol. 94, p. 045112, 2016. 117, 118, 138, 139

[438] *private communication, Y. F. Guo, School of Physical Science and Technology, ShanghaiTech University, Shanghai 201210, China and Jian Rui Soh, Clarendon Laboratory, University of Oxford, Parks Road, Oxford OX1 3PU, UK*. 117

[439] J. Strempfer, S. Francoual, D. Reuther, D. K. Shukla, A. Skaugen, H. Schulte-Schrepping, T. Kracht, and H. Franz, "Resonant scattering and diffraction beamline P09 at PETRA III," *J. Synchr. Rad.*, vol. 20, no. 4, pp. 541–549, 2013. 124, 125, 126, 128

[440] S. Francoual, J. Strempfer, D. Reuther, D. K. Shukla, and A. Skaugen, "Double phase-retarder set-up at beamline P09 at PETRA III," *J. Phys. Conference Series*, vol. 425, no. 13, p. 132010, 2013. 124, 128, 129

[441] W. R. Busing and H. A. Levy, "Angle calculations for 3- and 4-circle X-ray and neutron diffractometers," *Acta Crystallogr.*, vol. 22, no. 4, pp. 457–464, 1967. 128

[442] A. C. Payne, A. E. Sprauve, M. M. Olmstead, S. M. Kauzlarich, J. Y. Chan, B. Reisner, and J. Lynn, "Synthesis, magnetic and electronic properties of single crystals of $EuMn_2P_2$," *J. Solid State Chem.*, vol. 163, no. 2, pp. 498–505, 2002. 129

[443] P. Schobinger-Papamantellos and F. Hulliger, "The magnetic structure of $EuAl_2Si_2$," *J. Less Comm. Met.*, vol. 146, pp. 327–335, 1989. 129

[444] J. C. Le Guillou and J. Zinn-Justin, "Critical exponents for the n-vector model in three dimensions from field theory," *Phys. Rev. Lett.*, vol. 39, pp. 95–98, LeGuillou1977. 130

[445] C. Mazzoli, S. B. Wilkins, S. Di Matteo, B. Detlefs, C. Detlefs, V. Scagnoli, L. Paolasini, and P. Ghigna, "Disentangling multipole resonances through a full x-ray polarization analysis," *Phys. Rev. B*, vol. 76, p. 195118, 2007. 132, 227

[446] N. Nagaosa, J. Sinova, S. Onoda, A. H. MacDonald, and N. P. Ong, "Anomalous Hall effect," *Rev. Mod. Phys.*, vol. 82, pp. 1539–1592, 2010. 138

[447] P. Zheng, Y. G. Shi, Q. S. Wu, G. Xu, T. Dong, Z. G. Chen, R. H. Yuan, B. Cheng, K. Yamaura, J. L. Luo, and N. L. Wang, "Continuous magnetic phase transition in half-frustrated $Ca_2Os_2O_7$," *Phys. Rev. B*, vol. 86, p. 195108, 2012. 141, 143, 144, 146, 149, 151, 164, 165, 166

[448] O. Knop, G. Demazeau, and P. Hagenmuller, "Pyrochlores. XI. high-pressure studies of the antimonates $A_2Sb_2O_7$ (A=Ca, Sr, Cd) and preparation of the weberite $Sr_2Bi_2O_7$," *Can. J. Chem.*, vol. 58, no. 21, pp. 2221–2224, 1980. 143

[449] L. Cai and J. C. Nino, "Complex ceramic structures. I. Weberites," *Acta Crystallogr. Sec. B*, vol. 65, no. 3, pp. 269–290, 2009. 143, 164, 166

[450] O. Knop and G. Demazeau, "The 1–6 weberite $Na_2Te_2O_7$ and some observations on compounds with the weberite structure," *J. Solid State Chem.*, vol. 39, no. 1, pp. 94–99, 1981. 143

[451] O. Knop, T. Cameron, and K. Jochem, "What is the true space group of weberite?," *J. Solid State Chem.*, vol. 43, no. 2, pp. 213–221, 1982. 143

[452] J. Reading, C. S. Knee, and M. T. Weller, "Syntheses, structures and properties of some osmates(iv,v) adopting the pyrochlore and weberite structures," *J. Mater. Chem.*, vol. 12, pp. 2376–2382, 2002. 144, 146

[453] R. F. Sarkozy and B. Chamberland, "The preparation of several new ternary oxides of osmium," *Mat. Res. Bull.*, vol. 8, no. 12, pp. 1351–1359, 1973. 145, 146

[454] A. W. Sleight, "New ternary oxides of Re, Os, Ir and Pt with cubic crystal structures," *Mat. Res. Bull.*, vol. 9, no. 9, pp. 1177–1184, 1974. 145, 146, 147, 149

[455] N. Tartoni, S. P. Thompson, C. C. Tang, B. L. Willis, G. E. Derbyshire, A. G. Wright, S. C. Jaye, J. M. Homer, J. D. Pizzey, and A. M. T. Bell, "High-performance X-ray detectors for the new powder diffraction beamline I11 at Diamond," *J. Synchr. Rad.*, vol. 15, no. 1, pp. 43–49, 2008. 147

[456] S. P. Thompson, J. E. Parker, J. Potter, T. P. Hill, A. Birt, T. M. Cobb, F. Yuan, and C. C. Tang, "Beamline I11 at Diamond: A new instrument for high resolution powder diffraction," *Rev. Sci. Inst.*, vol. 80, no. 7, p. 075107, 2009. 147

[457] Beamline 11-BM, Advanced Photon Source, Argonne National Laboratory. http://11bm.xray.aps.anl.gov/ absorption.html — retrieved 16.6.2017, 2013. 147

[458] A. Le Bail, "Whole powder pattern decomposition methods and applications: A retrospection," *Powder Diffraction*, vol. 20, no. 4, pp. 316–326, 2005. 147

[459] A. Hewat, "D2B, a new high resolution neutron powder diffractormeter at ILL Grenboble," in *High Resolution Powder Diffraction*, vol. 9 of *Materials Science Forum*, pp. 69–80, Trans Tech Publications, 1986. 153

[460] E. Suard and A. Hewat, "The Super-D2B project at the ILL," *Neutron News*, vol. 12, no. 4, pp. 30–33, 2001. 153

[461] L. C. Chapon, P. Manuel, P. G. Radaelli, C. Benson, L. Perrott, S. Ansell, N. J. Rhodes, D. Raspino, D. Duxbury, E. Spill, and J. Norris, "Wish: The new powder and single crystal magnetic diffractometer on the second target station," *Neutron News*, vol. 22, no. 2, pp. 22–25, 2011. 153, 154

[462] P. G. Radaelli and L. C. Chapon, "WISH - a high-resolution magnetic diffractometer for TS-II." Rutherford Appleton Laboratory Scientific Case. — retrieved 12.6.2017. 154

[463] Institut Laue-Langevin, "D2B - high-resolution two-axis diffractometer." https://www.ill.eu/instruments-support/instruments-groups/ instruments/d2b/description/ instrument-layout/ — retrieved 12.6.2017. 155

[464] P. J. Baker, A. Hillier, J. Lord, and S. Giblin, "MuSR Manual (2011)." http://www.isis.stfc.ac.uk/instruments/musr/documents/musr_manual6543.pdf — retrieved 12.6.2017. 155

[465] Leigh, ""WISH detector array at the ISIS neutron source is completed"." Tweet, 2014. 12:01 PM - 31 Oct 2014. 158

[466] J. S. Gardner, S. R. Dunsiger, B. D. Gaulin, M. J. P. Gingras, J. E. Greedan, R. F. Kiefl, M. D. Lumsden, W. A. MacFarlane, N. P. Raju, J. E. Sonier, I. Swainson, and Z. Tun, "Cooperative paramagnetism in the geometrically frustrated pyrochlore antiferromagnet $Tb_2Ti_2O_7$," *Phys. Rev. Lett.*, vol. 82, pp. 1012–1015, 1999. 160

[467] E. F. Bertaut, G. T. Rado, and H. Suhl, "Magnetism III," *New York: Academic*, vol. 149, 1963. 160

[468] R. Haegele, W. Verscharen, D. Babel, J.-M. Dance, and A. Tressaud, "Die Verfeinerung der Weberitstruktur der Verbindung Na_2NiFeF_7," *J. Solid State Chem.*, vol. 24, no. 1, pp. 77–84, 1978. 163

[469] Y. Laligant, Y. Calage, E. Torres-Tapia, J. Greneche, F. Varret, and G. Ferey, "Crystal structure of the inverse weberite $ZnFeF_5(H_2O)_2$, magnetic and Mössbauer study of the antiferromagnet $ZnFeF_5(H_2O)_2$ and ferrimagnet $MnFeF_5(H_2O)_2$," *J. Magn. Magn. Mater.*, vol. 61, no. 3, pp. 283–290, 1986. 163

[470] J. Greneche, J. Linares, F. Varret, Y. Laligant, and G. Ferey, "Mössbauer spectroscopy of the magnetic behaviour of the frustrated series $AFeF_5(H_2O)_2$: A = Mn, Fe, Co, Ni," *J. Magn. Magn. Mater.*, vol. 73, no. 1, pp. 115–122, 1988. 163

[471] N. Ruchaud, J. Grannec, P. Gravereau, P. Nuñez, A. Tressaud, W. Massa, G. Frenzen, and D. Babel, "Copper weberites: Crystal structure and magnetic investigation of Na_2CuGaF_7 and Na_2CuInF_7," *Z. Anorg. Allg. Chem.*, vol. 610, no. 4, pp. 67–74, 1992. 163

[472] Y. Laligant, M. Leblanc, J. Pannetier, and G. Ferey, "Ordered magnetic frustration. IV. the two magnetic structures of the inverse weberite $Fe_2F_5(H_2O)_2$: an example of the thermal evolution of the frustration character," *J. Phys. C: Solid State Physics*, vol. 19, no. 8, p. 1081, 1986. 164

[473] Y. Laligant, G. Ferey, G. Heger, and J. Pannetier, "Ordered magnetic frustration. XI. refinement of the crystal and frustrated magnetic structures of the direct weberite

Na_2NiCrF_7 by neutron powder diffraction," *Z. Anorg. Allg. Chem.*, vol. 553, no. 10, pp. 163–171, 1987. 164

[474] Y. Laligant, Y. Calage, G. Heger, J. Pannetier, and G. Ferey, "Ordered magnetic frustration," *J. Solid State Chem.*, vol. 78, no. 1, pp. 66–77, 1989. 164

[475] M. Leblanc, G. Ferey, Y. Calage, and R. D. Pape, "Idle spin behavior of the shifted hexagonal tungsten bronze type compounds $Fe(II)Fe(III)_2F_8(H_2O)_2$ and $MnFe_2F_8(H_2O)_2$," *J. Solid State Chem.*, vol. 53, no. 3, pp. 360–368, 1984. 164

[476] P. Khalifah, R. W. Erwin, J. W. Lynn, Q. Huang, B. Batlogg, and R. J. Cava, "Magnetic and electronic characterization of quasi-one-dimensional La_3RuO_7," *Phys. Rev. B*, vol. 60, pp. 9573–9578, 1999. 164

[477] M. Wakeshima, H. Nishimine, and Y. Hinatsu, "Crystal structures and magnetic properties of rare earth tantalates RE_3TaO_7 (RE=rare earths)," *J. Phys. Condens. Matter*, vol. 16, no. 23, p. 4103, 2004. 164

[478] M. Wakeshima and Y. Hinatsu, "Magnetic properties of lanthanide rhenium oxides Ln_3ReO_7 (Ln=Sm, Eu, Ho)," *J. Solid State Chem.*, vol. 179, no. 11, pp. 3575–3581, 2006. 164

[479] Z. Hiroi, J. Yamaura, T. Hirose, I. Nagashima, and Y. Okamoto, "Lifshitz metal–insulator transition induced by the all-in/all-out magnetic order in the pyrochlore oxide $Cd_2Os_2O_7$," *APL Materials*, vol. 3, no. 4, p. 041501, 2015. 165

[480] S. Calder, J. G. Vale, N. A. Bogdanov, X. Liu, C. Donnerer, M. H. Upton, D. Casa, A. H. Said, M. D. Lumsden, Z. Zhao, J. Q. Yan, D. Mandrus, S. Nishimoto, J. van den Brink, J. P. Hill, D. F. McMorrow, and A. D. Christianson, "Spin-orbit-driven magnetic structure and excitation in the $5d$ pyrochlore $Cd_2Os_2O_7$," *Nat. Commun.*, vol. 7, p. 11651, 2016. 165

[481] S. Tardif, S. Takeshita, H. Ohsumi, J.-i. Yamaura, D. Okuyama, Z. Hiroi, M. Takata, and T.-h. Arima, "All-in–all-out magnetic domains: X-ray diffraction imaging and magnetic field control," *Phys. Rev. Lett.*, vol. 114, p. 147205, 2015. 165

[482] M. C. Rahn, A. J. Princep, A. Piovano, J. Kulda, Y. F. Guo, Y. G. Shi, and A. T. Boothroyd, "Spin dynamics in the antiferromagnetic phases of the Dirac metals $A\mathrm{MnBi}_2$ ($A = \mathrm{Sr}, \mathrm{Ca}$)," *Phys. Rev. B*, vol. 95, p. 134405, 2017. 170

[483] R. D. Johnson, S. R. Bland, C. Mazzoli, T. A. W. Beale, C.-H. Du, C. Detlefs, S. B. Wilkins, and P. D. Hatton, "Determination of magnetic order of the rare-earth ions in multiferroic $TbMn_2O_5$," *Phys. Rev. B*, vol. 78, p. 104407, 2008. 227

[484] P. Hatton, R. Johnson, S. Bland, C. Mazzoli, T. Beale, C.-H. Du, and S. Wilkins, "Magnetic structure determination using polarised resonant x-ray scattering," *J. Magn. Magn. Mater.*, vol. 321, no. 7, pp. 810–813, 2009. 227

Appendix A

XRES multipolar coefficients

As stated in Eq. 2.63 (Chapter 2), the resonant elastic x-ray scattering amplitude for the multipolar process described by the indices (L,M) is given by

$$\mathcal{F}^{\text{res}}_{LM} = \frac{4\pi}{k_i} \sum_{M=-L}^{L} P^*_{LM} F_{LM}(\omega) \tag{A.1}$$

For a fixed initial state $|i\rangle$, the multipolar coefficients for transitions via the intermediate state $|n\rangle$ are given by (in the notation of Hannon [332] an Hill [338]):

$$F_{LM}(\omega) = \sum_n P_i P_i(n) \frac{1}{(x_n - i)} \frac{\Gamma_x}{\Gamma(n)} \tag{A.2}$$

here P_i is the probability of the initial state $|i\rangle$ and $P_i(n)$ is the probability that $|n\rangle$ is vacant if the system is in the state $|i\rangle$. x is the *resonance parameter* that measures how far off-resonant the incident photon energy $\hbar\omega_i$ is from the system's resonance at $E_n - E_i$ (in units of the total line width Γ_n of the state $|n\rangle$):

$$x_n(\omega_i) = \frac{E_n - E_i - \hbar\omega_i}{\Gamma_n/2} \tag{A.3}$$

The key observation is that F_{LM} is proportional to the ratio Γ_x/Γ_n. Γ_n is the *total line width* (*i.e.*, for decays including all available multipolar processes) of an excited state $|n\rangle$. It depends only weakly on a particular $|n\rangle$, but mainly on the core-hole.

The corresponding values $\Gamma_n|_{\text{any } n} \approx \Gamma_{\text{res}}$ have been tabulated for most relevant atomic absorption edges [336]. Γ_x is the *partial line width* which will depend on the particular choice of multipolar (L,M) decay path:

$$\Gamma_x = \langle i|J^\dagger_{LM}|n\rangle\langle n|J_{LM}|i\rangle / \lambda_{\text{res}} \quad \text{, with } \lambda_{\text{res}} = \frac{2\pi\hbar c}{E_n - E_i} \tag{A.4}$$

Here, J_{LM} are the Fourier components of the electric multipole operator [336]:

$$J_{LM} = -\frac{4\pi i^L k^L}{(2L+1)!!}\sqrt{\frac{L+1}{L}}\sum_j e\, r_j^L Y_{LM}(\hat{\boldsymbol{r}}_j) + \frac{\hbar\omega}{mc^2}\frac{1}{L+1}\sum_j e\, r_j^L Y_{LM}(\hat{\boldsymbol{r}}_j)\,\boldsymbol{l}_j\cdot\boldsymbol{s}_j \tag{A.5}$$

Where $(!!)$ is the double factorial $(5!! = 5\times 3\times 1)$.

To determine the relative strength of different resonant processes to the scattering amplitude 2.63, it is necessary to evaluate the multipolar coefficients F_{LM}. This has been discussed in detail by Hamrick [336]. In his notation,

$$F_{LM} = \frac{r_0}{4\pi\hbar c}\sum_n \frac{E_n - E_i}{x_n - i} A^n_{LM} \tag{A.6}$$

with *amplitude coefficients*

$$\begin{aligned} A^n_{LM} &= \frac{2\lambda_{\text{res}}}{r_0}\frac{\Gamma_x}{\Gamma_n} \\ &\approx 8\pi\frac{mc^2}{\Gamma_{\text{res}}}\frac{(L+1)(2L+1)}{L[(2L+1)!!]^2}\frac{2l_i+1}{2l_n+1}(ka_0)^{2L}\,|\langle R_n|(\frac{r}{a_0})^L|R_i\rangle|^2\, C^2(l_i,L,l_n,0,0,0)\,\tilde{C}_{LM}(l_n,l_i,j) \end{aligned} \tag{A.7}$$

As noted above, Γ_{res} is the (tabulated) total line-width of the absorption edge. k is the modulus of the wave vector at the resonance energy and a_0 is the Bohr radius.

As seen in Eq. A.7, the amplitude coefficients are also proportional to the squares of radial matrix elements, which measures the overlap between the radial wave function of initial and excited states. Hamrick has evaluated these terms for a number of lanthanide and actinide ions using a Hartree-Fock-Slater algorithm [336]. It turns out that the results vary only little among ions of the same series. For example, the orbital overlap relevant for the L_3, $2p_{\frac{3}{2}} \leftrightarrow 4f$ electric quadrupole (E2) transition is

$$|\langle R_{4f}|(\frac{r}{a_0})^L|R_{2p_{3/2}}\rangle|^2 \approx 0.0020\text{–}0.0025 \tag{A.8}$$

The multipolar transition / selection rules in Eq. A.7 are encoded in the *reduced amplitude coefficient* $\tilde{C}_{LM}$:

$$\tilde{C}_{LM}(l_n,l_i,j) = \sum_{m_l^n,m_s^n} p(m_l^n,m_s^n)\,C^2(l_i,L,l_n;m_l^n-M,M,m_l^n)\,C^2(l_i,\frac{1}{2},j;m_l^n-M,m_s^n,m_l^n-M+m_s^n) \tag{A.9}$$

Here, the initial (core) and intermediate (valence) states are denoted by the quantum numbers

$$|i\rangle = |\ l_i,\ j,\ m_j\ \rangle \quad \text{and} \quad |n\rangle = |\ l_n,\ m_l^n,\ m_s^n\ \rangle \tag{A.10}$$

For example, the electronic dipole transitions at the rare earth L_3 edge excite $2p_3/2$ core electrons into $4f$ states, so

$$|i\rangle = |\ 1,\ 3/2,\ (-3/2 ... +3/2)\ \rangle \quad \text{and} \quad |n\rangle = |\ 3,\ (-3 ... +3),\ (\pm 1/2)\ \rangle \tag{A.11}$$

The factors $p(m_l^n, m_s^n)$ in Eq. A.9 are the occupation probabilities for states in the valence shell. For the ion Eu^{2+} ($4f^7$), this is a particularly clear-cut case:

m_s \ m_l^{4f}	3	2	1	0	-1	-2	-3
$+\frac{1}{2}$	1	1	1	1	1	1	1
$-\frac{1}{2}$	0	0	0	0	0	0	0

Thus, the x-ray resonant exchange scattering coefficients can be estimated by substituting Eqs. A.9, A.8 and A.7 into Eq. A.6.

Appendix B

Linear spin-wave theory

In reference to the inelastic neutron study of Chapter 4, I demonstrate how linear spin-wave theory can be used to derive the magnon dispersion and neutron scattering cross section of a collinear antiferromagnet. I start by separating the Heisenberg spin Hamiltonian (Eq. 4.1) into its exchange and one-ion anisotropy parts:

$$\hat{\mathcal{H}} = \sum_{\langle i,j \rangle} J_{i,j}\, \hat{S}_i \hat{S}_j - \sum_i D\,(S_i^z)^2 \tag{B.1}$$

$$\equiv \hat{\mathcal{H}}_J + \hat{\mathcal{H}}_D \tag{B.2}$$

Using the spin creation and annihilation operators

$$S^+ = S^x + iS^y \qquad\qquad S^- = S^x - iS^y \quad , \tag{B.3}$$

$\hat{\mathcal{H}}_J$ can be rewritten

$$\hat{\mathcal{H}}_J = \sum_{\langle i,j \rangle} J_{i,j} \left\{ S_i^z S_j^z + \frac{1}{2}\left(S_i^+ S_j^- + S_i^- S_j^+ \right) \right\} \quad . \tag{B.4}$$

Next, the summation can be simplified as follows. Instead of summing over all pairs $\langle i,j \rangle$, for each magnetic ion at a position $\mathbf{r}$, one sums over all possible exchange partners at relative positions $\mathbf{d}$.

$$\sum_{\langle i,j \rangle} \rightarrow \quad \frac{1}{2} \quad \sum_{\mathbf{r}} \sum_{\mathbf{d}} \tag{B.5}$$

As indicated in Fig. 4.3, the explicit form of the relative positions or *exchange paths* $\mathbf{d}$ will be

$$\begin{aligned} &\text{SrMnBi}_2\text{:} \quad \boldsymbol{d}_1 = \left(\frac{a}{2}, \frac{a}{2}, 0\right) \quad \boldsymbol{d}_2 = (a,0,0) \quad \boldsymbol{d}_c = \left(0,0,\frac{c}{2}\right) \\ &\text{CaMnBi}_2\text{:} \quad \boldsymbol{d}_1 = \left(\frac{a}{2}, \frac{a}{2}, 0\right) \quad \boldsymbol{d}_2 = (a,0,0) \quad \boldsymbol{d}_c = (0,0,c) \end{aligned} \tag{B.6}$$

Where $\boldsymbol{d}_{1/2/c}$ correspond to the exchange interactions $J_{1/2/c}$. Thus, the exchange Hamiltonian takes the form

$$\hat{\mathcal{H}}_J = \frac{1}{2} \sum_{\mathbf{r}} \sum_{\mathbf{d}} J_{\mathbf{r},\mathbf{d}} \left(P^A_{\mathbf{r},\mathbf{d}} + P^B_{\mathbf{r},\mathbf{d}} \right) \tag{B.7}$$

Here, I have explicitly separated the summation over the two sublattices A and B that carry antiparallel magnetic moments. The lattices A and B are offset from each other by an arbitray vector $\mathbf{a}$, which will not appear in the derived formulae.

$$P^A_{\mathbf{r},\mathbf{d}} = S^z_{\mathbf{r}} S^z_{\mathbf{r}+\mathbf{d}} + \frac{1}{2} \left(S^+_{\mathbf{r}} S^-_{\mathbf{r}+\mathbf{d}} + S^-_{\mathbf{r}} S^+_{\mathbf{r}+\mathbf{d}} \right) \tag{B.8}$$

$$P^B_{\mathbf{r},\mathbf{d}} = S^z_{\mathbf{r}+\mathbf{a}} S^z_{\mathbf{r}+\mathbf{a}+\mathbf{d}} + \frac{1}{2} \left(S^+_{\mathbf{r}+\mathbf{a}} S^-_{\mathbf{r}+\mathbf{a}+\mathbf{d}} + S^-_{\mathbf{r}+\mathbf{a}} S^+_{\mathbf{r}+\mathbf{a}+\mathbf{d}} \right) \tag{B.9}$$

Similarly, I split the anisotropy Hamiltonian into two sublattices:

$$\hat{\mathcal{H}}_D = -D \sum_{\mathbf{r}} \left[(S^z_{\mathbf{r}})^2 + (S^z_{\mathbf{r}+\mathbf{a}})^2 \right] \tag{B.10}$$

To evaluate these terms, they are now stated in second quantization. The spin raising and lowering operators are expressed as creation ($a^\dagger$,$b^\dagger$) and destruction (a,b) operators acting on two boson fields describing the sublattices A and B. The *Holstein-Primakoff* transformation operators are given by

$$\begin{aligned} S^+_A &= \sqrt{2S}\, a & S^+_B &= \sqrt{2S}\, b^\dagger \\ S^-_A &= \sqrt{2S}\, a^\dagger & S^-_B &= \sqrt{2S}\, b \\ S^z_A &= S - a^\dagger a & S^z_B &= -S + b^\dagger b \end{aligned}$$

When substituting these into Eq. B.8, a distinction has to be made whether the exchange partners connected by $\boldsymbol{d}$ are parallel ($\uparrow\uparrow$) or antiparallel ($\uparrow\downarrow$):

$$\begin{aligned} P^{A\uparrow\downarrow}_{\mathbf{r},\mathbf{d}} &= (S - a^\dagger_{\mathbf{r}} a_{\mathbf{r}})(-S + b^\dagger_{\mathbf{r}+\mathbf{d}} b_{\mathbf{r}+\mathbf{d}}) + S(a_{\mathbf{r}} b_{\mathbf{r}+\mathbf{d}} + a^\dagger_{\mathbf{r}} b^\dagger_{\mathbf{r}+\mathbf{d}}) \\ &\approx -S^2 + S(a^\dagger_{\mathbf{r}} a_{\mathbf{r}} + b^\dagger_{\mathbf{r}+\mathbf{d}} b_{\mathbf{r}+\mathbf{d}} + a_{\mathbf{r}} b_{\mathbf{r}+\mathbf{d}} + a^\dagger_{\mathbf{r}} b^\dagger_{\mathbf{r}+\mathbf{d}}) \\ P^{B\uparrow\downarrow}_{\mathbf{r},\mathbf{d}} &= (-S + b^\dagger_{\mathbf{r}+\mathbf{a}} b_{\mathbf{r}+\mathbf{a}})(S - a^\dagger_{\mathbf{r}+\mathbf{a}+\mathbf{d}} a_{\mathbf{r}+\mathbf{a}+\mathbf{d}}) + S(b^\dagger_{\mathbf{r}+\mathbf{a}} a^\dagger_{\mathbf{r}+\mathbf{a}+\mathbf{d}} + b_{\mathbf{r}+\mathbf{a}} a_{\mathbf{r}+\mathbf{a}+\mathbf{d}}) \\ &\approx -S^2 + S(b^\dagger_{\mathbf{r}+\mathbf{a}} b_{\mathbf{r}+\mathbf{a}} + a^\dagger_{\mathbf{r}+\mathbf{a}+\mathbf{d}} a_{\mathbf{r}+\mathbf{a}+\mathbf{d}} + b^\dagger_{\mathbf{r}+\mathbf{a}} a^\dagger_{\mathbf{r}+\mathbf{a}+\mathbf{d}} + b_{\mathbf{r}+\mathbf{a}} a_{\mathbf{r}+\mathbf{a}+\mathbf{d}}) \end{aligned}$$

and similarly, in the case of parallel neighbours:

$$\begin{aligned} P^{A\uparrow\uparrow}_{\mathbf{r},\mathbf{d}} &= (S - a^\dagger_{\mathbf{r}} a_{\mathbf{r}})(S - a^\dagger_{\mathbf{r}+\mathbf{d}} a_{\mathbf{r}+\mathbf{d}}) + S(a_{\mathbf{r}} a^\dagger_{\mathbf{r}+\mathbf{d}} + a^\dagger_{\mathbf{r}} a_{\mathbf{r}+\mathbf{d}}) \\ &\approx S^2 + S(-a^\dagger_{\mathbf{r}} a_{\mathbf{r}} - a^\dagger_{\mathbf{r}+\mathbf{d}} a_{\mathbf{r}+\mathbf{d}} + a_{\mathbf{r}} a^\dagger_{\mathbf{r}+\mathbf{d}} + a^\dagger_{\mathbf{r}} a_{\mathbf{r}+\mathbf{d}}) \\ P^{B\uparrow\uparrow}_{\mathbf{r},\mathbf{d}} &= (-S + b^\dagger_{\mathbf{r}+\mathbf{a}} b_{\mathbf{r}+\mathbf{a}})(-S + b^\dagger_{\mathbf{r}+\mathbf{a}+\mathbf{d}} b_{\mathbf{r}+\mathbf{a}+\mathbf{d}}) + S(b^\dagger_{\mathbf{r}+\mathbf{a}} b^\dagger_{\mathbf{r}+\mathbf{a}+\mathbf{d}} + b_{\mathbf{r}+\mathbf{a}} b_{\mathbf{r}+\mathbf{a}+\mathbf{d}}) \\ &\approx S^2 + S(-b^\dagger_{\mathbf{r}+\mathbf{a}} b_{\mathbf{r}+\mathbf{a}} - b^\dagger_{\mathbf{r}+\mathbf{a}+\mathbf{d}} b_{\mathbf{r}+\mathbf{a}+\mathbf{d}} + b^\dagger_{\mathbf{r}+\mathbf{a}} b_{\mathbf{r}+\mathbf{a}+\mathbf{d}} + b_{\mathbf{r}+\mathbf{a}} b^\dagger_{\mathbf{r}+\mathbf{a}+\mathbf{d}}) \end{aligned}$$

The anisotropy Hamiltonian (Eq. B.10) can also be stated in terms of Holstein-Primakoff operators:

$$\begin{aligned}\hat{\mathcal{H}}_D &= -D\sum_{\mathbf{r}}\left[(S-a^\dagger_{\mathbf{r}}a_{\mathbf{r}})^2+(-S+b^\dagger_{\mathbf{r}+\mathbf{a}}b_{\mathbf{r}+\mathbf{a}})^2\right]\\ &\approx -2DS\sum_{\mathbf{r}}\left[S-a^\dagger_{\mathbf{r}}a_{\mathbf{r}}-b^\dagger_{\mathbf{r}+\mathbf{a}}b_{\mathbf{r}+\mathbf{a}}\right]\end{aligned} \tag{B.11}$$

In the case of AMnBi$_2$, the nearest neighbours ($\boldsymbol{d}_1$, J_1) are antiparallel, the next nearest neighbours ($\boldsymbol{d}_2$, J_2) are parallel, and the stacking of the layers ($\boldsymbol{d}_c$, J_c) is parallel for A =Ca and antiparallel for A =Sr (see Fig. 4.3(a)). The sum over $\sum_{\mathbf{d}} J_{\mathbf{r},\mathbf{d}}$ in Eq. B.7 will therefore split into six parts:

$$\begin{aligned}\hat{\mathcal{H}}_J = \frac{1}{2}\sum_{\mathbf{r}}\Bigg\{&\sum_{\mathbf{d}_1}J_1\left(P^{A\uparrow\downarrow}_{\mathbf{r},\mathbf{d}_1}+P^{B\uparrow\downarrow}_{\mathbf{r},\mathbf{d}_1}\right)+\sum_{\mathbf{d}_2}J_2\left(P^{A\uparrow\uparrow}_{\mathbf{r},\mathbf{d}_2}+P^{B\uparrow\uparrow}_{\mathbf{r},\mathbf{d}_2}\right)+\sum_{\mathbf{d}_c}J_c\left(P^{A}_{\mathbf{r},\mathbf{d}_c}+P^{B}_{\mathbf{r},\mathbf{d}_c}\right)\Bigg\}\\ :=\quad &\hat{\mathcal{H}}^A_{J1}+\hat{\mathcal{H}}^B_{J1}+\hat{\mathcal{H}}^A_{J2}+\hat{\mathcal{H}}^B_{J2}+\hat{\mathcal{H}}^A_{Jc}+\hat{\mathcal{H}}^B_{Jc}\end{aligned} \tag{B.12}$$

These $\hat{\mathcal{H}}_J$ are now evaluated by Fourier transformation of the exchange parameters:

$$\mathcal{J}_1(\mathbf{Q})=\sum_{\mathbf{d}_1}J_1\,e^{i\,\mathbf{Q}\mathbf{d}_1}\qquad \mathcal{J}_2(\mathbf{Q})=\sum_{\mathbf{d}_2}J_2\,e^{i\,\mathbf{Q}\mathbf{d}_2}\qquad \mathcal{J}_c(\mathbf{Q})=\sum_{\mathbf{d}_c}J_c\,e^{i\,\mathbf{Q}\mathbf{d}_c}$$

And Fourier transformation of the Holstein Primakoff operators:

$$a_{\mathbf{r}}=\frac{1}{\sqrt{N}}\sum_{\mathbf{Q}}e^{i\,\mathbf{Q}\mathbf{r}}a_{\mathbf{Q}}\qquad b_{\mathbf{r}}=\frac{1}{\sqrt{N}}\sum_{\mathbf{Q}}e^{i\,\mathbf{Q}\mathbf{r}}b_{\mathbf{Q}}$$

$$a^\dagger_{\mathbf{r}}=\frac{1}{\sqrt{N}}\sum_{\mathbf{Q}}e^{-i\,\mathbf{Q}\mathbf{r}}a^\dagger_{\mathbf{Q}}\qquad b^\dagger_{\mathbf{r}}=\frac{1}{\sqrt{N}}\sum_{\mathbf{Q}}e^{-i\,\mathbf{Q}\mathbf{r}}b^\dagger_{\mathbf{Q}}$$

By carrying out these sums, one gets, for example:

$$\begin{aligned}
\hat{\mathcal{H}}^A_{J1} &= \frac{1}{2}\sum_{\mathbf{r}}\sum_{\mathbf{d}_1} J_1\, P^{A\uparrow\downarrow}_{\mathbf{r},\mathbf{d}_1} \\
&\approx \frac{1}{2}\sum_{\mathbf{r}}\sum_{\mathbf{d}_1} J_1\, \left[-S^2 + S(a^\dagger_{\mathbf{r}} a_{\mathbf{r}} + b^\dagger_{\mathbf{r}+\mathbf{d}_1} b_{\mathbf{r}+\mathbf{d}_1} + a_{\mathbf{r}} b_{\mathbf{r}+\mathbf{d}_1} + a^\dagger_{\mathbf{r}} b^\dagger_{\mathbf{r}+\mathbf{d}_1})\right] \\
&= -\frac{1}{2}S^2 \sum_{\mathbf{r}}\sum_{\mathbf{d}_1} J_1 + \frac{1}{2}S\sum_{\mathbf{Q}}\sum_{\mathbf{d}_1} J_1 \left(a^\dagger_{\mathbf{Q}} a_{\mathbf{Q}} + b^\dagger_{\mathbf{Q}} b_{\mathbf{Q}} + e^{i\mathbf{Q}\mathbf{d}_1} a_{-\mathbf{Q}} b_{\mathbf{Q}} + e^{i\mathbf{Q}\mathbf{d}_1} a^\dagger_{\mathbf{Q}} b^\dagger_{-\mathbf{Q}}\right) \\
&= -\frac{1}{2}NS^2\, \mathcal{J}_1(0) + \frac{1}{2}S\sum_{\mathbf{Q}} \left[\mathcal{J}_1(0)\,(a^\dagger_{\mathbf{Q}} a_{\mathbf{Q}} + b^\dagger_{\mathbf{Q}} b_{\mathbf{Q}}) + \mathcal{J}_1(\mathbf{Q})\,(a_{-\mathbf{Q}} b_{\mathbf{Q}} + a^\dagger_{\mathbf{Q}} b^\dagger_{-\mathbf{Q}})\right] \\
&= -\frac{1}{2}NS^2\, \mathcal{J}_1(0) - \frac{1}{2}NS\mathcal{J}_1(0) + \frac{1}{4}S\sum_{\mathbf{Q}} \Big[\mathcal{J}_1(0)\,(a^\dagger_{\mathbf{Q}} a_{\mathbf{Q}} + a_{-\mathbf{Q}} a^\dagger_{-\mathbf{Q}} + b^\dagger_{\mathbf{Q}} b_{\mathbf{Q}} + b_{-\mathbf{Q}} b^\dagger_{-\mathbf{Q}}) + \\
&\qquad + \mathcal{J}_1(\mathbf{Q})\,(a_{-\mathbf{Q}} b_{\mathbf{Q}} + a^\dagger_{\mathbf{Q}} b^\dagger_{-\mathbf{Q}} + b^\dagger_{\mathbf{Q}} a^\dagger_{-\mathbf{Q}} + b_{-\mathbf{Q}} a_{\mathbf{Q}})\Big] \\
&\equiv -\frac{1}{2}NS(S+1)\,\mathcal{J}_1(0) + \frac{1}{4}S\sum_{\mathbf{Q}} [\mathcal{J}_1(0)\,\hat{v}_1 + \mathcal{J}_1(\boldsymbol{Q})\,\hat{v}_2]
\end{aligned}$$

Here, I have used the commutation relations of Holstein-Primakoff operators,

$$\begin{pmatrix}
[a_{\mathbf{Q}}, a^\dagger_{\mathbf{Q}}] & [a_{\mathbf{Q}}, b^\dagger_{\mathbf{Q}}] & [a_{\mathbf{Q}}, a_{-\mathbf{Q}}] & [a_{\mathbf{Q}}, b_{-\mathbf{Q}}] \\
[b_{\mathbf{Q}}, a^\dagger_{\mathbf{Q}}] & [b_{\mathbf{Q}}, b^\dagger_{\mathbf{Q}}] & [b_{\mathbf{Q}}, a_{-\mathbf{Q}}] & [b_{\mathbf{Q}}, b_{-\mathbf{Q}}] \\
[a^\dagger_{-\mathbf{Q}}, a^\dagger_{\mathbf{Q}}] & [a^\dagger_{-\mathbf{Q}}, b^\dagger_{\mathbf{Q}}] & [a^\dagger_{-\mathbf{Q}}, a_{-\mathbf{Q}}] & [a^\dagger_{-\mathbf{Q}}, b_{-\mathbf{Q}}] \\
[b^\dagger_{-\mathbf{Q}}, a^\dagger_{\mathbf{Q}}] & [b^\dagger_{-\mathbf{Q}}, b^\dagger_{\mathbf{Q}}] & [b^\dagger_{-\mathbf{Q}}, a_{-\mathbf{Q}}] & [b^\dagger_{-\mathbf{Q}}, b_{-\mathbf{Q}}]
\end{pmatrix} = \begin{pmatrix}
1 & 0 & 0 & 0 \\
0 & 1 & 0 & 0 \\
0 & 0 & -1 & 0 \\
0 & 0 & 0 & -1
\end{pmatrix} \quad . \tag{B.13}$$

Along with the relations $b_{-\mathbf{Q}} a_{\mathbf{Q}} = b_{\mathbf{Q}} a_{-\mathbf{Q}}$ (etc.), this allows some terms to be written in a more symmetrical form:

$$\begin{aligned}
a^\dagger_{\mathbf{Q}} a_{\mathbf{Q}} &= {}^1\!/_2\,(a^\dagger_{\mathbf{Q}} a_{\mathbf{Q}}) \;+\; {}^1\!/_2\,(a_{-\mathbf{Q}} a^\dagger_{-\mathbf{Q}}) \;-\; {}^1\!/_2 \\
b^\dagger_{\mathbf{Q}} b_{\mathbf{Q}} &= {}^1\!/_2\,(b^\dagger_{\mathbf{Q}} b_{\mathbf{Q}}) \;+\; {}^1\!/_2\,(b_{-\mathbf{Q}} b^\dagger_{-\mathbf{Q}}) \;-\; {}^1\!/_2 \\
a_{-\mathbf{Q}} b_{\mathbf{Q}} &= {}^1\!/_2\,(a_{-\mathbf{Q}} b_{\mathbf{Q}}) \;+\; {}^1\!/_2\,(b_{-\mathbf{Q}} a_{\mathbf{Q}}) \\
a^\dagger_{\mathbf{Q}} b^\dagger_{-\mathbf{Q}} &= {}^1\!/_2\,(a^\dagger_{\mathbf{Q}} b^\dagger_{-\mathbf{Q}}) \;+\; {}^1\!/_2\,(b^\dagger_{\mathbf{Q}} a^\dagger_{-\mathbf{Q}}) \quad ,
\end{aligned} \tag{B.14}$$

and thus introduce the abbreviations

$$\begin{aligned}
\hat{v}_1 &:= (a^\dagger_{\mathbf{Q}} a_{\mathbf{Q}} + a_{-\mathbf{Q}} a^\dagger_{-\mathbf{Q}} + b^\dagger_{\mathbf{Q}} b_{\mathbf{Q}} + b_{-\mathbf{Q}} b^\dagger_{-\mathbf{Q}}) \\
\hat{v}_2 &:= (a_{-\mathbf{Q}} b_{\mathbf{Q}} + a^\dagger_{\mathbf{Q}} b^\dagger_{-\mathbf{Q}} + b^\dagger_{\mathbf{Q}} a^\dagger_{-\mathbf{Q}} + b_{-\mathbf{Q}} a_{\mathbf{Q}})
\end{aligned} \tag{B.15}$$

Futhermore, by use of the commutation relations, one finds that

$$\hat{\mathcal{H}}^A_{J1} \;=\; \hat{\mathcal{H}}^B_{J1}$$

and similarly, it follows that

$$\begin{aligned}
\hat{\mathcal{H}}^A_{J2} &= \frac{1}{2}NS(S+1)\,\mathcal{J}_2(0)+\frac{1}{2}S\sum_{\mathbf{Q}}\left[(-\mathcal{J}_2(0)+\mathcal{J}_2(\mathbf{Q}))\,(a^\dagger_{\mathbf{Q}}a_{\mathbf{Q}}+a_{-\mathbf{Q}}a^\dagger_{-\mathbf{Q}})\right]\\
\hat{\mathcal{H}}^B_{J2} &= \frac{1}{2}NS(S+1)\,\mathcal{J}_2(0)+\frac{1}{2}S\sum_{\mathbf{Q}}\left[(-\mathcal{J}_2(0)+\mathcal{J}_2(\mathbf{Q}))\,(b^\dagger_{\mathbf{Q}}b_{\mathbf{Q}}+b_{-\mathbf{Q}}b^\dagger_{-\mathbf{Q}})\right]\\
\hat{\mathcal{H}}_D &= -NS(S+1)\,(2D)+\frac{1}{2}S\sum_{\mathbf{Q}}[2D\,\hat{v}_1]
\end{aligned}$$

The interlayer $\hat{\mathcal{H}}^{A,B}_c$ terms correspond directly to $\hat{\mathcal{H}}^{A,B}_1$ or $\hat{\mathcal{H}}^{A,B}_2$, in the cases of antiferromagnetic ($SrMnBi_2$) or ferromagnetic ($CaMnBi_2$) stacking, respectively. Therefore, adding the terms of the two sublattices back together gives

$$\begin{aligned}
\hat{\mathcal{H}}^A_{J1}+\hat{\mathcal{H}}^B_{J1} &= -NS(S+1)\,\mathcal{J}_1(0)+\frac{1}{2}S\sum_{\mathbf{Q}}[\mathcal{J}_1(0)\,\hat{v}_1+\mathcal{J}_1(\mathbf{Q})\,\hat{v}_2]\\
\hat{\mathcal{H}}^A_{J2}+\hat{\mathcal{H}}^B_{J2} &= +NS(S+1)\,\mathcal{J}_2(0)+\frac{1}{2}S\sum_{\mathbf{Q}}[-\mathcal{J}_2(0)\,\hat{v}_1+\mathcal{J}_2(\mathbf{Q})\,\hat{v}_1]\\
\left(\hat{\mathcal{H}}^A_{Jc}+\hat{\mathcal{H}}^B_{Jc}\right)\ {\scriptstyle\begin{matrix}\mathrm{Sr}\\ \mathrm{Ca}\end{matrix}} &= {\scriptstyle\begin{matrix}-\\+\end{matrix}}\ NS(S+1)\,\mathcal{J}_c(0)+\frac{1}{2}S\sum_{\mathbf{Q}}\left[\ {\scriptstyle\begin{matrix}+\\-\end{matrix}}\ \mathcal{J}_c(0)\,\hat{v}_1+\mathcal{J}_c(\mathbf{Q})\ {\scriptstyle\begin{matrix}\hat{v}_2\\ \hat{v}_1\end{matrix}}\ \right]
\end{aligned} \tag{B.16}$$

After collecting all terms, the Fourier transformation of Eq. B.1 becomes

$$\boxed{\mathcal{H}\ {\scriptstyle\begin{matrix}\mathrm{Sr}\\ \mathrm{Ca}\end{matrix}}\ =-NS(S+1)\left(\mathcal{J}_1(0)-\mathcal{J}_2(0)\ {\scriptstyle\begin{matrix}+\\-\end{matrix}}\ \mathcal{J}_c(0)+2D\right)+\frac{1}{2}\sum_{\mathbf{Q}}[\hat{v}_1 A+\hat{v}_2 B]} \tag{B.17}$$

where

$$\begin{aligned}
A &= S\,(\mathcal{J}_{\mathrm{AF}}(0)-\mathcal{J}_{\mathrm{F}}(0)+\mathcal{J}_{\mathrm{F}}(\boldsymbol{Q})+2D)\\
B &= S\,\mathcal{J}_{\mathrm{AF}}(\boldsymbol{Q})
\end{aligned} \tag{B.18}$$

and the ferromagnetic and antiferromagnetic exchange terms have been collected as

$$\mathcal{J}_{\mathrm{F}}=\begin{cases}\mathcal{J}_2\\ \mathcal{J}_2+\mathcal{J}_c\end{cases}\quad\text{and}\quad\mathcal{J}_{\mathrm{AF}}=\begin{cases}\mathcal{J}_1+\mathcal{J}_c & (SrMnBi_2)\\ \mathcal{J}_1 & (CaMnBi_2)\end{cases} \tag{B.19}$$

The boson operators from Eq. B.15 can be substituted back to obtain a general expression of Eq. B.17 in the basis of $X=(a_{\mathbf{Q}},b_{\mathbf{Q}},a^\dagger_{-\mathbf{Q}},b^\dagger_{-\mathbf{Q}})$:

$$\mathcal{H}=\mathcal{H}_0+\frac{1}{2}\sum_{\mathbf{Q}}X^\dagger_{\mathbf{Q}}H_{\mathbf{Q}}X_{\mathbf{Q}} \tag{B.20}$$

with

$$H_{\mathbf{Q}} = \begin{pmatrix} A & 0 & 0 & B \\ 0 & A & B & 0 \\ 0 & B & A & 0 \\ B & 0 & 0 & A \end{pmatrix} \quad , \tag{B.21}$$

The eigenvalue E is given by the condition

$$|\boldsymbol{g} H_{\mathbf{Q}} - E\mathbb{1}| \stackrel{!}{=} 0 \quad , \text{ with } \quad \boldsymbol{g} = [X, X^{\dagger}] = \begin{pmatrix} 1 & 0 & 0 & 0 \\ 0 & 1 & 0 & 0 \\ 0 & 0 & -1 & 0 \\ 0 & 0 & 0 & -1 \end{pmatrix} \quad . \tag{B.22}$$

Thus, one obtains the magnon dispersion

$$\boxed{E = \sqrt{A^2 - B^2}} \tag{B.23}$$

As introduced in Eq. 2.37 (Chapter 2.3.2), the double differential magnetic neutron scattering cross section is given by

$$\frac{\mathrm{d}\sigma}{\mathrm{d}\Omega \mathrm{d}\omega} = \left(\frac{\gamma r_0 g}{2}\right)^2 \frac{k_f}{k_i} F^2(\boldsymbol{Q})\, e^{-2W(\boldsymbol{Q})} \sum_{\alpha,\beta} \left(\delta_{\alpha\beta} - \hat{Q}_\alpha \hat{Q}_\beta\right) S_{\alpha\beta}(\boldsymbol{Q}, \omega) \ , \tag{B.24}$$

In the present case of a c axis collinear antiferromagnet, all off-diagonal terms of $S_{\alpha\beta}$ vanish and S_{zz} contributes only elastic scattering. From Eq. 2.38, (with the same notation as in Chapter 2.3.2),

$$S_{xx}(\boldsymbol{Q}, \omega) = \sum_{\lambda_i, \lambda_f} p_{\lambda_i} \langle \lambda_i | S^{x\dagger}(\boldsymbol{Q}) | \lambda_f \rangle \langle \lambda_f | S^{x}(\boldsymbol{Q}) | \lambda_i \rangle \, \delta(\hbar\omega - (E_f - E_i)) \tag{B.25}$$

In analogy to the diagonalization of the Hamiltonian, these terms are evaluated in second quantization, with the result (for neutron energy-loss processes)

$$S_{xx} = S_{yy} = NS \frac{A - B}{E} \frac{1}{1 - e^{-\beta\hbar\omega}} \delta(\hbar\omega - E) \tag{B.26}$$

By substituting this ino Eq. B.24, the orientation factor can be simplified and the cross section becomes

$$\boxed{\frac{\mathrm{d}\sigma}{\mathrm{d}\Omega \mathrm{d}\omega} = \left(\frac{\gamma r_0 g}{2}\right)^2 \frac{k_f}{k_i} F^2(\boldsymbol{Q})\, e^{-2W(\boldsymbol{Q})} \left(1 + \hat{Q}_z^2\right) NS \frac{A - B}{E} \frac{1}{1 - e^{-\beta\hbar\omega}} \delta(\hbar\omega - E)} \tag{B.27}$$

To avoid clutter, the Debye-Waller factor has been omitted in the main text (Eq. 4.4).

Appendix C

REXS polarization analysis

The formalism of x-ray full polarization analysis (FPA) has been summarized by Detlefs *et al.* [337]. Useful discussions of the technique are also found in several reports of successful FPA studies [445, 483, 484]. Here I give a brief presentation of the concepts that are relevant to the data analysis of Chapter 5.

The electric field $\boldsymbol{E}$ of an x-ray beam of energy $\hbar\omega$ and wave vector $\boldsymbol{k}$ can be decomposed into two orthogonal amplitudes V_1 and V_2.

$$\boldsymbol{E}(t,\boldsymbol{r}) = \Re\left[(V_1\,\hat{\boldsymbol{\varepsilon}}_\sigma + V_2\,\hat{\boldsymbol{\varepsilon}}_\pi)\cdot e^{-i(\omega t - \boldsymbol{k}\cdot\boldsymbol{r})}\right] \quad , \tag{C.1}$$

where $\Re$ signifies the real part of this field. This is not relevant in the linearly polarized case, where the *Jones* polarization vector,

$$\hat{\boldsymbol{\varepsilon}} = \begin{pmatrix} V_1 \\ V_2 \end{pmatrix} = \begin{pmatrix} \cos\eta \\ \sin\eta \end{pmatrix} \tag{C.2}$$

has no imaginary components. As shown in Fig. 5.5(a,b), the unit vectors $\hat{\boldsymbol{\varepsilon}}_\sigma$, $\hat{\boldsymbol{\varepsilon}}_\pi$ and $\hat{\boldsymbol{k}}$ form a right-handed coordinate system. For linearly polarized light, the Jones vector can thus be reduced to the polarization angle η, as shown in Fig. 5.5(c).

The polarization state of the beam is described by the Poincaré-Stokes vector (P_1, P_2, P_3), which is defined as

$$\begin{aligned} P_1 &= \frac{|V_1|^2 - |V_2|^2}{|V_1|^2 + |V_2|^2} \\ P_2 &= \frac{|V_1 + V_2|^2 - |V_1 - V_2|^2}{2\,(|V_1|^2 + |V_2|^2)} \\ P_3 &= \frac{(|V_1 - iV_2|^2 - |V_1 + iV_2|^2)}{2\,(|V_1|^2 + |V_2|^2)} \end{aligned} \tag{C.3}$$

For fully linearly polarized light, P_3 vanishes and the degree of linear polarization is unity,

$$P_{\mathrm{lin}} = \sqrt{P_1^2 + P_2^2} \to 1 \tag{C.4}$$

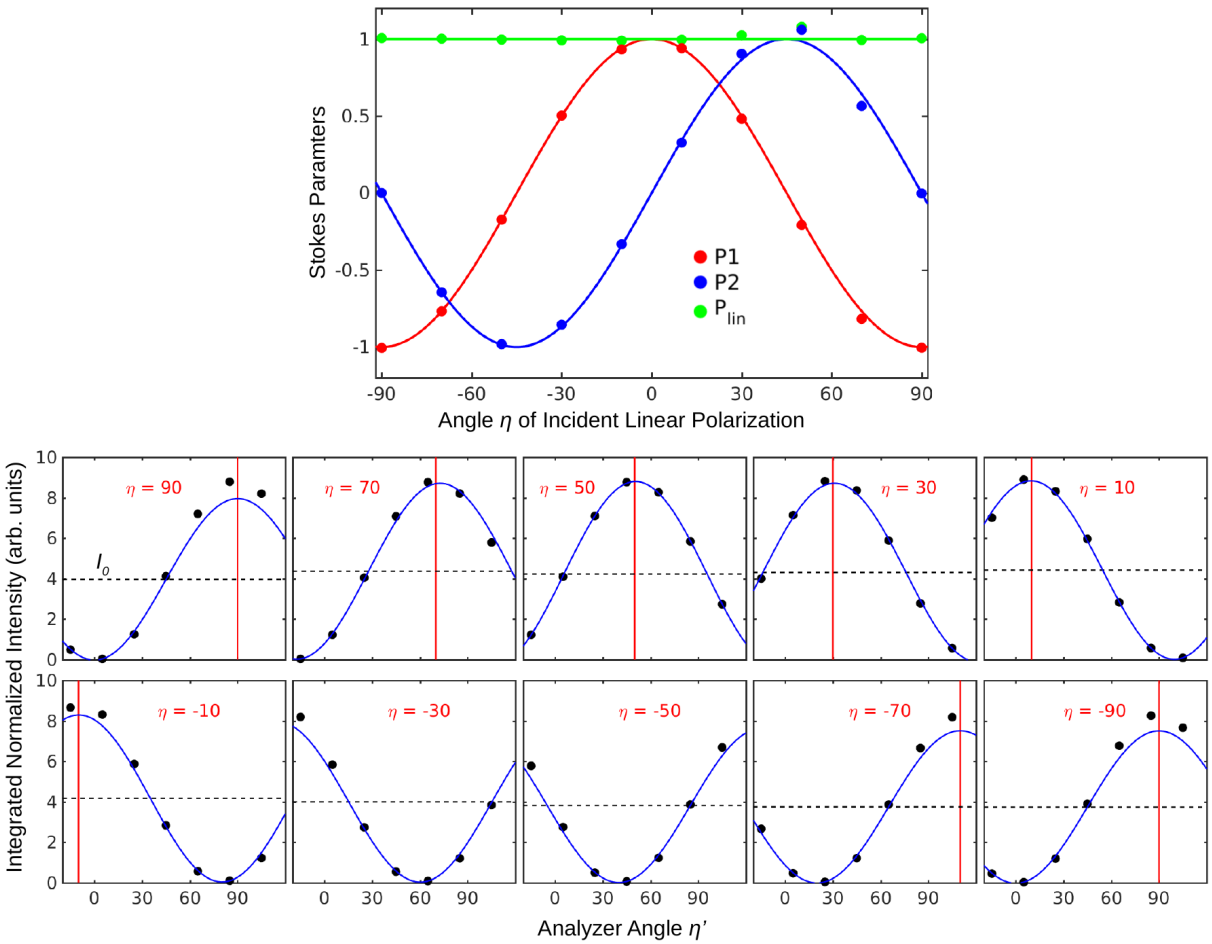

Figure C.1: Full polarization analysis of the direct beam at beamline P09 (DESY). The Stokes parameters follow Eq. C.5, which confirms that the beam is fully linearly polarized for any setting of the phase retarder. Each set of (P_1, P_2) plotted in the top panel is obtained by fitting Eq. C.6 to the integrated intensities (black markers) shown in the bottom panels (best fit indicated as a blue line).

By combining Eqs. C.2 and C.3, it also follows that in this case

$$P_1 = \cos 2\eta \quad \text{and} \quad P_2 = \sin 2\eta \quad . \tag{C.5}$$

These characteristics are confirmed by the FPA scan of the direct beam at beamline P09 (DESY) shown in Figure C.1, top panel. To obtain these parameters, the phase plates were rotated in ten steps, corresponding to ten angles of incident linear polarization η between $-90°$ and $+90°$. For each incident polarization, rocking scans of the analyzer crystal were measured at seven analyzer angles η' between $-15°$ and $+105°$. The integrated intensities of these rocking curves are shown in the bottom panels of Fig. C.1.

As gleaned from Eq. C.5, the Stokes parameters P_1, P_2 quantify whether these η'-scans are more cosine- or sine-like. They can thus be extracted by fitting the relation

$$I(\eta') = I_0 + I_0 \left(P_1 \cos 2\eta' + P_2 \sin 2\eta'\right) \tag{C.6}$$

In the study of $EuCd_2As_2$ in Chapter 5, I used the same type of analysis to obtain the Stokes parameters (P_1', P_2') of magnetically scattered x-rays (shown in Figs. 5.9 and 5.10). The effect of the scattering process on the polarization state can be obtained in the *coherency matrix* formalism [337]. The incoming beam is described by the density matrix

$$\rho = c/2\,(\mathbf{1} + \sigma \cdot \mathbf{P}) \tag{C.7}$$

where c is an arbitrary intensity constant, $\mathbf{P} = (P_1, P_2, P_3)$ and $\sigma = (\sigma_1, \sigma_2, \sigma_3)$ is the vector of Pauli matrices,

$$\sigma_1 = \begin{pmatrix} 1 & 0 \\ 0 & -1 \end{pmatrix} \quad , \quad \sigma_2 = \begin{pmatrix} 0 & 1 \\ 1 & 0 \end{pmatrix} \quad , \quad \sigma_3 = \begin{pmatrix} 0 & i \\ -i & 0 \end{pmatrix} \tag{C.8}$$

For a scattering process with a tensor scattering amplitude

$$F = \begin{pmatrix} \sigma\sigma' & \pi\sigma' \\ \sigma\pi' & \pi\pi' \end{pmatrix} \tag{C.9}$$

The scattered beam is described by the density matrix

$$\rho' = F \cdot \rho \cdot F^{\dagger} \tag{C.10}$$

And the Stokes parameters describing the scattered intensity are then obtained from

$$P_i' = \frac{\mathrm{tr}(\sigma_i \cdot \rho')}{\mathrm{tr}(\rho')} \qquad (i = 1,2,3) \tag{C.11}$$

By substituting the relevant REXS scattering amplitude for F, the Stokes parameters can thus be simulated for a given magnetic structure.

In the context of Chapter 5, I also considered situations in which the probed sample volume contains several magnetic domains. To determine the effect of these contributions, I calculated Stokes parameters $P_1'^i$ and $P_2'^i$ for N domains ($i = 1$–N). Each domain contributes an intensity $I^i(\eta') \propto I_0^i$ as in Eq. C.6 which add to the total signal:

$$I(\eta') = I_{\mathrm{tot}} + I_{\mathrm{tot}} \left(P_1^{\mathrm{eff}} \cos 2\eta' + P_2^{\mathrm{eff}} \sin 2\eta' \right) \tag{C.12}$$

The *effective* Stokes parameters are therefore obtained as weighted sums,

$$P_1^{\mathrm{eff}} = \frac{\sum I_0^i P_1'^i}{I_{\mathrm{tot}}} \quad , \quad P_2^{\mathrm{eff}} = \frac{\sum I_0^i P_2'^i}{I_{\mathrm{tot}}} \quad , \text{with } \; I_{\mathrm{tot}} = \sum I_0^i \tag{C.13}$$